



저작자표시-비영리-변경금지 2.0 대한민국

이용자는 아래의 조건을 따르는 경우에 한하여 자유롭게

- 이 저작물을 복제, 배포, 전송, 전시, 공연 및 방송할 수 있습니다.

다음과 같은 조건을 따라야 합니다:



저작자표시. 귀하는 원저작자를 표시하여야 합니다.



비영리. 귀하는 이 저작물을 영리 목적으로 이용할 수 없습니다.



변경금지. 귀하는 이 저작물을 개작, 변형 또는 가공할 수 없습니다.

- 귀하는, 이 저작물의 재이용이나 배포의 경우, 이 저작물에 적용된 이용허락조건을 명확하게 나타내어야 합니다.
- 저작권자로부터 별도의 허가를 받으면 이러한 조건들은 적용되지 않습니다.

저작권법에 따른 이용자의 권리는 위의 내용에 의하여 영향을 받지 않습니다.

이것은 [이용허락규약\(Legal Code\)](#)을 이해하기 쉽게 요약한 것입니다.

[Disclaimer](#)

Ph. D. DISSERTATION

Soft, Fully-Integrated Electronic Skin
Based on Printing Techniques

인쇄 공정 기법을 이용한 통합된 소프트
전자 피부 구현에 관한 연구

BY

JUNGHWAN BYUN

AUGUST 2017

DEPARTMENT OF ELECTRICAL ENGINEERING AND
COMPUTER SCIENCE
COLLEGE OF ENGINEERING
SEOUL NATIONAL UNIVERSITY

Abstract

Soft, Fully-Integrated Electronic Skin Based on Printing Techniques

JUNGHWAN BYUN

DEPARTMENT OF ELECTRICAL ENGINEERING AND
COMPUTER SCIENCE

COLLEGE OF ENGINEERING

SEOUL NATIONAL UNIVERSITY

Electronics is generally rigid and brittle, possessing intrinsic dissimilarity in physical forms with human and nature. Nowadays, introducing softness in electronic devices and circuits has substantially advanced a new class of electronics that can provide numerous opportunities to bridge the gap between electronics and nature in terms of interfacing and associated functionalities. Significant insights and technologies were engaged into establishing novel materials, architectural modeling, and underlying mechanics, all of which formed the basis of soft-type electronics beyond flexible; concurrently allowing unprecedented capabilities of soft interfacing with biological organs

and gleaning a wide spectrum of intimate bio-signals. On the basis of accumulated knowledge, an extended stream of studies on soft electronics now leads to a system-level integration, not settling for the scheme of a single device level. However, existing studies that approached system-level soft electronics mostly addressed incomplete configurations in which softness was satisfied only for a small portion of an entire system, mainly interconnects and sensors; functionally deficient in data processing and computing parts. The resulting situation proclaimed the use of “rigid” circuits (like printed circuit boards, PCBs) and bulky wires for computation and data transmission in most soft electronic systems. These requirements, rising from the inability to design and fabricate the miniaturized form of soft data processing/computing circuits, are counterintuitive and limit the further advancement in soft electronics. As a result, it is easy to conclude that there still exist substantial hurdles in soft electronics with a link to human and nature.

In this dissertation, such discrepancy in layouts and functions of soft electronics—partially soft in most cases— is surmounted by the concept of “Fully-Integrated Electronic Skin” that offers integrated functionalities of sensing, high-speed data processing/computing, signal modulation, and even wireless RF communication “in the skin”. In this concept, bulky wires for data transmission/reception and rigid PCBs located in external sites as computational backbones are not required, rather fully integrated in a soft platform with custom-built, miniaturized, hybrid-type designs. From a

technical point of view, the fully-integrated concept is achieved by a fully printable methodology that addresses both soft substrate engineering for reliable device integration and electronic functionalization for stretchable circuit fabrication. For soft substrate engineering, printed architectures—namely, “Printed Rigid Islands”—are exploited to build reliable sites on a soft foundation with in-depth consideration of geometry/morphology engineering and corresponding quantitative surface strain analysis for structural optimization of rigid islands through a digital image correlation method. For stretchable (or soft) circuit design and fabrication, combinational methodologies of inkjet-printed multilayer interconnection wiring, image-based customizable circuit routing, and robust surface-mountable device bonding establish an optimized scheme for printing-based implementation of system-level, hybrid-type soft electronics. To verify the feasibility of this methodology, various complete examples of soft electronic systems with distinct circuit configurations are demonstrated.

Advanced capabilities of rapid prototyping, high-performance operation, and “in-skin” functionalities suggest that our fully-integrated e-skin concept would provide potential for grafting soft electronics into unprecedented subjects with the ability to construct much complex network layouts and functions between numerous IC devices. In this respect, we extend the study to an unexplored field of highly integrated, high-speed self-computable electronic skin. Given the geometric insight of double-side capability, the first demonstration of fully-printed, double-side integrated,

stretchable 1 MHz computational logic networks that offer practical data processing is accomplished. Furthermore, as an exceptional application with augmented in-skin functionalities, a newly devised concept of wirelessly interfaced electronic skins for innervating soft robots is demonstrated—the first conceptual demonstration of implanting integrated soft electronics into soft robotics as an embedded driving circuit. Suggestive of physical appearance in biological models, this soft electronic skin innervates and wirelessly controls soft robots, which is initially dormant, in a fully embedded form.

Although a range of applications this dissertation covers is not sufficient for covering all subjects of soft features, it is significant that the presented methodology could offer an invaluable solution to the bottleneck in implementing stretchable computing circuits, the most critical hurdle for “entirely” stretchable electronics. Also, it is strongly expected that a newly exploited concept of the innervating e-skin as an electronic nervous system in soft robots would inspire upcoming studies to bring into unexplored perspectives that might address soft IoTs between e-skins and/or intimate communication (or automated feedback) with biological living bodies such as plants.

Keywords : Stretchable electronics, Electronic skin, Printed electronics, Skin computer, Soft robot

Student Number : 2011-20858

Contents

Abstract	i
Contents	v
List of Tables	ix
List of Figures	x
Chapter 1. Introduction	1
1.1 Stretchable Electronics	2
1.2 Core Technologies for Stretchable Electronics	7
1.2.1 Interconnection Architecture	7
1.2.2 Novel Materials	13
1.2.3 Strain Isolation Structure for Device Protection	19
1.3 Motivation and Main Concept: Fully-Integrated Soft Electronics	23

Chapter 2. Printing-based Soft Substrate Engineering	29
2.1 Printed Rigid Island (PRI)	30
2.1.1 Materials and Equipment	30
2.1.2 Piezoelectric Control Inkjet-based PRI	32
2.1.3 Pneumatic Control Nozzle-jet-based PRI	37
2.1.4 PRI-embedded Soft Substrate (PRISS)	41
2.2 Surface Strain Analysis of Engineered Soft Substrate	50
2.2.1 Digital Image Correlation (DIC)	50
2.2.2 Surface Strain Analysis and Structural Optimization of Inkjet-based PRI	53
2.2.3 Surface Strain Analysis and One-step Double-side Strain-isolation of Nozzle-jet-based PRI	60
Chapter 3. Printing-based Electronic Functionalization on Engineered Soft Substrates	70
3.1 Inkjet-printed Stretchable Silver (Ag) Interconnects	71
3.1.1 Principle of Prestrain-induced Wrinkling in Bilyaer Structures	74
3.1.2 Geometry and Electrical Characteristics	79
3.1.3 Stretchable Crossovers	94
3.2 Image-based Customizable Circuit Design for Hybrid-type Electronic Functionalization	97

3.2.1 Total Procedure	99
3.2.2 Home-made Circuit Routing Program	102
3.2.3 Robust Surface Mountable Device (SMD) Bonding	104
3.2.4 Various Circuit Design Examples	108
Chapter 4. Self-Computable Electronic Skin	119
4.1 Introduction	120
4.2 Soft, Fundamental Logic Circuits in Single-side Designs	123
4.3 Self-Computable Electronic Skin Based on Double-side Universal Soft Electronic (Double-side USE) Platform	129
4.3.1 Concept, Design, and Fabrication	129
4.3.2 Overall Strain and Conductivity Mapping	146
4.3.3 Stretchable, Double-side Integrated 1 MHz Binary Decoder	150
Chapter 5. Wirelessly Interfaced, Fully-Integrated Electronic Skins for Innervating Soft Robots	163
5.1 Introduction	164
5.2 Fabrication, Layouts, and Physical Designs	168
5.3 Stretch-tolerant Wireless Signal Interfaces	180

5.4 E-Skin-Mediated Wireless Innervation of Soft Robots	193
Chapter 6. Conclusion	201
Bibliography	204
Publication List	221
Abstract in Korean	224

List of Tables

Table 2.1 Comparison between printing methods for PRI fabrication.	40
Table 5.1 Specification of SMDs used in e-skins [197].	170

List of Figures

Figure 1.1 | Concept of stretchable electronics: Electronics that can be flexed, stretched, and deformed without degradation [1-3].....3

Figure 1.2 | Progress from bendable, twistable to stretchable electronics...5

Figure 1.3 | Young’s modulus of materials ranging from liquid metals, gels, elastomers, polymers to metals, semiconductors, and carbon-based solids [2]. Stretchable electronics usually combine viscoelastic, plastic, and even brittle materials with many orders of magnitude differences in Young’s modulus.5

Figure 1.4 | In-plane architectures for stretchable interconnects. (a) Representative behaviors of gold interconnects with “in-plane” architectures under tensile stretching test [52]. In-plane architectures with higher amplitudes endured higher strains in terms of augmented failure strains. (b) Plastic strain distribution in copper conductor line for three different in-plane architectures: elliptical, “U”, and horseshoe shape [54]. All the architectures show highly localized strains at peak and trough of each wavelength.....8

Figure 1.5 | Kirigami architectures for stretchable interconnects. (a) An

artistic geometry of the kirigami concept that folds and cuts paper.
 (b) A highly stretchable graphene transistor that can be stretched by 240% without observable degradation, with the deformation mechanism that meets kirigami physics [67]. 10

Figure 1.6 | Out-of-plane architectures for stretchable interconnects. (a) Schematic illustrations of representative out-of-plane architectures driven by prestretching and selective bonding process [50]. (b) Non-coplanar serpentine structures consisting of trilayer stacks of polymer/metal/polymer [50] for improved stretchability. (c) Versatile 3D buckling in multi-materials based on prestretching and selective bonding [86]..... 12

Figure 1.7 | Novel materials for stretchable electronics. (a) SEM image of CNT entanglement [78]. (b) 3D printed liquid metal architectures [115]. (c) Highly stretchable hydrogel that can be stretched to 21 times its initial length [123]..... 18

Figure 1.8 | Architecture of stretchable electronic circuits. Cells with optoelectronic functions are made on islands and are connected with stretchable interconnects on a common soft substrate [2]... 20

Figure 1.9 | Typical geometric layouts of rigid island systems: (a) a protruding form, (b) an embedded form, and (c) an integrated form. 20

Figure 1.10 | Limitations in existing stretchable electronics. (a) Schematic diagram of signal flows in general stretchable electronic systems. Gleaned data obtained from soft, stretchable sensors and interconnects are transmitted to the rigid part where signal amplification, processing, and computing are conducted [146]. (b) Examples of stretchable networks of sensors and interconnects that possess arrays of pads for outward data extraction [146, 147].

Figure 2.1 | Materials and equipment for printed rigid island embedded soft substrates (PRISSs). (a) Chemical structures of PMMA, PGMEA, and PDMS. (b) Images of inkjet printer (DMP 2831, Dimatix corp.) and pneumatic control nozzle-jet printer (SHOTmini 200Sx, Musashi Engineering Inc.)..... 31

Figure 2.2 | Sequential image frames of real-time PMMA ink jetting. Each volume of jetted ink droplet is 10 pL. 34

Figure 2.3 | Sequential image frames of real-time formation process of an individual PRI and corresponding SEM images. The first printing input pattern (normally square form) decides the PRI diameter; and subsequent steps of inkjet-printing with the reduced size of input pattern lead to the gradual increase in PRI thickness, driven by the effect of contact line pinning. Time delay between each step is dependent on the diameter of PRIs. 35

Figure 2.4 | (a) SEM images of PRI array with different printing steps (1 to 3 steps), thus different thickness, and (b) different size (diameter) [153]. 36

Figure 2.5 | Morphological features of multistep-printed inkjet-based PRIs. (a) SEM images of multi-layered PRIs (M_w 97,000). (b) Size dependency of PRIs on printing steps (or the amount of ink droplets). (c and d) Structural parameters of multi-layered PRIs with different M_w (15,000 and 97,000) [153]..... 36

Figure 2.6 | Morphological features of nozzle-jet-printed PRIs. (a) Photograph of real-time nozzle-jet printing of PMMA ink. (b) Morphology profiles of PRIs with different PMMA concentration (4, 10, 15, 17, 20 wt%). Diameters of each PRI are fixed to ~1,500

μm for an effective parametric sweep. (c) Morphology profiles of 17 wt% PRIs formed by different pairs of air pressure level and duration time (diameter was fixed to $\sim 1,500 \mu\text{m}$). The profile data advocate that the geometry of PRIs is prominently determined by ink concentration rather than printing condition [154].....39

Figure 2.7 | Conceptual schematic illustration of stretchable bead network. The bead and spring represent the PRI and inkjet-printed wrinkled interconnects, respectively [153].....41

Figure 2.8 | Preparation of large-area, customizable PRISSs. (a) Photograph of the PRISS representing a “maple leaf”. (b) Photograph of a very large-scale PRISS (~ 14 inch, $\sim 3,200$ PRIs). (c) Fabrication process of a PRISS [153].....42

Figure 2.9 | PDMS (20:1 mixing ratio) membrane thickness vs. spin-coating condition.44

Figure 2.10 | Cross-sectional geometry of PRISSs. (a) Typical cross-sectional SEM image of a PRISS. (b) Geometric parameters of a PRISS [154].46

Figure 2.11 | A large-scale, multi-featured, customized PRISS. (i) Photograph of a PRISS that contains multi-scale/multi-structured PRIs in a customized configuration (dolphin, maple leaf, letters). Inset image shows a skin-like deformable property of the PRISS. Each PRI subsection either a dolphin or a maple leaf can be separately obtained by a physical cutting for individual uses. (ii) Owing to the transparency, PRIs are perceived only if illuminated by the tilted light incidence. (iii) The PRISS shows superb skin-conformability under sequential stretching/compressing [153].48

Figure 2.12 | Multistep-printed, multi-structured inkjet-based PRIs embedded

in the PRISS of Figure 2.11. (a) SEM images of multistep-printed PRIs (diameter $\sim 1,500 \mu\text{m}$) constructing the dolphin and maple leaf. (b) SEM images of micro-size PRIs (diameter $\sim 80 \mu\text{m}$) constructing the letter “SNU” [153]......49

Figure 2.13 | Process flow of DIC method. (a) First, randomly distributed speckle patterns (baking powder, average size $\sim 20 \mu\text{m}$) are uniformly formed, and then the interesting region is captured by an optical microscope or digital camera. (b) Second, the captured images are transformed into grayscale to enhance the contrast level. (c) Finally, the sequential image frames are analyzed by an image-processing tool (Vic-2D 2009, Correlated Solutions) to evaluate the maximum principal strain [153]......52

Figure 2.14 | Structural properties of various inkjet-based PRISSs. (a) Schematic illustration of the unit structure of PRISSs comprised of three parts: top PDMS (TPDMS), PRI, and bottom PDMS (BPDMS). (b) 3D surface profiler images of 1-, 3-, 5-layered PRIs with M_w 15,000 and 97,000. (c) Optical images of elongated PRISSs (applied uniaxial strain, $\epsilon_{\text{appl}} = 0\text{--}50\%$) containing 1-, 3-, 5-layered inkjet-based PRIs with M_w 15,000 and 97,000 for comparison [153]......54

Figure 2.15 | Cracking tendency of inkjet-based PRIs with different structure and M_w . Starting from 42 PRIs for each condition, the number of intact PRIs is counted together with increasing tensile strain (0–50%). Both of molecular chain length and structural parameter affect the stability of the PRI and PRISS [153]......55

Figure 2.16 | Detailed description on $AR_{2\%}$ for inkjet-based PRIs. (a) Electrical characteristics of inkjet-printed Ag electrode directly fabricated on the bare PDMS. Cracking strain is around 2% (inset

image: optical image of the cracked Ag film under the small strain). (b) AR_{2%} of the PRISS (PRI diameter ~1.5 mm, t_{TPDMS} ~20 μm, 5-layered PRI) with different PRI robustness (PMMA M_w 15,000 and 97,000). Surface strain is evaluated from DIC, and AR_{2%} is calculated by image processing [153].....57

Figure 2.17 | Effect of top PDMS thickness (t_{TPDMS}) and PMMA M_w on the stability of 5-layered PRIs in terms of (a) PRI center strain (ε_{center}) and (b) strain-free area (AR_{2%}). Each factor is measured along with an increasing applied strain (0 to 50%) [153].58

Figure 2.18 | Stability parameters for inkjet-based PRISSs. (a) ε_{center} and (b) AR_{2%} as a function of ε_{appl}. AR_{2%} at 50% ε_{appl} showing a compact strain-free area that covers the SMD LED chip whose dimension is 1 × 0.6 × 0.2 mm³. (d) Optical image of the real LED chip (1 × 0.6 × 0.2 mm³) mounted on the strain-free area of ~1,500 μm PRI [153].59

Figure 2.19 | Morphology engineering of nozzle-jet-based 17 wt% PRIs through varying dispensing duration time with a specific air pressure (150 kPa). (a) Diameter engineering, and (b) thickness engineering. Highlighted blue regions indicate applicable PRI diameters for effective double-side strain isolation [154].....62

Figure 2.20 | Mechanical stability and surface strain distribution of engineered PRIs. (a) Typical morphology profiles of engineered PRIs (PMMA concentration: 4, 10, 15, 17, 20 wt%). (b and c) Surface strain distribution (rainbow spectrum) and evaluated strain-free area (green area contrary to white background) on top (b) and bottom (c) surfaces of PRISSs [154].....63

Figure 2.21 | Cross-sectional SEM images of PRISSs. (a) SEM images of 15, 17, 20 wt% PRISSs. The diameter of each PRI is equally set to

~1,500 μm , and values of t_{TPDMS} and t_{BPDMS} are equally defined to be ~20 μm . (b) Magnified SEM image of the 17wt% PRISS [154].
 64

Figure 2.22 | Difference in strain-free areas between top and bottom surface of PRISSs. (a) Surface strain (evaluated maximum principal strain) distribution on top and bottom surface of the 17 wt% PRI-embedded soft platform under 30% ϵ_{appl} . Location of the PRI is marked as the dotted blue circle. (b) Surface strain profile of top and bottom surface along the line (A-B) as depicted in (a). The strain data clearly advocate the large correlation between the size of diameter (outer /inner) and the extent of strain-free area (top/bottom) [154]. 66

Figure 2.23 | Effect of PMMA wt% and corresponding structural parameters on the stability of PRIs. (a) Correlation graph between ϵ_{center} (top and bottom surfaces), t_{center} , and PMMA wt%. (b) Correlatoin graph between $\text{AR}_{2\%}$ (top and bottom surfaces), inner diameter, and PMMA wt% [154]. 68

Figure 2.24 | Stability parameters for nozzle-jet-based 17wt% PRISSs. (a) ϵ_{center} and (b) $\text{AR}_{2\%}$ as a function of ϵ_{appl} [154]. 69

Figure 3.1 | Typical structural designs of 3D interconnection architectures at rest and stretched conditions [85]. 72

Figure 3.2 | Deterministic interconnection configurations and elastic mechanics, showing the capability of engineering available strain regimes [59]. 73

Figure 3.3 | Schematics of wrinkle formation through buckling instability in a bilayer system [167]. 75

Figure 3.4 | Principle and examples of prestrain-induced out-of-plane

buckling. (a) Sequential configurations of the thin film/substrate buckling process. (b) Typical SEM image of buckled, single-crystal Si ribbons [71].	77
Figure 3.5 Wavelength and amplitude of buckled structures of Si (100 nm thickness) on PDMS as a function of the prestrain. The finite-deformation buckling model expects wavelengths and amplitudes that agree well with experiments [71].	78
Figure 3.6 Fabrication process for prestrain-induced inkjet-printed wrinkled Ag interconnects.	80
Figure 3.7 Typical optical image of inkjet-printed wrinkled Ag interconnects on PDMS prestrained to ~30% in 1D.	82
Figure 3.8 Typical optical (a) and 3D profiler image (b) of inkjet-printed wrinkled Ag interconnects on PDMS prestrained to ~20% in 2D [153].	83
Figure 3.9 Minimum feature size of inkjet-printed wrinkled interconnects. (a) Optical image of the wrinkled interconnects fabricated by using a 1 pL cartridge of the inkjet-printing system (DMP-2831, Dimatix Corp.). (b) Optical image of the finer interconnects fabricated by using a super inkjet printer (SIJ-S050, SIJTechnology Inc.) [153].	84
Figure 3.10 Gradual strain-absorbing design near the PRI. (a) Typical surface strain distribution on the PDMS surface near the PRI area. The strain values are evaluated from DIC. (b) Optical image of the gradually wrinkled PRISS driven by prestrain (~30%) and UVO ₃ treatment, showing self-constructed gradual strain-absorbing design with a stress-matched amplitude. (c) 3D profiler image and corresponding line profile of the wrinkled area described in b [153].	86, 87

Figure 3.11 | Optical image of high-density inkjet-printed Ag interconnects directly fabricated upon the PRISS. Flatness of the PRISS allows direct printing of stretchable conductors, and prestrain-induced gradual strain-absorbing design makes fragile Ag films stretchable. Notably, the strain-free effect of the PRI suppresses wrinkle formation inside the PRI region [153]...... 89

Figure 3.12 | Optical (a) and SEM image (b) of inkjet-printed 2D PRI interconnection networking. ~350 μm PRIs with a triangular lattice configuration are used, and each strain-free property is verified by wrinkle suppression phenomena [153]...... 90

Figure 3.13 | Failures in forming gradual strain-absorbing designs on printed interconnects, caused by instabilities of cracking and/or collapsing in PRIs. 91

Figure 3.14 | Electrical characteristics of inkjet-printed wrinkled Ag interconnects formed by 50% prestrain. (a) Normalized resistance profile as a function of ϵ_{appl} (0–50%). (b) Cyclic reliability under 30% repeated stretching condition. Stretching speed is equally 10 mm min⁻¹ [153]. 92

Figure 3.15 | Cyclic reliability of inkjet-printed wrinkled Ag interconnects encapsulated by 20:1 PDMS (a) and 30:1 PDMS (b). The applied strain is 30%, and stretching speed is 10 mm min⁻¹ [153]...... 93

Figure 3.16 | Stretchable crossovers fabricated by printing processes. (a) Optical image of as-printed crossover Ag line onto the printed PDMS (20:1) dielectric. (b) Optical image of large-area PDMS dielectric and multi-line crossovers [153]. 96

Figure 3.17 | Optial images and calculated displacement anisotropy of rearranged PRIs under a sequential biaxial stretching ($\epsilon_x = \epsilon_y = 0\text{--}40\%$). Displacement anisotropy is defined as “(x displacement – y

	displacement) / (x displacement + y displacement)” [153].....	98
Figure 3.18	Experimental details on automated, printing-based electronic functionalization process on a PRISS [153].....	101
Figure 3.19	Home-made circuit routing program. (a) A total layout. (b) Generated files for interconnection printing, crossover patterning, and chip placing [153].....	103
Figure 3.20	Printing-based SMD assembly. (a) Process flow of Ag epoxy/epoxy bonding with various SMDs including LED, logic gate, and resistor. (b) Photographs of the whole system layout of SMD pick-and-place machine and the prepared SMD chips in tape and reel packaging including logic gates (XOR, AND, OR) and LEDs with different colors [153].....	106
Figure 3.21	Photograph showing the robustness of Ag epoxy bonding [153].	107
Figure 3.22	Topological inter-PRI networks. (a) Schematics of three different types of topological inter-PRI networks based on the smile PRI configuration: ring, tree, and cluster. (b) Snapshot images of designed topological networks in the circuit routing program. Orthogonal layouts are adopted for a facile circuit networking. (c) Optical images of the inkjet-printed topological networks designed in b.	109
Figure 3.23	Stretchable display in a maple leaf design. (a) Optical image of the as-fabricated stretchable display system. (b) Snapshot image of the designed circuit. (c and d) Optical image of the system laminated onto the human skin (c), and stretched at a freestanding state (d) [153].	111
Figure 3.24	Stretchable display in a dolphin design. Based on the PRI configuration embodying a dolphin (inset image), the stretchable	

system can be operated in sequences of deformation [153]. . 111

Figure 3.25 | Stretchable multi-mode displays in a “sha” design. (a) Photographs of three different layouts of stretchable display characterized by different LED colors, interconnection geometries, and network topologies between LEDs. (b) Snap shot images of designed designed topological networks in the circuit routing program. (c) Optical images of the highlighted areas of the system: operating LEDs upon the PRI areas (i, ii), the rigid-to-soft transition area with a wrinkle transition phenomenon (iii), and wrinkled areas conformable to straight (iv, v) and kinked (vi) interconnects [153]. 112

Figure 3.26 | Photographs of the stretchable multi-mode “sha” display at a freestanding state (a), laminated onto the human finger (b), stretched (c), and laminated onto the crumpled Al foil (d) [153]. 113

Figure 3.27 | Fully printed, wearable analog watch. (a) Exploded-view schematic illustration of the printed wearable analog watch system. (b) Optical image of the as-fabricated wearable watch, indicating “4:59:34”. (c) Photographs of the watch operation under sequential wrist movements. Top inset: Enlarged optical image of the wire-bonded MCU region. Bottom inset: Operating input signals of twelve LEDs before and after deformation under 20% biaxial strain [153]. 116

Figure 3.28 | Fully printed, wearable passive matrix (PM) display. (a) Photograph of the whole PM display circuit consisting of a MCU and 35 LEDs. (b and c) Photographs of the PM display deformed like the human skin (b) and folded (c) while exhibiting sequential letters “AXEL”, Advanced fleXible Electronics Laboratory [153].

.....	117
Figure 3.29 Fully printed, wearable temperature monitoring system. (a) Optical image and corresponding logic diagram of temperature monitoring system. (b) Output characteristics of the temperature sensor IC as temperature increases from 0 to 60 °C. (c) Output characteristics of LEDs integrated in the temperature monitoring system. Each LED is sequentially turned on at 5, 18, 31, 44, 56 °C [153].	118
Figure 4.1 Potential of fully-integrated e-skin, providing advanced capabilities of engrafting soft electronics into both on-going and unprecedented subjects including human, robot, and nature.....	122
Figure 4.2 Soft digital full adders in a single-side miniaturized design. (a) Photograph of digital full adders with a customized design directly fabricated on the PRISS which contains pentagonal PRI arrangements. Owing to the wrap-like conformability, the full adders are easily adhered to human nails and skin (inset image). (b) Photograph of stretched/twisted full adders. Several full adders can be fabricated in a single batch. (c) Input/output characteristics of full adders both at an initial and stretched state ($\epsilon_x = \epsilon_y \sim 30\%$) [153].	124
Figure 4.3 A soft 2-bit digital multiplier in a single-side design. (a) Photograph and corresponding logic diagram of 2-bit multiplier laminated on the human skin. (b and c) Photographs of the stretched 2-bit multiplier indicating “ $3 \times 3 = 9$ ” (b), and wrapped around a finger (“ $3 \times 1 = 3$ ”) and a ball pen (inset image) [153].	126

Figure 4.4 | Full operation of the wearable 2-bit multiplier [153]..... 127

Figure 4.5 | A soft 2-bit digital multiplier based on a large PRI (diameter ~5.6 mm). (a) Photograph of the whole system comprised of 4-channel AND gate (SN74LV08ARGVR, Texas Instruments (TI), $3.5 \times 3.5 \text{ mm}^2$), 2-channel AND gate (SN74AUP2G08, TI, $1.5 \times 1.5 \text{ mm}^2$), and 2-channel XOR gate (NC7WZ86, Fairchild Semiconductor, $1.6 \times 1.6 \text{ mm}^2$). (b) Magnified optical image of 4-channel AND gate mounted on the large size PRI (diameter ~5.6 mm). (c) Magnified optical image of 2-channel XOR gate mounted on the medium size PRI (diameter ~2.5 mm). (d) Output characteristics (C_0 — C_3) of initial, stretched, and 100-times stretched multiplier in multiple states ($A \times B$). The system was equi-biaxially stretched at a speed of 1 mm s^{-1} [153]..... 128

Figure 4.6 | Conceptual schematic of a double-side USE platform and printing-based system-level integration. Inset illustrations show key features of double-side strain-isolation (or double-side device integration) with a single PRI and double-side vertical-interconnection with a core-shell via [154]..... 130

Figure 4.7 | A double-side integrated, fully printed, system-level soft electronic circuit fabricated on the double-side USE platform. Inset image: cross-sectional optical image of double-side integrated SMDs. (a and b) Photographs of a double-side USE platform (a) and integrated circuits (b) [154]..... 131

Figure 4.8 | Salient steps in fabrication process for a double-side USE platform. (a) Simplified fabrication process: (i) substrate preparation, (ii) PRI array printing, (iii) core-shell via array formation and completion of a double-side USE platform, and (iv) printing-based double-side electronic functionalization (detailed

fabrication steps are depicted in Figure 4.9). (b) Process steps of single droplet printing of a PRI: as-printed PMMA ink (left) is formed into specific island structures (right) along with PMMA concentration. (c) Process steps of single droplet printing of a core-shell via: as-printed Ni/PDMS(5:1)/silicone resin mixture (left) is covered by PDMS matrix (middle) and then formed into the core-shell structure (right) driven by a highly focused magnetic field [154]..... 133

Figure 4.9 | Total fabrication process of a double-side USE platform [154].
..... 134

Figure 4.10 | Magnetic field focusing equipment. (a) Photograph of original [173] and modified iron mold. (b and c) Optical images of high aspect ratio iron structures in the original mold (b) and upgraded mold (c). Cross-sectional area of each iron structure was reduced from $1.6 \times 1.6 \text{ mm}^2$ to $1 \times 1 \text{ mm}^2$ and aspect ratio was increased from 5.625 to 9. This modified dimension provided capabilities of more densified via design and geometric compatibility with PRIs [154]. 136

Figure 4.11 | Structure of a stretchable core-shell via. (a) Top-view optical image of a core-shell via. (b) Cross-sectional optical image of a core-shell via. Total thickness of the via was $\sim 100 \mu\text{m}$ [154]. 137

Figure 4.12 | SEM images of magnetically aligned Ni microparticles in a core area. Several cross-sectional SEM images validate that Ni particles (average size $< 5 \mu\text{m}$) were densely aligned in a vertical direction (= magnetic field direction) in the core part of core-shell vias, and formed vertical conduction paths with greatly improved electrical conductivity [154]..... 138

Figure 4.13 | Surface strain distribution and average strain levels of a core-

sell via as a function of ϵ_{appl} (0–50%). All evaluated strain values were calculated in the form of maximum principal strain based on DIC [154].	140
Figure 4.14 Electrical characteristics of a stretchable core-shell via. (a) Normalized resistance profile curve of a core-shell via during a large deformation ($\epsilon_{\text{appl}} = 0\text{--}100\%$). Initial resistance of the via was 10–20 Ω , and stretching speed was 1 mm min ⁻¹ . (b) Resistance profile of a core-shell via during repeated deformation ($\epsilon_{\text{appl}} = 50\%$). Stretching speed was 100 mm min ⁻¹ [154].	141
Figure 4.15 Electrical characteristics of a core-shell via under 2D stretching. (a) Resistance profile of the core-shell via undergoing 2D biaxial stretching (0 to 30%). The initial resistance of the via was 6.93 Ω , and the stretching speed was ~ 1 mm s ⁻¹ . (b) Resistance of the via undergoing repetitive 30% biaxial stretching [154].	142
Figure 4.16 Frequency response of a core-shell via to sinusoidal waves [154].	144
Figure 4.17 Input/output signal (1 kHz, 1 MHz square waves) characteristics at an initial and stretched (biaxial strain $\sim 30\%$) state (a) and the magnified view (b) in a positive-edge triggered region that shows the signal delay ~ 3.2 ns [154].	145
Figure 4.18 Large-area surface strain mapping on both top and bottom surface under 20% biaxial strain [154].	148
Figure 4.19 Schematic illustration of the circuit designed to line 9 vias through 7 steps of vertical conduction (PRIs are omitted for simplicity). Two-step inkjet-printing processes were carried out for fabrication [154].	149
Figure 4.20 Temperature gradient mapping of the operating circuit on both top and bottom surfaces. Bias voltage of ~ 2 V was applied for a	

few seconds to obtain observable temperature gradients (~5 °C) [154]. 149

Figure 4.21 | Circuit layout of the BCD to 7-segment binary decoder. A layout design of the decoder is inspired by the circuit diagram of programmable logic array (PLA), consisting of 4 inverters, 9 multi-input AND gates, and 7 multi-input OR gates. For actual demonstration, we used 6 inverters (2 SMDs of 3-channel inverter), 12 2-input AND gates (6 SMDs of 2-channel 2-input AND gates), and 18 2-input OR gates (9 SMDs of 2-channel 2-input OR gates)—total 17 SMDs of 36 logic gates for dimensional standardization ($1.5 \times 1.5 \text{ mm}^2$) of SMDs. For double-side integration, the whole circuit layout is divided into two functional groups (blue: AND part, red: OR part) through 9 core-shell vias [154]. 151

Figure 4.22 | Layout and user-interface of the home-made circuit routing program “Image Based Router” (refer to Figure 3.19) [154].153

Figure 4.23 | Predefined circuit designs and corresponding circuit routing of the double-side integrated binary decoder. (a and b) Screen shot images of predefined top circuit design implemented on the schematic background image (a) and actual top circuit routing on the captured image of the pretrained double-side USE platform (b). In the top circuit, functional networks highlighted in the blue rectangle in Figure 4.21 is demonstrated. (c and d) Screen shot images of predefined bottom circuit design implemented on the schematic background image (c) and actual bottom circuit routing on the captured image of the flipped top circuit (d). In the bottom circuit (highlighted in the red rectangle in Figure 4.21), 9 core-shell vias provide 9 combinational signals transmitted from 9

AND gates, and combinational networks between them generate individual 7-segment signals (C_0 – C_6) [154].	154
Figure 4.24 Inkjet-printed Ag interconnection networks before and after releasing prestrain. (a) Optical images of as-printed Ag interconnection network together with crossover lines. (b) Optical images of Ag interconnection network near the PRI areas after releasing prestrain. Due to the strain-free effect, wrinkle formation on printed Ag films and oxidized PDMS surfaces (induced by UVO_3 treatment) was perfectly suppressed inside the PRI areas [154].	155
Figure 4.25 A single-side integrated stretchable BCD-to-7-segment signal decoder fabricated on the PRI-embedded soft substrate where PRIs were arranged in a square-lattice configuration (spacing ~ 4.5 mm) [154].	157
Figure 4.26 A double-side integrated stretchable binary decoder fabricated on the double-side USE platform. The whole circuit was fabricated by two-step printing-based electronic functionalization processes. Compared to the single-side implementation in a, utilized PRIs were approximately reduced in half (from 17 to 9), and the number of crossover lines was decreased about 42% (From 197 to 114) [154].	158
Figure 4.27 Optical images of a single SMD device (1.5×1.5 mm ²) supported on a PRI (diameter ~ 2.3 mm) at an initial state and stretched state (biaxial strain $\sim 20\%$). Inside the PRI was suppressed the wrinkle formation due to the strain-free effect [154].	159
Figure 4.28 Photograph of the twisted, double-side integrated binary decoder [154].	161

Figure 4.29 Input/output characteristics of the decoder operating at $f_0 = 1.024$ kHz input. No meaningful degradation of output signals at a stretched state (biaxial strain $\sim 20\%$) was observed [154].	161
Figure 4.30 Output characteristics of the decoder operating at $f_0 = 1$ MHz input after several stretching cycles [154].	162
Figure 5.1 Conceptual illustration of wirelessly interfaced e-skins for innervating a soft robot [197].	167
Figure 5.2 Schematic logic diagrams of the interfacing e-skin (a) and the innervating e-skin (b) [197].	169
Figure 5.3 Screenshot images of specific circuit routing for the interfacing e-skin (a) and the innervating e-skin (b) in the home-made circuit routing program [197].	169
Figure 5.4 Layouts and functions of e-skins (interfacing e-skin and innervating e-skin). (a) Photograph of the interfacing e-skin (or Tx e-skin) composed of sensors, analog-to-digital (A/D) converter, custom-built serializing encoder, and Tx module. (b) Photograph of the innervating e-skin (or Rx e-skin) composed of Rx module, custom-built deserializing decoder, digital mixer, and current driver for actuators [197].	171
Figure 5.5 Exploded-view schematic illustration of the fully-integrated e-skins [197].	171
Figure 5.6 Fabrication process for e-skins. (a) Sequential steps of printing-based SMD assembly. (b) Total fabrication process for e-skins [197].	172
Figure 5.7 Multilayer interconnection design in e-skins. (a and b) Spatial locations of line-crossing points in the interfacing e-skin (157 crossing points) (a) and innervating e-skin (153 crossing points)	

(b). (c) Optical images of typical regions that showed the formation of crossover lines [197]..... 173

Figure 5.8 | 2D wrinkled morphologies on the entire surfaces of e-skins. (a and b) Large-area optical images (a) and corresponding magnified images (b) of 2D surface wrinkles both on the printed multilayer Ag interconnects and PDMS surface. These out-of-plane geometries are originated from the compressed bilayer structures of Ag/PDMS and SiO_x/PDMS (the SiO_x layer is generally formed by a UVO₃ treatment process during fabrication steps). (c) Optical images of wrinkled and corresponding flattened surfaces (Ag interconnects and PDMS) in response to the biaxial stretching ($\epsilon_x = \epsilon_y = 25\%$) [197]..... 174

Figure 5.9 | 3D Finite element analysis (FEA) on printed strain-isolating architectures. (a) Optical image of the assembled SMD with printed epoxy architectures. The engineered wrinkle profile indirectly verified the engineered strain field. (b) Strain field distribution (maximum principal strain) in a SMD region obtained from FEA results. (c) Consecutive strain field distribution as a function of a specific length (L_0) of the extended epoxy bank structure (cases: $L_0 = 800, 400, 0 \mu\text{m}$, and no epoxy bank). (d and e) Surface strain profile along with the OX' line (d) and OY' line (e), both of which are defined in (c) [197]. 177

Figure 5.10 | Fading SiO_x/PDMS wrinkles near the contact areas of a SMD. (a) Optical image of the assembled SMD with printed epoxy architectures ($L_0 \sim 800 \mu\text{m}$), exhibiting the engineered wrinkle profile. (b) Magnified optical images of fading wrinkles near the contact areas, driven by gradual strain mitigation as evaluated in Figure 5.13. (c) Optical image of the assembled SMD without

extended epoxy architectures ($L_0 = 0 \mu\text{m}$). (d) Magnified optical images of deep wrinkles near the contact areas [197]...... 178

Figure 5.11 | Physical resilience and skin-conformability of e-skins. Soft features of e-skins allowed physical adaptations under multidimensional deformations such as crumpling with sequential hand movements (a), wrapping around a finger (b), stretching (c), and adhering to a neck [197]...... 179

Figure 5.12 | Schematic diagram of an entire wireless signal interfacing flow in the pair of e-skins (interfacing and innervating e-skins) [197]. 181

Figure 5.13 | Signal quantizing module in the interfacing e-skin. (a) Unit circuit diagram for signal quantization (A/D converter module). The circuit is composed of a sensor, a voltage-dividing resistor ($3 \text{ k}\Omega$), a comparator, and a sampler (D flip flops). V_{sensor} is defined as the divided voltage and thus could be controlled just by varying the voltage-dividing resistor ($3 \text{ k}\Omega$ in this case). (b) Resistance and V_{sensor} profiles of a piezoresistive pressure sensor (Velostat, Adafruit) as a function of the applied pressure [197]...... 182

Figure 5.14 | Customized serializing encoder/deserializing decoder. (a and b) Schematic diagram of the encoder (a) and decoder (b). (c) Encoding (decoding) mechanism of customized serializing encoder (deserializing decoder) [197]...... 184

Figure 5.15 | Digital mixing of output signals in the innervating e-skin. (A) Miniaturized schematic of the innervating e-skin. (B) Examples of digital mixing of output signals. Inclusion of a few logic gates (OR, AND, inverter gates), connected to the output terminals of the decoder, can lead to the versatile combinations of output signals. Examples include the output sets of (A+B, A+C, A+D), (A+B+C,

B+C, C+D), and (A, C, B'D', D'), and further combinations can be easily addressed. The output combination of (A, A+B, A+C, A+D) is used in this work [197]. 185

Figure 5.16 | Schematic of an experimental setup for a reliability test of wireless communication between e-skins [197]. 186

Figure 5.17 | Typical waveforms of randomized, non-encoded/encoded signals [197]. 188

Figure 5.18 | Fourier analysis data on randomized, non-encoded and encoded signals [197]. 188

Figure 5.19 | Data transmission yield of non-encoded and encoded signals as a function of d_{T-R} [197]. 189

Figure 5.20 | Real-time in-skin signal modulation and specific encoded signal profiles in each state of finger touches. (a) Short-term continuous monitoring (20 s) of encoded signals in the interfacing and innervating e-skins in each state. (b) Enlarged view of encoded waveforms in each state (default, A to D) [197]. 191

Figure 5.21 | Stretch-tolerant feature of the wireless signal interfaces between e-skins. (a) Typical transmitting (blue and gray lines, measured just after the signal encoding process in the interfacing e-skin) and receiving (red and black lines, measured just after the signal restoring process in the innervating e-skin) waveforms in the “C” state. The encoded signals show the stretch-tolerant feature in both e-skins (25% biaxial strain). (b) Magnified view of the waveform in a. Wireless communication delay of $\sim 12.6 \mu\text{s}$ is observed without meaningful degradation under 25% biaxial strain [197]. 191

Figure 5.22 | Real-time decoding process of serialized, encoded signal sequences in response to dynamic sequences of 4-bit random

signals [197].	192
Figure 5.23 E-skin-mediated wireless formation of an electronic nervous system onto a soft robot. (a) Schematic, (b) photographic, and (c) thermographic images of process steps for e-skin-mediated wireless innervation [197].	194
Figure 5.24 Inkjet-printed PEDOT:PSS thin-film soft actuators. (a) Schematic design of the fabricated soft robotic hands with specific positions of soft actuators (or artificial muscles). (b) Schematic design of the printed PEDOT:PSS pattern. (c) Sequential optical images of the actuation mode of an individual bilayer (PEDOT:PSS/PDMS) soft actuator. (d) Curvature data of the individual soft actuator as a function of the applied voltage [197].	195
Figure 5.25 Thermographic images of the operating interfacing e-skin (top) and innervating e-skin (bottom) in each input state. Based on the specific digital mixing, each input state was programmed to activate different robotic fingers (A: “1, 2, 3, 4, 5”, B: “1, 2”, C: “3”, D: “4, 5”). Because of the larger resistance of the PEDOT:PSS thin films (~1.3–1.8 kΩ) than Ag interconnects (~20 Ω for the same length), the prevailing Joule heat was clearly observed near the actuator region [197].	197
Figure 5.26 Sequential thermographic and corresponding photographic images of the innervated soft robotic hand under physical deformations such as bending (left), stretching (middle), and folding (right) [197].	198
Figure 5.27 E-skin-mediated consecutive multi-robot innervation. (a) A process flow of consecutive innervation of distinct soft robots by sequential lamination processes. Specifically, three different soft	

robotic hands with distinct “muscle” designs and physical states were utilized. (b) Enlarged view of each soft robotic hand before a lamination process. (c) Enlarged view of wireless manipulation of soft robotic hands with distinct operation states. For comparison, different actuation states in response to the input types (C, D, and B states) were demonstrated for each robot [197]......200

Chapter 1

Introduction

In this chapter, we briefly review the recent progress in stretchable (or soft) electronics. First, significance, recent progress, and key issues of stretchable electronics are handled. Subsequently, representative core technologies for this state-of-the-art system are introduced in terms of interconnection architectures, materials, and strain-isolation structures together with associated fields of applications. In the last part, motivation and main concept of this dissertation are described.

1.1 Stretchable Electronics

Stretchable (or soft) electronics literally means electronic devices and systems that can be stretched and/or deformed like soft materials. More scientifically, the meaning and pursuing goal of stretchable electronics includes technologies for building electronic devices, circuits, and systems onto (or into) soft, stretchable substrates—such as various curvilinear surfaces, silicone rubber (poly(dimethyl siloxane), ecoflex), polyurethane, and even human skin— to overcome the fundamental mismatch in mechanics and form factors between biology (soft, elastic, and curved) and conventional electronics (rigid, planar, and brittle) (Figure 1.1)[1–3]. Studies toward mechanically unconventional forms of electronics began, in earnest, ~20 years ago with capabilities of enduring small deformations like bending [4–9]. In particular, advances in printing [10–14] and related patterning techniques [15–20] triggered much of the initial progress in this field. Based on the bending mechanics in film-on-substrate systems [21, 22], it was figured out that mechanical features of such electronics mainly conformed to the physical geometry and deformation states of the flexible/bendable foundations such as plastic foils or papers: devices and circuits would become flexible and rollable if their thickness is reduced to 1/1000 of the targeted radius of curvature. However, on plastic (or paper) substrates, undesired out-

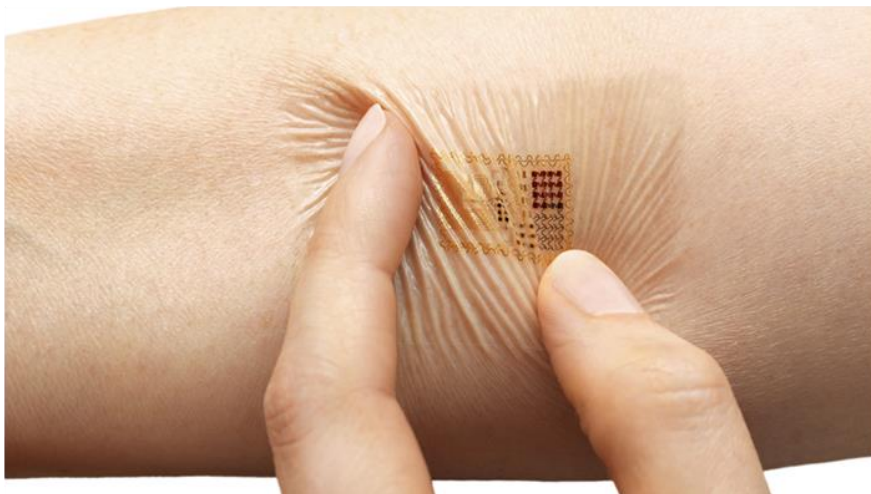
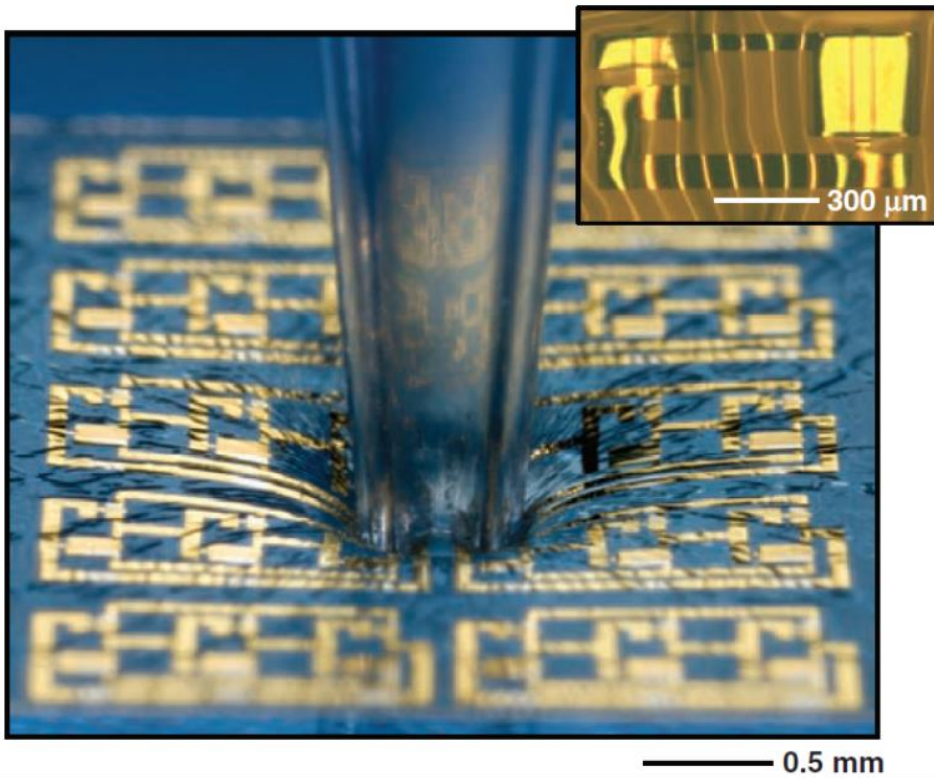


Figure 1.1 | Concept of stretchable electronics: Electronics that can be flexed, stretched, and deformed without degradation [1–3].

of-plane stress that might occur when covering curvilinear or spherical surfaces [23] could lead to plastic deformation that is irreversible and thus inimical to practical usages. Moreover, the fundamental mismatch in interfacing geometries between curvilinear bodies and “just” bendable planar surfaces could not be overcome because of the regulated displacement in the out-of-plane direction.

More recently, the stream of research has been strongly rooted in opportunities for soft, biointegrated devices and focused on more compelling technical challenges, “Stretchable” [3]. Beyond flexible property, the goal of this newest class of electronics is to maintain levels of mechanical/electrical performance, reliability, and integration that approach those of conventional electronics under reversible and arbitrary-dimensional deformation. In virtue of unprecedented geometries and functionalities that (1) allow conformable interfaces between electronics and soft, curvilinear (especially hemispherical) objects [24–27] and (2) make electronics durable to high level deformations [28–30], enormous opportunities have conjoined to realize multidisciplinary—material science, electronics, mechanics, medical science, biotechnology, and robotics—future dreams such as soft IoTs (internet of things) [31], electronic skin [32, 33], soft robots [34, 35], ubiquitous health monitoring [36, 37], neural interfacing [38, 39], etc. The key technical challenge is to effectively absorb (or disperse) mechanical stress that exponentially increases along with the deformation state from bending to stretching (Figure 1.2).



Figure 1.2 | Progress from bendable, twistable to stretchable electronics.

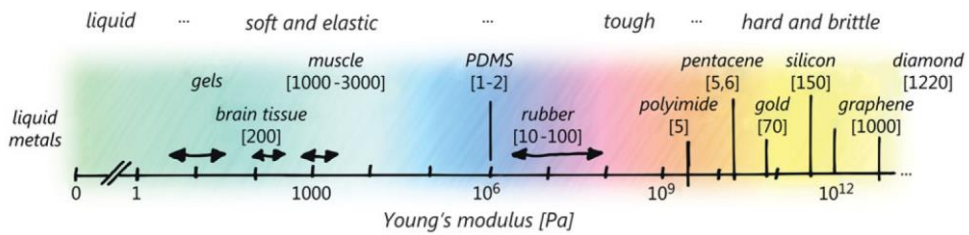


Figure 1.3 | Young's modulus of materials ranging from liquid metals, gels, elastomers, polymers to metals, semiconductors, and carbon-based solids [2]. Stretchable electronics usually combine viscoelastic, plastic, and even brittle materials with many orders of magnitude differences in Young's modulus.

Especially, discontinuity in Young's modulus (E) between electronic circuit (normally GPa \sim TPa) and a soft substrate (Pa \sim MPa) is the main obstacle (Figure 1.3). The large gap in E induces stress in thin films under elongation and even leads to irreversible cracks on the films or delamination of the whole system [40-43]. As the initial studies, several works have offered theoretical [44-46] and experimental [47-49] insights into the fundamental structure of stretchable electronics, a rigid thin film-soft substrate bilayer system. This accumulated knowledge, nowadays, helps avoid structural failure and thus achieve stretchable electronics mainly in two conceptually different, but complementary, ways in accompany with novel methodologies. One relies on new strain-absorbing architectures in conventional materials [50], the other on new materials in conventional layouts [51]. In this respect, the following sections will address the core enabling technologies, representative applications, and prospects of stretchable electronics.

1.2 Core Technologies for Stretchable Electronics

1.2.1 Interconnection Architecture

Stretchable circuits should have the geometric or intrinsic capacity to absorb large levels of strain ($\gg 1\%$) without fracture or significant degradation in their electronic properties. One strategy to achieve such response is to combine architectural design into the device itself and/or interconnections [50]. In this section, we introduce three kinds of architectures that cleverly absorb or distribute applied stress. The first layout is “in-plane architectures” (Figure 1.4). Inspired by an in-plane design of an accordion, many studies focused on the “wavy” or “horseshoe” layout of metallic wires deposited on a soft substrate by using standard lithography techniques. Although in-depth considerations were made to optimize the horseshoe design in terms of the geometry (wavelength and amplitude) [52-54] and high-frequency application [55], there still remains intrinsic limitations in the issues on localized strains at peak and valley of each wavelength and on the capacity for multidimensional strain-absorbing (Figure 1.4b). Furthermore, the localized strain induced from the geometric peculiarity restricted the maximum applicable level of strain to ~50 to 70% [52–54], thereby reducing the field of applications. Circumventing these outcomes, multiaxial designs [56-58] with liquid alloy and sophisticated fractal designs [59] have been

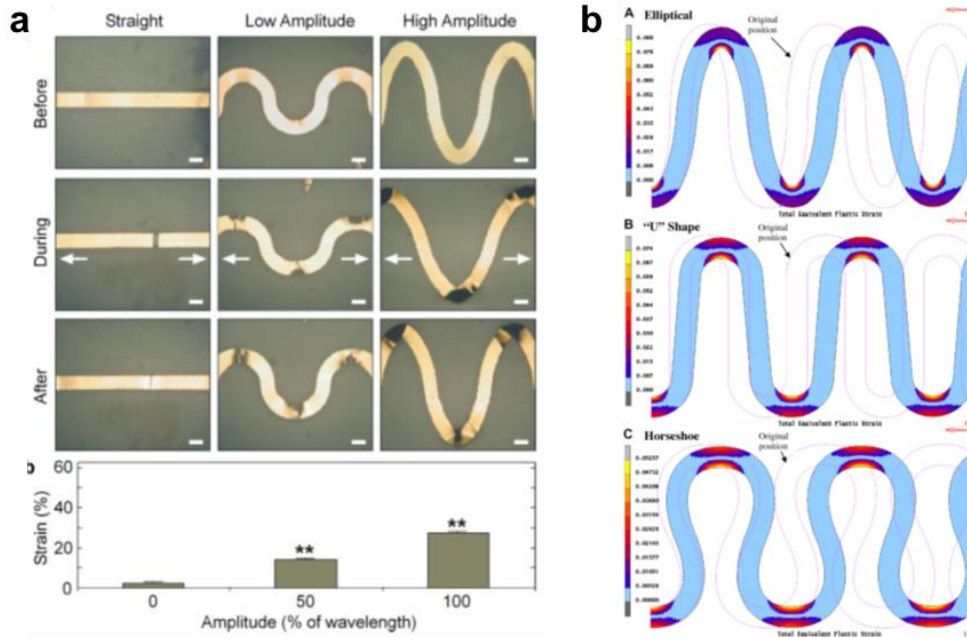


Figure 1.4 | In-plane architectures for stretchable interconnects. (a) Representative behaviors of gold interconnects with “in-plane” architectures under tensile stretching test [52]. In-plane architectures with higher amplitudes endured higher strains in terms of augmented failure strains. (b) Plastic strain distribution in copper conductor line for three different in-plane architectures: elliptical, “U”, and horseshoe shape [54]. All the architectures show highly localized strains at peak and trough of each wavelength.

presented.

The second approach is “kirigami architectures”, the arts of folding and cutting paper, plastic, and/or functional membrane into decorative shapes [60, 61] (Figure 1.5a). Based on this methodology, shape, structure, and electrical properties typically unattainable in traditional metals, ceramics, polymers, and composites can be easily obtained. Especially for metallic sheets, although a monolithically connected metallic film typically undergoes fracture at a strain level of 1–2%, physical patterning of kirigami over the substrate, either elastomer or plastic, can increase the failure strain dramatically, by at least a couple of orders (more than 200–300%) [62]. This is because the tiny cuts contribute to reducing the localized stress in the designed layout. Compared to the horseshoe-type in-plane methodology, the capability of forming periodic pattern arrays allowed practical uses of this strategy in stretchable active-matrix platforms with transistors [63, 64], sensors [65], and energy harvesters [66]. Furthermore, given the mechanical similarity between paper and nanomembranes (graphene [67], MoS₂ [68], and nanocomposites [62]), analogous architectures were established in nano- or sub-nanoscales for stretchable applications, in conjunction with the underlying physics (Figure 1.5b) [69]. The superiority of the kirigami approach attributes to (i) tunable, extendable, and multidimensional stretchability of the system (more than hundreds %) with regard to the geometric parameters, (ii) unlimited ranges of material choice, (iii) multi-scalability from macroscale to nano- and sub-nanoscale, and (iv) geometric compatibility of device integration. However, intricate fabrication process and relatively low device density— concomitants from a physical cutting process— remain unsolved issues.

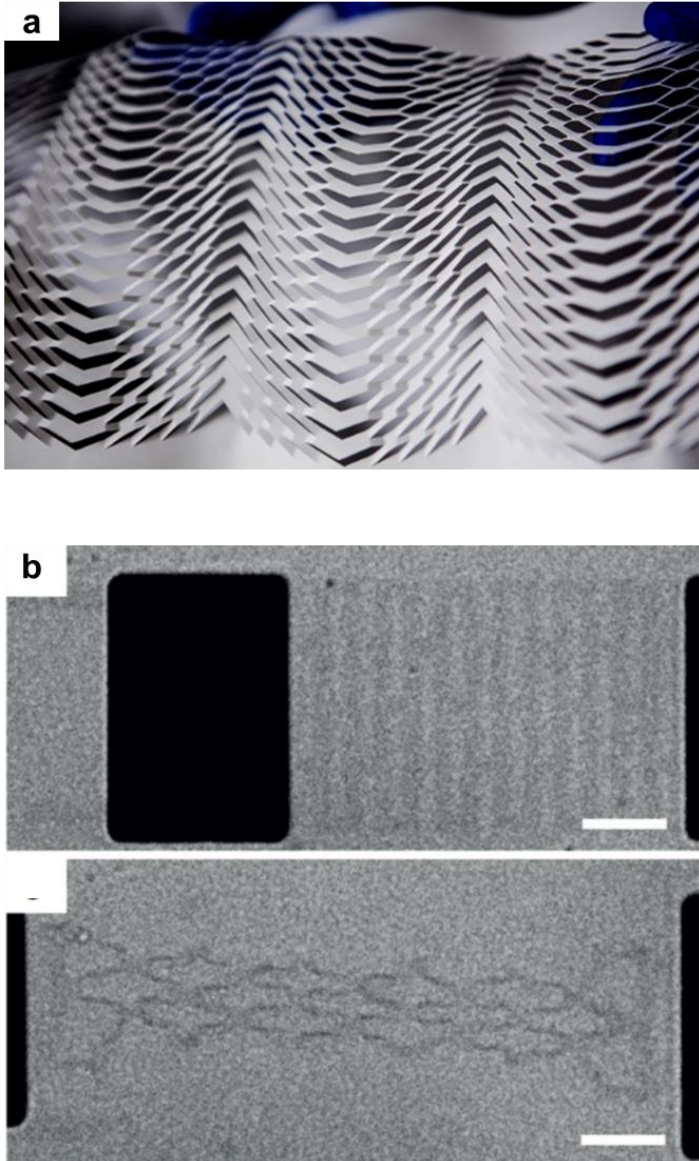


Figure 1.5 | Kirigami architectures for stretchable interconnects. (a) An artistic geometry of the kirigami concept that folds and cuts paper. (b) A highly stretchable graphene transistor that can be stretched by 240% without observable degradation, with the deformation mechanism that meets kirigami physics [67].

The third layout is “out-of-plane architectures”, the most prominent and practically useful methodology for stretchable electronics. In this concept, the out-of-plane motion accompanied by hybrid systems that mainly use “rigid” and “brittle” films bonded to or embedded in elastomeric substrates advocates reliable, reversible responses to large deformations [50]. Representative architectures exploited in the initial progress are described in Figure 1.6a. Combined with the simple prestretching process, micro-wavy structures (1D or 2D) could be spontaneously built, following the physical law that minimizes the entire energy on the film-substrate bilayer system [70, 71], in layouts that prescribed final geometries with engineered bonding positions: (1) if initially flat, rigid films (single-crystalline inorganic [72, 73], oxide [74, 75], organic [76], graphene [77, 78], nanowires [79, 80], etc.) were bonded at all points on their bottom surfaces to the prestrained (prestrain level $>$ critical strain) soft foundation, the system would undergo “wavy” deformations, generating well-defined wrinkles with controllable geometric parameters (wavelength and amplitude) [70, 71] (the first and third layout in Figure 1.6a) (physical mechanism of wrinkling in bilayer structures will be further discussed in section 3.1.1); (2) similar mechanics could be applied to the geometry that possessed selective bonding positions (the second and fourth layout in Figure 1.6a). In this case, releasing the prestrain leads to large, out-of-plane bridge structures, due to the delamination of the non-bonded regions from the substrate [81]. Different from the former case, the geometric parameter like wavelength can be defined more precisely, and thus more

accurate engineering of architectural design can predict the range of stretchability [82, 83]. Furthermore, extended from the initial schemes, functionalities including improved stretchability [84, 85] and variety of material compositions and architectures [86] provided advanced schemes for stretchable electronics (Figure 1.6b, c).

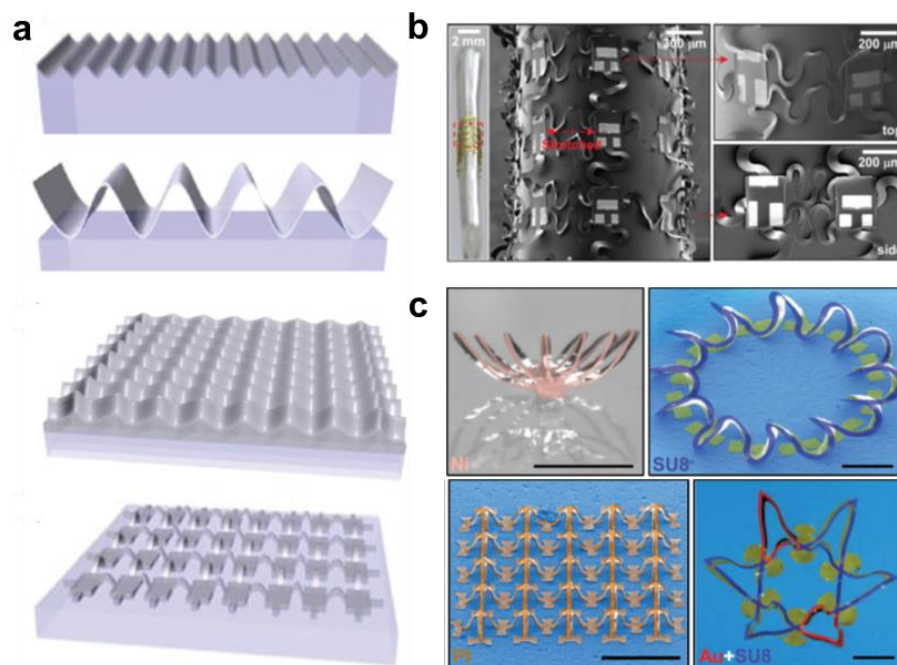


Figure 1.6 | Out-of-plane architectures for stretchable interconnects. (a) Schematic illustrations of representative out-of-plane architectures driven by prestretching and selective bonding process [50]. (b) Non-coplanar serpentine structures consisting of trilayer stacks of polymer/metal/polymer [50] for improved stretchability. (c) Versatile 3D buckling in multi-materials based on prestretching and selective bonding [86].

1.2.2 Novel Materials

The other strategy to achieve stretchable electronics is to develop and employ novel materials and interfaces that exhibit good conductivity and mechanical robustness under stretching [87]. In this section, classes of materials for stretchable electronics are introduced with categorical division into three groups: 1D materials (carbon nanotube (CNT), metal nanowire, etc.), liquid metals, and other novel materials (2D materials and hydrogel). Distinct from typical metallic thin films that generally crack into small micro/nano-grains without any entanglement under stress, 1D materials feature (1) the augmented toughness induced from entanglements between themselves, (2) the capability of directional alignment, and (3) transparency (Figure 1.7a) [87]. Also, abilities to print and/or form composite films with proper dopants and matrices suggest that 1D materials can lead to large-area stretchable electronics. Among 1D materials, particularly, outstanding properties of high mechanical strength, elastic modulus, thermal conductivity, and electrical conductivity [88, 89] have advocated the use of CNTs together with various synthesizing methods [90]. Starting from the studies on fabricating a single-walled carbon nanotube (SWNT)-fluorinated copolymer composite, Someya and coworkers opened a pathway for demonstrating stretchable electronics based on CNT composites [63, 91]. The composite showed good conductivity ($50\text{--}100\text{ S cm}^{-1}$) and stretchability ($\sim 100\%$), the levels of which enabled modest operation of active-matrix organic transistors. Following this stream,

a great number of strategies with multiple sets of CNT (single- or multi-walled) and elastomer matrix (fluorinated copolymer [63, 91, 92], polyurethane [93], PDMS [94], poly(tert-butyl acrylate) [95], etc.) have been made to demonstrate meaningful applications (active-matrix [63, 91], LED interconnects [92], energy textiles [96], Li-ion batteries [97], etc.) in a composite form. Also, additional attempts of CNT nanoribbons/films have been addressed to involve transparency and easy patterning combined with printing methodologies [98-102]. In this case, the capability of ultrafine CNT alignment allowed continuous CNT films and yarns with further improved tensile strengths, Young's moduli, and electrical conductivity; concurrently showing the potential of spring-like geometry for advanced applications [102].

In spite of superb properties of CNTs in several aspects, relatively low electrical conductivity ($10 - 100 \text{ S cm}^{-1}$ in most studies) of CNT-based stretchable conductors was the critical issue. To surmount this, metal nanowires (silver nanowire (AgNW), copper nanowire (CuNW), etc.) have appeared to be an alternative solution. Together with facile synthesizing methodologies [103], metal nanowires greatly reduced resistivity and also encouraged the use of much simple and scalable methods like spray coating [104]. Besides excellent electrical conductivity, the aggregating tendency of metal nanowires generally forms a nanowire network that allows a high transmittance for a wide range of wavelengths: Leem and coworkers reported AgNW network with $R_s \approx 35 \text{ } \Omega \text{ sq}^{-1}$ at 98% transmittance [105]. Moreover, advanced technologies of laser-assisted nanowelding [106] and multi-

material electrospinning [107–110] provided additional functionalities in terms of novel geometries (joint networks [106] and nanotrough structures [107, 110]) and improved electrical conductivity. In company with nanowire growth control, geometric design, well-defined alignment, and multi-material composition, metal nanowire-based stretchable conductors exhibited an extensive set of stretchable applications including transparent conductors [107, 108, 110], strain sensors [111], and heaters [112].

Distinct from film-like or composite-like characteristics of conventional materials, an unusual concept of “liquid” has recently been arising along with the stream of stretchable electronics. Attractive features of shape-reconfiguring and stretch-tolerating with tendency to maintain electrical conductivity have stimulated the introduction of liquid metals (eutectic gallium-indium (EGaIn), etc.) as one of the most promising candidates [56-58, 113-119]. Attributing to its liquid-like property, fatal degradation caused by stretch-induced microcracks or geometric failure in aforementioned conducting films or composites can be circumvented, thereby enabling geometric peculiarities of reversible shape-reconfiguring [113] and self-healing [114]. More interestingly, such a property provided opportunities for realizing stretchable electronics in conjunction with versatile printing techniques [115, 116] and microfluidic approaches [117]. In practice, Dickey and coworkers suggested freestanding liquid metal microstructures fabricated by a novel 3D printing process (Figure 1.7b) [115]. Functionalities were much extended when liquid metals met fibers [118] and soft lithography [117, 119].

In particular, given the multilayer circuit design, liquid metals offered an exceptionally promising route for fabricating a stretchable form of vertical interconnection that was normally failed in forms of films or composites owing to the issues on cracks and conductivity, respectively [119]. Simply by a physical injection process, a liquid metal filled the predefined microchannels that penetrated each layer for successful interconnection, and the completed structure showed very low resistivity and good stretch-tolerance. Despite fruitful achievements, there still remain challenges in handling, forming contacts between devices, and storing in predefined channels as a liquid phase.

Most recently, additional promising attempts have been made to offer deep and wide insights into material choice and patterning tools for adequate applications. After the development of CVD-based large-scale synthesizing methodology of graphene [120], novel 2D materials have joined to the field of stretchable electronics. Although diversity and ranges of applications are limited compared to 1D materials, 2D materials also have a great potential in stretchable electronics, addressing larger grains, ultrathin thickness, and corresponding superb transparency. Representative features of a graphene film included a modest sheet resistance $\sim 280 \Omega \text{ sq}^{-1}$ and transmittance $> 80\%$ with a level of stretchability $\sim 10\text{--}20\%$ [120]; the stretchability of graphene conductors could be further extended by applying a prestretching method [77] and/or forming 3D graphene foams [121]. Successful development of novel nanosheet structures (Au, etc.) broadened the choice of 2D materials in

stretchable electronics [122]. Furthermore, the unique property of extreme stretchability (tensile strain $> 2000\%$ and area strain $> 150\%$) have been recently reported in soft hydrogels that formed ionically crosslinked networks containing $\sim 90\%$ water (Figure 1.7c) [123, 124]. This conceptually new material further extended the applicable fields to transparent loudspeaker [124], highly stretchable touch panel [125] and bio-compatible ionic skin [126].

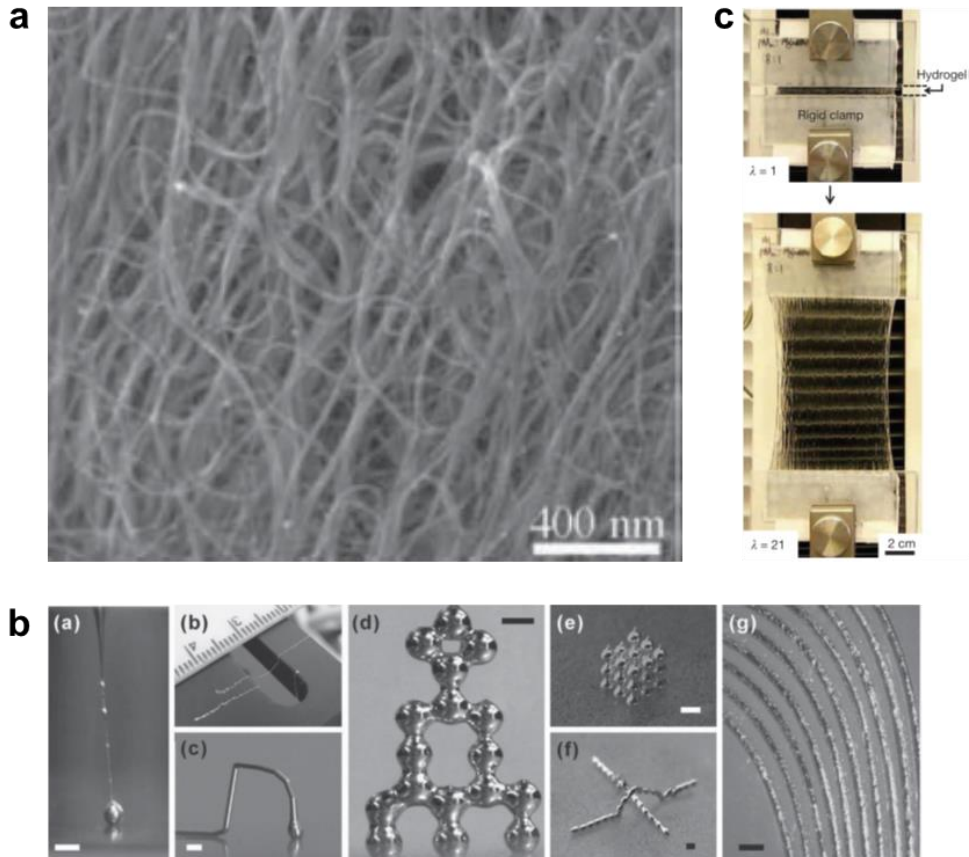


Figure 1.7 | Novel materials for stretchable electronics. (a) SEM image of CNT entanglement [78]. (b) 3D printed liquid metal architectures [115]. (c) Highly stretchable hydrogel that can be stretched to 21 times its initial length [123].

1.2.3 Strain Isolation Structure for Device Protection

Besides the interconnection architectures described in section 1.2.1, new conceptual architectures need to be established for electronic (optoelectronic) devices and circuits themselves for the “stretchable” concept (Figure 1.8) [2]. For their protection, generally, locally strain-isolating structures (or associated geometries) have been developed. The most representative structure is a rigid island that is stiff enough to keep a surface strain level below the fracture strain of devices or corresponding contacts [127]. Together with stretchable interconnects with enabling technologies as highlighted in sections 1.2.1 and 1.2.2, this island concept can ideally construct stretchable system-level electronics, with form factors that bridge adjacent functionalized islands in which electrical components of receptors (or sensors), processors, and displays or actuators are integrated. Key points of these rigid islands are materials, geometric layouts, and structural parameters (size and thickness). According to the geometric layout, the islands can be classified into three groups (Figure 1.9): (1) a protruding form on a soft substrate [128–133], (2) an embedded form in a soft substrate [134, 135], and (3) an integrated form as one of the circuit materials [136–142].

Most simply, the protruding island can be defined onto the soft substrate by conventional lift-off process, soft lithography, or additive techniques. Numerous sets of materials with proper thickness can be

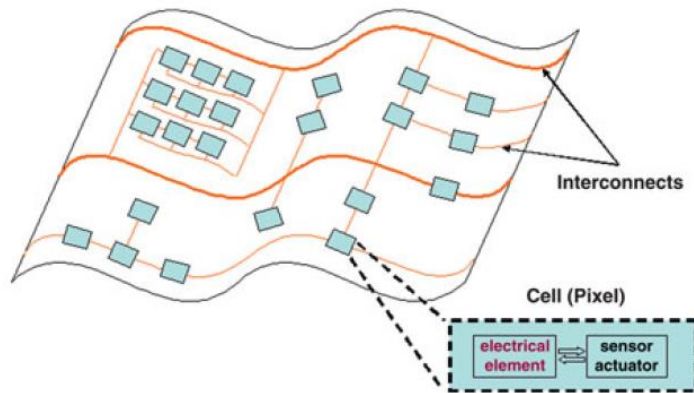


Figure 1.8 | Architecture of stretchable electronic circuits. Cells with optoelectronic functions are made on islands and are connected with stretchable interconnects on a common soft substrate [2].

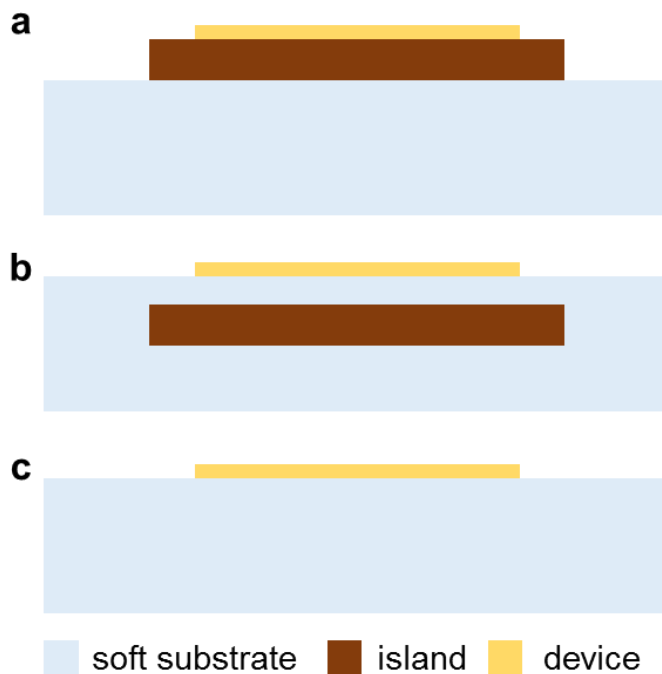


Figure 1.9 | Typical geometric layouts of rigid island systems: (a) a protruding form, (b) an embedded form, and (c) an integrated form.

integrated, and serve as rigid islands including PI [128, 129], PET [130], , synthetic composite [131], and even elastomer (PDMS) with designed geometries [132, 133]. An attractive feature of this architecture is that conventional device fabrication steps (e.g. photolithography) can be similarly applied only with subsequent steps of defining island areas and additive bonding of device-island unit structures onto a soft substrate. However, this type of islands usually underwent fracture or total delamination—depending on their Young’s moduli or thicknesses— under a strain level of 20 – 30%, restricting the field of applications [43]. Furthermore, the clearly defined discontinuity in thickness profile (from the substrate to islands) impeded a facile implementation of stretchable wiring between islands; hence, artistic geometries—such as freestanding wavy [132] or penetrating structures [130, 133]— or relatively thick (> few micrometers) conductive composites [128] should be employed to bypass this hurdle.

Circumventing these limitations, an embedded form of rigid islands has been deeply investigated for a decade. Starting from the Lacour’s work, attempts on fabricating devices directly onto strain-free areas, defined by embedded islands, have been made [134, 135]. Despite advantages coming from continuous surface profiles near the island boundary, further advancement in this approach was hindered by the challenging issues on (1) limited process conditions induced by intrinsic properties of elastomeric substrates that feature vulnerability to organic solvents and temperature (< 200 °C), (2) predefined positions of islands that might incur alignment

problems between multiple steps of masking process, and (3) localized stress near the islands that might cause irreversible degradation on outward interconnection wirings.

Distinct from the separately designed island structures, an integrated layout has been arising along with the methodology to transfer patterned Si nanomembranes. In conjunction with a prestretching process, Rogers and coworkers devised a non-coplanar mesh layout for curvilinear electronics that involved an array of patterned Si islands interconnected by narrow strips of Pi/metal interconnects [136]. In accordance with the underlying mechanics, a prestrain level and design parameter led to the stretchability of ~50% [137]. Extended from this work, further stretchability (> 100%) was achieved in modified layouts of island-bridge systems only by adopting a trilayer system of Si-PDMS-PI with adequate mesh layouts as interconnects [138, 139]. Also, the capability of controlling system stretchability allowed customized island-bridge layouts for targeted demonstrations such as soft electronic eye cameras [140], balloon catheters for cardiac electrophysiological mapping [141], and stretchable optoelectronics [142]. Advanced features of this layout are that (1) precise control of island-bridge geometry is attainable by predefined membrane thickness, (2) stretchability of the whole system can be precisely engineered [82–85, 137–139], and (3) process steps are compatible with the conventional photolithography process. However, the methodological constraint that transfer steps should be involved in key steps isolated this unusual strategy from other implementing tools such as printing techniques.

1.3 Motivation and Main Concept: Fully-Integrated Soft Electronics

Introducing softness in electronic devices and circuits has substantially advanced a new class of electronics that can interact with humans without any mechanical and electrical failure; as well as contributed to developments in novel materials and architectural modeling (section 1.2). Nowadays, on the basis of accumulated knowledge, researchers have agreed that a system-level integration of soft electronics beyond developing a single device, sensor or electrode design is a promising aim. Based on this stream, it is clear that the true meaning of “stretchable (or soft)” electronics will arrive when the following four aspects are fulfilled in a common substrate: stretchable forms of (1) independent power sources, (2) receptors (sensors), (3) data processing and computing circuits, and (4) displays. Numerous efforts have been made to suggest a promising pathway with regard to materials and device architectures for the key technologies of (1) power sources, (2) sensors, and (4) displays. Specifically, several layouts of system-level soft electronics that involve sensor arrays have been proposed to glean a wide spectrum of intimate bio-signals such as electrocardiogram (ECG), electromyogram (EMG), electroencephalogram (EEG) [36, 143, 144], and blood flow [145].

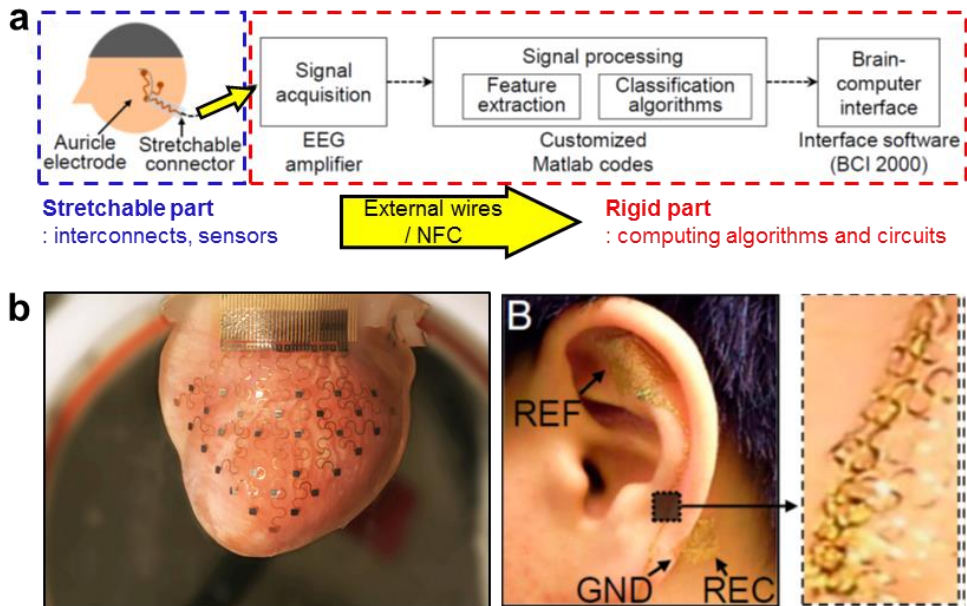


Figure 1.10 | Limitations in existing stretchable electronics. (a) Schematic diagram of signal flows in general stretchable electronic systems. Gleaned data obtained from soft, stretchable sensors and interconnects are transmitted to the rigid part where signal amplification, processing, and computing are conducted [146]. (b) Examples of stretchable networks of sensors and interconnects that possess arrays of pads for outward data extraction [146, 147].

However, as described in Figure 1.10, stretchability (or softness) was permitted only for a small portion—mainly interconnects and sensors rather than data processing and computing parts— of an entire system in most studies thought to handle system-level soft electronics [36, 140–148]. For example, in the study on a persistent brain-computer interface based on the integrated design of auricle electrodes [146], EEG signal was measured from soft auricle electrodes, and then transmitted to the rigid part comprising an EEG amplifier and processor boards for signal acquisition and processing. Of course, the salient point is the soft design in electrodes and sensors for intimate interfacing, and proper demonstrations can be completed with data processing in external “rigid” circuits; but, this is counterintuitive in terms of “soft electronics”. This intrinsic limitation was come from the lack of consideration in the third aspect “(3) stretchable data processing and computing circuits”, the most critical hurdle for “entirely soft” electronics. The main reason that advances in the third aspect have been retarded is difficulties in IC design and fabrication steps directly onto a soft substrate. This situation consequently proclaimed the need of “rigid” circuits (like PCBs)—usually connected with bulky wires— as computational backbones in most soft electronic systems.

In recent years, as an alternative to the foregoing limitations, a hybrid concept of flexible, stretchable electronics that brings together soft and hard electronics into a single platform has been arising [149–152]. In this concept, soft materials and designs construct stretchable interconnects and conformal

interfaces; and co-integrated rigid silicon-based devices and circuits enable high-speed data processing and computation, simultaneously achieving both of high level system integration and advanced computational functionality. A few strategies for reliable integration of rigid devices into a soft platform have been introduced to alleviate the dissimilarity with conventional PCB technology: microfluidic assembly [150], transfer-combined modified flip-chip bonding [151], and reflow soldering on a flexible substrate [152]. In most approaches, however, complexity in fabrication process (multistep photolithography) and limited design freedom (several photo-/shadow-masks) restricted the ability to form advanced networks between numbers of IC devices and multilayer design. Furthermore, the general use of bulky size chips ($> 4\text{--}5$ mm, one side) degraded system-level stretchability and skin-conformability.

In this dissertation, we point out the discrepancy in the meaning of “soft” electronics. Surpassing the limitations in previous studies, our goal is to realize system-level soft electronics where all of interconnects, sensory parts, and data processing/computing circuits are integrated into a common soft substrate, thus leading to “Fully-Integrated Electronic Skin (E-Skin)”. In this concept, no external wires and no additional rigid PCBs are necessary for data transmission and processing. Indeed, all sequences of sensing, encoding/decoding of gleaned signals, high-speed data computation, and even wireless RF communication can be carried out “in the skin” with customized, miniaturized, hybrid-type designs. For implementation, a fully

printable methodology from substrate preparation (soft substrate engineering for device protection) to stretchable circuit fabrication (stretchable interconnection wiring and surface-mountable device (SMD) bonding) is developed. This facile and novel methodology offers advanced capabilities of (1) large-area surface strain engineering on a soft substrate, (2) customized and miniaturized circuit design, (3) large-area stretchable interconnection wiring, and (4) numerous sets of IC devices bonding, without any transfer step. The superiority of this simple and versatile approach enables the realization of unprecedented demonstrations of stretchable, high-speed (~1 MHz) self-computable e-skin for the potential of stretchable computers and soft, skin-like interfaces for wirelessly activating soft robots.

This dissertation is composed of six chapters including Introduction and Conclusion.

Chapter 1 briefly introduces the recent progress in stretchable electronics with representative core technologies and associated fields of applications.

Chapter 2 explains a printing-based facile and scalable methodology that suggests architectural designs of “Printed Rigid Islands (PRIs)” for effective surface strain engineering on a soft substrate. Materials, equipment, experimental tools for analysis, and structural optimization of PRIs will be discussed.

Chapter 3 describes combinational methodologies for printing-based implementation of system-level soft electronics on engineered soft substrates.

Fabrication, geometry, physical mechanism, and electrical characteristics of inkjet-printed wrinkled silver interconnects are firstly addressed. Subsequently, a novel concept of image-based customizable circuit routing and associated implementation process are introduced as an optimized scheme for printing-based implementation of system-level, hybrid-type soft electronics. Numerous complete examples of custom-designed soft electronics are included.

Chapter 4 covers the complete applications of soft, fully-integrated e-skins that feature the capability of high-speed (~ 1 MHz) computation, namely self-computable e-skin. Particularly, a novel geometric design of double-side integration is addressed together with a universal-concept platform.

Chapter 5 introduces a novel concept of fully-integrated electronic skins that are wirelessly interfaced and operate to wirelessly innervate dormant soft robots, as the simplest but most attractive way to activate several types of soft robots through consecutive e-skin-mediated innervation. This is also the first use of integrated soft electronics to an embedded driving circuit for soft robots.

Chapter 6 summarizes the concept, methodology, and meaningful demonstrations of fully-integrated electronic skins, and also suggests the future perspective.

Chapter 2

Printing-based Soft Substrate Engineering

In this chapter, a printing-based facile and scalable methodology that suggests architectural designs—namely, “Printed Rigid Islands (PRIs)” — for effective surface strain engineering on a soft substrate is investigated. Materials and equipment for PRI fabrication, experimental tools for quantitative analysis on surface strain of PRI-embedded soft substrates, and structural optimization of PRIs are sequentially presented.

2.1 Printed Rigid Island (PRI)

2.1.1 Materials and Equipment

PRI is a rigid structure that mainly serves as a fundamental building block for soft substrate engineering in a fully-embedded form [153, 154]. Along with a facile printing process, various factors should be addressed for PRI material selection: rigidity, solubility, surface tension, viscosity, glass transition temperature, etc. In this work, poly(methyl methacrylate) (PMMA) (Sigma Aldrich) was chosen as a main material for PRIs because of its sufficient level of rigidity (Young's modulus ~ 2 GPa), proper solubility in a typical solvent, propylene glycol monomethyl ether acetate (PGMEA) (Sigma Aldrich, $\geq 99.5\%$), and diversity in molecular chain length (M_w 15,000–350,000, available in Sigma Aldrich). Specific molecular weight (M_w $\sim 97,000$, 120,000) and weight concentration (4–20 wt%) were tuned according to the printing method: piezoelectric inkjet-printing or pneumatic control nozzle-jet printing. For a soft substrate (or matrix), poly(dimethyl siloxane) (PDMS) elastomer (Sylgard 184, Dow Corning) with a mixing ratio of 20:1 (elastomer base : curing agent) was adopted (Figure 2.1a).

Two different kinds of printing method in which the operating mechanism is completely different were addressed according to the target diameter of PRIs. First, a piezoelectric inkjet-printing (DMP 2831, Dimatix

corp.) process was employed to fabricate PRIs with a diameter range of 50–1500 μm . For larger diameters, typically 1–3 mm, on the other hand, pneumatic control nozzle-jet printing technique (SHOTmini 200Sx, Musashi Engineering Inc.) was utilized with higher ink (PMMA) concentration (Figure 2.1b).

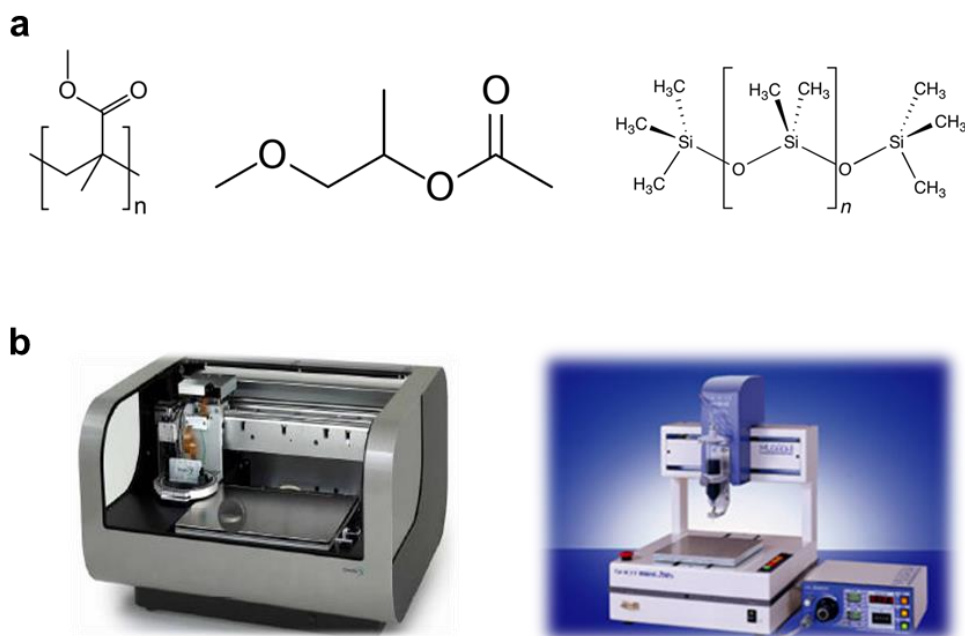


Figure 2.1 | Materials and equipment for printed rigid island embedded soft substrates (PRISSs). (a) Chemical structures of PMMA, PGMEA, and PDMS. (b) Images of inkjet printer (DMP 2831, Dimatix corp.) and pneumatic control nozzle-jet printer (SHOTmini 200Sx, Musashi Engineering Inc.).

2.1.2 Piezoelectric Control Inkjet-based PRI

A piezoelectric control inkjet-printing methodology offered an opportunity of forming a hemispherical—crater-like or coffee-ring structure, exactly— rigid island structure through multi-pass (1–5 passes) and multi-droplet ($\sim 10^3$ – 10^5 ink droplets) printing process [153]. Based on the voltage-controlled piezoelectric effect, 4 wt% PMMA ink (M_w 97,000) was spewed from a 21 μm nozzle, forming a spherical droplet whose volume is ~ 10 pL. Specifically, an applied voltage level of 25–32 V was set to stabilize the ink jetting with the velocity of 7–9 m/s; and multi-nozzle jetting with 4 to 6 nozzles was addressed to reduce the process time as well as to properly form the balanced PRI structure, circumventing hasty drying of as-printed ink (Figure 2.2). To construct a balanced PRI which involved an isotropic morphology without partially over- or less-printed regions, the contact line pinning effect was introduced that sequentially printed ink droplets entirely contributed to the balanced increase in the morphology profile rather than to the expansion of the predefined coffee-ring diameter or overflow, as described in Figure 2.3. In combination with gradually reduced input patterns and optimized delay between printing steps (usually 30–60 s), a multistep printing (usually 3 to 5 steps) strategy provided the capability of fabricating large-area, well-defined PRIs with discretely tunable structural parameters (Figure 2.4). For a quantitative description, morphology variation in multistep (1 to 5) printed ~ 1450 μm PRIs was investigated. Importantly, it is worth noting that the first

step printing process ($\sim 3 \times 10^4$ droplets) obviously determined the outer diameter of the PRI and subsequent steps of printing did not cause an observable increase in the diameter. Instead, other parameters like thickness in center and coffee-ring area are gradually tunable along with additional printing steps (Figure 2.5). Taken together, the methodology of piezoelectric control inkjet-based PRI fabrication based on the contact line pinning effect offered opportunities of forming various types of PRIs with different size (50–1500 μm) and structure (typically 1- to 5-layered) just in a single batch, and corresponding in-depth study on structural optimization.

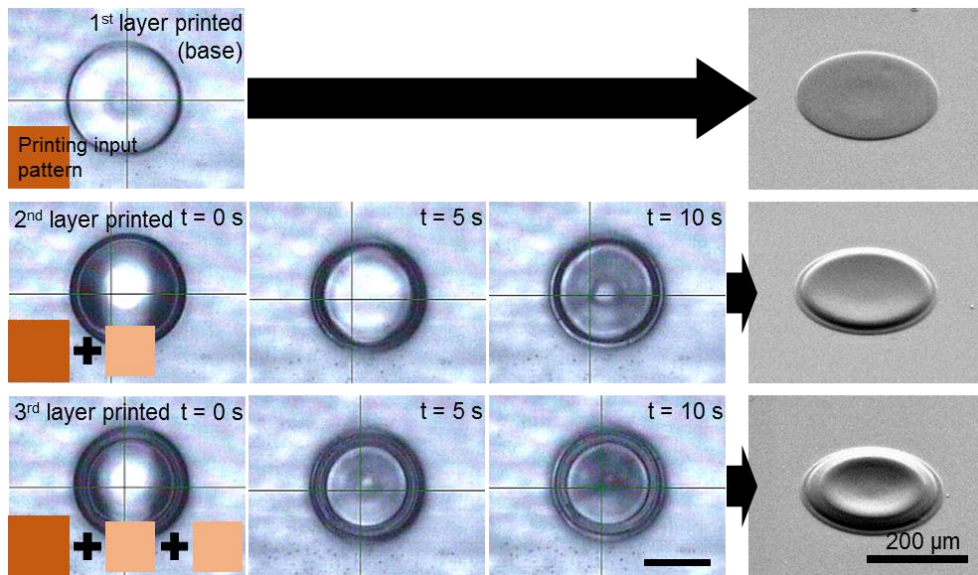


Figure 2.3 | Sequential image frames of real-time formation process of an individual PRI and corresponding SEM images. The first printing input pattern (normally square form) decides the PRI diameter; and subsequent steps of inkjet-printing with the reduced size of input pattern lead to the gradual increase in PRI thickness, driven by the effect of contact line pinning. Time delay between each step is dependent on the diameter of PRIs.

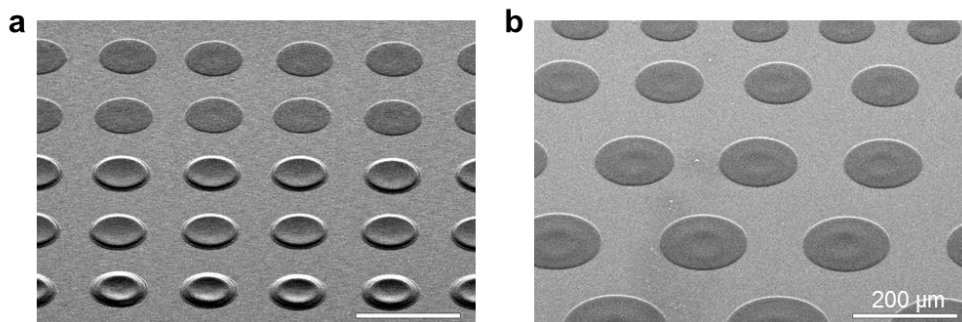


Figure 2.4 | (a) SEM images of PRI array with different printing steps (1 to 3 steps), thus different thickness, and (b) different size (diameter) [153].

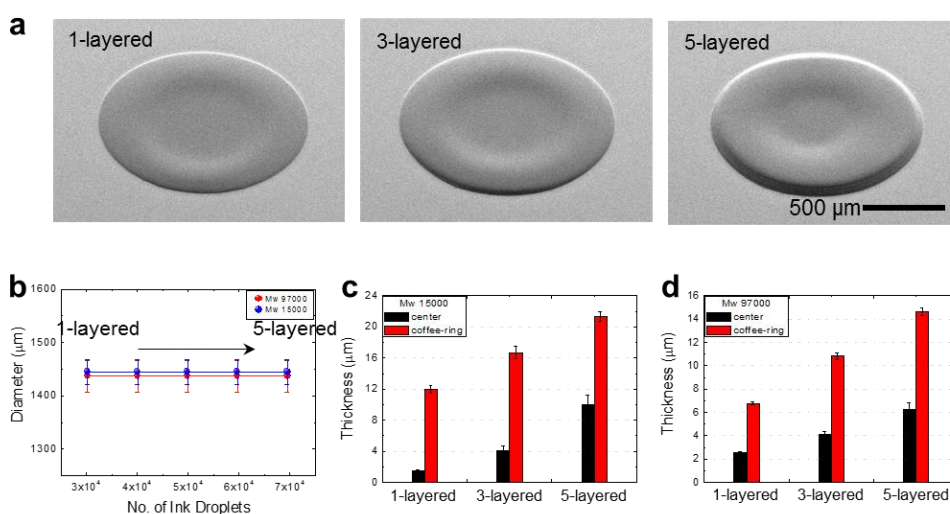


Figure 2.5 | Morphological features of multistep-printed inkjet-based PRIs. (a) SEM images of multi-layered PRIs (M_w 97,000). (b) Size dependency of PRIs on printing steps (or the amount of ink droplets). (c and d) Structural parameters of multi-layered PRIs with different M_w (15,000 and 97,000) [153].

2.1.3 Pneumatic Control Nozzle-jet-based PRI

For pneumatic control nozzle-jet-based PRIs, a high concentration poly (methylmethacrylate) (PMMA) (M_w 120,000) solution was used. Contrary to the aforementioned piezoelectric inkjet-printer [153], a pneumatically controllable nozzle-jet printer was employed to dispense high concentration (4-20 wt%) polymeric ink with high viscosity. Hence, just a single shot printing (air pressure = 150 kPa, duration time < 4 s) of proper ink completely formed a PRI that possessed a sufficient level of size (> 1 mm) and robustness in company with a room temperature drying process [154]. To be specific, a printing condition was stipulated by two parametric values of air pressure and duration time according to the specific solution concentration (or viscosity). During a room temperature drying process, as-printed PRIs were formed into coffee-ring like island structures. Noting that a coffee-ring structure of a polymeric solution droplet is affected by solution concentration and thus controllable in a stepwise manner [155, 156], we observed that concentration variation in PMMA ink (4–20 wt%) primarily contributed to stepwise splitting of PRI structural parameters at the equal drying condition (Figure 2.6). For an effective parametric sweep, a diameter was fixed to $\sim 1,500 \mu\text{m}$; and specific printing conditions were adjusted in accordance with ink concentration (4–20 wt%): air pressure level was controlled from 10 to 400 kPa relying on the concentration level to form PRIs of equal size; and duration time was < 2 s (Figure 2.6). Although various pairs of air pressure level and

duration time allowed an analogous PRI morphology (Figure 2.6), air pressure level was regulated by proper duration time (~2 s) for reliable PRI formation. From a cross section profile depicted in Figure 2.6, it is observed that an overall thickness of PRIs was increased as the PMMA concentration increased. Along with the increase in PMMA concentration, in particular, an internal volume—an empty space of a coffee-ring structure—of each PRI was gradually filled with an additional PMMA, and thus the increasing rate of the center thickness was larger than that of the coffee-ring thickness with the fixed diameter of printed droplets that was defined by the effect of contact line pinning. As a result, the PRI morphology was controllable from a coffee-ring structure (< 17 wt%) to a truncated cone (~17 wt%) and a blunt cone structure (> 17wt%). Comparison between printing methods to form PRIs is summarized in Table 2.1.

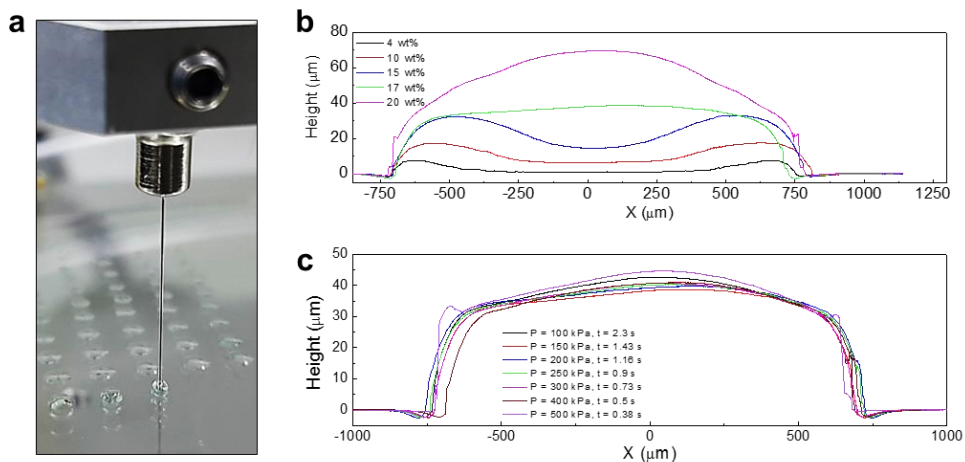


Figure 2.6 | Morphological features of nozzle-jet-printed PRIs. (a) Photograph of real-time nozzle-jet printing of PMMA ink. (b) Morphology profiles of PRIs with different PMMA concentration (4, 10, 15, 17, 20 wt%). Diameters of each PRI are fixed to $\sim 1,500 \mu\text{m}$ for an effective parametric sweep. (c) Morphology profiles of 17 wt% PRIs formed by different pairs of air pressure level and duration time (diameter was fixed to $\sim 1,500 \mu\text{m}$). The profile data advocate that the geometry of PRIs is prominently determined by ink concentration rather than printing condition [154].

Table 2.1 Comparison between printing methods for PRI fabrication

	Inkjet-printing	Dispensing
Diameter [μm]	50 – 1,500	1,000 – 3,000
PMMA M_w	15,000 – 97,000	All (120,000 used)
PMMA wt% [%]	< 5	4 – 24
Nozzle type	Multi (1 – 6)	Single
Printing time	~90 s for 1-layer (~10 min for 5-layered PRI)	< 3 s
Morphology engineering	Multistep printing	Ink wt% control

2.1.4 PRI-embedded Soft Substrate (PRISS)

Inspired by a stretchable bead network connected by springs where gradual compression/expansion of spring effectively absorbs mechanical stress (Figure 2.7), we developed a fully printable, PRI-embedded soft substrate (PRISS) as a fundamental framework for printing-based hybrid-type e-skin implementation (Figure 2.8a,b) [153]. Detailed fabrication steps are as follow (Figure 2.8c):

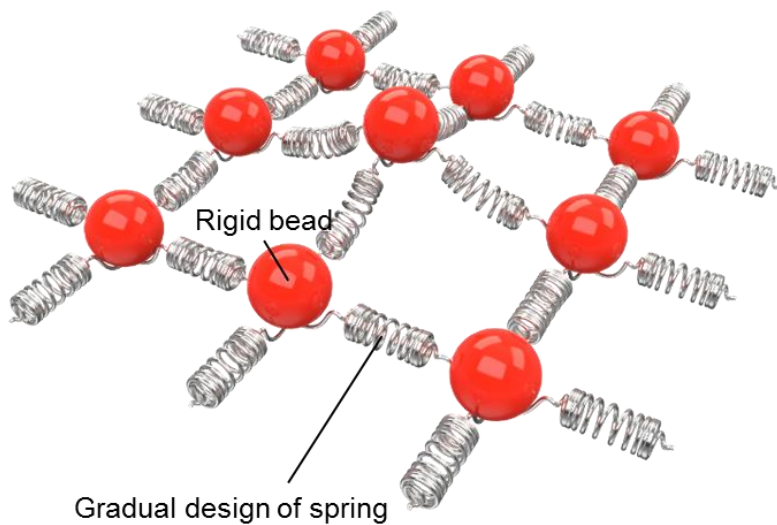


Figure 2.7 | Conceptual schematic illustration of stretchable bead network. The bead and spring represent the PRI and inkjet-printed wrinkled interconnects, respectively [153].

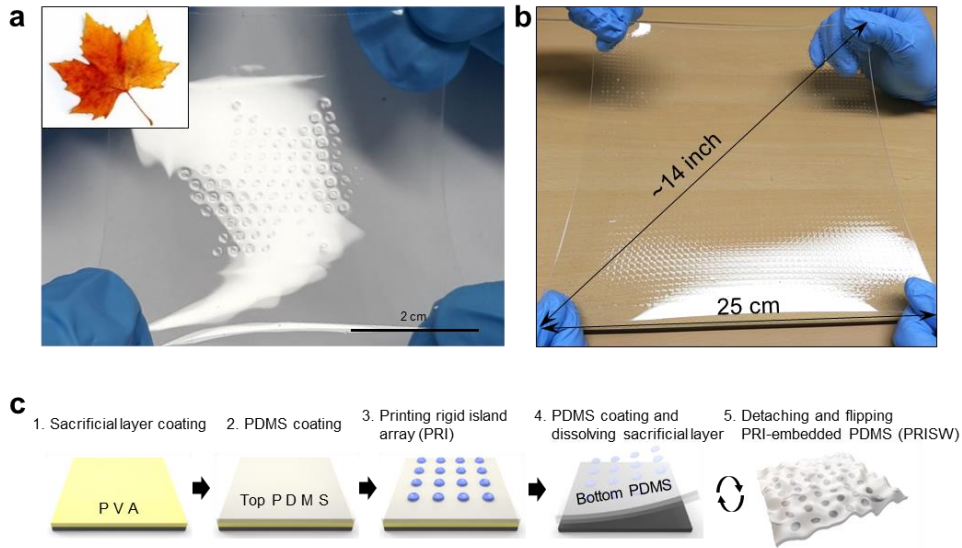


Figure 2.8 | Preparation of large-area, customizable PRISSs. (a) Photograph of the PRISS representing a “maple leaf”. (b) Photograph of a very large-scale PRISS (~14 inch, ~3,200 PRIs). (c) Fabrication process of a PRISS [153].

1. 5 wt% poly (vinyl alcohol) (PVA) (Sigma Aldrich, average Mw 31000–50000, 87–89% hydrolyzed) solution which can be dissolved in deionized (DI) water was spin-coated upon the cleaned glass substrates (700 μm thickness), and the coated layer was thermally annealed for 1 hr at 90°C.
2. Subsequently, poly (dimethylsiloxane) (PDMS) elastomer (Sylgard 184, Dow Corning), mixed at 20:1 ratio, was poured onto the PVA-coated glass substrate, and spin-coated for the top PDMS layer. The coated substrate was then partially cured for 15 min on a 75°C hot plate. The thickness of the PDMS membrane was ~ 20 μm (data of PDMS membrane thickness vs. spin-coating condition is shown in Figure 2.9).
3. After 5 min of ultraviolet-ozone (UVO_3) treatment, PRIs were printed following the steps as described in section 2.1.2 and 2.1.3. Owing to its maskless drop-on-demand (DOD) property, the size and position of PRIs were easily tunable. As-printed PMMA PRIs were heated on a 90°C hotplate for 30 min to evaporate residual solvents.
4. After an additional 5 min of UVO_3 treatment for enhancing the adhesion between PDMS and PMMA PRIs, the upper PDMS was spin-coated as the bottom PDMS layer. The thickness of the upper

PDMS layer (or bottom PDMS after being flipped) was dependent on the parameters of embedded PRIs. Subsequently, the sample was immersed in deionized water to dissolve the sacrificial layer for freestanding.

5. Finally, the freestanding PRISS was flipped for targeted applications. The total thickness of the PRISW was ~50-100 μm .

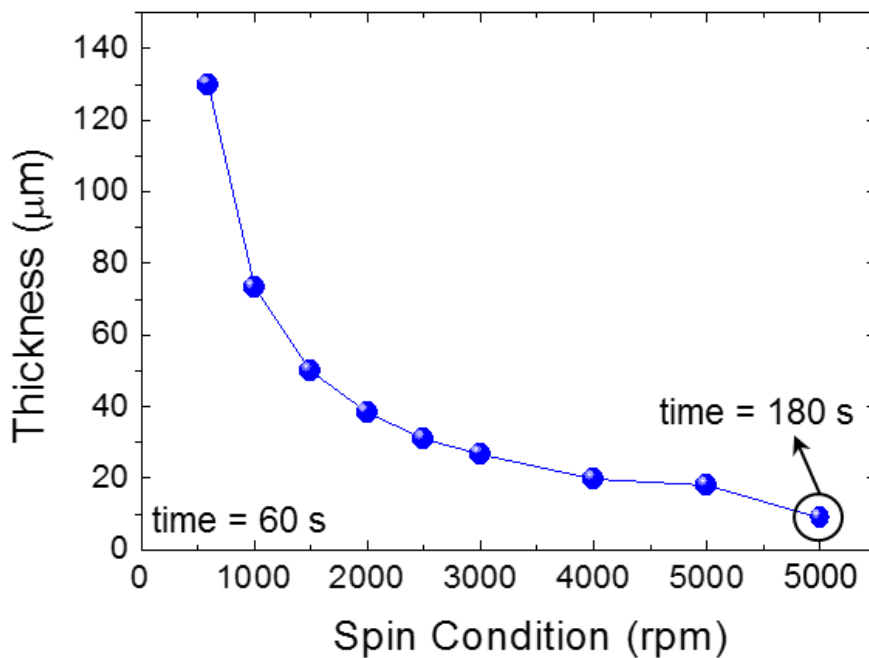


Figure 2.9 | PDMS (20:1 mixing ratio) membrane thickness vs. spin-coating condition.

Compared to the previous studies on developing various types of island materials (PI [128, 129], PET [130], synthetic composite [131], PDMS [132, 133], SU-8 [157], PCB [158]), PMMA provided capabilities of a sufficient level of robustness and printing-processability. Also, an embedded form of island structures into a soft matrix was addressed to provide flatness of the system for one-step printing of interconnection networks over the whole platform. Figure 2.10a shows the representative cross-sectional image of a PRISS in which several structural parameters comprising a PRI were clearly described. Based on this geometry, specific structural parameters of a PRISS were defined to simplify the following studies on PRI morphology and related surface strain analysis of PRISSs (Figure 2.10b): At first, the top side—compared to the other side (bottom side)—of a platform was set as equal to the flat side (or bottom side) of PRIs (refer to detailed fabrication steps in Figure 2.8c); accordingly, thicknesses between PDMS surfaces (top and bottom) and the PRI were defined as the top PDMS thickness (t_{TPDMS}) and bottom PDMS thickness (t_{BPDMS}). For accurate strain-isolating and stability, a geometric position of PRIs inside the PDMS matrix was of interest because t_{TPDMS} and t_{BPDMS} considerably affect the capability of strain-isolating. In this respect, a PRISS was designed to have t_{TPDMS} and t_{BPDMS} that maximized strain-free area in the interesting platform side without physical delamination or irreversible mechanical collapse (Specific values about PDMS thickness and optimization will be discussed in section 2.2.2 and 2.2.3). Furthermore, four kinds of structural parameters were defined to

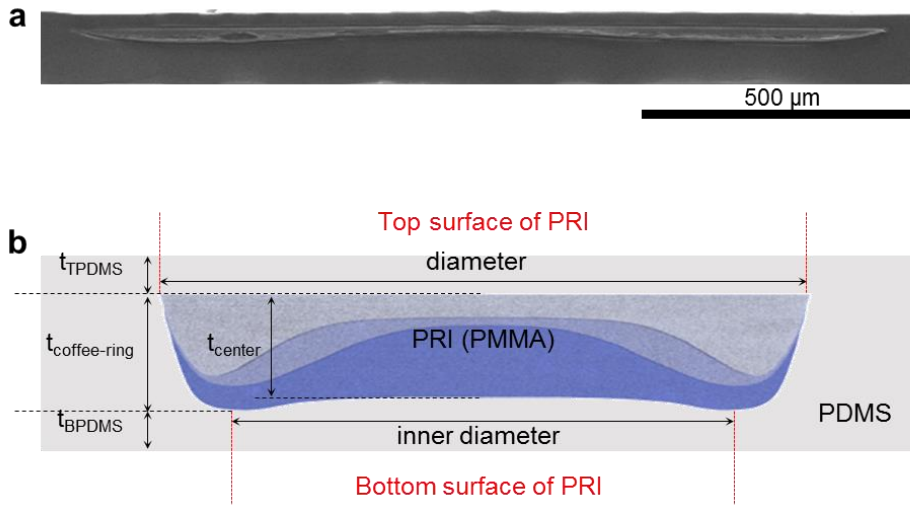


Figure 2.10 | Cross-sectional geometry of PRISSs. (a) Typical cross-sectional SEM image of a PRISS. (b) Geometric parameters of a PRISS [154].

describe a PRI morphology: outer diameter (shortly, diameter), inner diameter (defined as the distance between two local maxima, mainly coffee-ring structures), thickness at the PRI center (t_{center}) and coffee-ring structure ($t_{\text{coffee-ring}}$).

Methodology of printing-based island formation (explained in section 2.1.2 and 2.1.3) easily offered (1) the utmost scalability, (2) free patterning, and (3) diversity in size and structural morphology, thereby leading to a large-area, customized PRISS (Figure 2.11). The total thickness of the PRISS was $\sim 50\text{--}100\ \mu\text{m}$ according to the PRI parameters, comparable to that of the human epidermis ($50\text{--}100\ \mu\text{m}$) [159], and its stretchability allowed wrap-like conformability (Figure 2.11 (i–iii)). Due to the transparency, PRIs were rarely perceived unless illuminated by the tilted light incidence (Figure 2.11 (ii)). In virtue of DOD property of printing methods (either inkjet or pneumatic nozzle-jet printing), various types of PRIs with different size ($80, 500, 1450\ \mu\text{m}$) and structure (1- to 5-layered) (Figure 2.12) could be fabricated just in a single batch of the PRISS, simultaneously forming customizable arrangements with abilities to perfectly match the predesigned circuit and functional specification (“dolphin”, “maple leaf”, and letters indicating “ISLAND” and “SNU” were demonstrated with different types of PRIs in this case). Furthermore, the utmost scalability driven by printing techniques allowed rapid implementation of a large-area PRISS (~ 14 inch) containing ~ 3200 PRIs (only limited by the lab equipment specification), with versatile uses of physically cut subsections (Figure 2.8b).

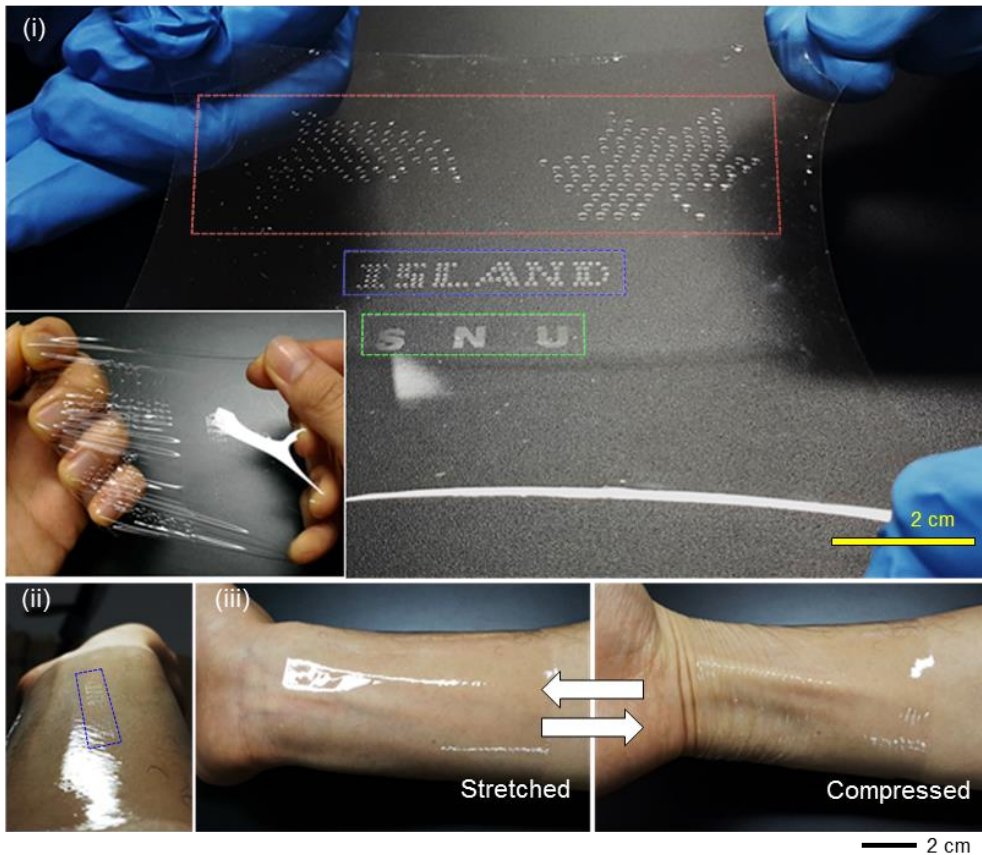


Figure 2.11 | A large-scale, multi-featured, customized PRISS. (i) Photograph of a PRISS that contains multi-scale/multi-structured PRIs in a customized configuration (dolphin, maple leaf, letters). Inset image shows a skin-like deformable property of the PRISS. Each PRI subsection either a dolphin or a maple leaf can be separately obtained by a physical cutting for individual uses. (ii) Owing to the transparency, PRIs are perceived only if illuminated by the tilted light incidence. (iii) The PRISS shows superb skin-conformability under sequential stretching/compressing [153].

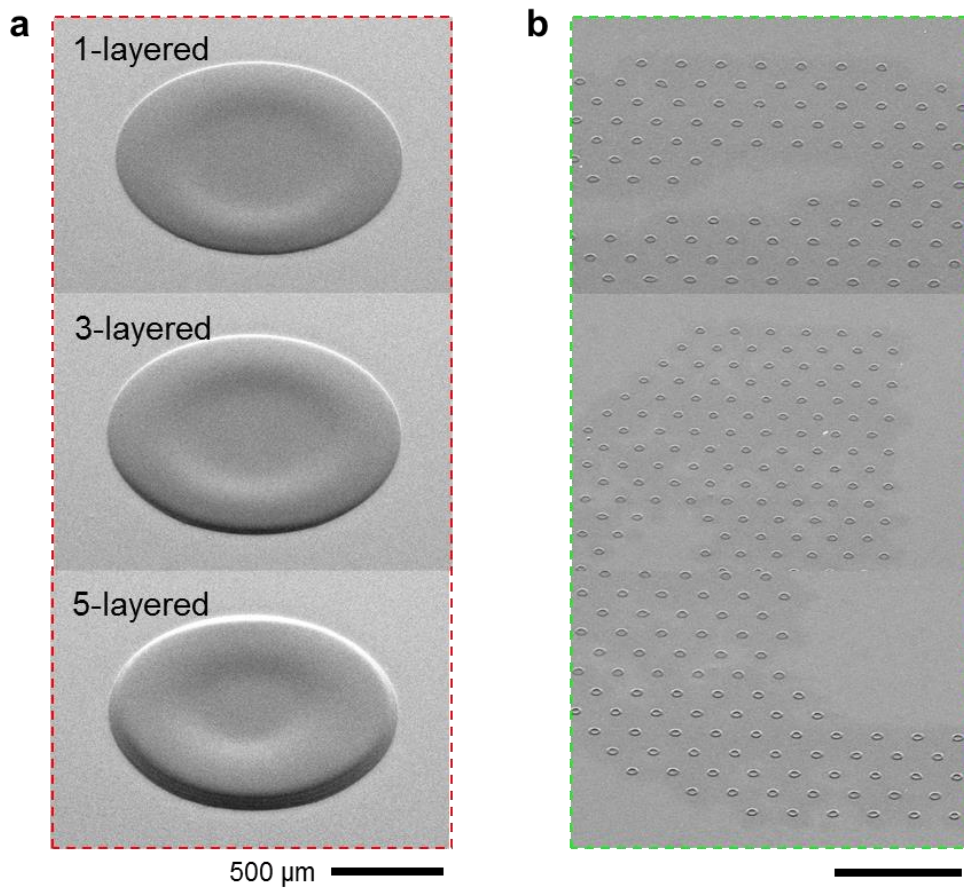


Figure 2.12 | Multistep-printed, multi-structured inkjet-based PRIs embedded in the PRISS of Figure 2.11. (a) SEM images of multistep-printed PRIs (diameter $\sim 1,500 \mu\text{m}$) constructing the dolphin and maple leaf. (b) SEM images of micro-size PRIs (diameter $\sim 80 \mu\text{m}$) constructing the letter “SNU” [153].

2.2 Surface Strain Analysis of Engineered Soft Substrate

2.2.1 Digital Image Correlation (DIC)

In general, visualization of surface strain field has been an abstruse challenge because of difficulties in creating distributed reference points and calculating time-variant displacement field to evaluate exact strain field. Especially, the problem can get worse if the interesting object is a hetero-composite that generates spatially anisotropic strain field over the surface under mechanical stresses. Accordingly, most studies that handled soft devices integrated on a soft substrate have tried to analyze the stability and reliability of devices and systems indirectly, in terms of finite element analysis (FEA) [3, 140–148, 150]. In spite of its usefulness, it should be considered that FEA cannot fully represent the real material properties, mechanics in hetero-interfaces and binding forces between components comprising soft composites such that inevitable inaccuracies and errors occur. To circumvent these limitations, in this work, we adopted the methodology of visualizing surface strain field on PRISSs in a direct way, digital image correlation (DIC) method [160]. Distinct from FEA, the DIC method could experimentally visualize a surface strain field of real samples through evaluating a displacement field between randomly distributed micro-size speckle patterns, offering more precise information about strain distribution

(or isolation) near the PRIs. An experimental flow for DIC process was as follows (Figure 2.13):

1. Upon the PRI (or via) area, baking powders (average particle size ~ 20 μm) were dredged to form randomly distributed speckle patterns.
2. In interesting areas, sequence of image frames was captured by an optical microscope as the platform was slowly elongated with a strain level of 0 to 40%. In particular, dark background was prepared to enhance the contrast level. Each optical image had a resolution of 720×480 pixels.
3. The sequential image frames were analyzed by comparing the relative movement of each speckle pattern, easily available by an image-processing tool (Vic-2D 2009, Correlated Solutions).
4. Then, displacement field data were automatically converted into Hencky strain values to evaluate maximum principal strain.

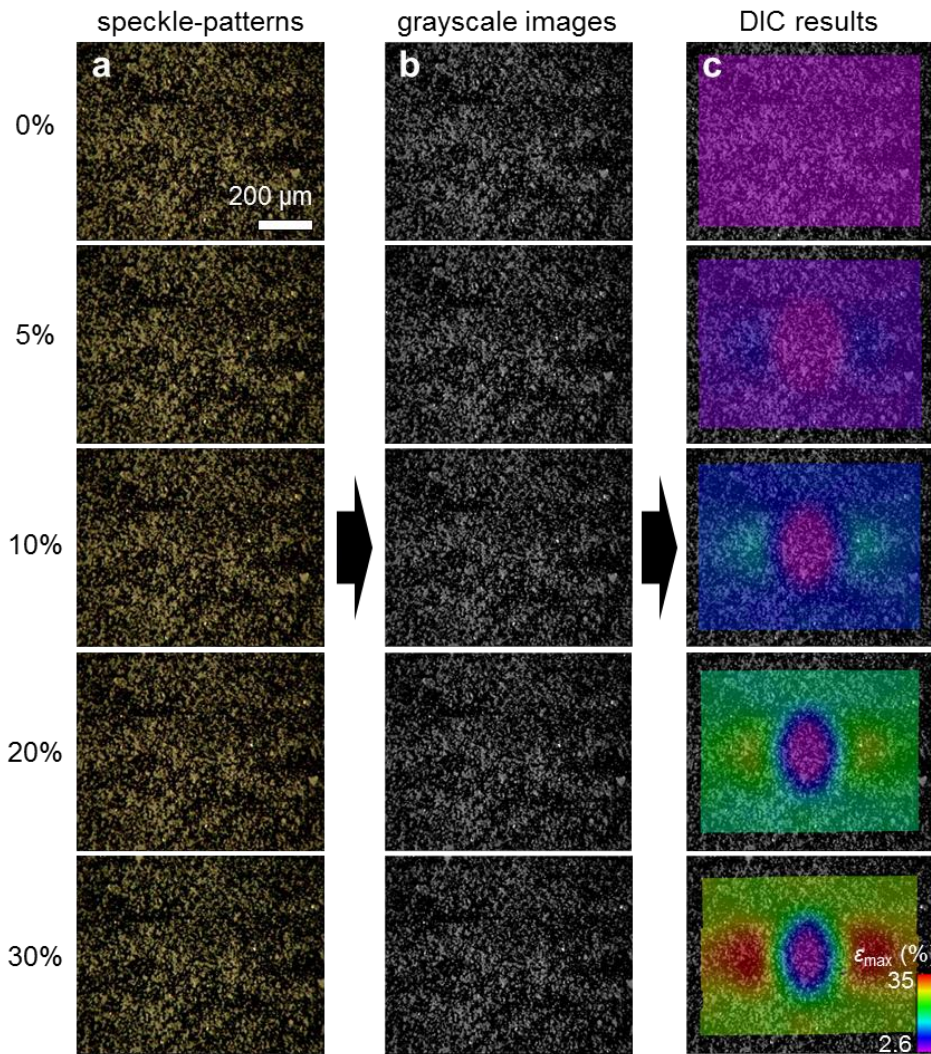


Figure 2.13 | Process flow of DIC method. (a) First, randomly distributed speckle patterns (baking powder, average size $\sim 20 \mu\text{m}$) are uniformly formed, and then the interesting region is captured by an optical microscope or digital camera. (b) Second, the captured images are transformed into grayscale to enhance the contrast level. (c) Finally, the sequential image frames are analyzed by an image-processing tool (Vic-2D 2009, Correlated Solutions) to evaluate the maximum principal strain [153].

2.2.2 Surface Strain Analysis and Structural Optimization of Inkjet-based PRI

The analysis on mechanical stability and structural optimization of PRISSs are important for improving the system compactness (or device-to-island fill factor) and conformability by reducing the total thickness while keeping a sufficient level of mechanical reliability. In this section, both of qualitative and quantitative analyses are performed based on the unit structure of PRISSs described in Figure 2.10 and Figure 2.14a. For analysis, a diameter of all PRIs embedded in PRISSs was fixed to $\sim 1,500 \mu\text{m}$, the value of which was chosen to provide the minimum applicable size to safely preserve a miniaturized SMD light-emitting diode (LED) ($1 \times 0.6 \text{ mm}^2$). First, we investigated the effect of PRI robustness (PMMA molecular weight, M_w) and structure on the stability. Two different kinds of M_w (15,000 and 97,000) were addressed (PMMA with larger M_w was excluded from comparison due to the excessive viscosity for inkjet-printing). The structural parameters of PRIs were engineered by a few steps of repeated printing that uniformly increased the thickness of crater-shaped PRIs meanwhile keeping the outer diameter fixed ($\sim 1.45 \text{ mm}$) through the contact line pinning effect (3D profiler images in Figure 2.14b); thus, we designated the structure of PRIs as “ N -step printed PRI” or shortly “ N -layered PRI” instead of the exact values of structural parameters. As shown in Figure 2.14c, it is observed that PRIs with M_w 15,000 clearly exhibited fragile characteristics both in single- and multi-

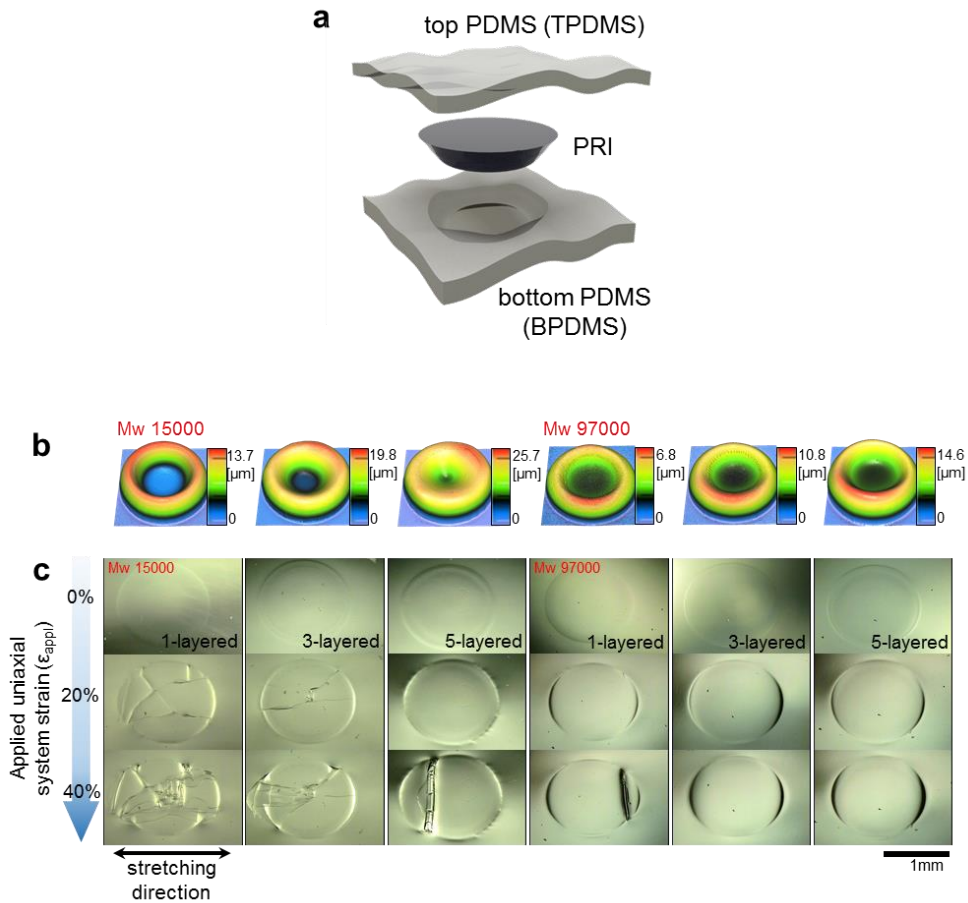


Figure 2.14 | Structural properties of various inkjet-based PRISs. (a) Schematic illustration of the unit structure of PRISs comprised of three parts: top PDMS (TPDMS), PRI, and bottom PDMS (BPDMS). (b) 3D surface profiler images of 1-, 3-, 5-layered PRIs with M_w 15,000 and 97,000. (c) Optical images of elongated PRISs (applied uniaxial strain, $\epsilon_{\text{appl}} = 0 - 50\%$) containing 1-, 3-, 5-layered inkjet-based PRIs with M_w 15,000 and 97,000 for comparison [153].

layered structures even under small applied uniaxial system strain (ϵ_{appl}). By contrast, in a qualitative perspective, the 1-layered PRI with M_w 97,000 possessed the robustness comparable to the 5-layered PRI with M_w 15,000, and the 5-layered PRIs with M_w 97,000 met the optimized stability: keeping their morphologies without deformation even under 50% ϵ_{appl} (Figure 2.15).

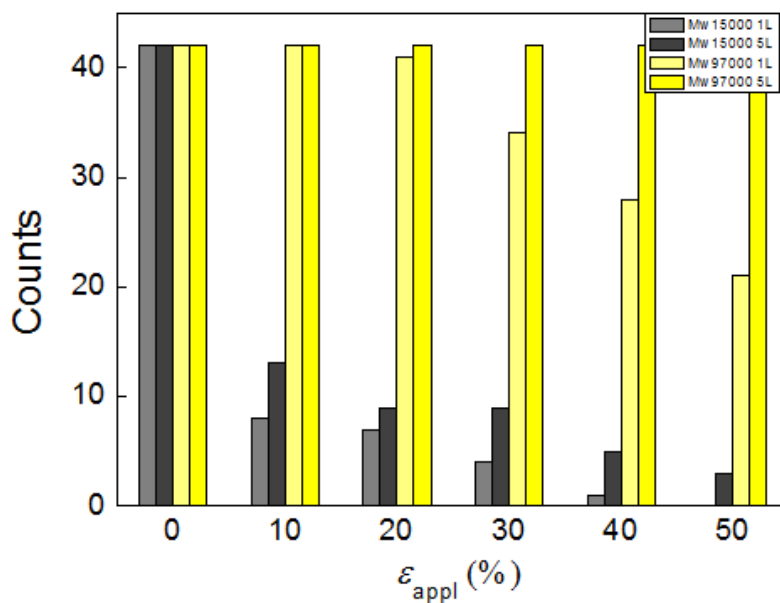


Figure 2.15 | Cracking tendency of inkjet-based PRIs with different structure and M_w . Starting from 42 PRIs for each condition, the number of intact PRIs is counted together with increasing tensile strain (0–50%). Both of molecular chain length and structural parameter affect the stability of the PRI and PRISS [153].

Additional quantitative studies were made to investigate the effect of t_{TPDMS} in conjunction with the comparison between 5-layered PRIs with different M_w . Two kinds of indices were defined to convert the PRI stability to numerical values: (1) maximum principal strain at the PRI center position (ϵ_{center}) and (2) strain-free area ratio in PRI ($\text{AR}_{2\%}$) that is defined by the ratio of strain-free area (internal strain $< 2\%$) to the whole PRI area. Typically, ϵ_{center} and $\text{AR}_{2\%}$ express the PRI robustness and the extent of applicable PRI areas for reliable device protection, respectively. The specific value of 2% was adopted as the cracking strain of inkjet-printed silver (Ag) lines (Figure 2.16). In case of PRIs (M_w 97,000), it is identified that the decrease in t_{TPDMS} caused drastic increase in $\text{AR}_{2\%}$ while keeping the stable value of ϵ_{center} ($< 1\%$) at the entire ϵ_{appl} regime (0–50%) (Figure 2.17). PRISSs with $t_{\text{TPDMS}} < 20 \mu\text{m}$ were excluded from analysis because PRIs were protruded from the PRISS as being strained in most samples. On the other hand, instability in PRIs (M_w 15,000) prevailed in most conditions, showing much higher ϵ_{center} and degraded $\text{AR}_{2\%}$ (Figure 2.17) in all t_{TPDMS} consistent with the fragile characteristics exhibited in Figure 2.14c. It is apparent from these results that the PRISS containing 5-layered PRIs (M_w 97,000) with $t_{\text{TPDMS}} \sim 20 \mu\text{m}$ exhibited the optimized mechanical characteristics over the entire ϵ_{appl} regime (0–50%) for practical wearable applications: $\epsilon_{\text{center}} < 1\%$ and $\text{AR}_{2\%} > 59\%$ (Figure 2.18). To be specific, the optimized PRI was strain-free under ϵ_{appl} up to 50%, and its maximum strain remains to be smaller than 2% in $\sim 60\%$ area of PRIs. In this regard, it is verified that the minimum applicable diameter of

~1,500 μm was well-defined to provide a compact strain-free area for effective protection of a miniaturized SMD LED (Figure 2.18c).

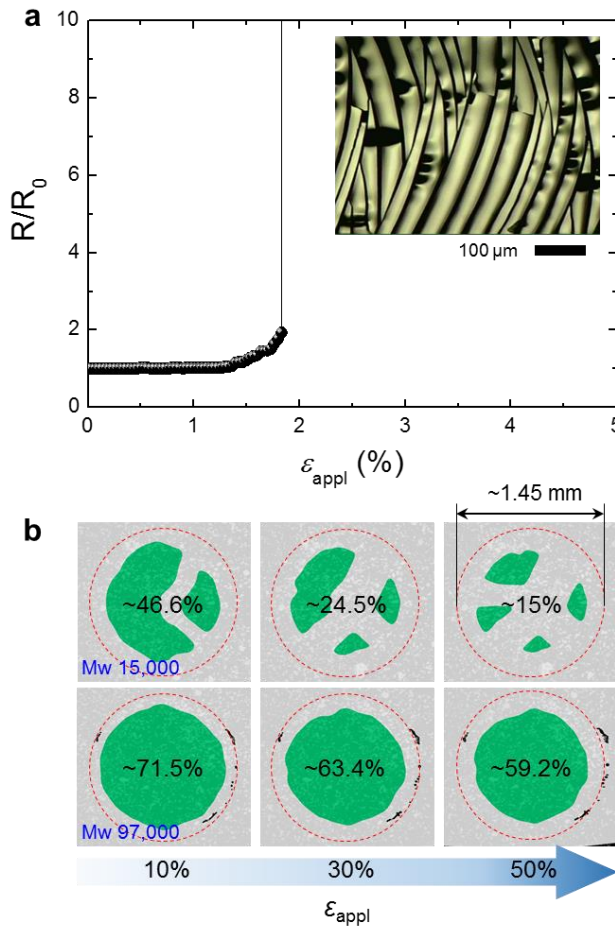


Figure 2.16 | Detailed description on $\text{AR}_{2\%}$ for inkjet-based PRIs. (a) Electrical characteristics of inkjet-printed Ag electrode directly fabricated on the bare PDMS. Cracking strain is around 2% (inset image: optical image of the cracked Ag film under the small strain). (b) $\text{AR}_{2\%}$ of the PRISS (PRI diameter $\sim 1.5 \text{ mm}$, $t_{\text{PDMS}} \sim 20 \mu\text{m}$, 5-layered PRI) with different PRI robustness (PMMA M_w 15,000 and 97,000). Surface strain is evaluated from DIC, and $\text{AR}_{2\%}$ is calculated by image processing [153].

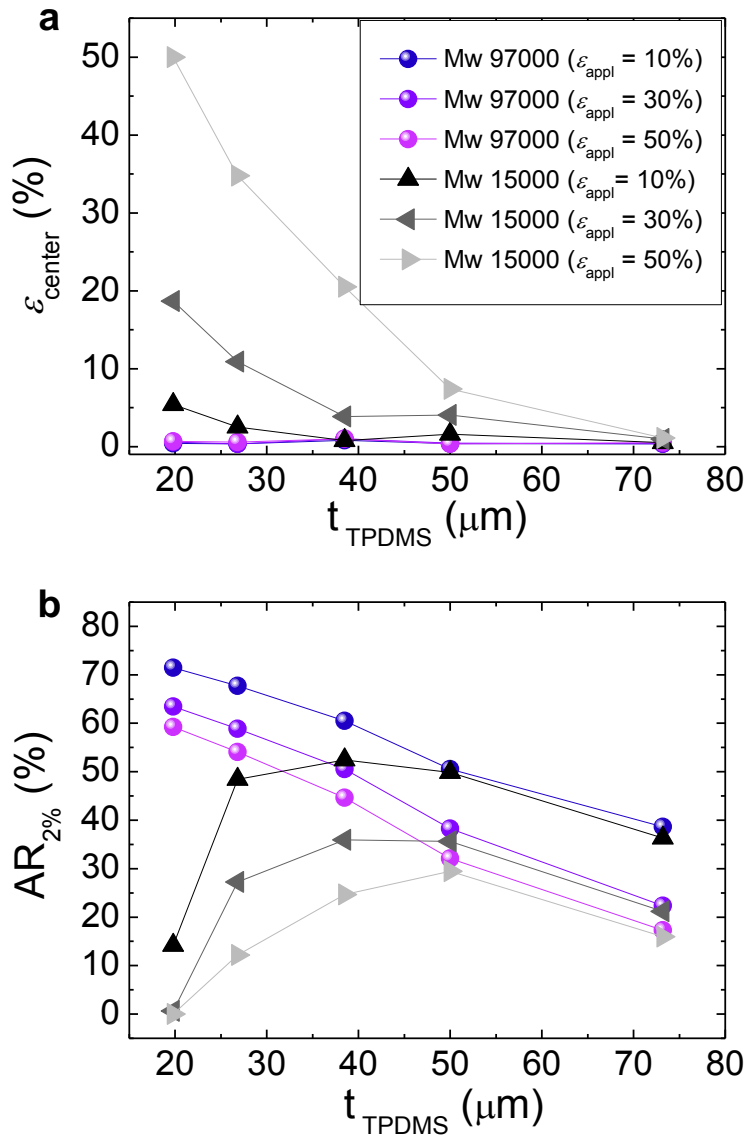


Figure 2.17 | Effect of top PDMS thickness (t_{TPDMS}) and PMMA M_w on the stability of 5-layered PRIs in terms of (a) PRI center strain (ϵ_{center}) and (b) strain-free area ($AR_{2\%}$). Each factor is measured along with an increasing applied strain (0–50%) [153].

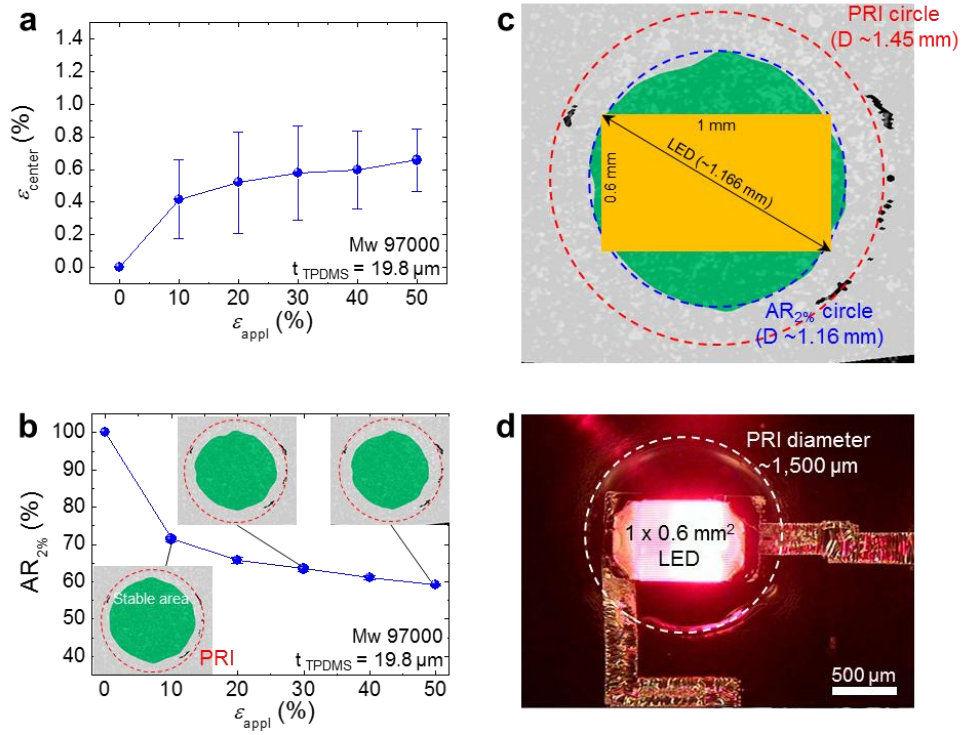


Figure 2.18 | Stability parameters for inkjet-based PRISs. (a) ϵ_{center} and (b) $AR_{2\%}$ as a function of ϵ_{appl} . $AR_{2\%}$ at 50% ϵ_{appl} showing a compact strain-free area that covers the SMD LED chip whose dimension is $1 \times 0.6 \times 0.2 \text{ mm}^3$. (d) Optical image of the real LED chip ($1 \times 0.6 \times 0.2 \text{ mm}^3$) mounted on the strain-free area of $\sim 1,500 \text{ }\mu\text{m}$ PRI [153].

2.2.3 Surface Strain Analysis and One-step Double-side Strain-isolation of Nozzle-jet-based PRI

In case of PRIs fabricated by nozzle-jet printing (nozzle diameter $\sim 100\ \mu\text{m}$), augmented PMMA concentration led to considerable increase in PRI thickness ($10\text{--}80\ \mu\text{m}$) (Figure 2.6) compared to the inkjet-based PRI case ($5\text{--}15\ \mu\text{m}$ for 1 to 5-layered) (Figure 2.5). Therefore, overall thickness of the PRISS—normally related to skin-conformability of the soft system—slightly increased. Instead, the augmented PRI thickness and advanced capabilities of PRI morphology engineering with concentration tuning as depicted in Figure 2.6 achieved a novel technique of one-step double-side strain-isolating that produced well-defined strain-isolated areas in both top and bottom surfaces of PRISSs just by single PRIs, with form factors that possessed an equal value of t_{TPDMS} and t_{BPDMS} (refer to the cross-sectional schematic in Figure 2.10) [154]. In conjunction with the fabrication strategy explained in section 2.1.3 that exhibited single droplet printing-based geometric transformation from a coffee-ring structure (PMMA (M_w 120,000) concentration $< 17\ \text{wt}\%$) to a truncated cone ($\sim 17\ \text{wt}\%$) and a blunt cone structure ($> 17\ \text{wt}\%$), a sufficient level of robustness and strain-free areas on both surfaces should be fulfilled in a wide range of PRI diameters to accomplish an optimized double-side strain-isolating in versatile applications. As an optimized building block of a double-side strain-isolated PRISS (DS-PRISS), here we adopted a 17 wt% PRI—which exhibited the most balanced structure ($t_{\text{center}} \approx t_{\text{coffee-ring}}$) at the

minimum applicable diameter ($\sim 1,500 \mu\text{m}$) (Figure 2.6), and also held the specific relation ($t_{\text{center}} \leq t_{\text{coffee-ring}}$, necessary condition for optimized double-side strain isolating) in an entire applicable diameter range ($\geq 1,500 \mu\text{m}$) (Figure 2.19).

Figure 2.20 shows systematic studies on correlation between structural parameters of PRIs and double-side strain-isolating effect. Specifically, mechanical feature of each PRISS was speculated from direct strain mapping over both top and bottom surfaces, and also from evaluation of exact strain levels and strain-free area inside each PRI area based on DIC method. In accordance with gradually engineered PRI morphologies as discussed in Figure 2.6, several kinds of PRISS samples were prepared for analysis, mandatorily satisfying structure features: a diameter of each PRI was equally set to $\sim 1,500 \mu\text{m}$, and values of t_{TPDMS} and t_{BPDMS} of each platform were equally defined to be $20 \mu\text{m}$ for maximizing strain-free areas without structural delamination [153] (Figure 2.21). 8 distinct PRISSs for each PRI morphology (4 for top and 4 for bottom analysis)—thus, totally 40 samples— were separately investigated, and representative samples were addressed in Figure 2.20. DIC analysis was conducted on both surfaces of each PRISS while being slowly elongated by applied uniaxial strain ($\varepsilon_{\text{appl}}$) level of 0 to 40%, visualizing surface strain distribution of the whole PRI area (rainbow spectrum) and evaluated strain-free area (green area contrary to white background) that represents a specific domain with internal strain $< 2\%$ (top surface: Figure 2.20b, bottom surface: Figure 2.20c).

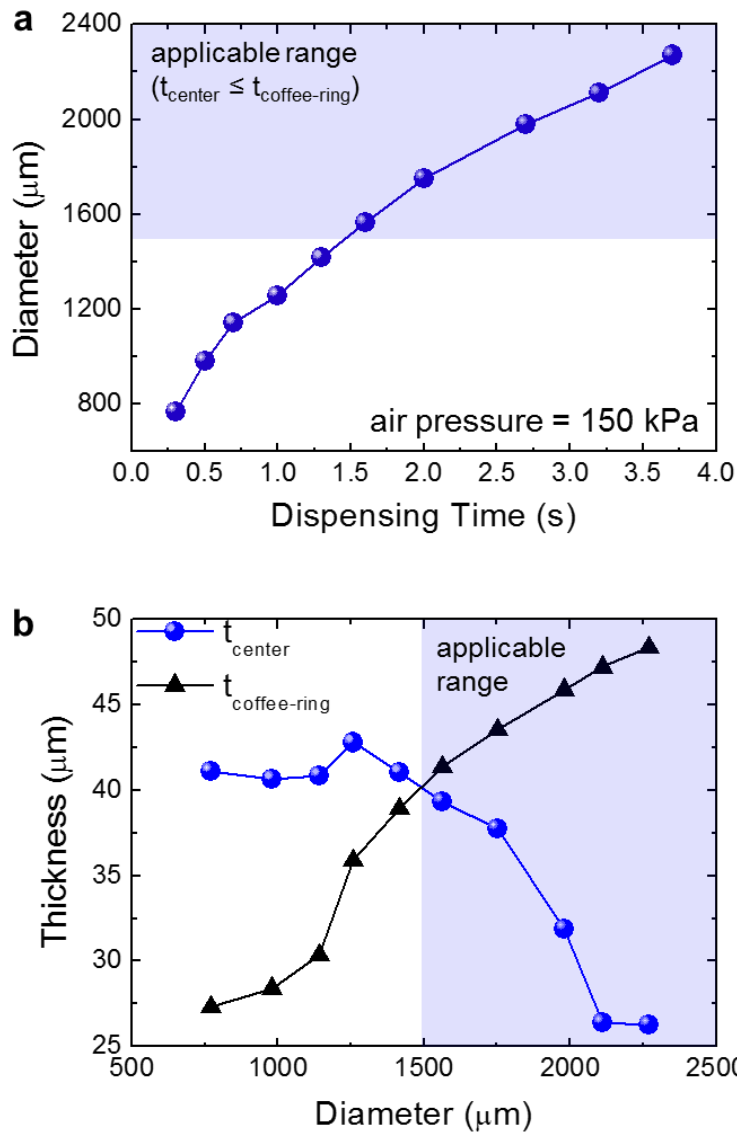


Figure 2.19 | Morphology engineering of nozzle-jet-based 17 wt% PRIs through varying dispensing duration time with a specific air pressure (150 kPa). (a) Diameter engineering, and (b) thickness engineering. Highlighted blue regions indicate applicable PRI diameters for effective double-side strain isolation [154].

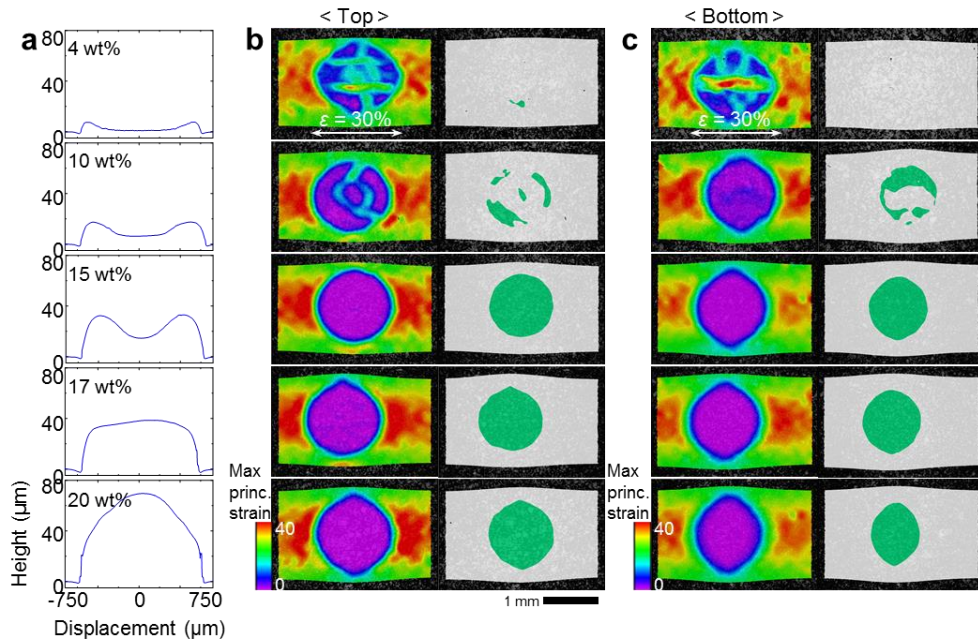


Figure 2.20 | Mechanical stability and surface strain distribution of engineered PRIs. (a) Typical morphology profiles of engineered PRIs (PMMA concentration: 4, 10, 15, 17, 20 wt%). (b and c) Surface strain distribution (rainbow spectrum) and evaluated strain-free area (green area contrary to white background) on top (b) and bottom (c) surfaces of PRISs [154].

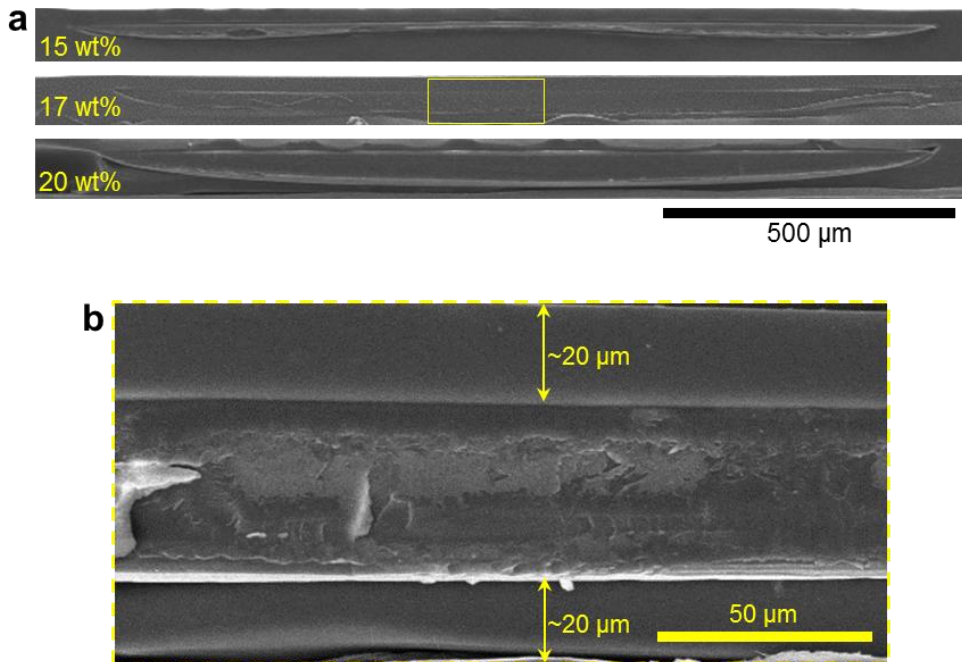


Figure 2.21 | Cross-sectional SEM images of PRISs. (a) SEM images of 15, 17, 20 wt% PRISs. The diameter of each PRI is equally set to $\sim 1,500 \mu\text{m}$, and values of t_{PDMS} and t_{BPDMS} are equally defined to be $\sim 20 \mu\text{m}$. (b) Magnified SEM image of the 17wt% PRIS [154].

The DIC results suggested that t_{center} played a crucial role in determining robustness of PRIs and DS-PRISs: an insufficient t_{center} ($< 10 \mu\text{m}$ in 4, 10 wt% PRIs) gave rise to fatal fracture of the PRI, leading to total destruction of the whole platform; by contrast, PRIs with a sufficient level of t_{center} ($> \sim 15 \mu\text{m}$ in 15, 17, 20 wt% PRIs) perfectly absorbed the applied stress, exhibiting well-defined strain isolation upon the both top and bottom surfaces regardless of structural morphologies (Figure 2.20b, c). Focusing on the strain-free areas of robust PRIs, it is noted that difference in the extent of strain-free areas between top and bottom surface inevitably occurred in every samples, regulated by the outer and inner diameter of each embedded PRI (Figure 2.22). Taken together, transformation of the PRI morphology from a coffee-ring structure (15 wt%) to a blunt cone structure (20 wt%) dynamically increased t_{center} ; and accordingly decreased the inner diameter, resulting in the unexpected reduction of strain-free areas at the bottom surface.

Based on the DIC results, additional quantitative studies were made to specify the robustness of the PRIS in a numerical form and also to figure out the optimized platform. Same numerical indices of $\varepsilon_{\text{center}}$ and $AR_{2\%}$ defined in section 2.2.2 were addressed. Commensurate with the tendency described in Figure 2.20b, c, PRIs with a sufficient level of t_{center} (15, 17, 20 wt% PRIs) not only kept their structural morphology without fracture but showed a very low level of $\varepsilon_{\text{center}}$ ($< 0.7 \%$) both on the top and bottom surfaces under the 30% tensile strain; by contrast, $\varepsilon_{\text{center}}$ of relatively thin PRIs formed by low concentration ink was drastically increased as a concomitant

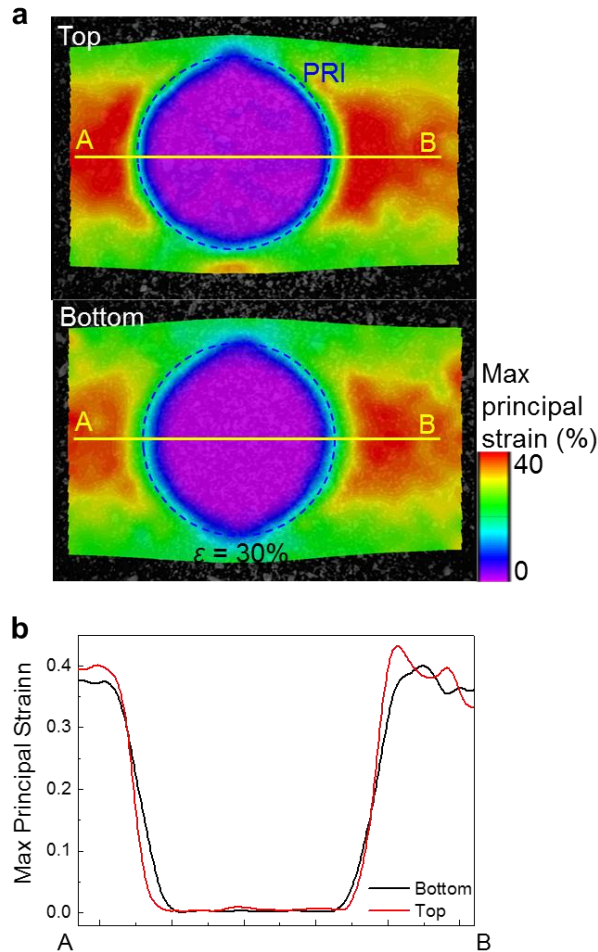


Figure 2.22 | Difference in strain-free areas between top and bottom surface of PRISSs. (a) Surface strain (evaluated maximum principal strain) distribution on top and bottom surface of the 17 wt% PRI-embedded soft platform under 30% ϵ_{appl} . Location of the PRI is marked as the dotted blue circle. (b) Surface strain profile of top and bottom surface along the line (A-B) as depicted in (a). The strain data clearly advocate the large correlation between the size of diameter (outer /inner) and the extent of strain-free area (top/bottom) [154].

of PRI fracture (Figure 2.23a). Also, the $AR_{2\%}$ index supported the foregoing result that the inner diameter of robust PRIs primarily affected the strain-free area of the bottom surface (Figure 2.23b): the reduced inner diameter of the blunt cone PRI morphology (20 wt%) led to substantial degradation in $AR_{2\%}$ of the bottom surface. On the other hand, despite the difference in PRI morphology, $AR_{2\%}$ of 15 and 17 wt% PRI was kept in a similar level both on the top (~70%) and bottom surface (~60%) since both of them possessed comparable structural parameters of outer/inner diameters and t_{PRI} . In this regard, the specific relation of $t_{center} \leq t_{coffee-ring}$ was defined to be necessary condition for optimized double-side strain isolation; and adoption of a 17 wt% PRI as an optimized building block for DS-PRISSs was advocated in terms of robustness and $AR_{2\%}$ as well as structural balance. Individual properties of such PRIs suggested that adequate stability ($\epsilon_{center} < 1\%$) (Figure 2.24a) and a sufficient extent of strain-free areas ($AR_{2\%}$ ~53% or ~73% in a length scale) (Figure 2.24b) could be guaranteed even under 40% external tensile strain.

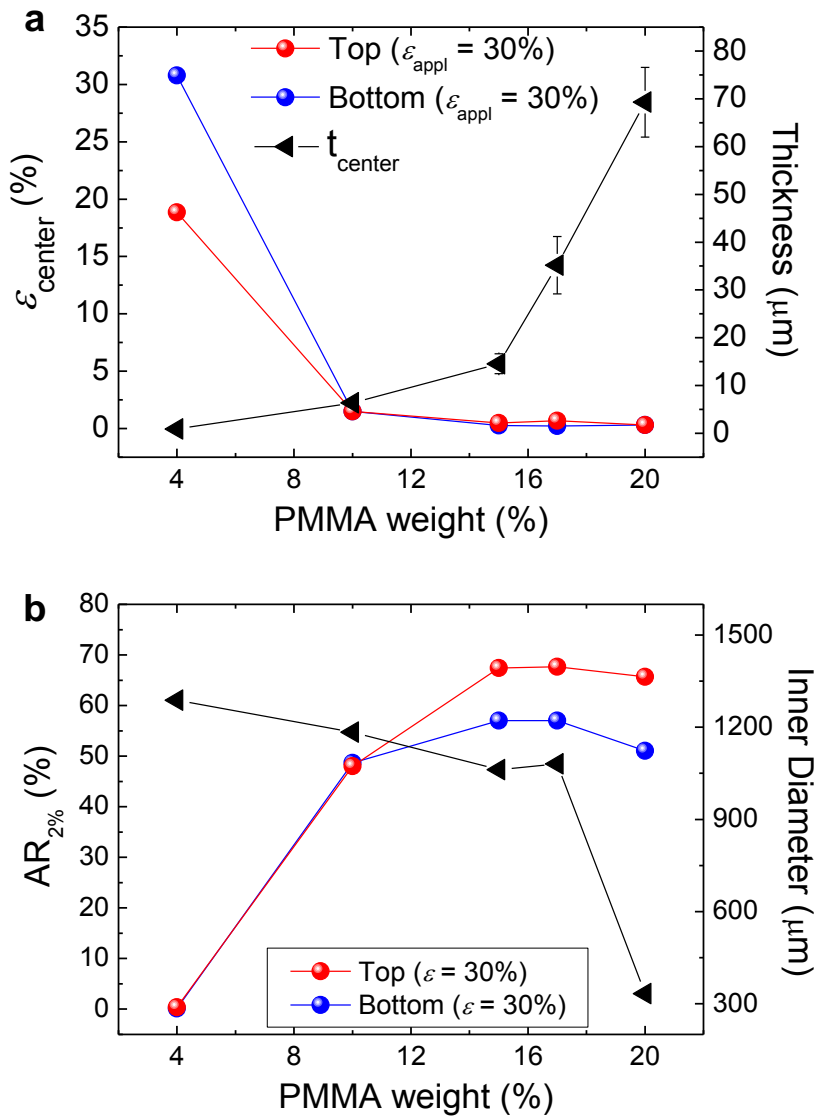


Figure 2.23 | Effect of PMMA wt% and corresponding structural parameters on the stability of PRIs. (a) Correlation graph between ϵ_{center} (top and bottom surfaces), t_{center} , and PMMA wt%. (b) Correlation graph between $AR_{2\%}$ (top and bottom surfaces), inner diameter, and PMMA wt% [154].

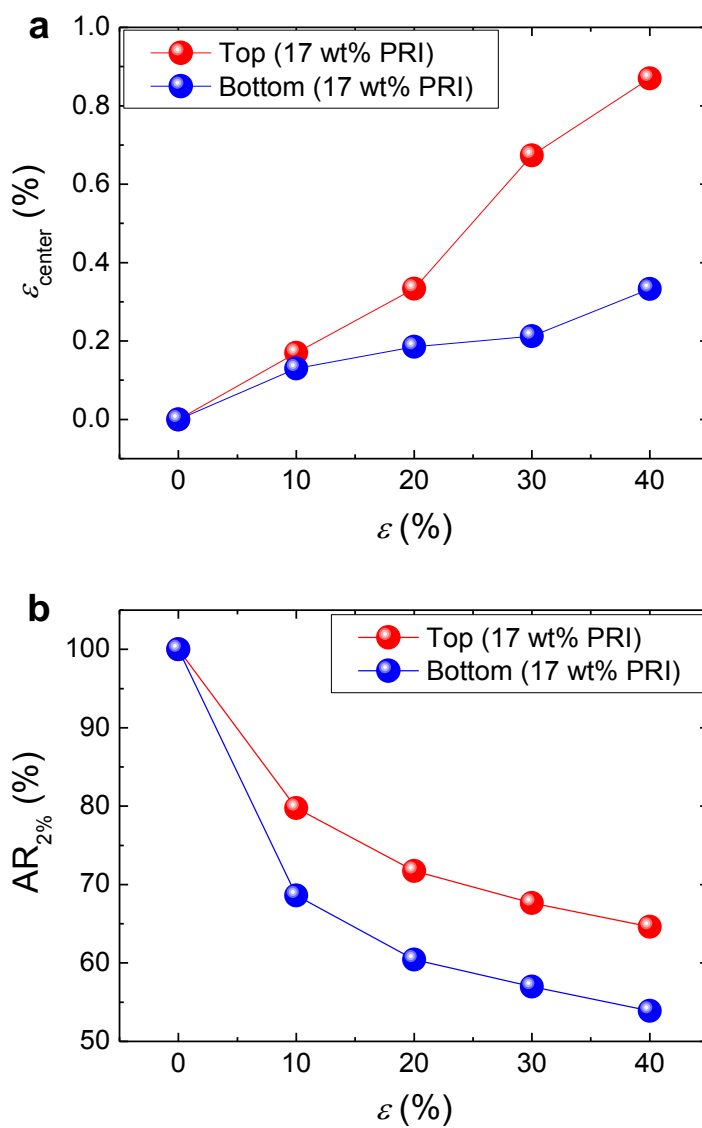


Figure 2.24 | Stability parameters for nozzle-jet-based 17wt% PRISs. (a) ϵ_{center} and (b) $AR_{2\%}$ as a function of ϵ_{appl} [154].

Chapter 3

Printing-based Electronic Functionalization on Engineered Soft Substrates

In this chapter, combinational methodologies for printing-based implementation of system-level soft electronics on engineered soft substrates are presented. Based on the characterization of inkjet-printed wrinkled silver (Ag) interconnects, a novel concept of image-based customizable circuit routing is demonstrated in conjunction with robust device bonding as an optimized scheme for printing-based implementation of system-level, hybrid-type soft electronics. Finally, numerous complete examples of soft electronics with various circuit configurations are demonstrated to verify the feasibility of this methodology.

3.1 Inkjet-printed Stretchable Silver (Ag) Interconnects

A high-performance stretchable conductor is an essential component for stable operation of electronic devices and system-level circuits under skin-like deformations. Numerous efforts have been made to develop advanced materials and/or well-defined strain-absorbing architectures for stretchable conductors: representative approaches include elastic conductors [63, 91–97, 128], patterned nanomaterials [79, 98–112, 120–122], and metallic conductors with in-plane [52–58], vertical wavy [72, 73, 81, 136, 153, 161, 162], serpentine [59, 84–86, 138, 139], and nano-/micro-structure [163, 164]. Among these candidates, various types of structural configurations of 3D architectures have been established to be a promising solution for stretchable interconnects (Figure 3.1) [85]. An attractive feature of this approach is that sufficient amounts of material choices and, particularly, electrical conductivity nearly analogous to that of bulky metals can be allowed. In addition, according to the architectural modeling, stretchability of the interconnect can be engineered (tens to hundreds %) apart from the material's unique robustness (Figure 3.2) [59, 82, 83]. Given these structural advances and printing-processability, we adopted a prestrain-induced vertically wrinkled, inkjet-printed Ag interconnects. In this section, the physical mechanism of prestrain-induced wrinkling, geometry and electrical characteristics of inkjet-printed wrinkled Ag interconnects are presented.

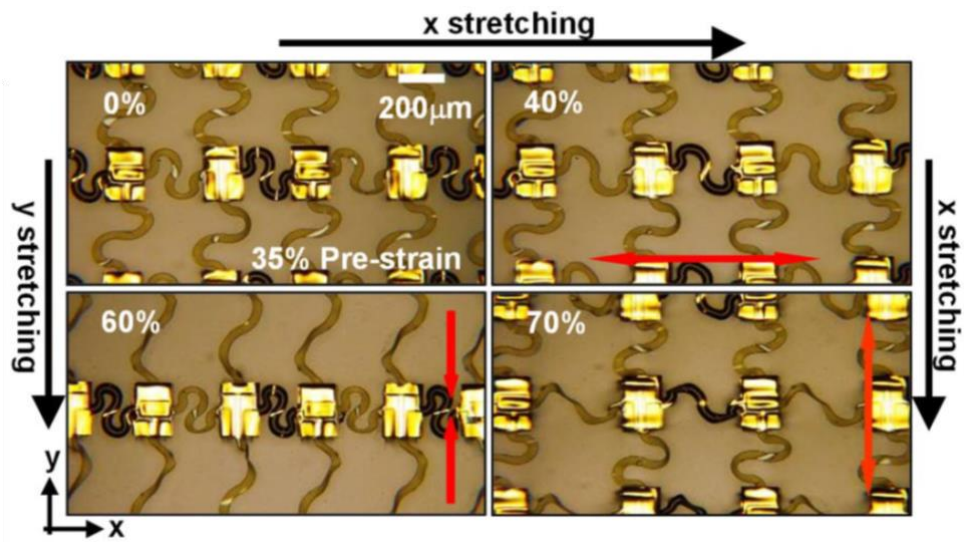


Figure 3.1 | Typical structural designs of 3D interconnection architectures at rest and stretched conditions [85].

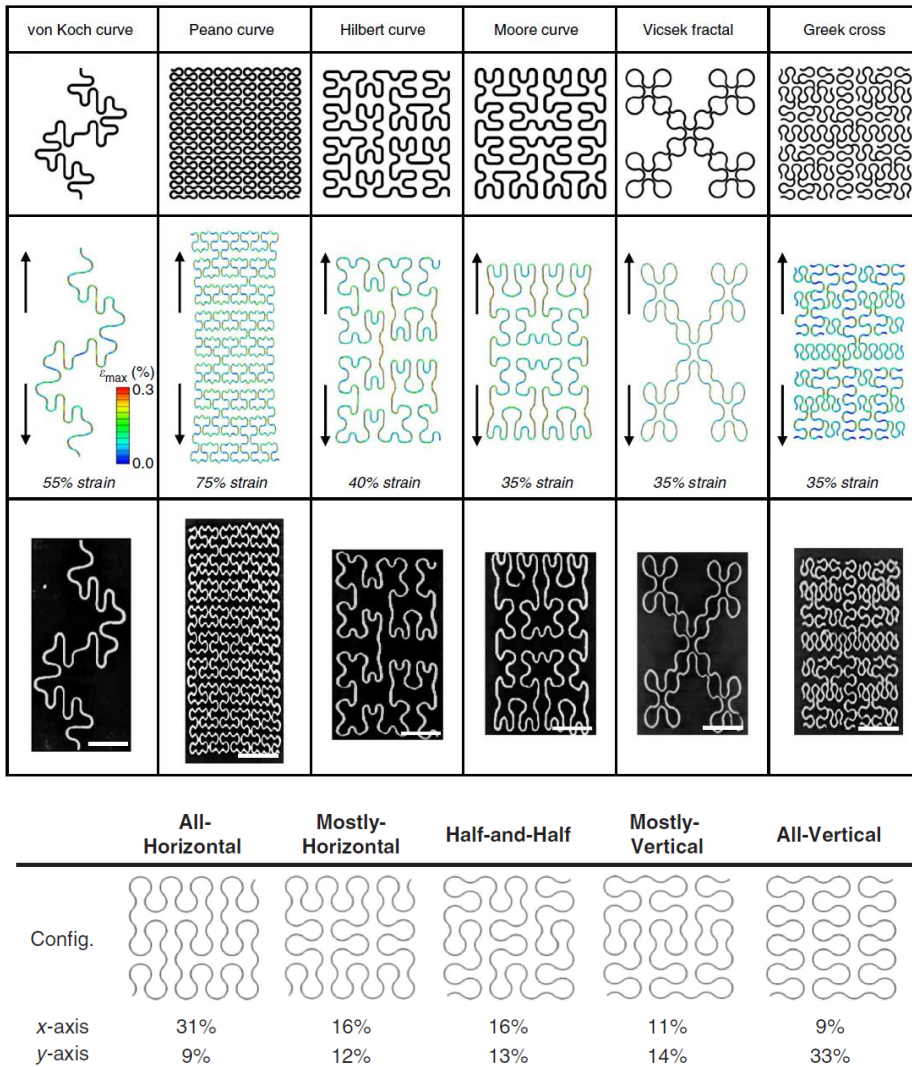


Figure 3.2 | Deterministic interconnection configurations and elastic mechanics, showing the capability of engineering available strain regimes [59].

3.1.1 Principle of Prestrain-induced Wrinkling in Bilayer Structures

Before investigating geometric features and electrical characteristics of inkjet-printed wrinkled Ag interconnects, the underlying principle of prestrain-induced wrinkling is outlined in this subsection. When a compressive stress (larger than a critical value) is applied to the bilayer structure comprised of a hard thin film (subscript: f) and a soft substrate (subscript: s), wrinkles are generally formed following a pre-distributed stress field. Various types of stress including thermal stress, swelling or dehydration induced stress, and osmotic pressure can stimulate the compressive stress [165]. Based on the theoretical studies [166, 167], the compressive force on the surface of the bilayer structure is expressed by:

$$F = E_f \left[\left(\frac{\pi}{\lambda} \right)^2 \frac{wt^3}{3(1 - \nu_f^2)} + \frac{\lambda}{\pi} \frac{E_s w}{4(1 - \nu_f^2)E_f} \right] \quad (3.1)$$

where E , ν , t , w , and λ denote the elastic modulus, Poisson's ratio, film thickness, film width, and wavelength of the wrinkle pattern along the force direction (Figure 3.3). For macroscopic elongations like prestretching ($\varepsilon_{\text{pre}} \sim 20\text{--}50\%$ in most cases), the situation of the compressively stressed bilayer structure can be illustrated as in Figure 3.4a.

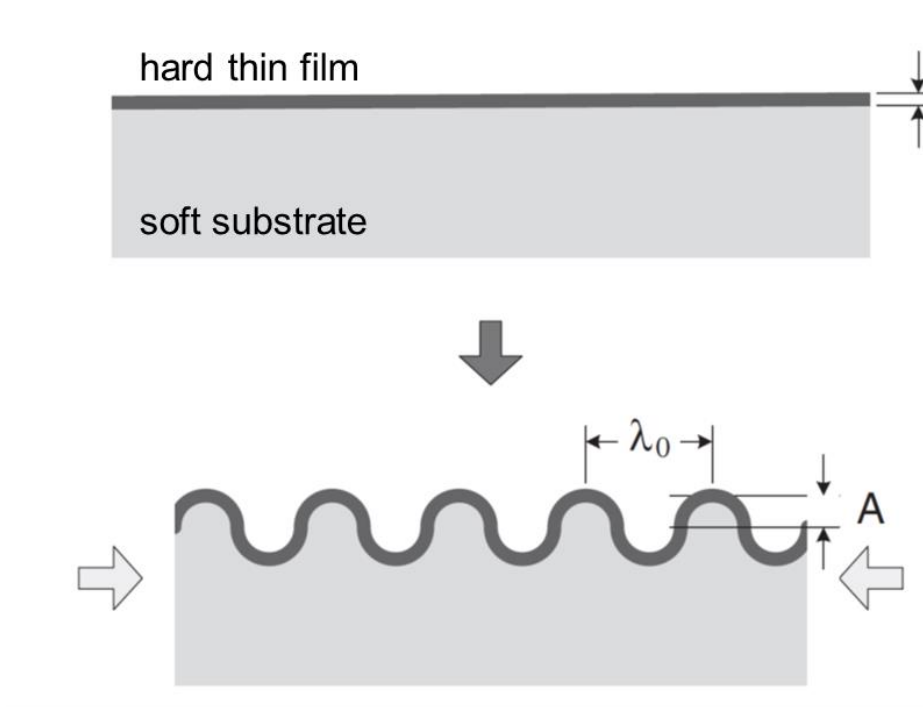


Figure 3.3 | Schematics of wrinkle formation through buckling instability in a bilayer system [167].

The film undergoing the compressive stress larger than the critical stress is deformed into the sinusoidal geometry with specific amplitude (A) and wavelength (λ) in ways that minimize the total elastic energy ($U(A, k)$) in the thin film and the soft substrate [70]; where $U(A, k)$ is expressed by:

$$U(A, k) = U^0 + \frac{1}{4} \left(\frac{tE_f\chi}{1 - \nu_f^2} - |F_{11}| \right) k^2 A^2 + \frac{t}{32} \frac{E_f}{1 - \nu_f^2} k^4 A^4, \quad (3.2)$$

with

$$\chi = \frac{(kt)^2}{12} + \frac{g(1 - v_f^2)E_s}{kt(1 - v_s^2)E_f} \quad (3.3)$$

where F_{11} is the membrane force along the 11 direction, k is the elastic constant, and g is the function of kH and v_s (H is the substrate thickness, $H \gg t$). The result of the minimization of $U(A, k)$ is the following geometric parameters [71]:

$$\lambda = \frac{\lambda_0}{(1 + \varepsilon_{pre})(1 + \xi)^{1/3}}, \quad A = \frac{A_0}{\sqrt{1 + \varepsilon_{pre}}(1 + \xi)^{1/3}} \quad (3.4)$$

Where

$$\lambda_0 = 2\pi t \left[\frac{(1 - v_s^2)E_f}{3(1 - v_f^2)E_s} \right]^{1/3}, \quad A_0 = t \sqrt{\frac{\varepsilon_{pre}}{\varepsilon_c} - 1} \quad (3.5)$$

And

$$\xi = \frac{5\varepsilon_{pre}(1 + \varepsilon_{pre})}{32}. \quad (3.6)$$

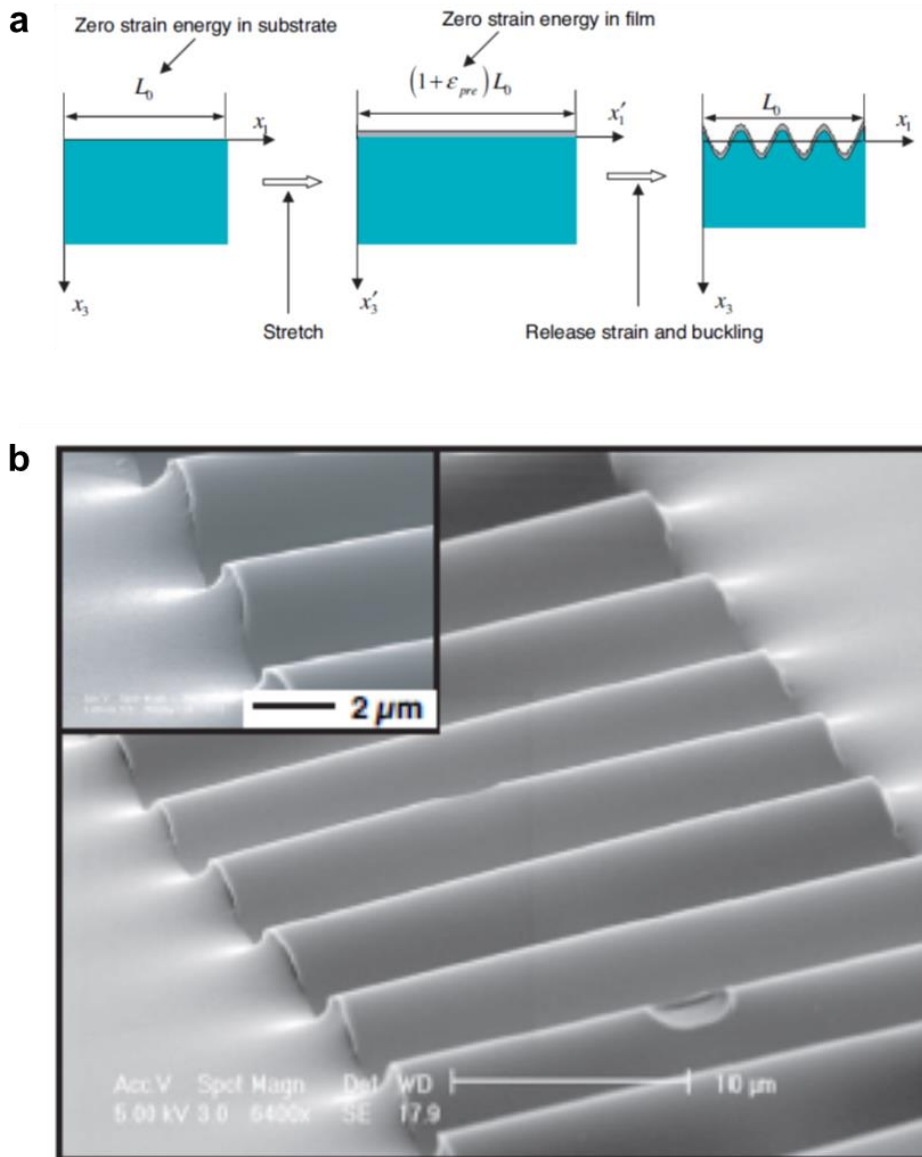


Figure 3.4 | Principle and examples of prestrain-induced out-of-plane buckling. (a) Sequential configurations of the thin film/substrate buckling process. (b) Typical SEM image of buckled, single-crystal Si ribbons [71].

Experimental verifications supported this theory that the transferred Si membrane (thickness 100 nm) onto the prestrained PDMS substrate exhibited well-defined sinusoidal wrinkles (Figure 3.4b-d) and the geometric parameters were well matched with those of predicted values derived from above equations (Figure 3.5). Based on this wrinkling (or buckling) theory, a great many of attempts to address such geometries and related functionalities for stretchable conductors have been reported. In particular, utilization of multiple sets of advanced materials like graphene [77, 78], Ag nanowire [79, 80], and printed Ag film [153, 162] advocated the potential of this strategy.

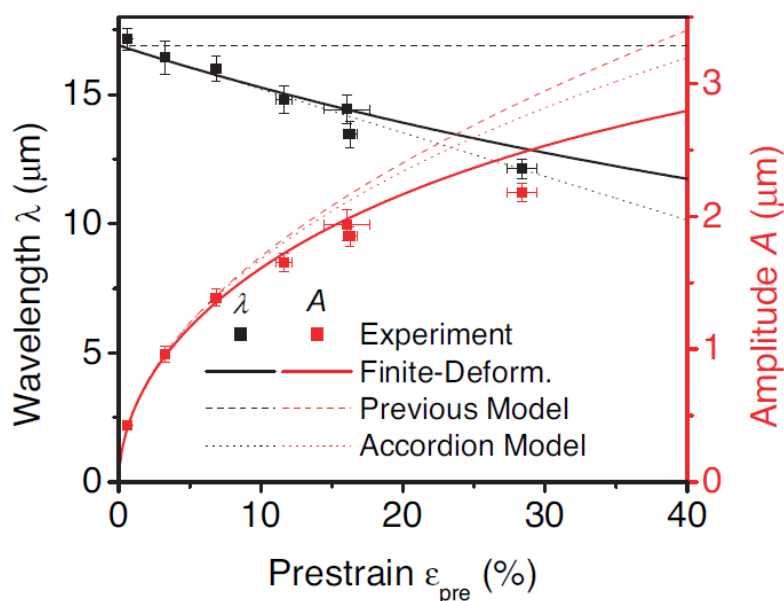


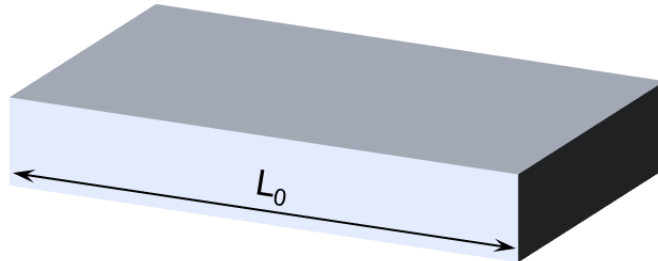
Figure 3.5 | Wavelength and amplitude of buckled structures of Si (100 nm thickness) on PDMS as a function of the prestrain. The finite-deformation buckling model expects wavelengths and amplitudes that agree well with experiments [71].

3.1.2 Geometry and Electrical Characteristics

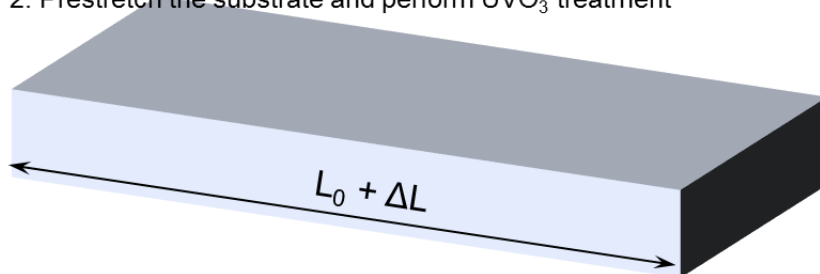
Given the physical geometry for stress absorption and printing-processability, we fabricated inkjet-printed wrinkled Ag interconnects. The fabrication step was quite simple such that interconnection networks could be easily extended to large-area with complex configurations (Figure 3.6) [162]:

1. A soft substrate (PDMS with 20:1 mixing ratio) was prepared.
2. The substrate was physically prestrained at specific directions and levels of stretchability (normally $\varepsilon_{\text{pre}} = 20\text{--}50\%$).
3. UVO_3 treatment was carried out (power = 29 mW cm^{-2}) for 26 min to improve the adhesion between the substrate and Ag ink (ANP corp.).
4. Ag ink was inkjet-printed through a 10 pL cartridge (nozzle diameter $\sim 21 \mu\text{m}$) forming predefined patterns.
5. As-printed Ag patterns were thermally annealed at $125 \text{ }^\circ\text{C}$ for 25 min.
6. Finally, the prestrain was released to generate well-defined wrinkles on the printed Ag film.

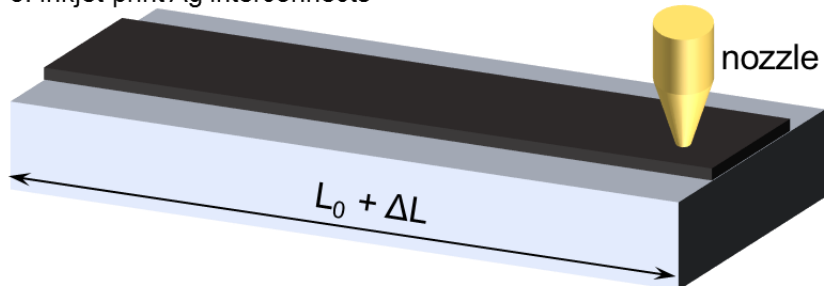
1. Prepare the PDMS (20:1 mixing ratio) substrate



2. Prestretch the substrate and perform UVO_3 treatment



3. Inkjet-print Ag interconnects



4. Release the prestrain

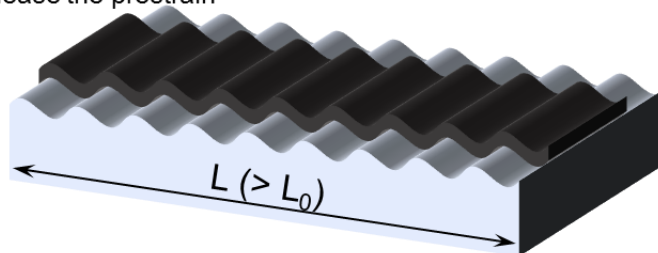


Figure 3.6 | Fabrication process for prestrain-induced inkjet-printed wrinkled Ag interconnects.

To avoid lateral cracking driven by combination of Poisson's effect and thermal expansion [162], in particular, we normally employed the 2D prestretching strategy. Attractive features of this methodology are as follow:

- (i) The whole process is completely compatible with the general inkjet-printing process with simple inclusion of two additional steps (prestretching and releasing), bestowing all of the advantages of a drop-on-demand (DOD) printing process such as rapid processability without vacuum processes and arbitrary patterning with minimized material waste.
- (ii) Stretchability of the fabricated conductors is easily tunable by controlling the level of prestrain and corresponding direction.
- (iii) A sufficient level of electrical conductivity (1/10–1/30 level of bulk metal conductivity) is achieved.
- (iv) One-step printing of multi-configured, customized stretchable interconnection network between spatially distributed electronic units could achieve adaptable functionalities in stretchable systems, together with well-developed substrate engineering technology as presented in Chapter 2.

Optical image in Figure 3.7 shows the representative surface geometry of the inkjet-printed wrinkled Ag interconnects. The 1D prestrain level of ~30% produced well-defined wrinkles with geometric parameters of λ ~30–40 μm and A ~2–3 μm . Also, the electrical conductivity of this interconnect was $\sim 2 \times 10^6 \text{ S m}^{-1}$ (bulk conductivity of Ag is $\sim 6.3 \times 10^7 \text{ S m}^{-1}$).

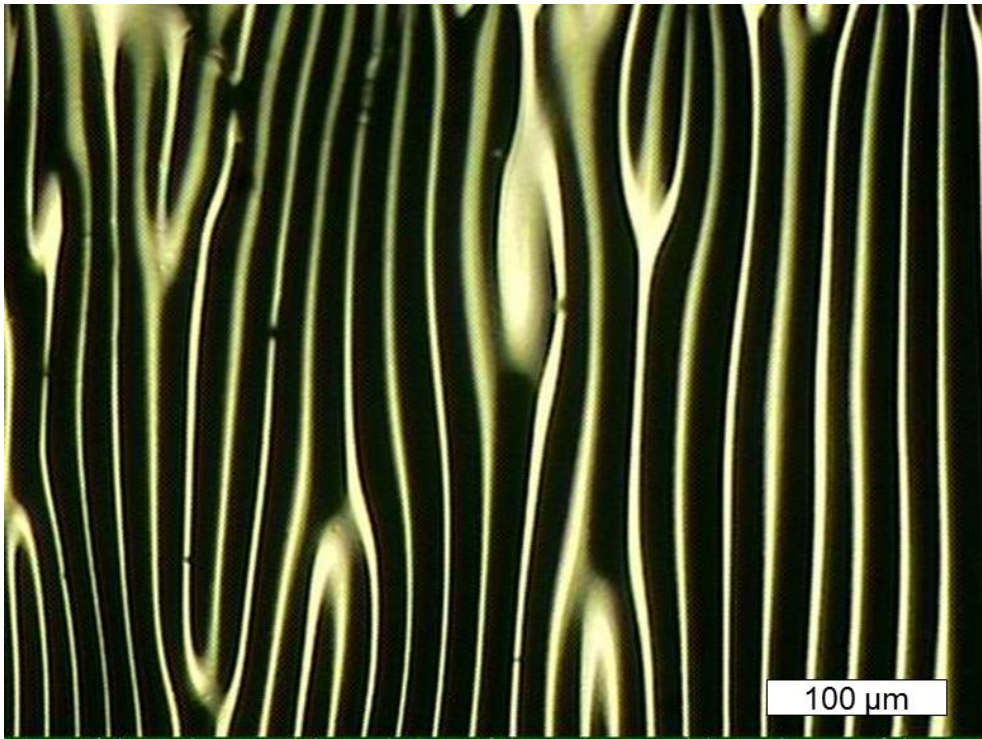


Figure 3.7 | Typical optical image of inkjet-printed wrinkled Ag interconnects on PDMS prestrained to ~30% in 1D.

Analogously, 2D biaxial prestrain induced sophisticated geometries of 2D wrinkles on printed Ag films like a herringbone or labyrinth structure (Figure 3.8a). 3D profiler images of the wrinkled interconnect validated that sequential stretching/releasing processes led to repeated flattening/wrinkling of the interconnect like the accordion-like physical behavior (Figure 3.8b). The minimum feature size (line width) of the inkjet-printed interconnect could reach ~30 μm with 1 pL cartridge nozzle and even < 10 μm by using a super inkjet printer (SIJ-S050, SIJTechnology Inc.) (Figure 3.9).

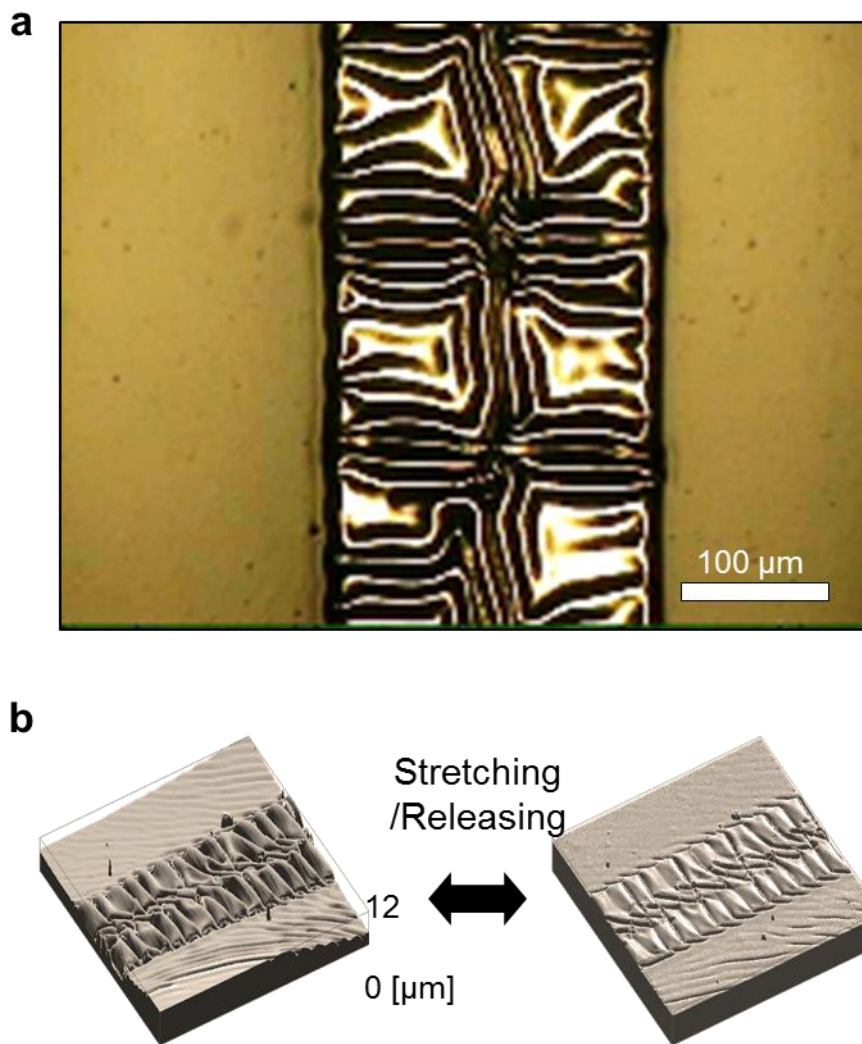


Figure 3.8 | Typical optical (a) and 3D profiler image (b) of inkjet-printed wrinkled Ag interconnects on PDMS prestrained to ~20% in 2D [153].

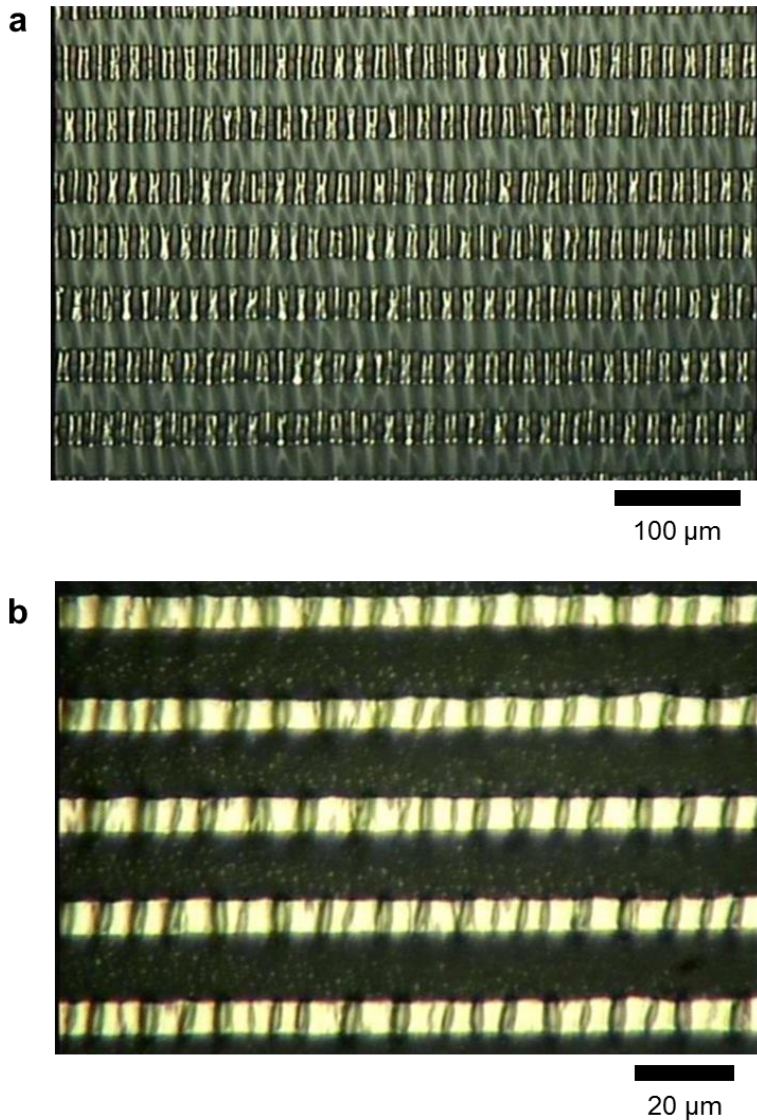
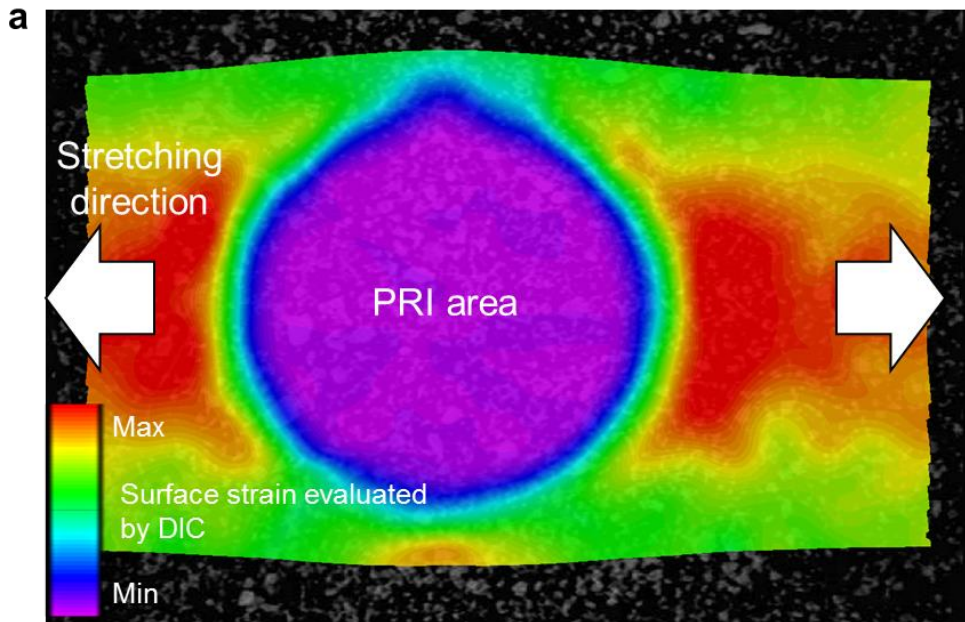


Figure 3.9 | Minimum feature size of inkjet-printed wrinkled interconnects. (a) Optical image of the wrinkled interconnects fabricated by using a 1 pL cartridge of the inkjet-printing system (DMP-2831, Dimatix Corp.). (b) Optical image of the finer interconnects fabricated by using a super inkjet printer (SIJ-S050, SIJTechnology Inc.) [153].

Distinct from the uniform wrinkle pattern of Ag films driven by the uniform stress field in a homogeneous matrix, our strategy is to fabricate wrinkled interconnects directly on the strain-engineered, mainly by embedded PRIs, soft substrate. In the case of such PRISS, a simple prestretching process can cause highly anisotropic, localized strain field so that geometries of prestrain-induced wrinkles should be re-explored (Figure 3.10a). To figure out the strain-absorbing mechanism near the PRIs of this PRISS, we investigated the prestrain-induced SiO_x wrinkles, driven by UVO_3 treatment [168], rather than printed Ag wrinkles; because the wrinkles formed by the UVO_3 -induced SiO_x/PDMS bilayer structure generally show relatively larger amplitude and wavelength than those formed by the printed Ag/PDMS bilayer structure. Interestingly, anisotropic stress distribution in the PRISS system induced by external prestrain ($\sim 30\%$) generated gradual wrinkles along the elongated direction (red arrow in Figure 3.10b). In particular, well matched with the theoretical background [169], localized stress near the PRI boundary caused bifurcated, dual-period wrinkles compared to the single period wrinkle at the far-field region. By contrast, wrinkle formation was suppressed in the PRI area; implying that the PRI accurately served as a strain-free area. From this gradual wrinkling phenomenon or gradual strain-absorbing design with a stress-matched amplitude, it is noteworthy that the stress-localizing instability occurred in rigid-to-soft transition area could be overcome with an engineered wrinkle profile compared to the profile with uniform amplitude and wavelength (Figure 3.10c) [43].



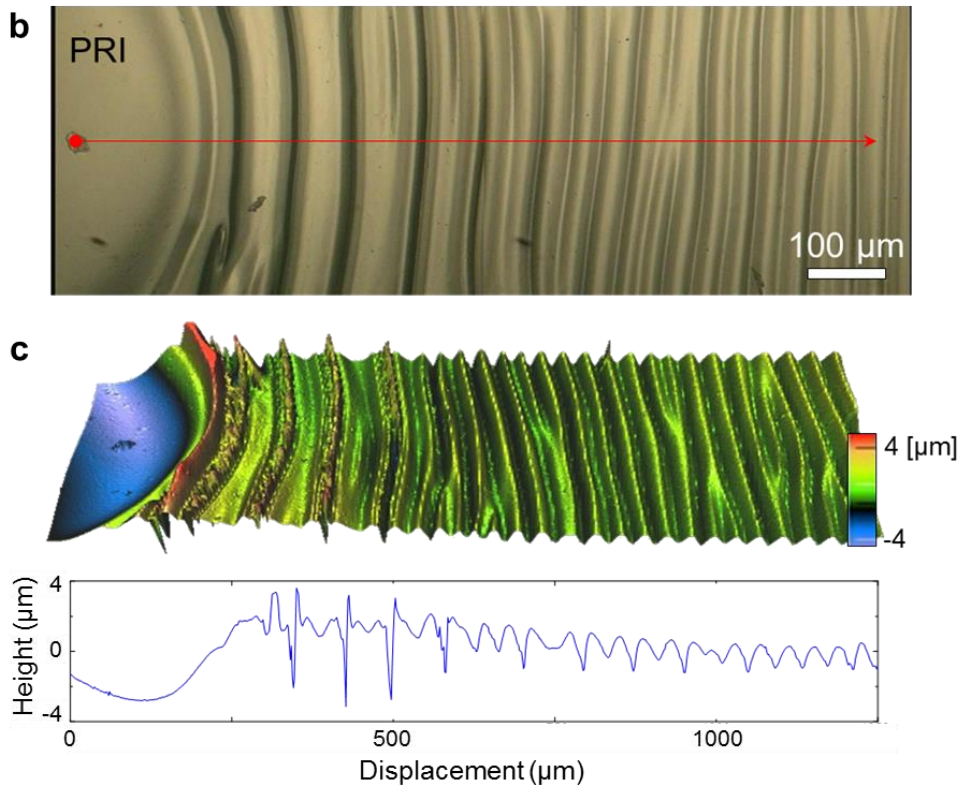


Figure 3.10 | Gradual strain-absorbing design near the PRI. (a) Typical surface strain distribution on the PDMS surface near the PRI area. The strain values are evaluated from DIC. (b) Optical image of the gradually wrinkled PRISS driven by prestrain ($\sim 30\%$) and UVO_3 treatment, showing self-constructed gradual strain-absorbing design with a stress-matched amplitude. (c) 3D profiler image and corresponding line profile of the wrinkled area described in b [153].

Given the underlying mechanism of gradual strain-absorbing design of UVO₃-treated PRISS, we fabricated stretchable high-density (minimum width ~50 μm with 10 pL nozzle, ~30 μm with 1 pL nozzle) Ag interconnects simply by one-step inkjet-printing process. Similar to the wrinkling phenomena on SiO_x/PDMS bilayer structure of UVO₃-treated PRISS, inkjet-printed Ag interconnects started to be wrinkled into the gradual strain-absorbing design with the stress-matched amplitude as the prestrain released, whereas the wrinkle formation was highly suppressed in the PRI area (Figure 3.11). This facile one-step printing and prestrain-induced wrinkling approach allowed versatile 2D stretchable multi-PRI interconnection networking in a triangular lattice configuration (Figure 3.12). One important aspect to consider is the correlation between PRI stability and reliable interconnect formation. If the geometry (or structural parameter) of PRIs was not optimized, undesired structural collapse and corresponding instability would occur; thereby resulting in much wrinkled and/or ripped surface morphologies on printed Ag films (Figure 3.13).

Electrical characteristics of the inkjet-printed wrinkled Ag interconnect was analyzed in terms of resistance variation as a function of applied uniaxial strain. For the 50% prestrained sample, variation in normalized resistance was negligible at strains up to ~40% (stretching speed = 1 mm min⁻¹) in virtue of the physically strain-absorbing geometry (Figure 3.14a). For repeated deformation ($\epsilon_{\text{appl}} = 30\%$), the resistance of interconnects exhibited stable increase in the acceptable range: the increase rate in

normalized resistance was $< 30\%$ after 1,000th stretching cycles (Figure 3.14b). For encapsulation of interconnects, a liquid PDMS (20:1 or 30:1 mixing ratio) was poured onto the 2D wrinkled interconnects and cured. The cyclic reliability data of encapsulated wrinkled interconnects suggest that the 30:1 PDMS cover delivered much less mechanical stress to the Ag wrinkles during cyclic deformation (Figure 3.15).

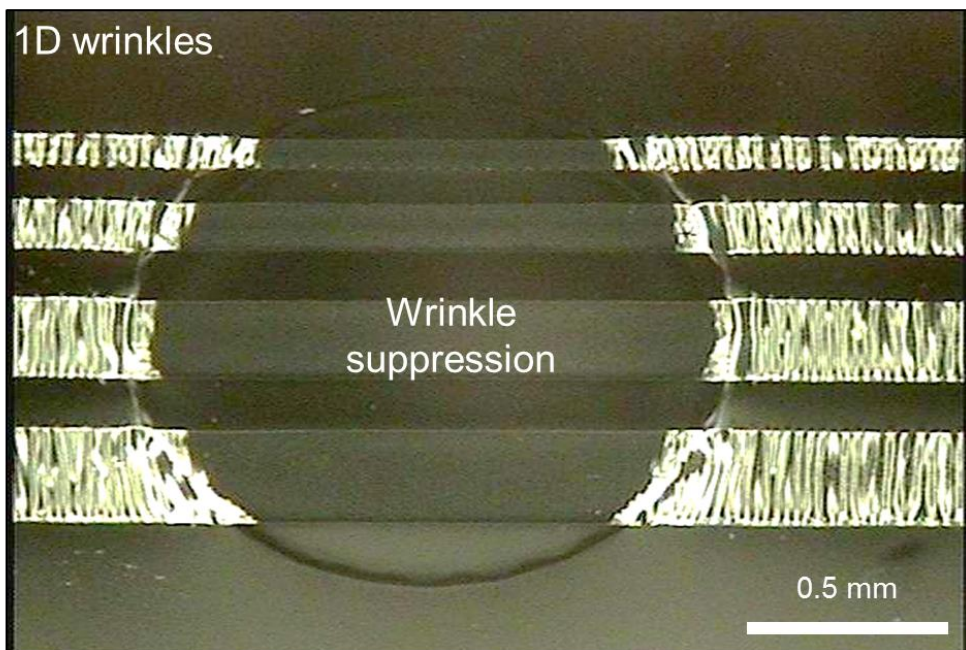


Figure 3.11 | Optical image of high-density inkjet-printed Ag interconnects directly fabricated upon the PRISS. Flatness of the PRISS allows direct printing of stretchable conductors, and prestrain-induced gradual strain-absorbing design makes fragile Ag films stretchable. Notably, the strain-free effect of the PRI suppresses wrinkle formation inside the PRI region [153].

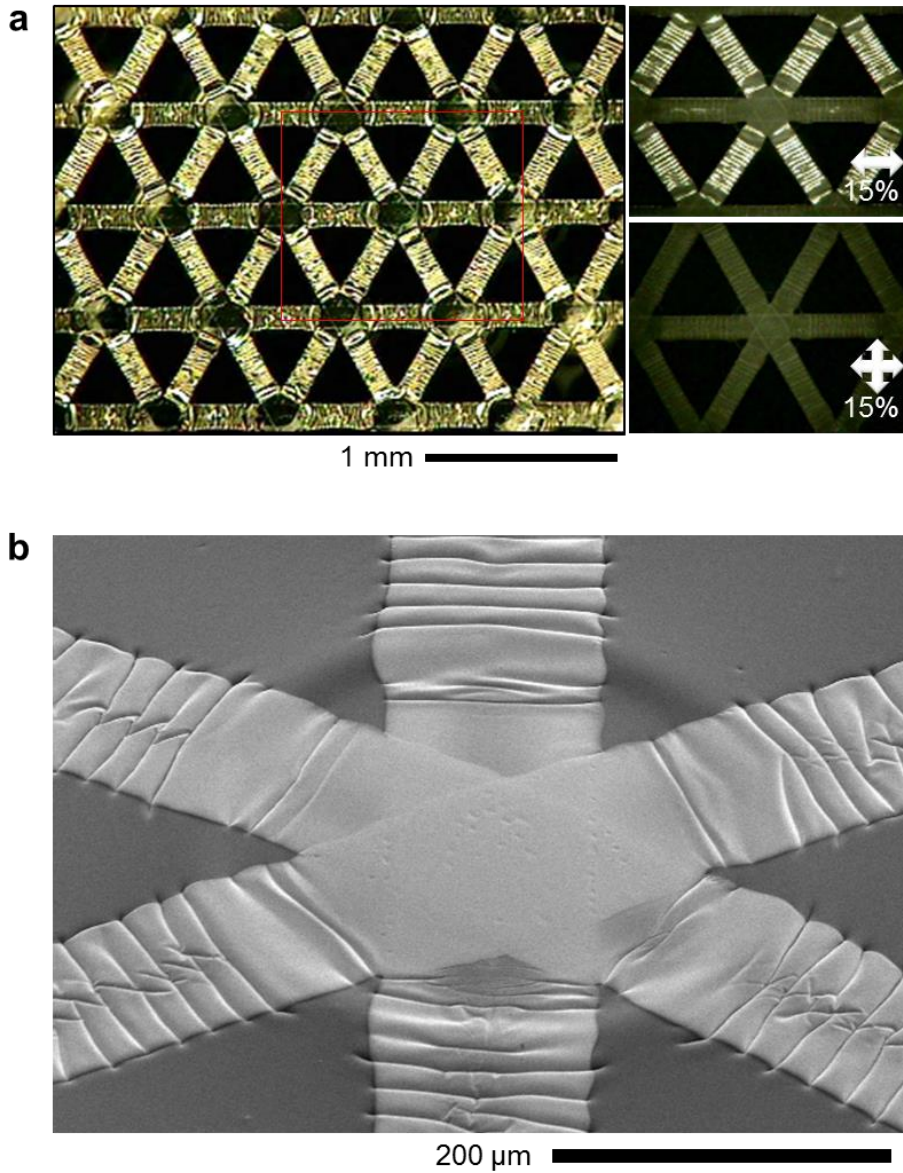


Figure 3.12 | Optical (a) and SEM image (b) of inkjet-printed 2D PRI interconnection networking. $\sim 350 \mu\text{m}$ PRIs with a triangular lattice configuration are used, and each strain-free property is verified by wrinkle suppression phenomena [153].

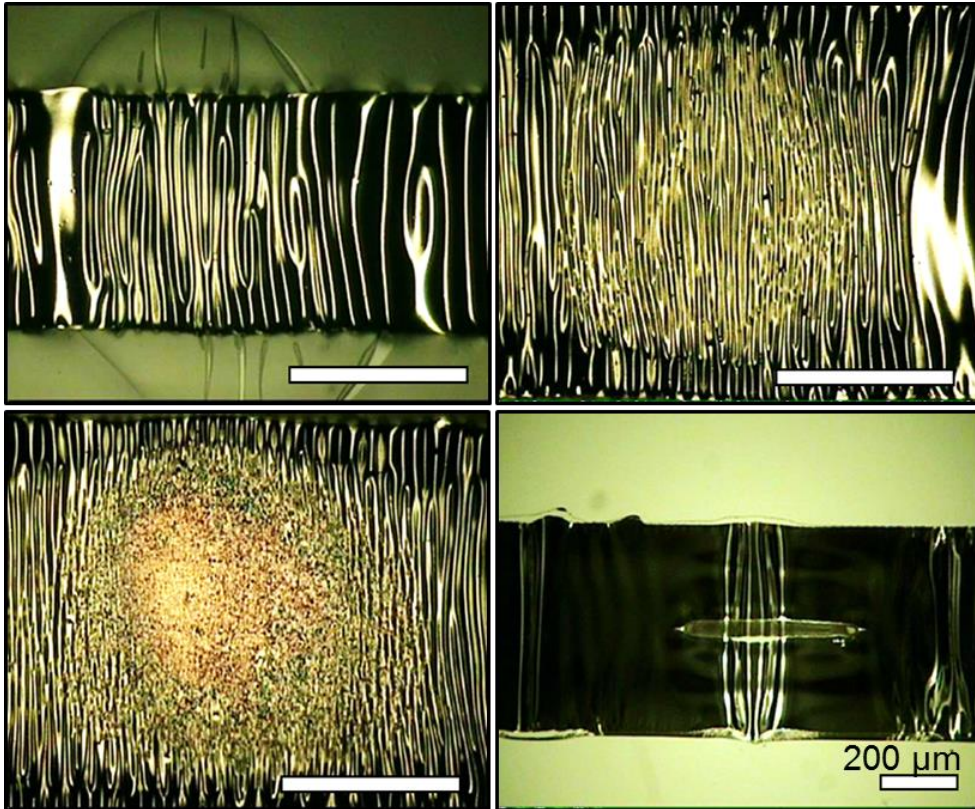


Figure 3.13 | Failures in forming gradual strain-absorbing designs on printed interconnects, caused by instabilities of cracking and/or collapsing in PRIs.

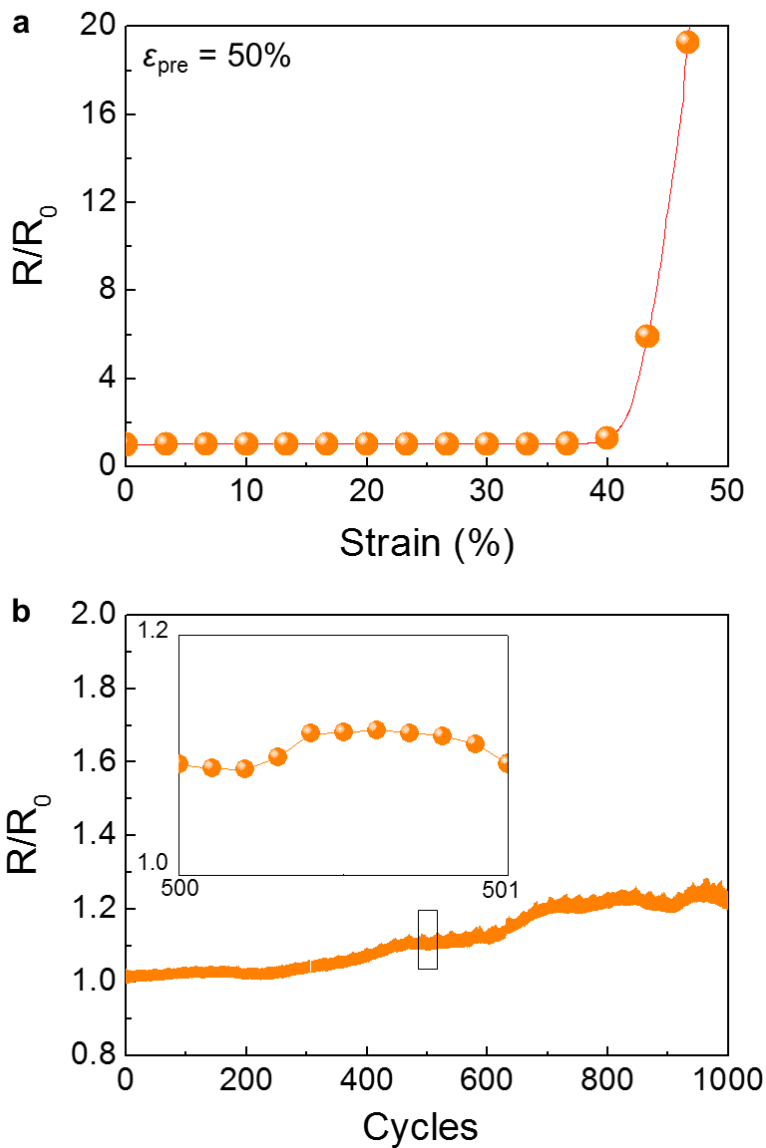


Figure 3.14 | Electrical characteristics of inkjet-printed wrinkled Ag interconnects formed by 50% prestrain. (a) Normalized resistance profile as a function of ϵ_{appl} (0–50%). (b) Cyclic reliability under 30% repeated stretching condition. Stretching speed is equally 10 mm min^{-1} [153].

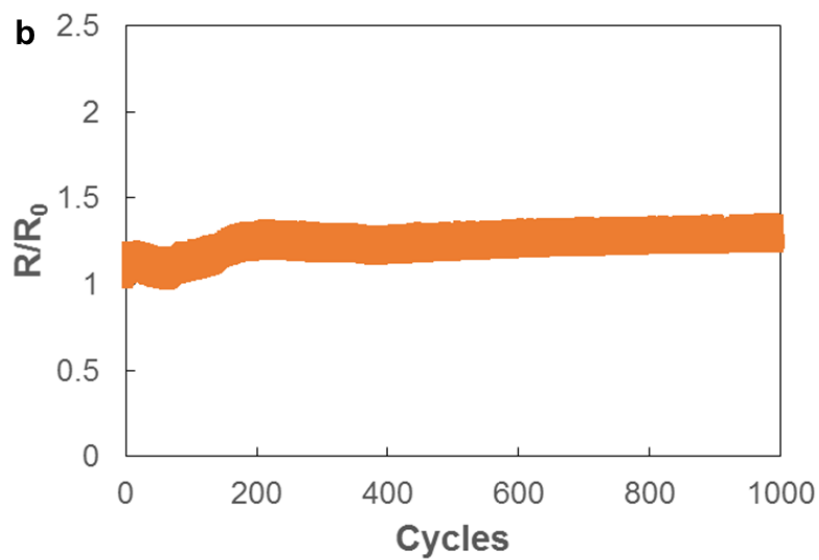
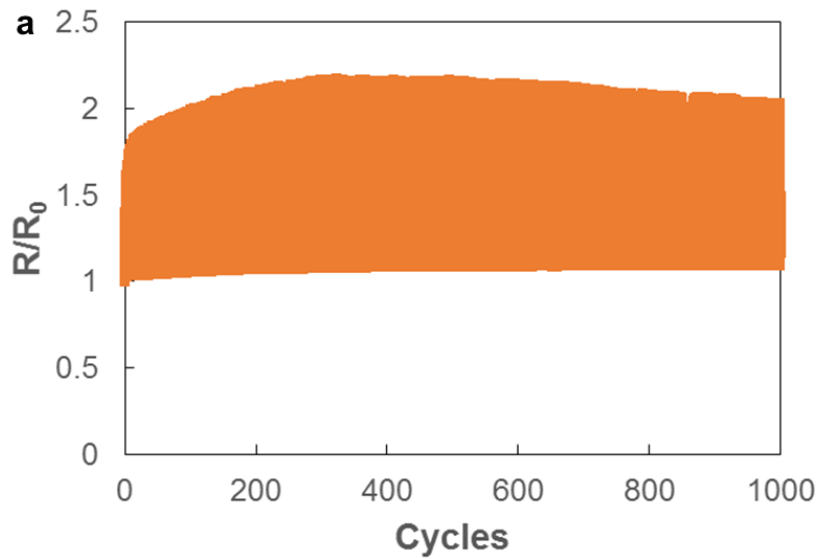


Figure 3.15 | Cyclic reliability of inkjet-printed wrinkled Ag interconnects encapsulated by 20:1 PDMS (a) and 30:1 PDMS (b). The applied strain is 30%, and stretching speed is 10 mm min^{-1} [153].

3.1.3 Stretchable Crossovers

In addition to the formation of stretchable interconnects on soft substrates, the methodology for implementing multilayer interconnection wiring was addressed in this section. For arbitrary circuit design, inevitable occurrence of line crossing advocates the need of a facile strategy for multilayer interconnection wiring. To meet this requirement, we developed a facile methodology of fabricating stretchable crossover lines that possessed geometric features described in section 3.1.2. Commensurate with the aforementioned process, the methodology was comprised of two steps (Figure 3.16a):

1. Proper shapes of PDMS (20:1 mixing ratio) structures were printed by a dispenser at line-crossing positions, and then cured at 90 °C for 120 min.
2. After 23 min of UVO_3 treatment, Ag ink was inkjet-printed to form crossover lines at the substrate temperature of 60 °C, the printing direction of which was perpendicular to that of lines; and annealed at 125 °C for 25 min.

Due to the printing processability, the shape and dimension of PDMS structures were easily controllable according to the position, length, and

density of crossover lines (Figure 3.16b). Moreover, analogous geometries of wrinkles were formed onto the printed Ag film driven by prestrain-induced compressive stress. Electrical characteristics of this stretchable crossover was similar with that of the inkjet-printed stretchable interconnects as displayed in Figure 3.14.

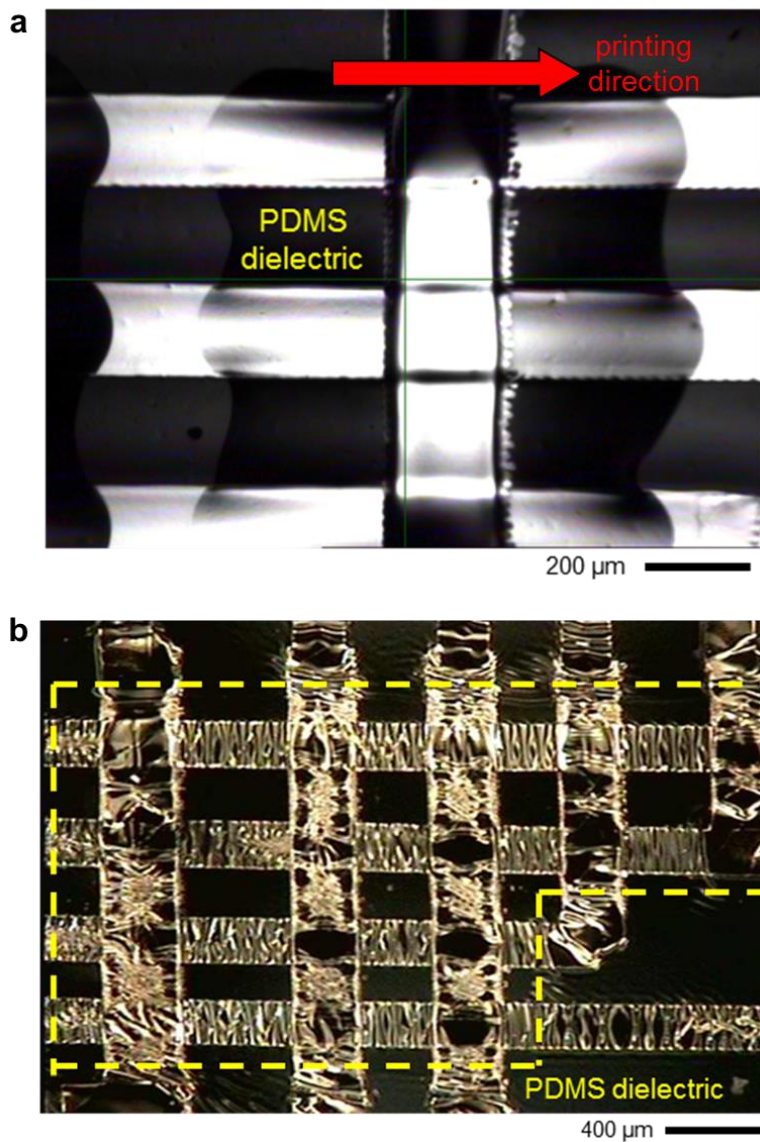


Figure 3.16 | Stretchable crossovers fabricated by printing processes. (a) Optical image of as-printed crossover Ag line onto the printed PDMS (20:1) dielectric. (b) Optical image of large-area PDMS dielectric and multi-line crossovers [153].

3.2 Image-based Customizable Circuit Design for Hybrid-type Electronic Functionalization

Based on the facile strategy of fabricating stretchable interconnection networks upon the engineered soft substrate, in this section, the optimized methodology for printing-based system-level implementation of soft electronics is presented. In spite of fruitful advantages, the employment of prestrain generally provokes anisotropic displacement of spatially predefined components or structures (PRIs in our case), and also causes an alignment issue on implementing desired electronic systems upon such system such as engineered PRISSs (Figure 3.17). As a result, the use of predefined (shadow- or photo-) masks and associated common methodologies is hindered. Indeed, prestrain-induced anisotropic rearrangements of PRIs are exacerbated as the number and density of PRIs increase. In large-area applications, therefore, prestrain-based direct fabrication approach has thoroughly been avoided. To overcome these restrictions, we developed a novel method that clearly solves the issue on anisotropic displacement of PRIs without losing both scalability and printing-based in situ processability. The key idea is to use the captured image of the prestrained PRISS as the background image for circuit design process. Based on the home-made automated circuit routing program, we cleverly provided a solution coping with unpredictable, anisotropic PRI rearrangement issue. Secondly, we developed a modified flip-chip bonding technique to afford versatile functionalities. In practice, multiple kinds of

surface mountable devices (SMDs) were directly integrated into the soft substrate, realizing printing-based hybrid-type electronic functionalization. In-depth consideration in process steps and strategies will be handled in the following subsections.

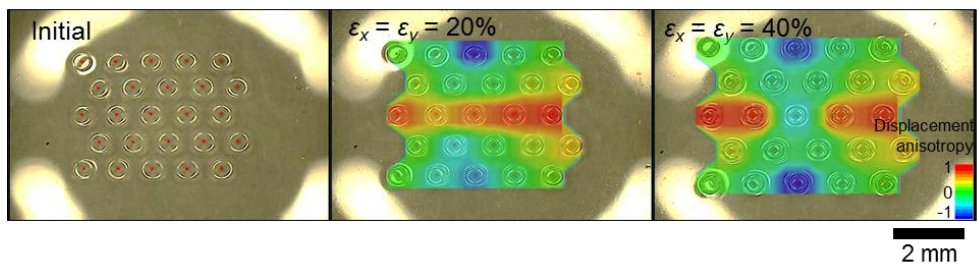


Figure 3.17 | Optical images and calculated displacement anisotropy of rearranged PRIs under a sequential biaxial stretching ($\epsilon_x = \epsilon_y = 0\text{--}40\%$). Displacement anisotropy is defined as “ $(x \text{ displacement} - y \text{ displacement}) / (x \text{ displacement} + y \text{ displacement})$ ” [153].

3.2.1 Total Procedure

The total procedure of image-based automated circuit design and printing-based electronic functionalization was comprised of nine steps, all of which were sequentially connected (Figure 3.18) [153]:

1. The appropriate PRISS was prepared. PRIs were arranged in the configuration embodying a “dolphin”.
2. The PRISS was biaxially prestrained ($\varepsilon_x = \varepsilon_y = 25\text{--}30\%$), and then the expanded state of the sample is captured by a digital camera. A biaxial prestrain level of 25–30% was set based on the elastic property of the skin itself, which typically shows an elastic response to tensile strain $< 30\%$ and irreversible effects under strains beyond 30% [170].
3. The captured image was loaded to the home-made circuit networking program as a background image.
4. The changed positions of each PRI driven by prestrain were automatically designated with specific pad layouts of functional elements (LED in this case).
5. A customized circuit was designed and drawn by bridging the functionalized PRIs. Since the captured image of the prestrained PRISS in the previous step provided pixelated coordinates of the

rearranged system, those of interconnection networks and electronic components that are configured upon the captured image by the program can be evaluated. The standard line width is set as 200 μm .

6. The given coordinates of the interconnection networks and functional chips were converted to the printing pattern files and coordinate files for Ag epoxy printing and chip placement via the program.
7. The interconnection network together with specified pad layouts as designed in the previous step was fabricated directly on the PRISS via an inkjet-printing process.
8. Functional IC chips and other SMD components were automatically placed by using a chip placement machine (TM220A, NeoDen Tech) in conjunction with robust Ag epoxy bonding (Detailed process for robust SMD bonding will be discussed in section 3.2.3.).
9. Prestrain was released to form spontaneous 2D wrinkles on overall printed Ag interconnects.

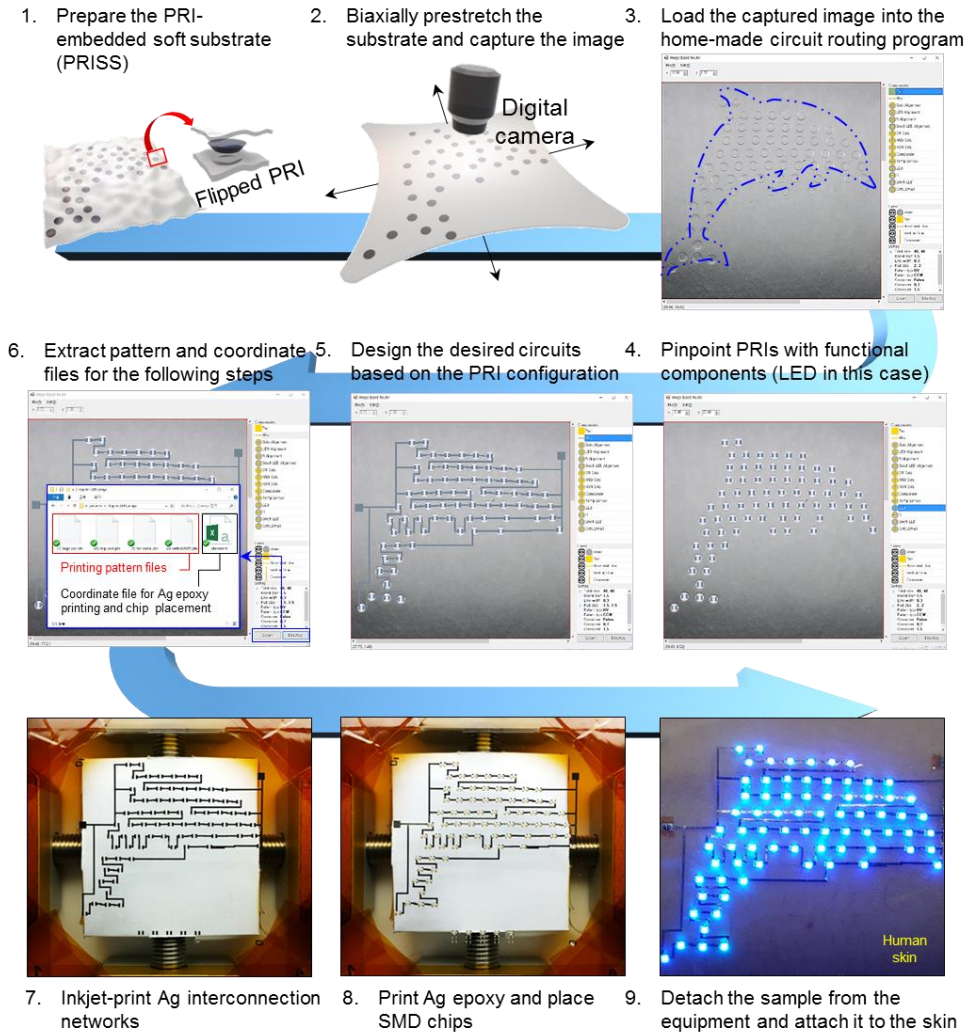


Figure 3.18 | Experimental details on automated, printing-based electronic functionalization process on a PRISS [153].

3.2.2 Home-made Circuit Routing Program

The layout and functions of the home-made circuit routing program is depicted in Figure 3.19. As described in the process step in section 3.2.1, the captured image of the prestrained PRISS was used for the background image of the program, enabling intuitive circuit routing and also providing accurate coordinate data of the rearranged heterogeneous system. The user-interface of the program offered multiple kinds of functional chip pad layouts (rectangular green line in Figure 3.19a) that would impart versatile functionalities to the PRIs such as LEDs, multiplexers, logic gates, IC sensors, RF modules, passive components, etc. Furthermore, commensurate with the user-interface of the inkjet-printer (DMP 2831), several control parameters for a proper inkjet-printing process were provided: total size of the to-be-printed block, line width, pattern type, and properties of crossovers (rectangular red line in Figure 3.19a). After the desired circuit was completely drawn, one-step click on the “Export” button generated printing pattern files, crossover data, and spatial coordinates of arranged SMDs (rectangular blue line in Figure 3.19a). The list of the automatically generated files was depicted in Figure 3.19b. Especially, printing pattern files were separately generated—pads, horizontal, and vertical direction—to reduce printing errors.

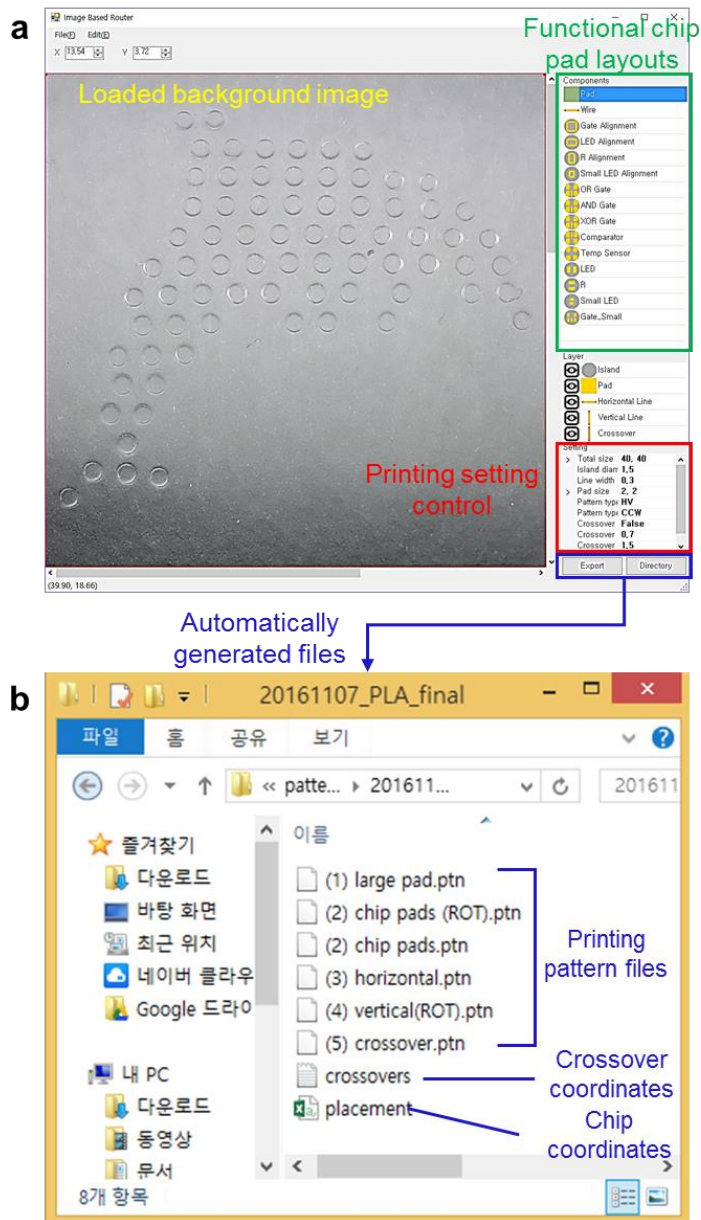


Figure 3.19 | Home-made circuit routing program. (a) A total layout. (b) Generated files for interconnection printing, crossover patterning, and chip placing [153].

3.2.3 Robust Surface Mountable Device (SMD) Bonding

For system-level integration of soft electronics, we adopted a hybrid concept of stretchable (or soft) electronics that combines soft and hard electronics into a single platform [149–152]. Especially focusing on the miniaturized, “fully-integrated” concept that offers opportunities to perform “in-system” (or “in-skin”) data collection, processing/computation, signal conversion/modulation, and even displaying, typical approaches of directly fabricating thin-film IC circuits on soft foundations necessarily encounter numerous limitations due to the abstruse features in thin-film IC design and dissimilarity in fabrication steps with conventional methodologies. In these respects, a few strategies for reliable integration of rigid packaged devices into a soft platform have been introduced: microfluidic assembly [150], transfer-combined modified flip-chip bonding [151], and reflow soldering on a flexible substrate [152].

Distinct from these approaches, in this subsection, we presented the much simpler method to integrate SMDs directly on the engineered soft substrate, concurrently holding the printing processability. The key aspect was to utilize two kinds of epoxy (Ag epoxy and pure epoxy). The total procedure of SMD chip bonding was comprised of four steps (Figure 3.20a) [153]:

1. A proper layout of inkjet-printed Ag pad that was designed relatively larger than SMD contact pads was fabricated inside the

PRI region at a prestrained state.

2. Two kinds of epoxy (Ag epoxy and pure epoxy) was printed at exact positions by the automatic dispenser (SHOTmini 200Sx, Musashi Engineering, Inc.). Specifically, pure epoxy was printed as a bank to prevent electrical short, and then Ag epoxy was printed directly onto the prepared pad layout for a robust contact. The amount of Ag epoxy was appropriately controlled according to the dimension of SMD contact pads.
3. Functional chips including LEDs, multiplexers, logic gates, IC sensors, RF modules, and passive components were picked and placed by the chip placement machine at exact positions (displacement error $\sim 25 \mu\text{m}$) (Figure 3.20b). After that, the sample was annealed on a 160°C hotplate for 60 min.
4. Finally, prestrain was released to generate well-defined 2D wrinkles. Due to the stress-shielding effect, wrinkles were suppressed inside the PRI.

The completely bonded SMD chips exhibited superb robustness even under extreme deformations like tweezing (Figure 3.21).

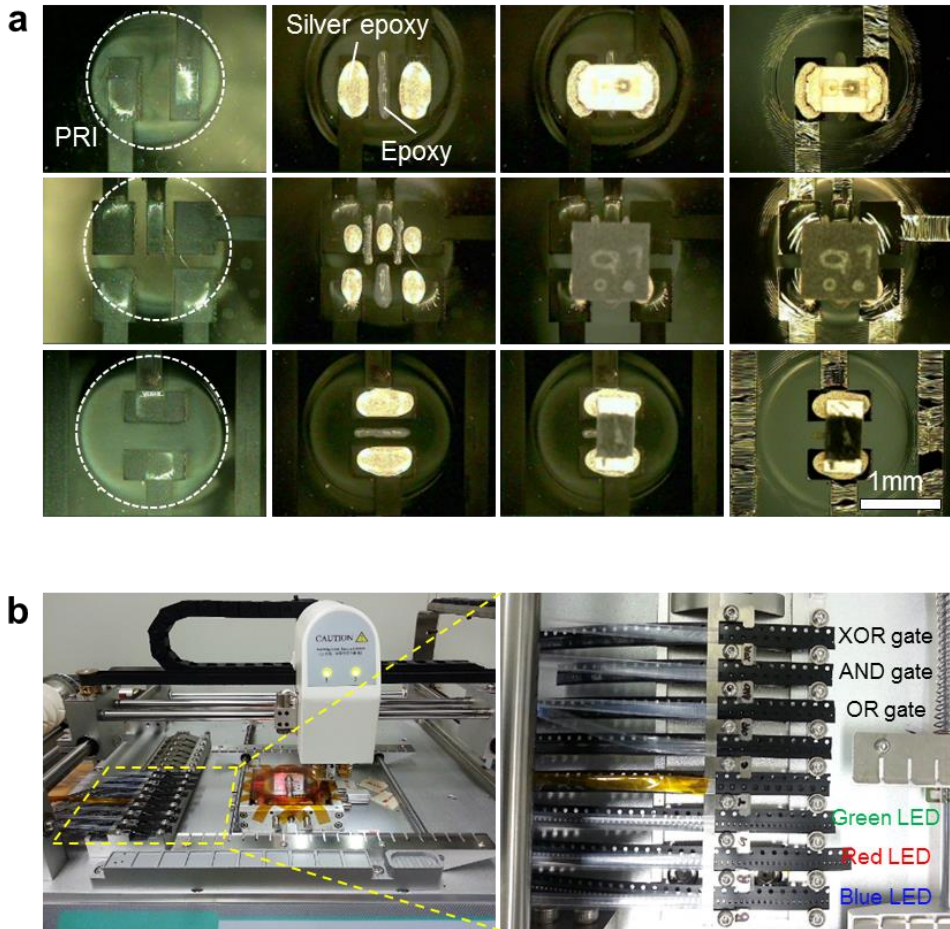


Figure 3.20 | Printing-based SMD assembly. (a) Process flow of Ag epoxy/epoxy bonding with various SMDs including LED, logic gate, and resistor. (b) Photographs of the whole system layout of SMD pick-and-place machining and the prepared SMD chips in tape and reel packaging including logic gates (XOR, AND, OR) and LEDs with different colors [153].

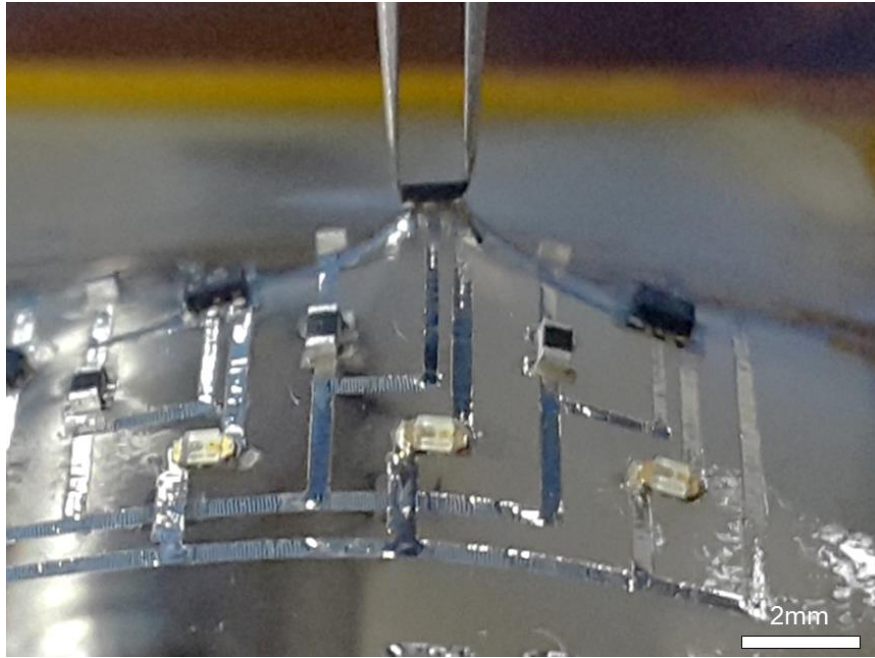


Figure 3.21 | Photograph showing the robustness of Ag epoxy bonding [153].

3.2.4 Various Circuit Design Examples

Attractive features of ultimate design freedom of PRI arrangements and customizable circuit routing allowed for numerous conceptual examples of system-level soft electronics. In this section, several soft electronic systems with versatile functions and configurations are presented to support the feasibility of our approach [153]. One of the strongest assets in our printing-based electronic functionalization process is the capability of programming PRI arrangement for targeted applications, enabled by the DOD property of printing process. In this respect, Figure 3.22 shows three different types of topological inter-PRI networks based on the smile PRI configuration (22 PRIs): “ring”, “tree”, and “cluster” topology. Regardless of the topological network, desired circuit layouts were simply “drawn” by the circuit routing program based on the background image of biaxially prestrained PRISs (Figure 3.22b), and then “actually drawn” onto the PRISs via an inkjet-printing process (Figure 3.22c). In addition, multiple sets of stretchable display applications with customized PRI arrangements advocated the strategies of specifying circuit designs and functions perfectly matched to the predefined PRI configurations: “maple leaf”, “dolphin”, “sha” (the symbol of Seoul National University) for information displays (Figures 3.23–3.26), “circle” for a wearable analog watch (Figure 3.27), “rectangular lattice” for a wearable passive-matrix (PM) display (Figure 3.27), and “triangular lattice” for a wearable, real-time temperature monitoring system (Figure 3.29).

Although PRI configurations and corresponding layouts of device integration were distinctly defined for each function, implementing steps were completely same: after the desired circuit was completely fabricated (Figure 3.23a) based on the predefined circuit layout (Figure 3.23b), the soft system was detached from the 2D stretching equipment and laminated on to the skin (Figure 3.23c) or directly stretched (Figure 3.23d).

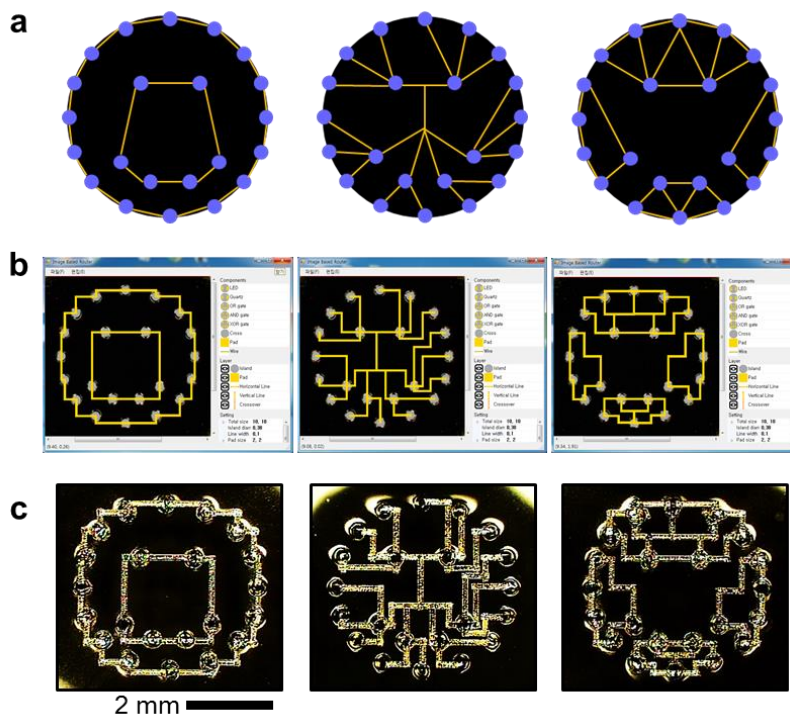


Figure 3.22 | Topological inter-PRI networks. (a) Schematics of three different types of topological inter-PRI networks based on the smile PRI configuration: ring, tree, and cluster. (b) Snapshot images of designed topological networks in the circuit routing program. Orthogonal layouts are adopted for a facile circuit networking. (c) Optical images of the inkjet-printed topological networks designed in b.

Distinct from the maple and dolphin displays, the stretchable “sha” display described the ability to make combinational “modes” in interconnection networks between functionalized PRIs (LEDs in this case) with the fixed arrangement (Figure 3.25). Three different “modes” were characterized by different colors (red, blue, green), interconnection geometries (stepped, meandered, and tilted layout), and network topologies between LEDs (grouped by circles). This stretchable “multi-mode” display concept supports the capabilities of functional networking and adaptable circuit implementation with differently functionalized PRIs (not only LEDs but other SMDs like sensors, logic gates, etc.) (Figure 3.25a). The mechanical reliability of these stretchable display was secured by both a stress-shielding effect driven by robust PRIs (diameter ~ 1.5 mm) and a wrinkled geometry of inkjet-printed Ag interconnects (width ~ 250 μm) (Figure 3.25c). The electrical contact between predefined Ag pads and the placed LEDs were stably protected by embedded PRIs and Ag epoxy (Figure 3.25c(i,ii)); and strain-free characteristics inside the PRI areas was clearly visualized by a wrinkle-transition at the rigid-to-soft-transition area (Figure 3.25c(iii)). Also, uniform wrinkles of Ag interconnects were well formed conformable to the shape of electrodes such as straight (Figure 3.25c(iv,v)) and kinked lines (Figure 3.25c(vi)). Based on these features, the stretchable “sha” displays showed reliable operation under a sequence of deformation conditions such as freestanding (Figure 3.26a), bending (Figure 3.26b), stretching ($\sim 20\%$) (Figure 3.26c), and laminating to the crumpled Al foil (Figure 3.26d).

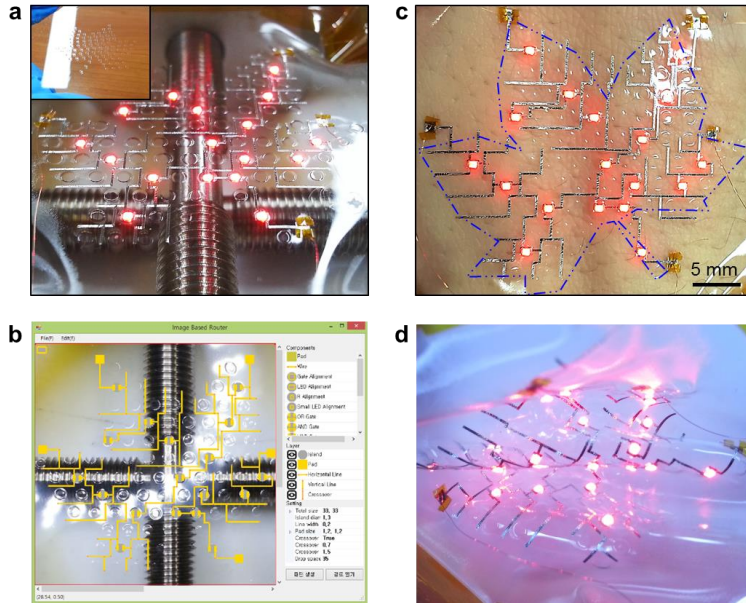


Figure 3.23 | Stretchable display in a maple leaf design. (a) Optical image of the as-fabricated stretchable display system. (b) Snap shot image of the designed circuit. (c and d) Optical image of the system laminated onto the human skin (c), and stretched at a freestanding state (d) [153].

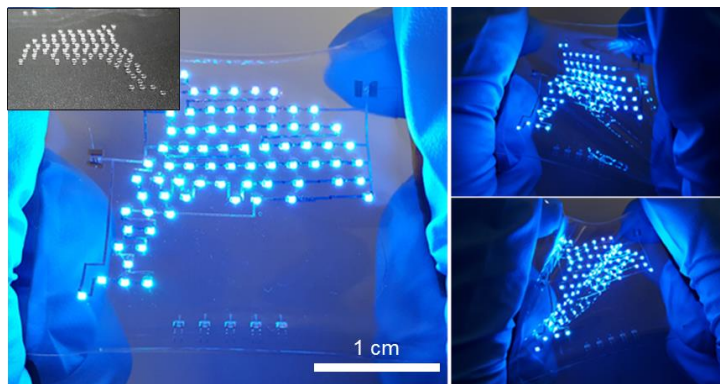


Figure 3.24 | Stretchable display in a dolphin design. Based on the PRI configuration embodying a dolphin (inset image), the stretchable system can be operated in sequences of deformation [153].

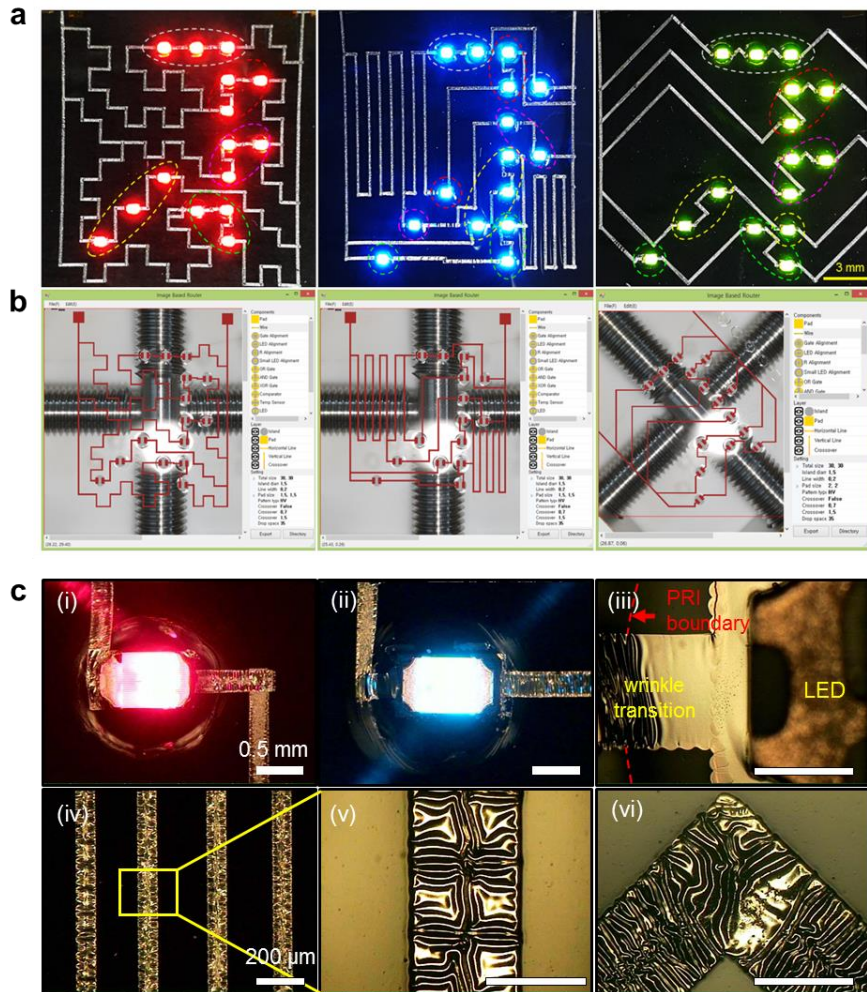


Figure 3.25 | Stretchable multi-mode displays in a “sha” design. (a) Photographs of three different layouts of stretchable display characterized by different LED colors, interconnection geometries, and network topologies between LEDs. (b) Snap shot images of designed topological networks in the circuit routing program. (c) Optical images of the highlighted areas of the system: operating LEDs upon the PRI areas (i, ii), the rigid-to-soft transition area with a wrinkle transition phenomenon (iii), and wrinkled areas conformable to straight (iv, v) and kinked (vi) interconnects [153].

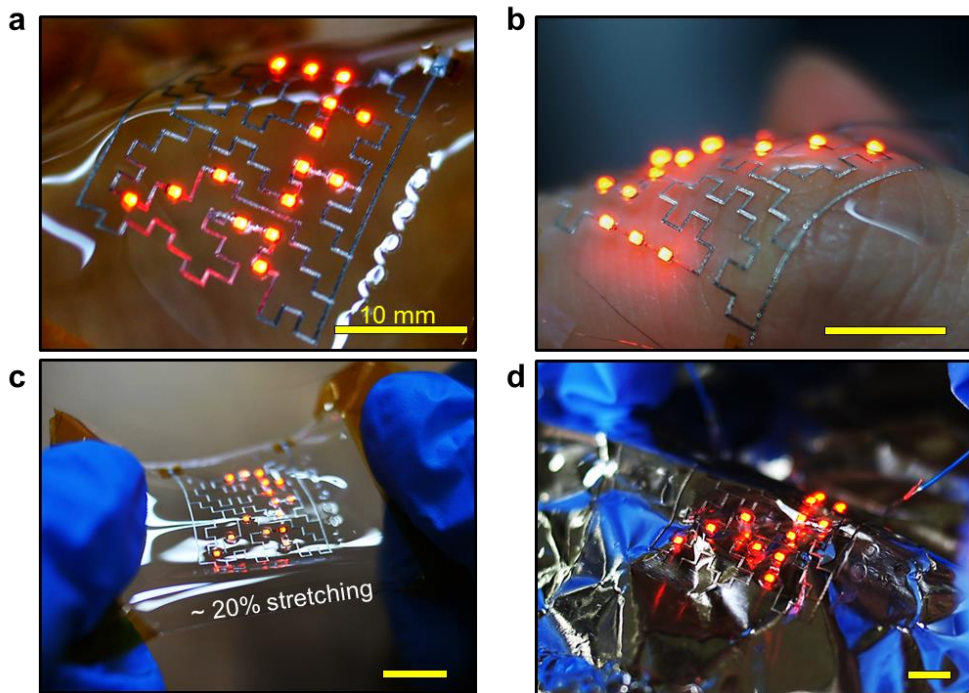


Figure 3.26 | Photographs of the stretchable multi-mode “sha” display at a freestanding state (a), laminated onto the human finger (b), stretched (c), and laminated onto the crumpled Al foil (d) [153].

For advanced functionalities of stretchable display, a programmable, 18-pin micro-controller unit (MCU) was employed. Specifically, based on the circle and rectangular lattice PRI configuration, a wearable watch (Figure 3.27) and PM display (Figure 3.28) were demonstrated with analogous SMD composition: a MCU (respectively programmed for watch operation and moving letters “AXEL”), numbers of LEDs (12 for watch and 35 for PM display), and a thin 3V battery. All electronic components were protected by PRIs and functionally bridged by inkjet-printed stretchable interconnects with customized layouts. While all LEDs were tightly bonded to inkjet-printed Ag pads via Ag epoxy, the MCU chip was directly connected to Ag pads by means of wire-bonding technology owing to the tiny size of MCU chip pads (top inset image in Figure 3.27c). Combinations of the strain-free effect in PRIs, wrinkled geometry, robust Ag epoxy bonding, and wire-bonding in integrated stretchable display systems revealed that harsh deformations like sequential wrist movements (Figure 3.27c), stretching/compressing with the skin (Figure 3.28b), and laminating onto the angled surface (Figure 3.28c) did not degrade the performance.

Given that the functionality of information display could be much augmented by active feedbacks from sensors, we integrated a temperature sensor onto an engineered soft substrate together with a proper amount of logic gates and passive elements that were used to divide a temperature level for digitized visualization (Figure 3.29). The wearable, real-time temperature monitoring system was comprised of a temperature sensor IC, 5 comparator

ICs, 10 resistors for voltage dividing, and 5 LEDs for output display. Each LED was sequentially turned on at 5, 18, 31, 44, 56 °C by exact comparison between the reference voltage and output voltage of the temperature sensor that linearly decrease as temperature increases (Figure 3.29b, c). As shown in Figure 3.29d, temperature monitoring LEDs worn onto the finger were sequentially turned on as a hair dryer approached, indicating that surrounding temperature was varied from room temperature (~25 °C) to around 60 °C.

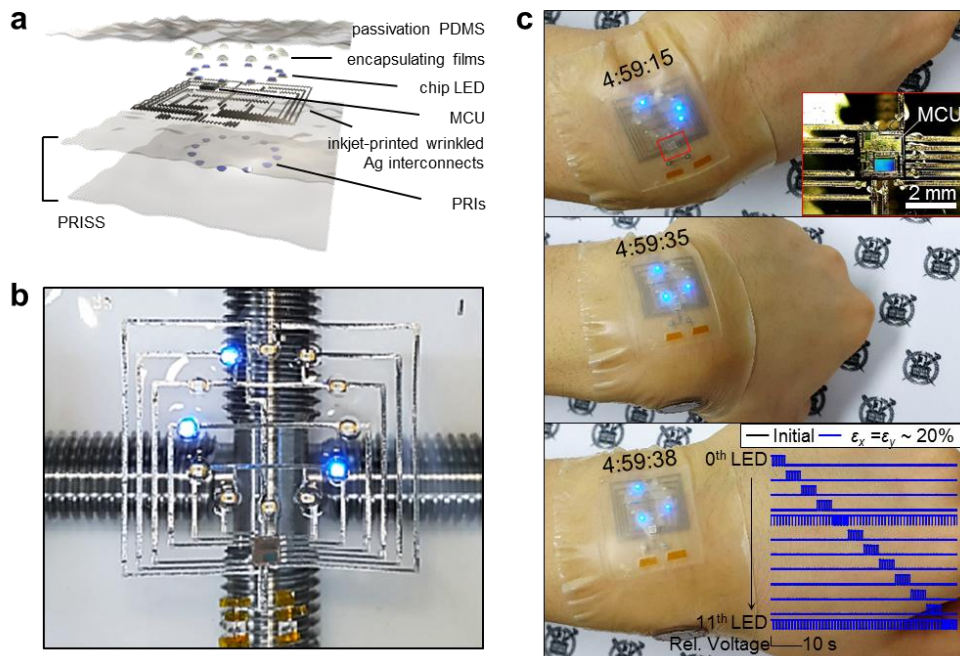


Figure 3.27 | Fully printed, wearable analog watch. (a) Exploded-view schematic illustration of the printed wearable analog watch system. (b) Optical image of the as-fabricated wearable watch, indicating “4:59:34”. (c) Photographs of the watch operation under sequential wrist movements. Top inset: Enlarged optical image of the wire-bonded MCU region. Bottom inset: Operating input signals of twelve LEDs before and after deformation under 20% biaxial strain [153].

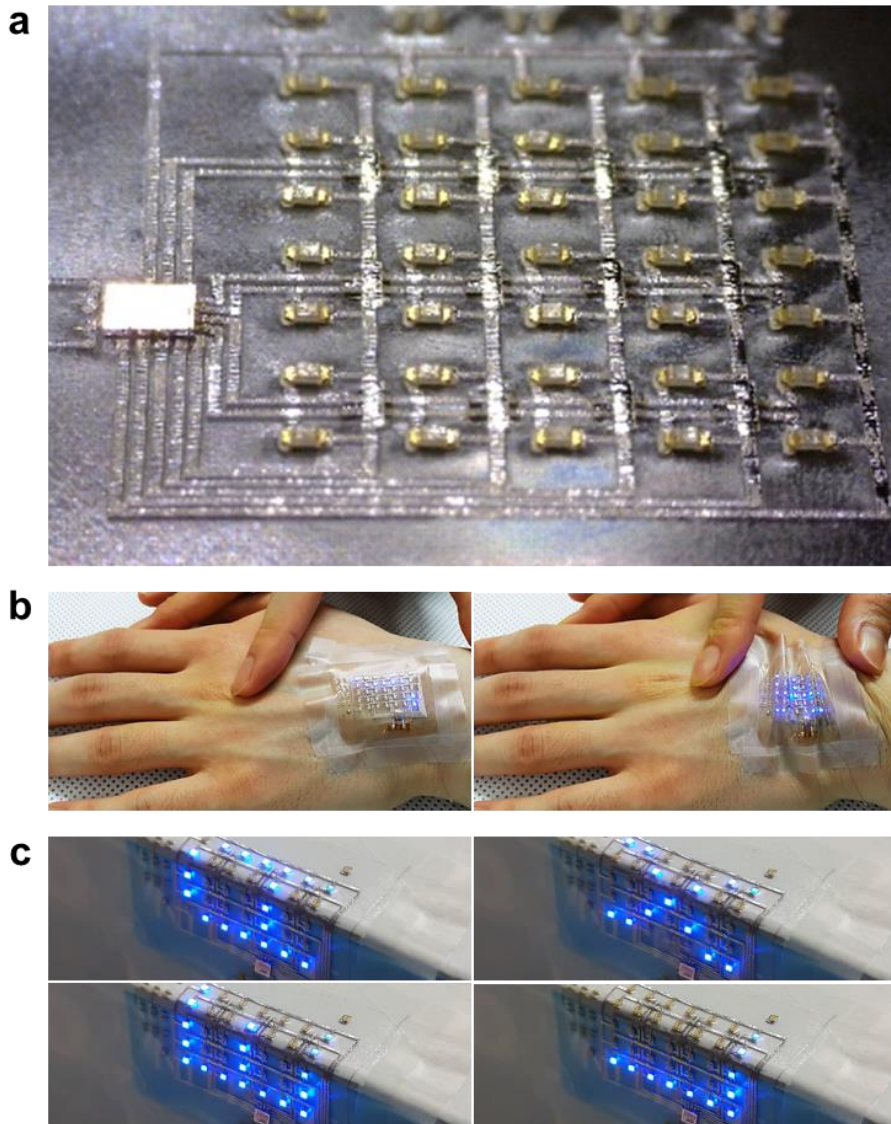


Figure 3.28 | Fully printed, wearable passive matrix (PM) display. (a) Photograph of the whole PM display circuit consisting of a MCU and 35 LEDs. (b and c) Photographs of the PM display deformed like the human skin (b) and folded (c) while exhibiting sequential letters “AXEL”, Advanced fleXible Electronics Laboratory [153].

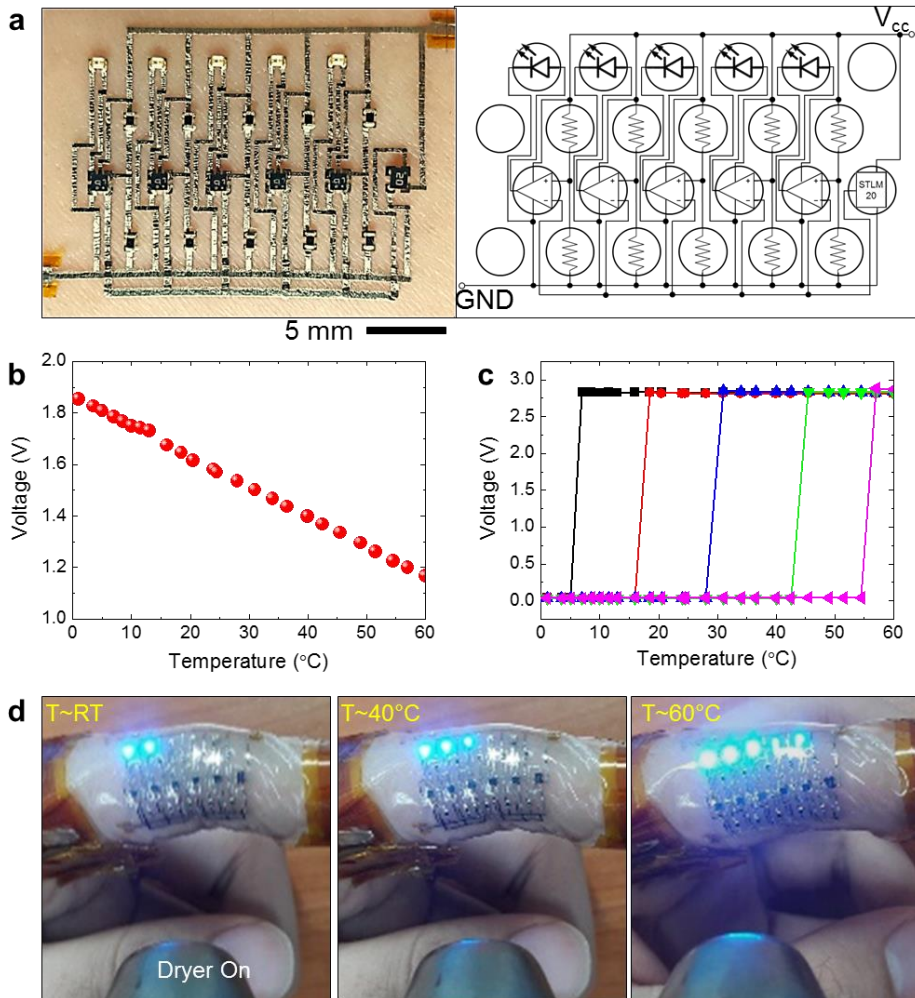


Figure 3.29 | Fully printed, wearable temperature monitoring system. (a) Optical image and corresponding logic diagram of temperature monitoring system. (b) Output characteristics of the temperature sensor IC as temperature increases from 0 to 60 °C. (c) Output characteristics of LEDs integrated in the temperature monitoring system. Each LED is sequentially turned on at 5, 18, 31, 44, 56 °C [153].

Chapter 4

Soft, Self-computable Electronic Skin

In this chapter, integrated soft electronic systems that involve “in-skin” functionalities of high-speed data processing and computation without outward data extraction (normally available by bulky wires) are presented, namely self-computable e-skin. Based on the printing-based soft substrate engineering and electronic functionalization processes described in the previous chapters, fully-integrated, self-computable e-skins that function as high-speed (1 MHz), stretchable computational logic circuits with consideration of multilayer integration and miniaturized designs are addressed.

4.1 Introduction

Advanced capabilities of (1) rapid prototyping with a large-area design, (2) high-speed, high-performance operation, and (3) “in-skin” functionalities including data processing, sensor-induced feedback, and computation suggest that our fully-integrated e-skin concept would provide potential not only for imparting advanced functionalities to on-going subjects with regard to soft interfaces but for grafting soft electronics into unprecedented subjects. Basically, the abilities to fabricate much complex network layouts between numerous IC devices that could not be tried to demonstrate by any other approaches allowed highly integrated, high-speed “in-skin” computation, leading to the concept of “self-computable” e-skin. Together with well-established soft sensor and associated electrode technologies (such as ECG, EMG, EEG) in the rising field of intimate health monitoring [36, 143–145], the self-computable functionality could enhance the capability of vital signal monitoring and diagnosis with in vivo data processing and feedbacks; avoiding further pathways of outward data extraction (either by bulky wires or wireless communication), processing in external sites (mainly in rigid PCBs), and re-transmission for diagnosis and therapy. Furthermore, it is strongly expected that this self-computable functionality, easily driven by our approach, could contribute to bridging the gap between soft electronics and human (not limited for health monitoring), robot, and even nature. For example, soft, self-computable (or fully-integrated) e-skins can be employed

for skin computer with functions that enable wireless interaction with machines, or even lead to soft IoTs; can serve as soft driving circuits in soft robots that are usually driven by bulky, pneumatic controllers [171]; and can even form intimate interfaces with biological living bodies, probably allowing communication and feedback-induced activation of biological organs (Figure 4.1) [172].

Among numerous possibilities, in this chapter, we addressed soft, self-computable e-skins that enable high-speed, integrated computing as a fundamental part of skin computer. Surpassing the low-level system integration such as stretchable display, we integrated computational functions into the soft substrate to offer an invaluable solution to the bottleneck in implementing stretchable computing circuits. A well-developed printing-based electronic functionalization process provided an opportunity for scalable assemblies of innumerable IC devices, creating “self-computable” e-skins. As a fundamental unit of computer, in this section, demonstrations of stretchable full adders, 2-bit multipliers, and binary decoders are described with consideration in miniaturized, multilayer designs [153, 154].

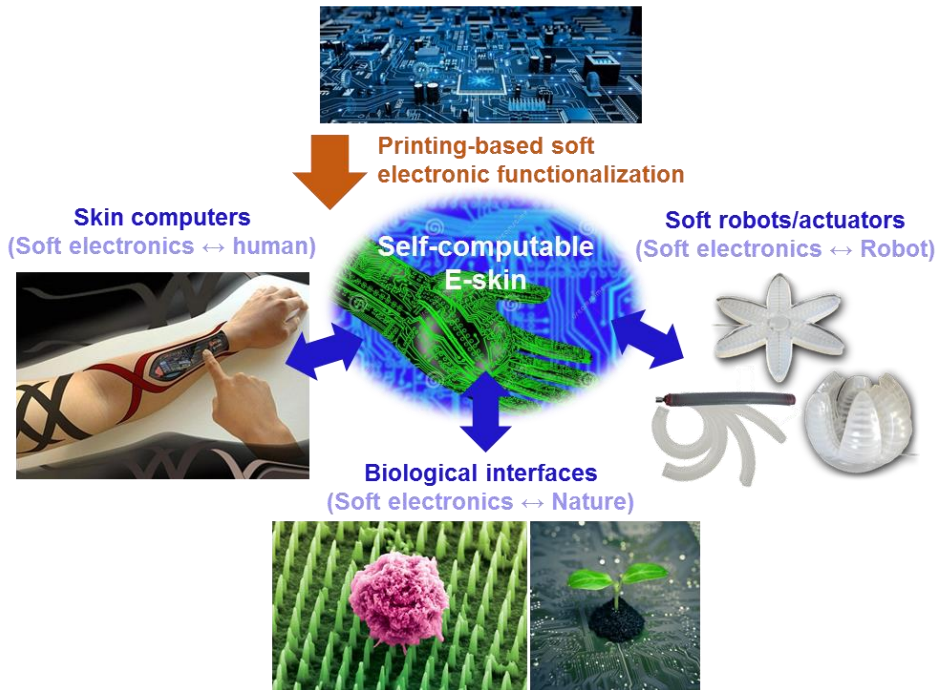


Figure 4.1 | Potential of fully-integrated e-skin, providing advanced capabilities of engrafting soft electronics into both on-going and unprecedented subjects including human, robot, and nature.

4.2 Soft, Fundamental Logic Circuits in Single-side Designs

The capability of integrating multiple types of IC chips and electronic units allows self-computing feature without external wirings for additional computation, thus “self-computable” e-skins. As a fundamental unit of digital computer, we first demonstrated fully-integrated tiny e-skins that function as a digital full adder with a highly compact design based on the pentagonal PRI arrangement, dimension of which is much smaller than human nails (Figure 4.2a). To miniaturize the design, we employed standardized SMD ICs whose dimension is $1 \times 1 \text{ mm}^2$. The well-established scalable implementing methodology allowed multiple samples in a single batch of engineered PRISSs (Figure 4.2b). Analogous to the cases of stretchable display, the engineered geometry of interconnection networks, stable crossovers, and optimized PRISS advocated 100 kHz operation with ~30% biaxial stretchability (Figure 4.2c).

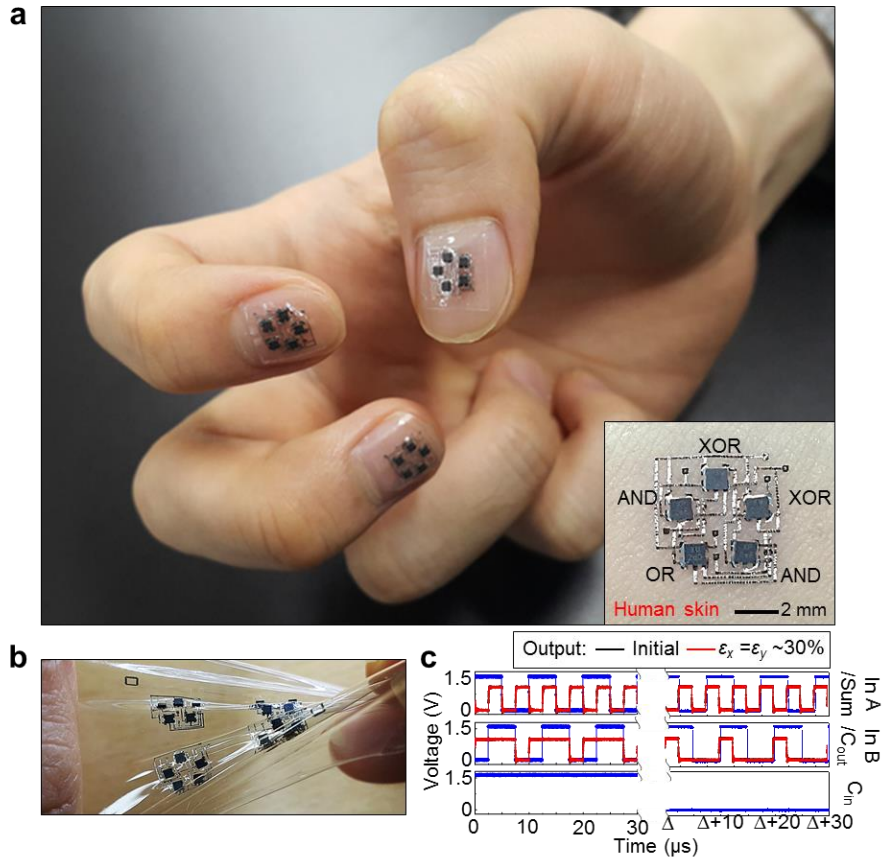


Figure 4.2 | Soft digital full adders in a single-side miniaturized design. (a) Photograph of digital full adders with a customized design directly fabricated on the PRISS which contains pentagonal PRI arrangements. Owing to the wrap-like conformability, the full adders are easily adhered to human nails and skin (inset image). (b) Photograph of stretched/twisted full adders. Several full adders can be fabricated in a single batch. (c) Input/output characteristics of full adders both at an initial and stretched state ($\epsilon_x = \epsilon_y \sim 30\%$) [153].

Integration of 8 logic gates (6 AND gates and 2 XOR gates) with more intricate interconnection networks—including 26 crossovers— into the 4×6 rectangular PRI lattice offered an opportunity of “one-step-advanced” computation of 2-bit multiplication (Figure 4.3). For direct visualization of the input/output signals, 8 LEDs were concurrently mounted on the PRISS. In particular, the universal arrangement of the rectangular lattice PRI configuration, rather than pre-specified layout such as maple leaf or dolphin, fulfilled the ultimate ability to customize circuit designs and functions. The full operation of the wearable 2-bit multiplier was verified by direct signal visualization of mounted LEDs, showing that all sequences of input pairs $(A_0, A_1) \times (B_0, B_1)$ generated exact output signals of 2-bit Z_i (Figure 4.4). For a 2-bit multiplier, the distinct circuit layout with large size IC chips was additionally fabricated to verify the feasibility of various SMD integration (Figure 4.5a-c). Reliable computational property under cyclic biaxial stretching supported the clear strain-free feature of large size PRIs (diameter > 5 mm) and robustness of printed stretchable interconnects (Figure 4.5d).

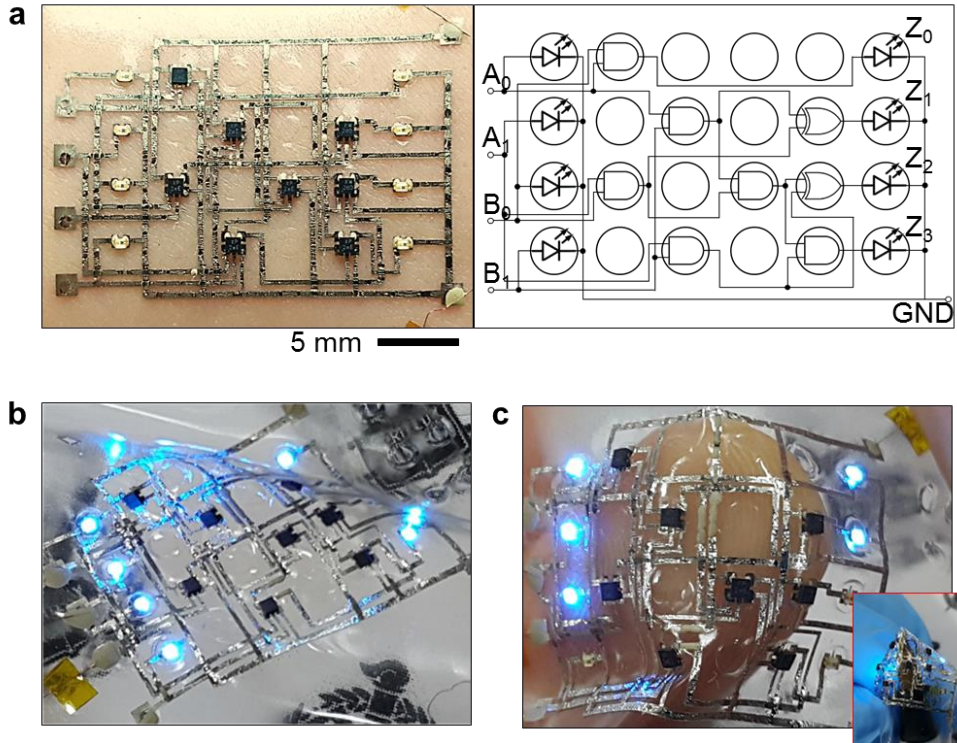


Figure 4.3 | A soft 2-bit digital multiplier in a single-side design. (a) Photograph and corresponding logic diagram of 2-bit multiplier laminated on the human skin. (b and c) Photographs of the stretched 2-bit multiplier indicating “ $3 \times 3 = 9$ ” (b), and wrapped around a finger (“ $3 \times 1 = 3$ ”) and a ball pen (inset image) [153].



Figure 4.4 | Full operation of the wearable 2-bit multiplier [153].

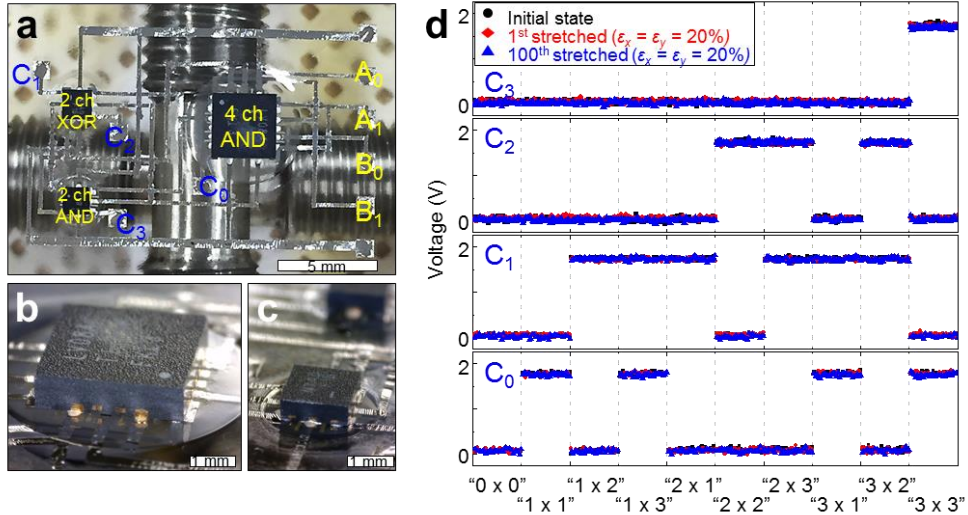


Figure 4.5 | A soft 2-bit digital multiplier based on a large PRI (diameter ~ 5.6 mm). (a) Photograph of the whole system comprised of 4-channel AND gate (SN74LV08ARGVR, Texas Instruments (TI), 3.5×3.5 mm²), 2-channel AND gate (SN74AUP2G08, TI, 1.5×1.5 mm²), and 2-channel XOR gate (NC7WZ86, Fairchild Semiconductor, 1.6×1.6 mm²). (b) Magnified optical image of 4-channel AND gate mounted on the large size PRI (diameter ~ 5.6 mm). (c) Magnified optical image of 2-channel XOR gate mounted on the medium size PRI (diameter ~ 2.5 mm). (d) Output characteristics (C₀—C₃) of initial, stretched, and 100-times stretched multiplier in multiple states (A x B). The system was equi-biaxially stretched at a speed of 1 mm s^{-1} [153].

4.3 Self-Computable Electronic Skin Based on Double-side Universal Soft Electronic (Double-side USE) Platform

4.3.1 Concept, Design, and Fabrication

For a practical computer or any computational logic circuits such as arithmetic logic units (ALUs) and micro-controller units (MCUs) allowing functions that can be applied in practical uses, innumerable numbers of devices (either a transistor level or IC level) should be integrated in conjunction with much complex interconnection networks in terms of multilayer routing. Also, given high-speed operation, such interconnection networks should satisfy the conditions of a sufficient level of electrical conductivity and negligible parasitic capacitance (or inductance) to avoid electrical degradation induced by high-frequency signal propagation. However, existing options in methodologies for fabricating stretchable electronic circuits usually lack the capability of scalable and multilayer implementation, just focusing on the device level (typically soft sensors) and/or low-speed patch-type electronics with bulky designs.

In these regards, we propose a geometric insight in terms of double-side capability. As an universal framework for implementing fully printable, system-level soft electronics with functions of practical data processing and computing, we developed a concept of a double-side universal soft electronic

(double-side USE) platform—one of PRISSs— in which co-embedded arrays of polymeric rigid islands and core-shell vias allowed site-selective, simultaneous double-side strain-isolating and vertical-interconnecting functionalities, respectively (Figure 4.6). Combined with a printing-based double-side electronic functionalization process, for the first time, a novel concept of fully printed, double-side integrated, stretchable 1 MHz computational logic circuits were demonstrated (Figure 4.7).

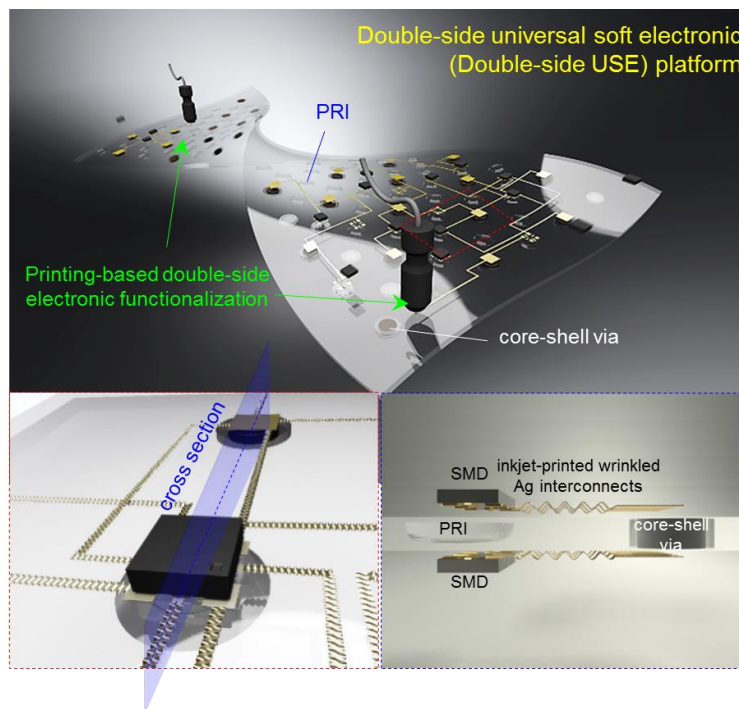


Figure 4.6 | Conceptual schematic of a double-side USE platform and printing-based system-level integration. Inset illustrations show key features of double-side strain-isolation with a single PRI and double-side vertical-interconnection with a core-shell via [154].

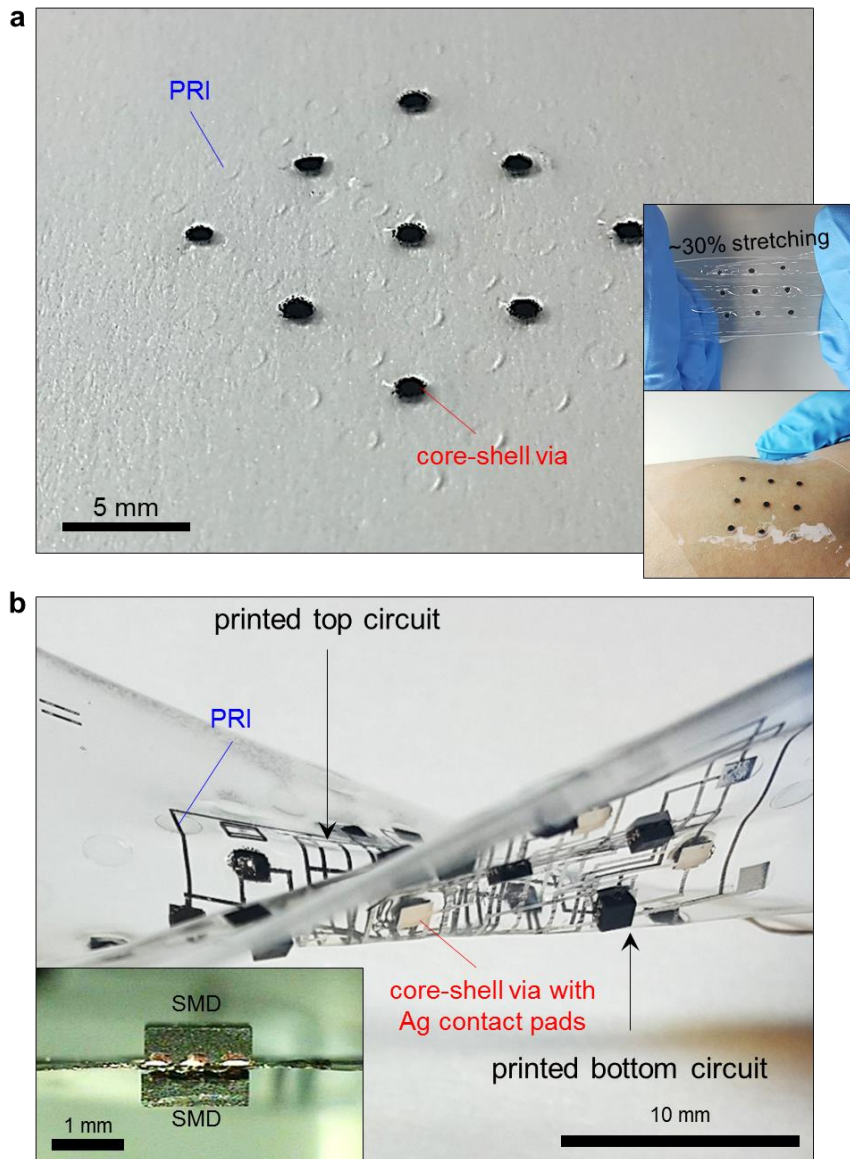


Figure 4.7 | A double-side integrated, fully printed, system-level soft electronic circuit fabricated on the double-side USE platform. Inset image: cross-sectional optical image of double-side integrated SMDs. (a and b) Photographs of a double-side USE platform (a) and integrated circuits (b) [154].

In this double-side USE platform, two main features of (i) double-side strain isolation with a single island structure and (ii) double-side electrical conduction through a core-shell via were concurrently integrated into a common soft substrate (Figure 4.6, 4.7). Thus, the fabrication procedure of a double-side USE platform was focused on such two major parts: (i) rigid island printing (Figure 4.8a(ii)) and (ii) core-shell via formation (Figure 4.8a(iii)). All steps were executed by a pneumatic control nozzle-jet printing process; to be specific, single droplets of functional inks printed by a single nozzle were formed into PRIs and stretchable core-shell via structures, respectively. More specific experimental steps were depicted in Figure 4.9. Both components embedded in an elastomer matrix PDMS played a role of mechanical and electrical backbones, respectively; leading to a double-side engineered soft substrate for multilayer stretchable hybrid electronics.

For PRIs, strategies of one-step double-side strain-isolating, as depicted in section 2.2.3, were employed. Specifically, 17 wt% PMMA (M_w 120,000) solution was dispensed from a pneumatically controllable nozzle-jet printer with specific conditions of air pressure = 150 kPa and duration time < 4 s, forming PRIs with adequate robustness and size (Figure 4.8b).

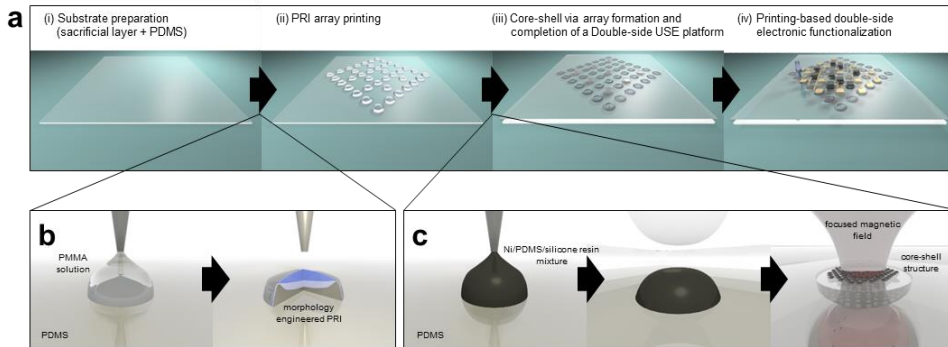


Figure 4.8 | Salient steps in fabrication process for a double-side USE platform. (a) Simplified fabrication process: (i) substrate preparation, (ii) PRI array printing, (iii) core-shell via array formation and completion of a double-side USE platform, and (iv) printing-based double-side electronic functionalization (detailed fabrication steps are depicted in Figure 4.9). (b) Process steps of single droplet printing of a PRI: as-printed PMMA ink (left) is formed into specific island structures (right) along with PMMA concentration. (c) Process steps of single droplet printing of a core-shell via: as-printed Ni/PDMS(5:1)/silicone resin mixture (left) is covered by PDMS matrix (middle) and then formed into the core-shell structure (right) driven by a highly focused magnetic field [154].

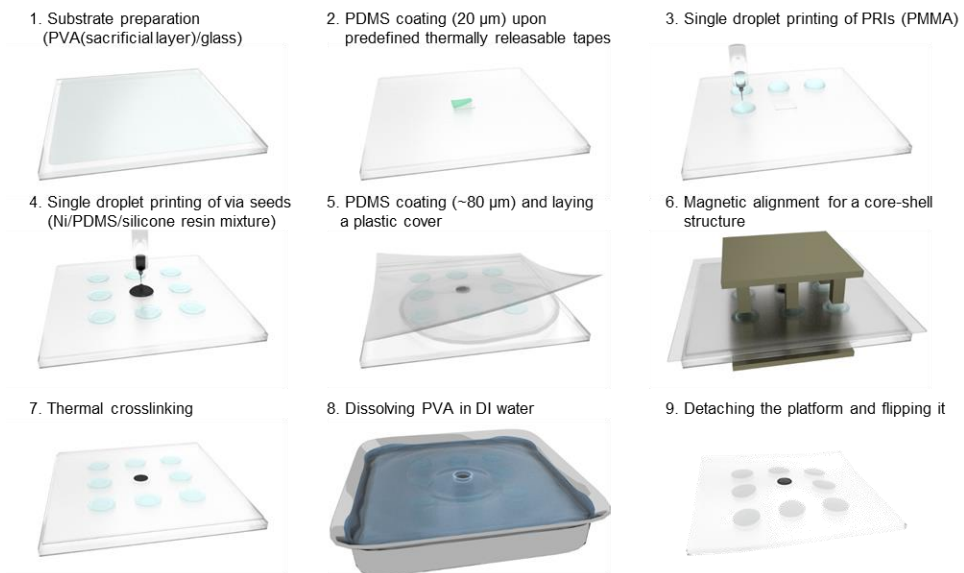


Figure 4.9 | Total fabrication process of a double-side USE platform [154].

For stretchable via fabrication, a single droplet of nickel (Ni) microparticles (average diameter $< 5 \mu\text{m}$)/PDMS (5:1 mixing ratio)/silicone resin (OE-6630, Dow Corning) mixture ink was printed as a seed structure (Figure 4.8c, left) [173]. After being embedded inside the PDMS matrix (Figure 4.8c, middle), the printed mixture was exposed to a highly focused magnetic field that was driven by a pair of high aspect ratio (~ 9) iron structures and magnets ($\sim 0.17 \text{ T}$) (Figure 4.10). Interacting with a focused magnetic field, ferromagnetic Ni microparticles were self-assembled into the center of the mixture; by contrast, the shape of PDMS and silicone resin residues was not affected by the magnetic field, spontaneously constructing a core (Ni/PDMS(5:1)/silicone resin)-shell (PDMS(5:1)/silicone) structure (Figure 4.8c, right and Figure 4.11). This vertical alignment of Ni particles offered huge increase in electrical conductivity ($\sim 10 \text{ S m}^{-1}$) in vertical direction (Figure 4.12), and the structural peculiarity of the core-shell geometry exhibited modulus-gradient property (Young's modulus: core $>$ shell $>$ elastomer matrix (PDMS(20:1))) for efficient stress absorption [173]; simultaneously satisfying both electrical and mechanical requirements for a stretchable via structure. Moreover, a strong magnetic field attracted Ni particles to the field sources (a pair of iron structures), and therefore embedded Ni particles were moved towards and exposed to both top and bottom surfaces of the platform; consequently forming protruding conductive contacts that facilitated a facile wiring between vias and electronic components. Dimension (thickness and diameter) of vias was optimized with

form factors that enabled geometric co-integration with PRIs and compact circuit design.

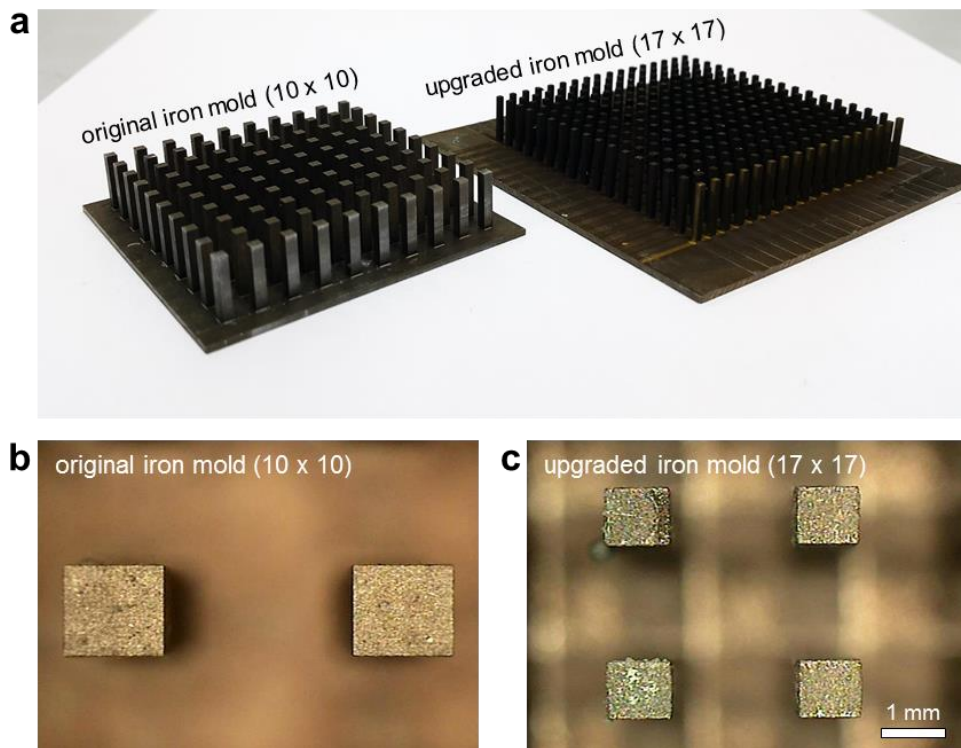


Figure 4.10 | Magnetic field focusing equipment. (a) Photograph of original [173] and modified iron mold. (b and c) Optical images of high aspect ratio iron structures in the original mold (b) and upgraded mold (c). Cross-sectional area of each iron structure was reduced from $1.6 \times 1.6 \text{ mm}^2$ to $1 \times 1 \text{ mm}^2$ and aspect ratio was increased from 5.625 to 9. This modified dimension provided capabilities of more densified via design and geometric compatibility with PRIs [154].

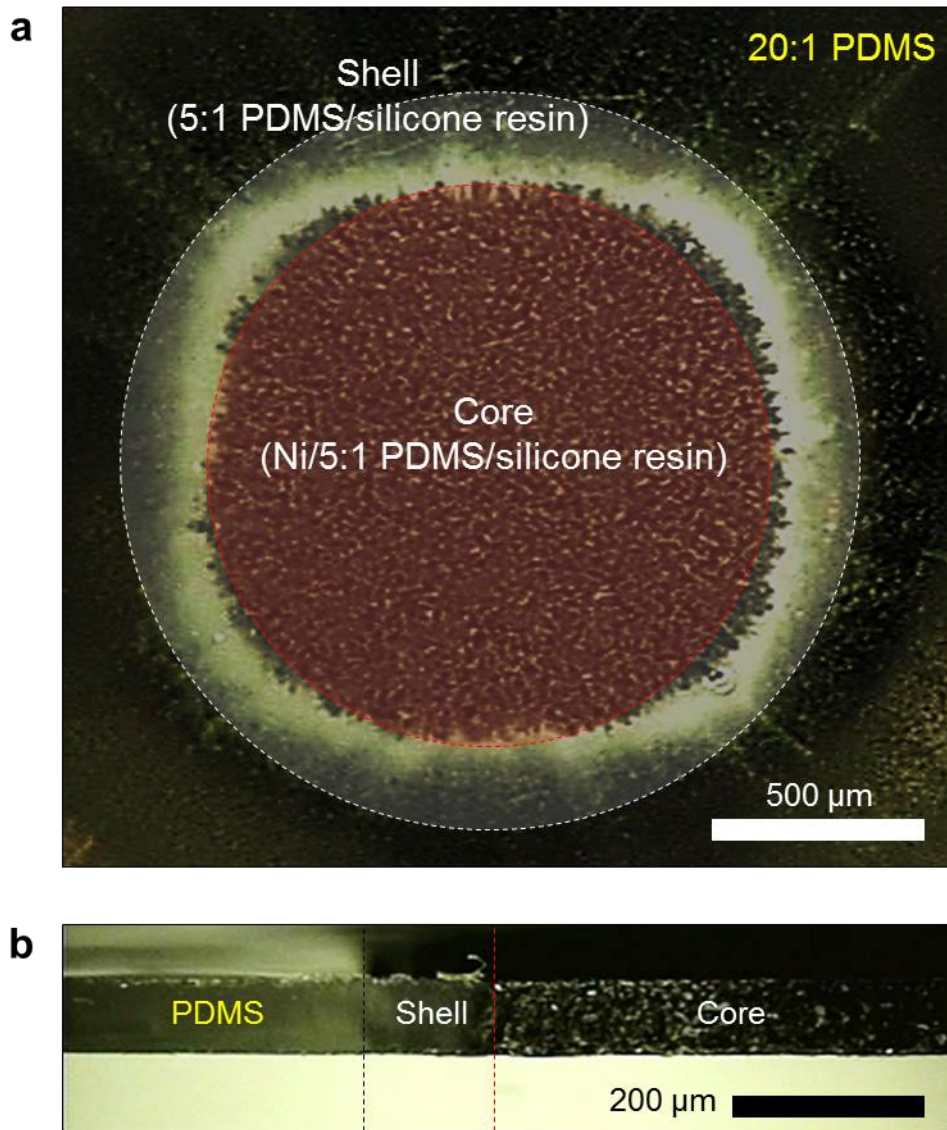


Figure 4.11 | Structure of a stretchable core-shell via. (a) Top-view optical image of a core-shell via. (b) Cross-sectional optical image of a core-shell via. Total thickness of the via was $\sim 100 \mu\text{m}$ [154].

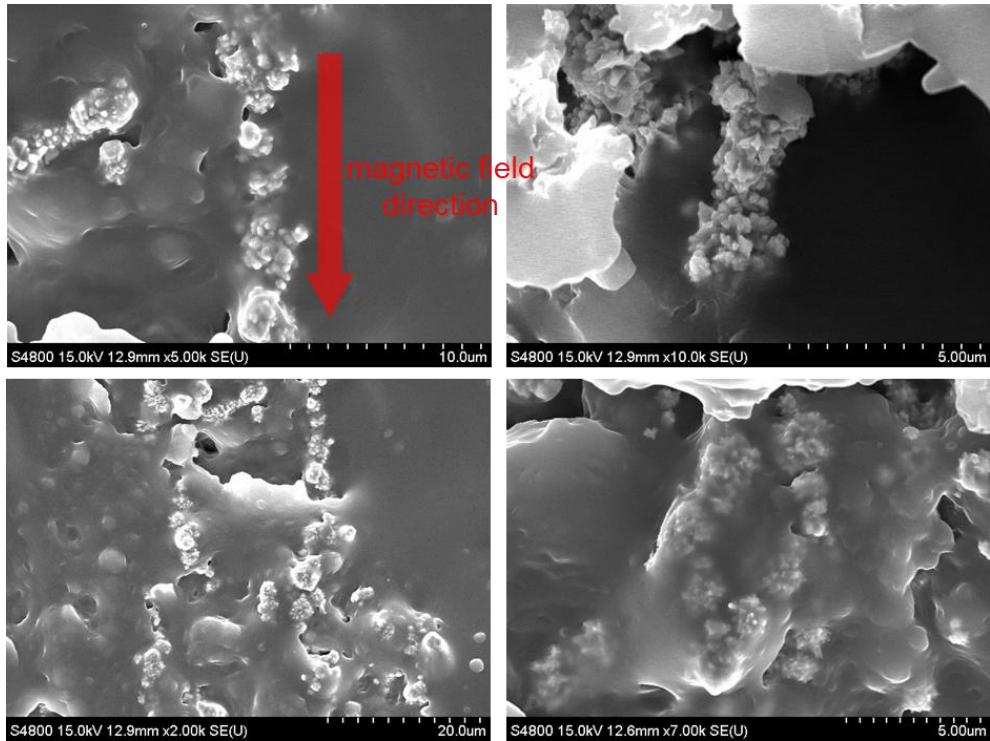


Figure 4.12 | SEM images of magnetically aligned Ni microparticles in a core area. Several cross-sectional SEM images validate that Ni particles (average size $< 5 \mu\text{m}$) were densely aligned in a vertical direction (= magnetic field direction) in the core part of core-shell vias, and formed vertical conduction paths with greatly improved electrical conductivity [154].

For further investigation on mechanical and electrical behaviors of core-shell vias, DIC-based surface strain analysis and a series of electrical characterization were conducted. At first, an average strain level (evaluated from the 50% internal via area) and actual strain distribution inside the via under sequential stretching (0–50%) were explored (Figure 4.13). From the result, we figured out that the obtained average strain level inside the via was low enough to keep its conductivity under large ($\epsilon_{\text{appl}} \sim 100\%$) and cyclic deformations. To be specific, the range of initial resistance of core-shell vias was around 10–20 Ω , and the resistance versus applied tensile strain profile suggests that the resistance slightly increased in the low strain regime ($\epsilon_{\text{appl}} < 20\%$), started to decrease, and was finally sustained in the high strain regime ($\epsilon_{\text{appl}} < 100\%$): resistance variation in the entire strain regime (0–100%) was lower than 10 Ω (Figure 4.14a). This is because an elastomer/conductive filler composite with anisotropic filler distribution (like vertical alignment) generally shows negative strain-resistance property, driven by total volume reduction of the composite under uniaxial stretching.^[36] For repeated deformation ($\epsilon_{\text{appl}} = 50\%$), the via underwent substantial increase in electrical resistance in first few cycles because of the misalignment of off-centered Ni particles that were relatively vulnerable to external stress; but, the resistance was stably maintained under 20 Ω during over 800 cycles with an increase rate of ~ 4.5 m Ω per a cycle (Figure 4.14b). Especially, similar to the resistance profile in Figure 4.14a, the repeated relocation and volume reduction of the via induced a double-peak profile in every stretching cycle

(inset in Figure 4.14b). Furthermore, it is notable that the addition of buffer PDMS (5:1) greatly contributed to alleviating the localized stress near the core/shell/matrix boundaries so that electrical conductivity of the via was maintained even under cyclic 30% biaxial strain (Figure 4.15).

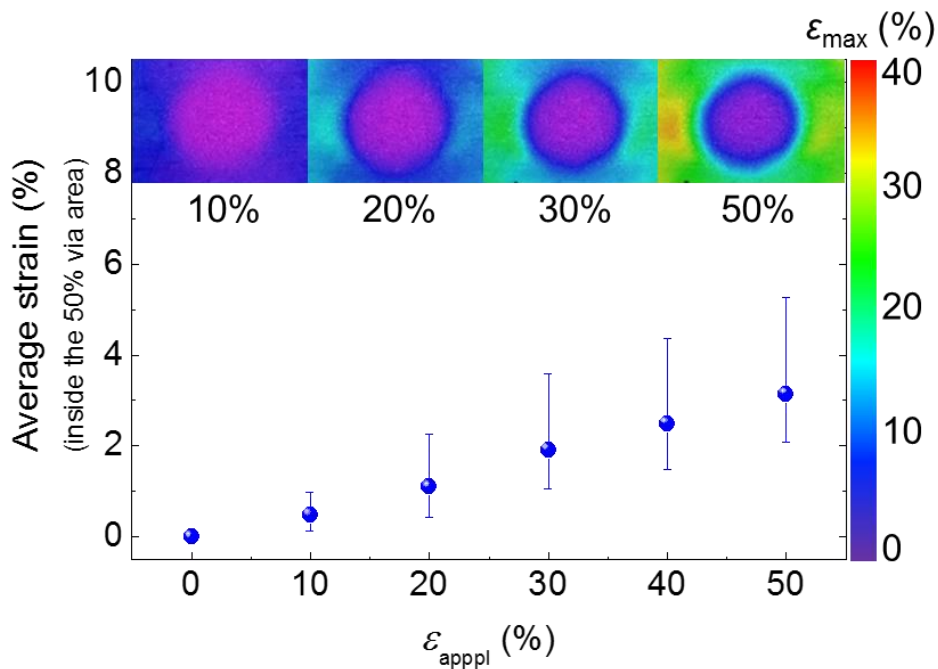


Figure 4.13 | Surface strain distribution and average strain levels of a core-shell via as a function of ϵ_{appl} (0–50%). All evaluated strain values were calculated in the form of maximum principal strain based on DIC [154].

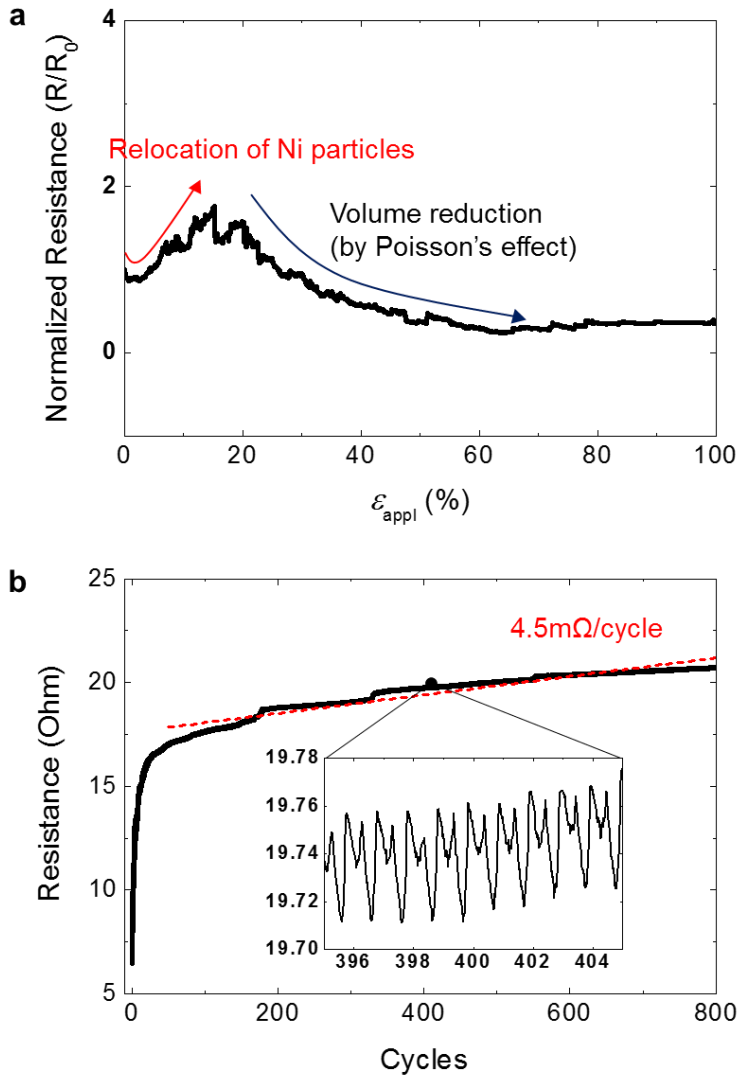


Figure 4.14 | Electrical characteristics of a stretchable core-shell via. (a) Normalized resistance profile curve of a core-shell via during a large deformation ($\epsilon_{\text{appl}} = 0\text{--}100\%$). Initial resistance of the via was $10\text{--}20 \text{ }\Omega$, and stretching speed was 1 mm min^{-1} . (b) Resistance profile of a core-shell via during repeated deformation ($\epsilon_{\text{appl}} = 50\%$). Stretching speed was 100 mm min^{-1} [154].

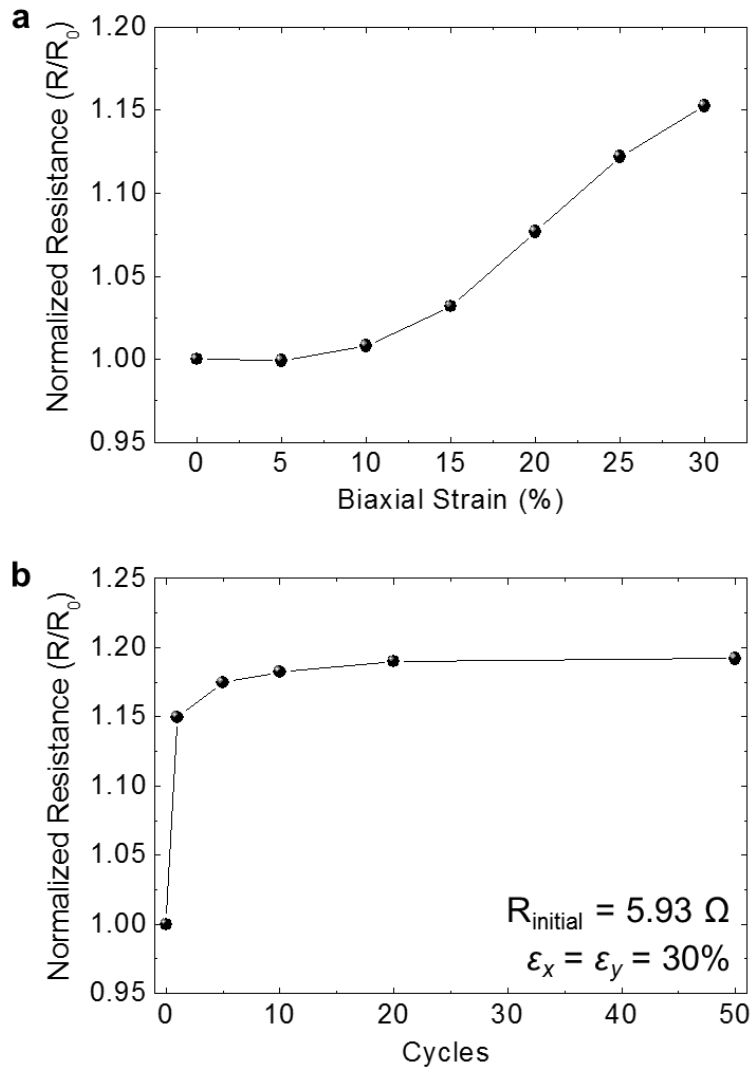


Figure 4.15 | Electrical characteristics of a core-shell via under 2D stretching. (a) Resistance profile of the core-shell via undergoing 2D biaxial stretching (0 to 30%). The initial resistance of the via was 6.93Ω , and the stretching speed was $\sim 1 \text{ mm s}^{-1}$. (b) Resistance of the via undergoing repetitive 30% biaxial stretching [154].

In addition to static electrical analysis (mainly related to resistance), we further explored the frequency response of core-shell vias to validate high-frequency operation. In particular, input/output gain and signal delay (or phase shift) were investigated. First, the gain of sinusoidal waves with increasing frequency (10 Hz–50 MHz) was measured both at an initial state and biaxially stretched state (~30%). The good consistency of gain (~0.97) in a specific frequency regime (10 Hz–1 MHz) validated the practical use of core-shell vias in middle-range-speed circuit operation (Figure 4.16). Also, the sharp increase of gain in the higher frequency regime (> 10 MHz) assumed that the resonant frequency ($\sim(LC)^{-1/2}$) of the via was located around 100 MHz. Input/output signal delay was also measured by two different input square waves (1 kHz, 1 MHz) (Figure 4.17a). From the magnified view of signals in Figure 4.17a, we identified that the signal delay (mainly related to RC constant) was ~3.2 ns, and no meaningful difference between delays in 1 kHz and 1 MHz input/output signals (either stretched or not) was observed (Figure 4.17b).

For an overall layout, in order to involve universality in device integration, PRIs and vias were arranged in a symmetric configuration comprising a 7×7 array whose unit structure was comprised of 8 PRIs and 1 via in a 45° -rotated square lattice configuration (Figure 4.8). Considering the specification of the field focusing equipment, the feasible amounts of PRIs and vias in a single platform could be extended to 280 and 81, respectively (Figure 4.10). The resulting design could create a great synergy together with

a printing-based electronic functionalization methodology that offered the capability of superb circuit design freedom along with a facile, mask-free fabrication procedure.

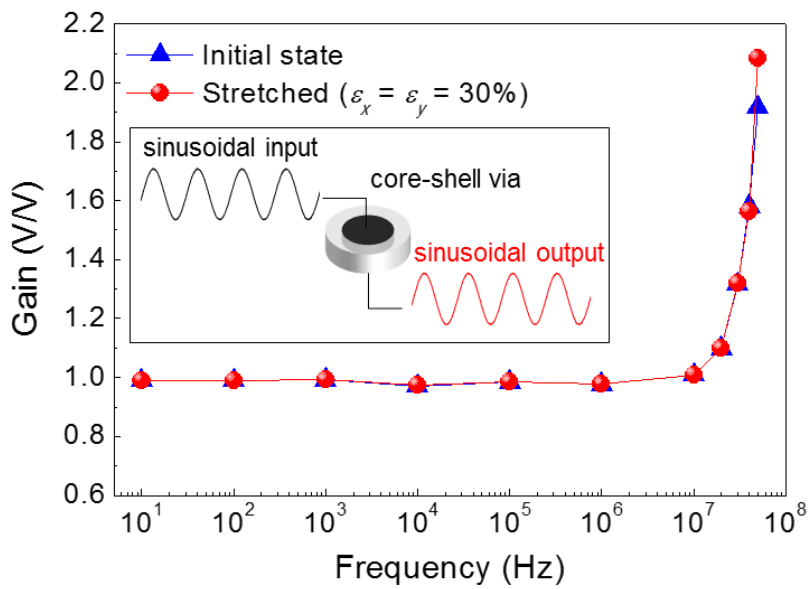


Figure 4.16 | Frequency response of a core-shell via to sinusoidal waves [154].

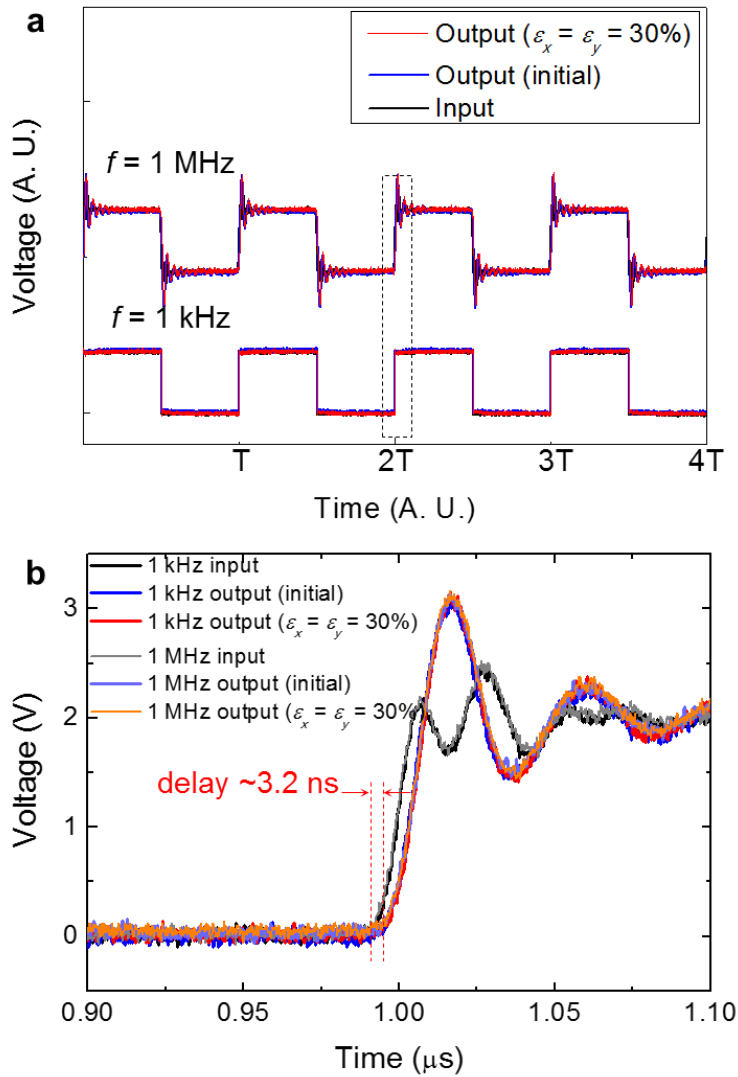


Figure 4.17 | Input/output signal (1 kHz, 1 MHz square waves) characteristics at an initial and stretched (biaxial strain $\sim 30\%$) state (a) and the magnified view (b) in a positive-edge triggered region that shows the signal delay $\sim 3.2 \text{ ns}$ [154].

4.3.2 Overall Strain and Conductivity Mapping

A universal concept arrangement of double-side strain-isolating PRIs and double-side vertical-interconnecting stretchable core-shell vias accorded universality in site-selection for device integration and ultimate circuit design (Figure 4.7a). Also, thin ($\sim 100\ \mu\text{m}$) and soft features of this platform enabled maintaining its own properties in response to a series of deformations (insets of Figure 4.7a). In addition to individual characteristics of the double-side strain-isolating PRIs and vertical-interconnecting core-shell vias as described in section 2.2.3 and 4.1.2 respectively, mechanical and electrical property of overall platform and feasibility of double-side electronic functionalization for stretchable systems needed to be investigated. In this respect, large-area ($\sim 12 \times 12\ \text{mm}^2$) surface strain mapping on both surfaces and thermal conductivity mapping for the operating circuit that was simply designed through interconnecting 9 vias were performed to visualize overall characteristics. First, surface strain distribution in a unit domain, containing 3×3 components of 8 PRIs and 1 via, of a double-side USE platform was explored in an analogous way as described in previous DIC processes; the difference was that DIC process was carried out under biaxial strains of 0 to 30% with a reduced resolution in a strain field induced from large-area imaging. The overall DIC result suggested that individual mechanical robustness of PRIs and via was fully reflected that surface strain was exactly isolated both in PRI and via areas, providing arrays of well-defined strain-free areas (Figure 4.18).

Also, addressing the geometry of PRIs in which the outer diameter (diameter in a top side view) was larger than the inner diameter (diameter in a bottom side view), it is worth noting that the strain localization between the via and adjacent PRIs was more enhanced on the top surface than the bottom surface.

Overall electrical characteristics of the platform was analyzed in terms of reliable vertical interconnection through 9 core-shell vias. To visualize the electrical conductivity of such via areas, an indirect way of infrared thermography that mapped thermal gradient of Joule heating generated from operating circuits was adopted. A simple circuit illustrated in Figure 4.19 (PRIs were omitted for simplicity) was designed to link 9 vias through 7 steps of vertical conduction, and was fabricated by two-step inkjet-printing processes. Once the bias (~ 2 V) was applied to the terminals, printed Ag interconnects and vias started to emit thermal radiation following the equation of $P = V^2/R$; within a few seconds, temperature gradient was observed around the interconnects and vias captured by a thermal imaging camera (T420, FLIR) (Figure 4.20). R Specific setting conditions were as follow: emissivity = 0.86, reflected temperature = 24 °C, ambient temperature = 24 °C, and humidity = 19%. Regulated by biasing time (few seconds) and circuit resistance (~ 300 – 350 Ω), temperature increase was ~ 5 °C. The thermographic profiles on the top and bottom surfaces of the double-side USE platform supported the spatial conductivity and thus double-side electrical conduction path through 9 vias.

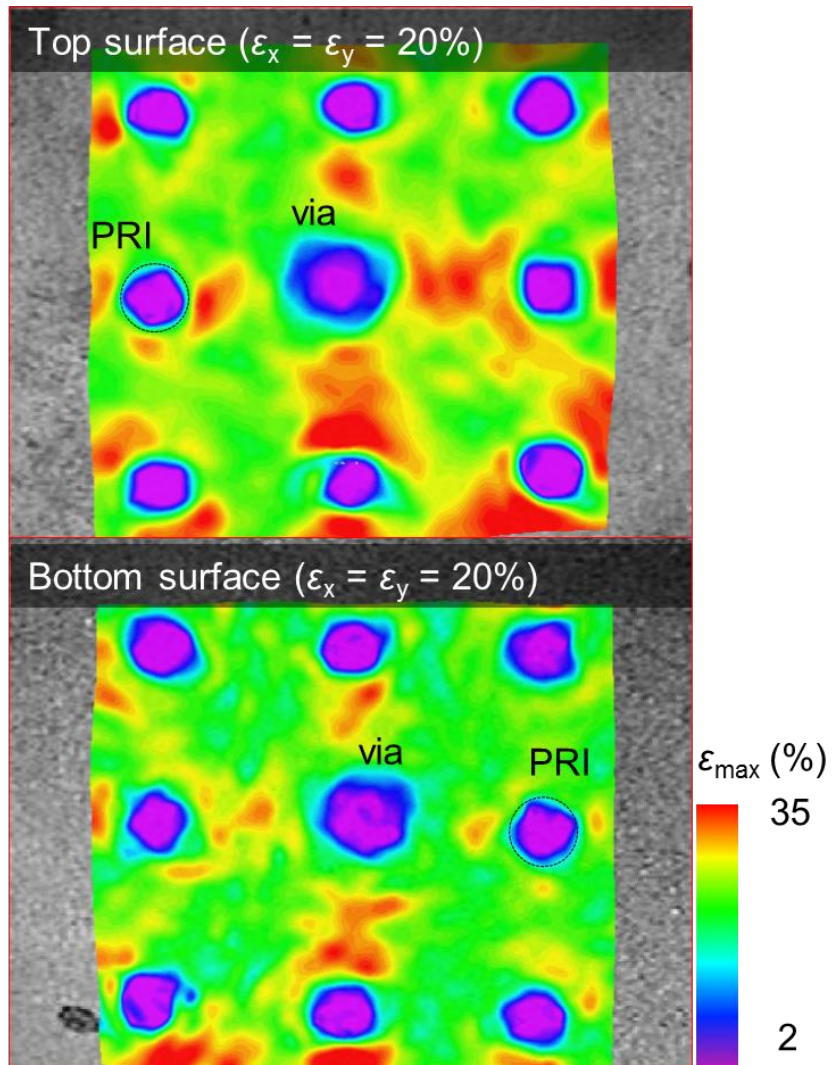


Figure 4.18 | Large-area surface strain mapping on both top and bottom surface under 20% biaxial strain [154].

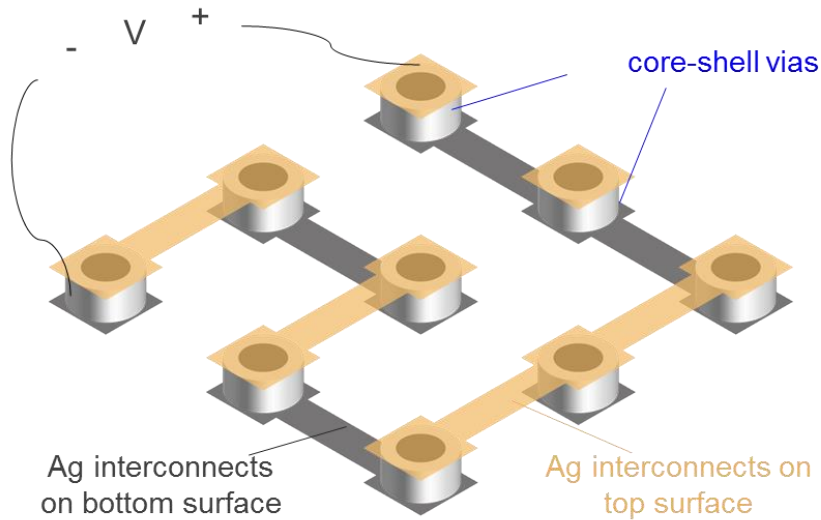


Figure 4.19 | Schematic illustration of the circuit designed to line 9 vias through 7 steps of vertical conduction (PRIs are omitted for simplicity). Two-step inkjet-printing processes were carried out for fabrication [154].

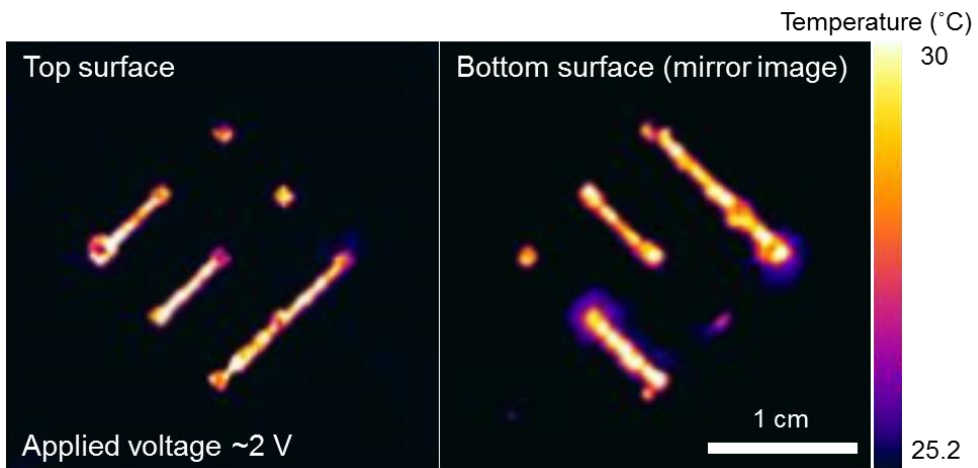


Figure 4.20 | Temperature gradient mapping of the operating circuit on both top and bottom surfaces. Bias voltage of ~ 2 V was applied for a few seconds to obtain observable temperature gradients (~ 5 °C) [154].

4.3.3 Stretchable, Double-side Integrated 1 MHz Binary Decoder

Based on the prepared double-side USE platform comprised of 7×7 arrays of 40 PRIs and 9 vias, the first demonstration of fully-printed, double-side integrated, stretchable computational logic networks that offered an opportunity of “in-system” computing and practical data processing was achieved by means of two-step printing-based electronic functionalization process. The targeted circuit was a kind of decoder that consisted of 4 inverters, 9 multi-input AND gates, and 7 multi-input OR gates, converting high-speed (~ 1 MHz) binary code decimal (BCD) to 7-segment signals (Figure 4.21). Detailed step-by-step fabrication process flow is as follows:

Top circuit design

1. Prepare the double-side USE platform (Figure 4.9).
2. Biaxially stretch ($\varepsilon_x = \varepsilon_y = 30\%$) the double-side USE platform; capture the image.
3. Open the home-made circuit routing program (“Image Based Router”), and load the captured image as the background image for circuit design (Figure 4.22).
4. Pinpoint PRIs with predefined functional pad layouts ($1.5 \times 1.5 \text{ mm}^2$ logic gate (inverter, AND, OR) in this case); draw the top circuit—addressing the predesigned circuit layout (Figure 4.23a, b)— by

bridging functional PRIs. The standard line width is set to 200 μm , and all core-shell vias are covered with square pads.

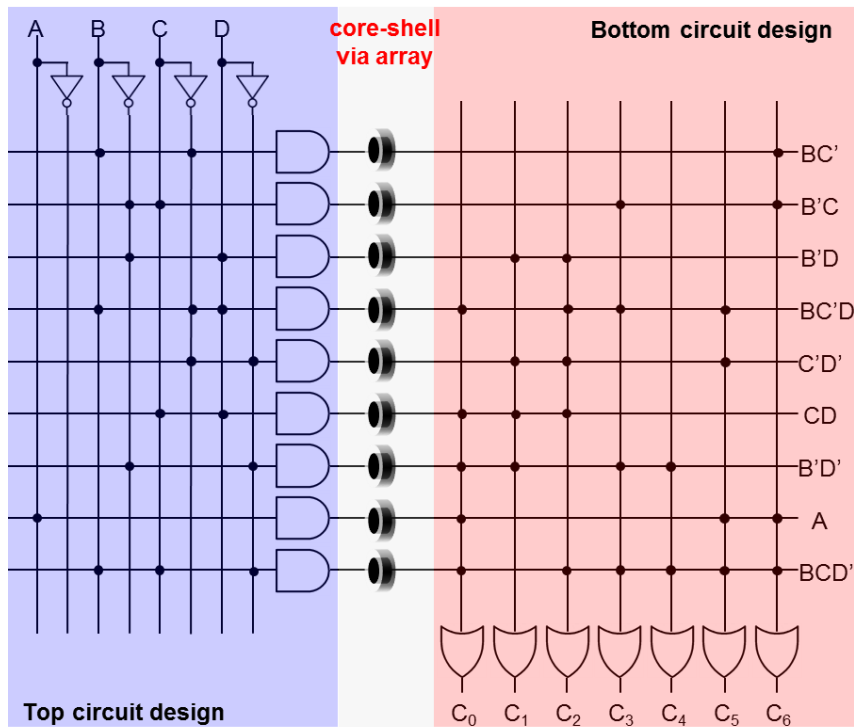


Figure 4.21 | Circuit layout of the BCD to 7-segment binary decoder. A layout design of the decoder is inspired by the circuit diagram of programmable logic array (PLA), consisting of 4 inverters, 9 multi-input AND gates, and 7 multi-input OR gates. For actual demonstration, we used 6 inverters (2 SMDs of 3-channel inverter), 12 2-input AND gates (6 SMDs of 2-channel 2-input AND gates), and 18 2-input OR gates (9 SMDs of 2-channel 2-input OR gates)—total 17 SMDs of 36 logic gates for dimensional standardization ($1.5 \times 1.5 \text{ mm}^2$) of SMDs. For double-side integration, the whole circuit layout is divided into two functional groups (blue: AND part, red: OR part) through 9 core-shell vias [154].

Top circuit fabrication

5. Click the “Export” button to extract printing pattern files, crossover data, and spatial coordinates of arranged logic gates (Figure 4.22).
6. Perform UVO_3 (power = 29 mW cm^{-2}) treatment for 26 min.
7. Fabricate the Ag (ANP corp.) interconnection network of the top circuit by an inkjet-printing process (DMP-2831 inkjet-printer, Dimatix Corp.); anneal at $125 \text{ }^\circ\text{C}$ for 20 min.
8. Form PDMS (20:1 mixing ratio) structures at line-crossing positions (Figure 4.22); cure at $90 \text{ }^\circ\text{C}$ for 120 min.
9. Perform UVO_3 (power = 29 mW cm^{-2}) treatment for 23 min.
10. Fabricate Ag crossover lines by an inkjet-printing process; anneal at $125 \text{ }^\circ\text{C}$ for 20 min (Figure 3.16).
11. Print two kinds of epoxy (Ag epoxy and pure epoxy) at exact positions, the information of which can be obtained from the extracted spatial coordinates of logic gates (step 4) (Figure 3.21).
12. Place proper logic gates; partially cure the epoxy at $130 \text{ }^\circ\text{C}$ for 30 min.
13. Release the prestrain. 2D wrinkles are generated over the whole surface following the pre-distributed strain field (Figure 4.24).

Bottom circuit design and fabrication

14. Flip and biaxially stretch ($\varepsilon_x = \varepsilon_y = 25\%$) the sample; capture the image (inset image of Figure 4.23d).

15. Perform same processes (3–13 steps) with different circuit configurations (Figure 4.23c, d) for the bottom circuit.

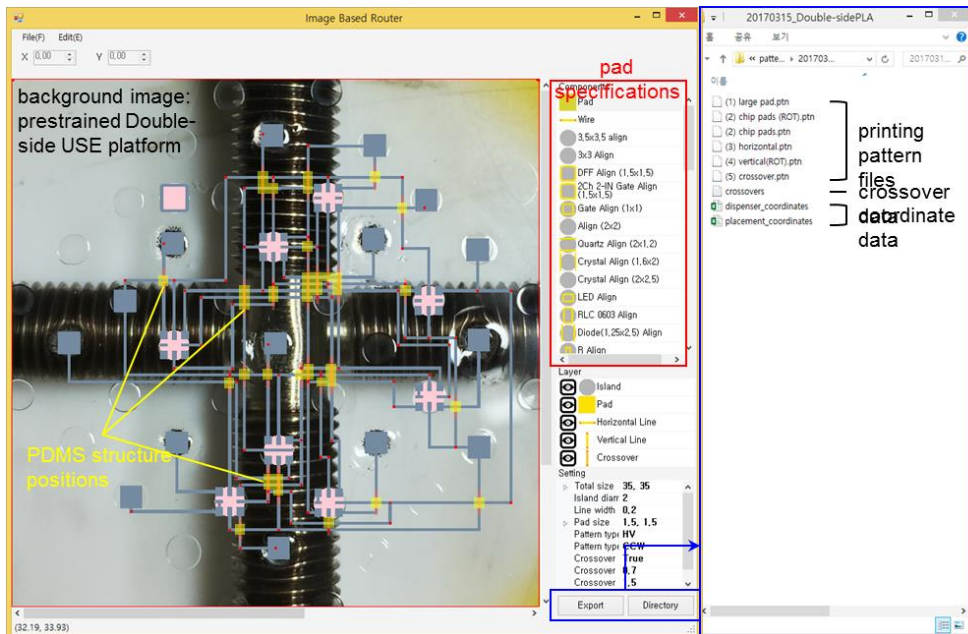


Figure 4.22 | Layout and user-interface of the home-made circuit routing program “Image Based Router” (refer to Figure 3.19) [154].

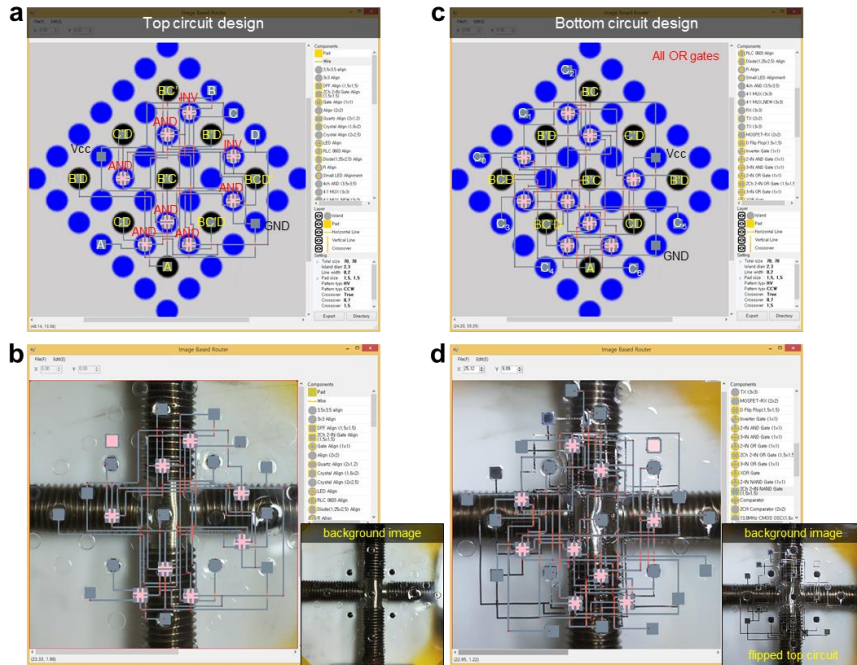


Figure 4.23 | Predefined circuit designs and corresponding circuit routing of the double-side integrated binary decoder. (a and b) Screen shot images of predefined top circuit design implemented on the schematic background image (a) and actual top circuit routing on the captured image of the prestrained double-side USE platform (b). In the top circuit, functional networks highlighted in the blue rectangle in Figure 4.21 is demonstrated. (c and d) Screen shot images of predefined bottom circuit design implemented on the schematic background image (c) and actual bottom circuit routing on the captured image of the flipped top circuit (d). In the bottom circuit (highlighted in the red rectangle in Figure 4.21), 9 core-shell vias provide 9 combinational signals transmitted from 9 AND gates, and combinational networks between them generate individual 7-segment signals (C_0 – C_6) [154].

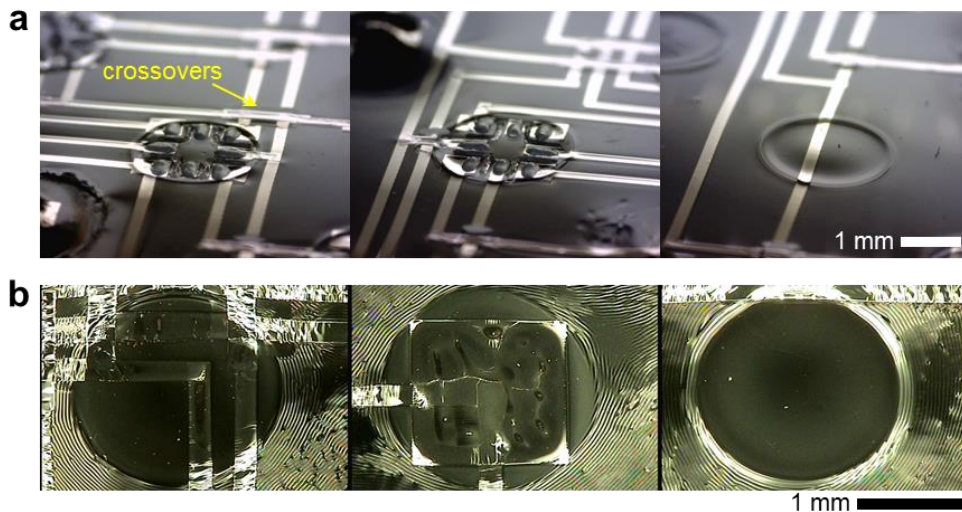


Figure 4.24 | Inkjet-printed Ag interconnection networks before and after releasing prestrain. (a) Optical images of as-printed Ag interconnection network together with crossover lines. (b) Optical images of Ag interconnection network near the PRI areas after releasing prestrain. Due to the strain-free effect, wrinkle formation on printed Ag films and oxidized PDMS surfaces (induced by UVO_3 treatment) was perfectly suppressed inside the PRI areas [154].

Given the miniaturization of SMDs to reduce bulky characteristics of the whole soft system, we used SMD components whose dimension is standardized to $1.5 \times 1.5 \text{ mm}^2$: thus the actual system was comprised of 6 inverters (2 SMDs of 3-channel inverter), 12 2-input AND gates (6 SMDs of 2-channel 2-input AND gates), and 18 2-input OR gates (9 SMDs of 2-channel 2-input OR gates) (Figure 4.23).

For direct comparison, firstly, we fabricated such binary decoder in a single-sided layout (Figure 4.25). In this layout, the same number of SMDs and equal topology of combinational networks as depicted in Figure 4.21 were employed. For effective double-side integration, on the other hand, the whole circuit layout was divided into two functional groups: top circuit design and bottom circuit design (highlighted in blue and red, respectively, in Figure 4.21). In the top circuit, combinations of 8 inputs ($A, A', B, B', C, C', D, D'$) generated 9 output signals ($BC', B'C, B'D, BC'D, C'D', CD, B'D', A, BCD'$) through 12 2-input AND gates. These output signals were connected to 9 core-shell vias, and each signal was transmitted to the bottom circuit through vias. In the bottom circuit that is comprised of 18 2-input OR gates, combinational networks between 9 signals obtained from 9 vias generated individual 7-segment signals (C_0-C_6) (Figures 4.26, also see Figures 4.21 and 4.23). Notably, compared to the single-side implementation (Figure 4.25), applicable area was increased twice due to the double-side area, whereas the number of utilized PRIs and crossover lines was approximately reduced in half through double-side functionalizing.

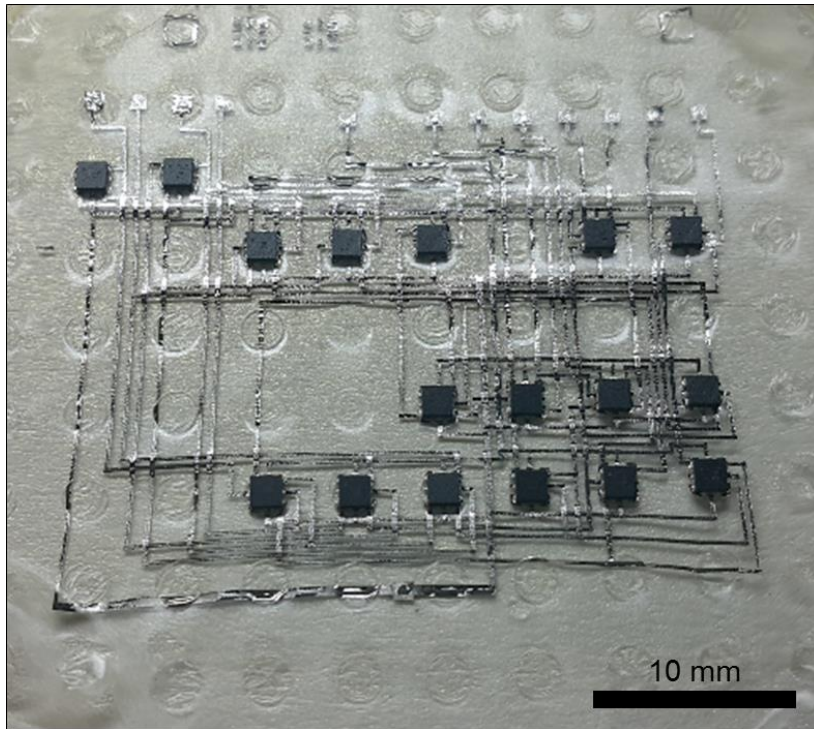


Figure 4.25 | A single-side integrated stretchable BCD-to-7-segment signal decoder fabricated on the PRI-embedded soft substrate where PRIs were arranged in a square-lattice configuration (spacing ~ 4.5 mm) [154].

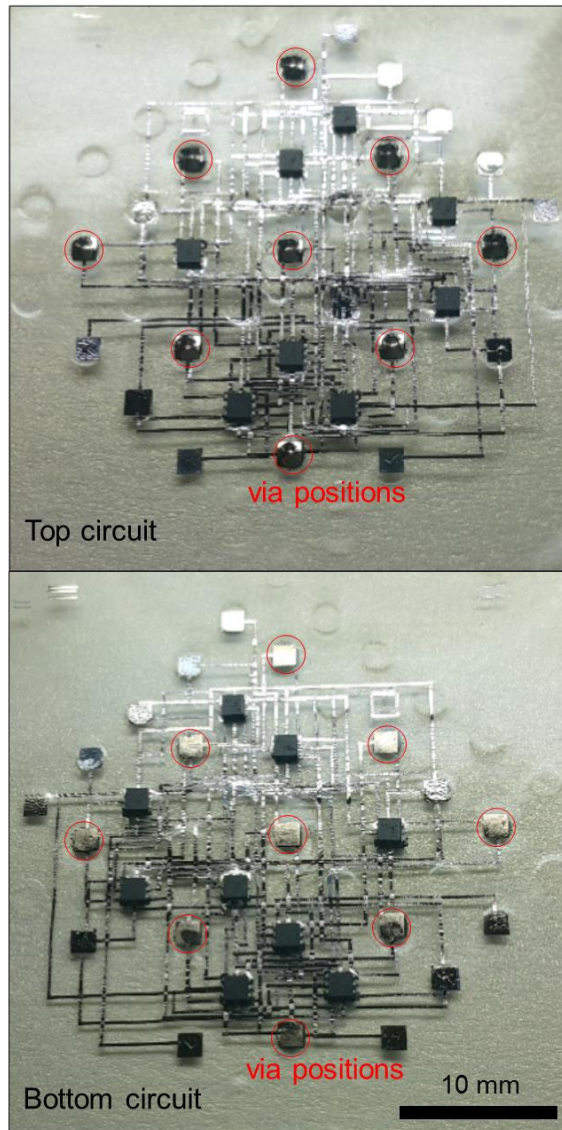


Figure 4.26 | A double-side integrated stretchable binary decoder fabricated on the double-side USE platform. The whole circuit was fabricated by two-step printing-based electronic functionalization processes. Compared to the single-side implementation in a, utilized PRIs were approximately reduced in half (from 17 to 9), and the number of crossover lines was decreased about 42% (From 197 to 114) [154].

Double-side strain-relief property of PRIs in stretchable logic circuits was indirectly advocated by a wrinkle-suppression phenomenon inside the PRI area which verified that both PRI surfaces were elongated not more than a critical strain for wrinkle formation both on oxidized PDMS surfaces (SiO_x , induced by UVO_3 treatment) and inkjet-printed Ag films during an initial prestretching process (biaxial $\sim 30\%$) (Figure 4.27 and Figure 4.24b). This structural peculiarity—wrinkle (or stress) transition around the PRI boundary— permitted smooth alleviation of applied mechanical stress through an accordion-like physical behavior such that contact areas of integrated SMD chips were safely protected from repetitive elongation (Figure 4.27).

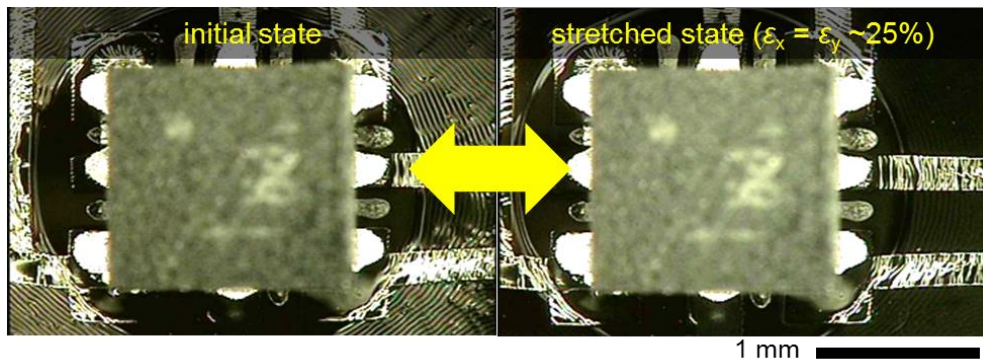


Figure 4.27 | Optical images of a single SMD device ($1.5 \times 1.5 \text{ mm}^2$) supported on a PRI (diameter $\sim 2.3 \text{ mm}$) at an initial state and stretched state (biaxial strain $\sim 20\%$). Inside the PRI was suppressed the wrinkle formation due to the strain-free effect [154].

Monolithically integrated robust core-shell vias were connected to logic devices simply by printing interconnects. Especially, roughened surface property induced by extruded Ni microparticles improved wetting property of Ag ink, and separately defined printed contact pads were added to the both sides of vias for reducing contact resistance. The complete design of double-side integrated stretchable decoder showed good stretchability under a harsh (stretching, twisting) elongation condition (Figure 4.28) without degrading its electrical performance operating at ~1 kHz input signals (Figure 4.29). Furthermore, combinations of reliable high-frequency characteristics of core-shell vias (Figures 4.14–4.17), good conductivity ($\sim 2 \times 10^6 \text{ S m}^{-1}$) of printed interconnects, and operational reliability of SMD logics enabled 1 MHz operation of the stretchable computational logic circuit (Figure 4.30). Although relatively high resistance of printed thin-film (~500 nm) Ag interconnects ($40\text{--}50 \text{ } \Omega \text{ cm}^{-1}$ with 250 μm average line width) and parasitic capacitance components incurred a perceptible degradation in terms of RC delay and signal distortion, we strongly expected that further studies on improving via characteristics (constituents, geometry, etc.) and reducing resistance and parasitic capacitance (or inductance) of inkjet-printed stretchable interconnects would reach stretchable and fully-printable GHz hybrid electronics.

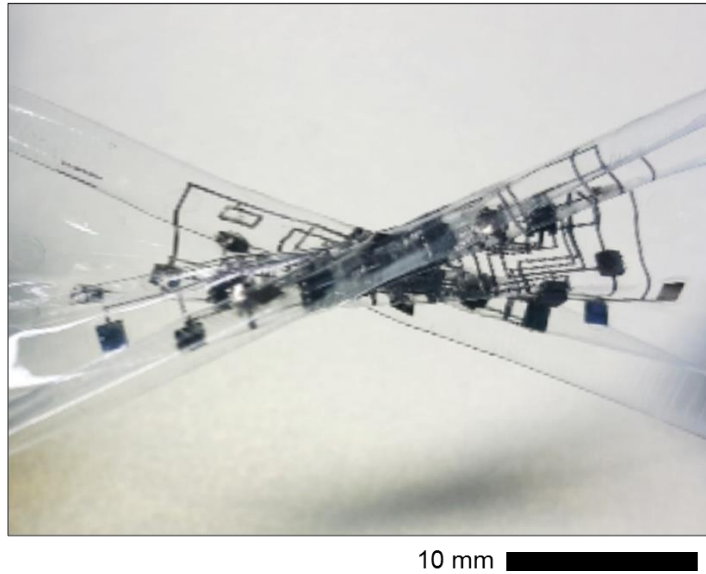


Figure 4.28 | Photograph of the twisted, double-side integrated binary decoder [154].

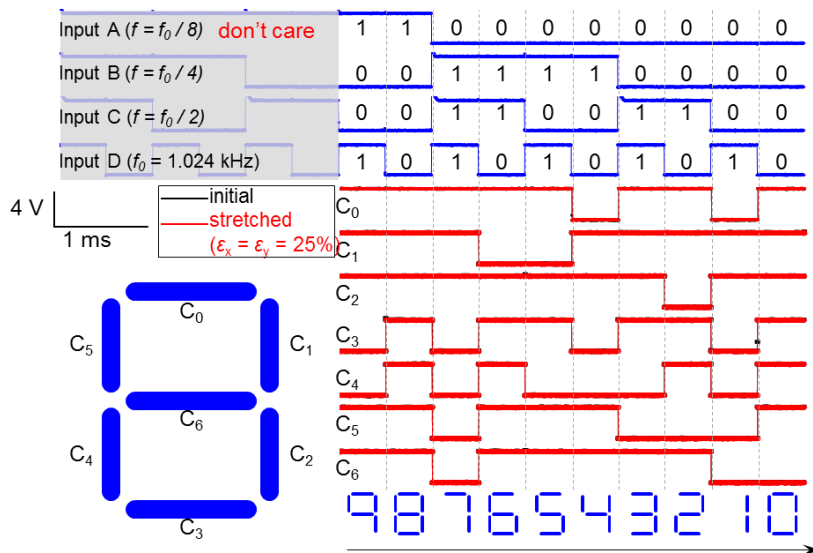


Figure 4.29 | Input/output characteristics of the decoder operating at $f_0 = 1.024$ kHz input. No meaningful degradation of output signals at a stretched state (biaxial strain $\sim 20\%$) was observed [154].

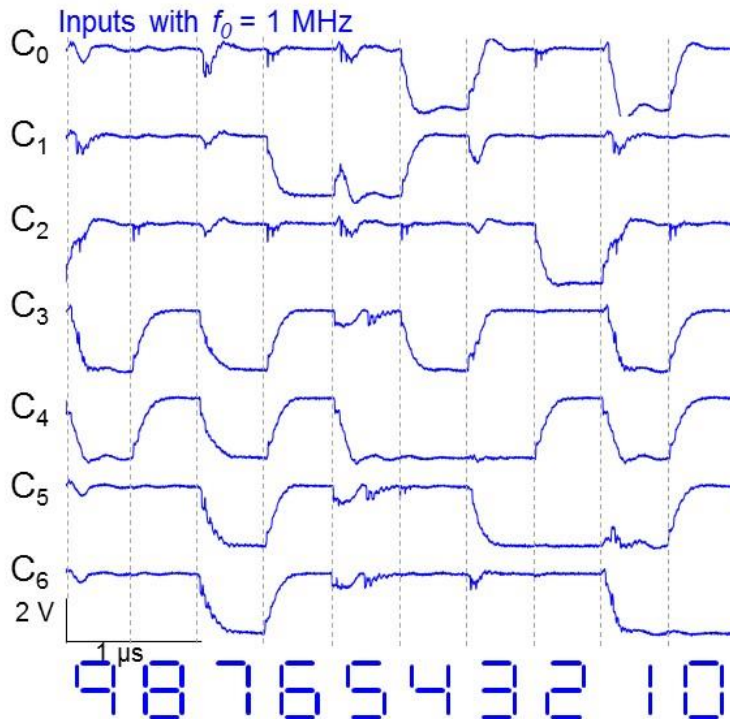


Figure 4.30 | Output characteristics of the decoder operating at $f_0 = 1$ MHz input after several stretching cycles [154].

Chapter 5

Wirelessly Interfaced, Fully-Integrated Electronic Skins for Innervating Soft Robots

In this chapter, soft, fully-integrated electronic skins that enable wireless activation of dormant soft robots through lamination are introduced. First, concept, layouts, and physical designs of fully-integrated e-skins are presented with newly developed physical strain-isolating designs and electrical stretch-tolerant wireless signal interfaces. The e-skin exhibits real-time, wireless innervation process with physical forms that allow intimate contacts to soft robots. In the last part, representative examples of e-skin-mediated consecutive vitalization of several types of soft robotic hands are demonstrated.

5.1 Introduction

Nature and biological organisms have long been a source of inspiration for human being. The most typical features of soft, continuous bodies and associated functions in nature have allowed that significant insights were engrafted into developing unprecedented systems such as soft, skin-like electronic systems [1–3, 36] and soft-bodied machines [174, 175]. Imitating the biological body that features continuous deformation and physical resilience to collisions, in particular, a new class of robots—soft robots—now has proven to be the most attractive machine together with the surge of interest in soft materials. Compared to their hard-bodied counterparts, the soft robot has extended the applicable field of machines with advanced capabilities of adaptable locomotion, movement with extended degree of freedoms, and shape recovery in response to multi-dimensional deformation.

In general, soft robots are primarily comprised of two parts: (i) a main body with bioinspired architectural designs for efficient, adaptable actuation [176–182] and (ii) a driving system based on a suitable underlying mechanism such as wire-driven [176–178], pneumatic and/or fluidic [179–181], light-driven [183], electrically-driven actuation [184], and even combustion [185]. For the main body, numerous combinations of soft materials and designs have established the standard of soft-bodied models appropriate for various environments and applications. Representative examples include designs with embedded tension cables [176–178] and

pneumatic networks, namely “Pneu-Net” [179, 186, 187]. For the driving system, however, an intrinsic dissimilarity in form factors to biological models still remains a great challenge. Indeed, a biological body is vitalized by integral motor neurons that innervate muscles *in vivo*, but the driving systems in existing soft robotic models are rigid, bulky, and physically separated from the soft body, rather than integrated. This discrepancy, rising from the inability to integrate softness both into the robotic body and the “machinery nervous system”, compels the use of bulky wires and physically separated hard control systems for locomotion control [176-179, 186, 188]. Even in untethered designs, the soft body must be equipped with numerous air valves and compressors for a pneumatic controller or rigid printed circuit boards (PCBs) for an electrical controller [180, 181, 185, 187, 189]. These requirements are counterintuitive and limit the potential of soft design. A 3D-printed soft microfluidic design was recently introduced as an alternative, but even this option displayed highly restricted operation speed and function [190].

For the past decade, established strategies for soft electronics have formed the basis of intimate interactions between soft surfaces (usually human skins) and electronics [1–3, 36, 191]. In view of soft robots, it is noteworthy that this novel platform could provide an opportunity to convert the “rigid and bulky” control algorithms into a “soft and miniaturized” form [192]. For the practical use of soft electronics as a driving core of soft robots, the following challenges should be satisfied: (i) complex data processing and

signal interfacing sequences should be stably conducted in the soft platform regardless of physical deformations, (ii) the use of bulky devices (> 3 mm) for soft system implementation needs to be evaded to maximize the potential of soft design, and (iii) additional soft user-interfaces should be established for manipulating the robots in a completely soft scheme. However, there still exist substantial hurdles between existing technologies and such tasks in terms of the inability to design and fabricate the miniaturized form of soft data processing/computing circuits with consideration of stretch-tolerant signal interfaces. Thus, the outcomes have been limited to the fundamental soft human-machine interfaces (HMIs) that mainly controlled rigid interacting objects such as PC [36, 193], a robot arm [194, 195] or drone [196], based on physically separate, rigid control circuits.

In this chapter, we present the first use of integrated soft electronics to an attachable “electronic nervous system” (or an embedded driving system) for soft robots. Suggestive of physical forms of biological nervous systems that are embedded into a body and innervate muscles, a pair of fully-integrated e-skins that feature stretch-tolerant wireless signal interfaces are developed to enable e-skin-mediated activation of dormant soft robots, simply by a lamination process. This “innervating” e-skin concept proposes the most attractive way to activate several types of soft robots through consecutive e-skin-mediated “innervation” (Figure 5.1) [197].

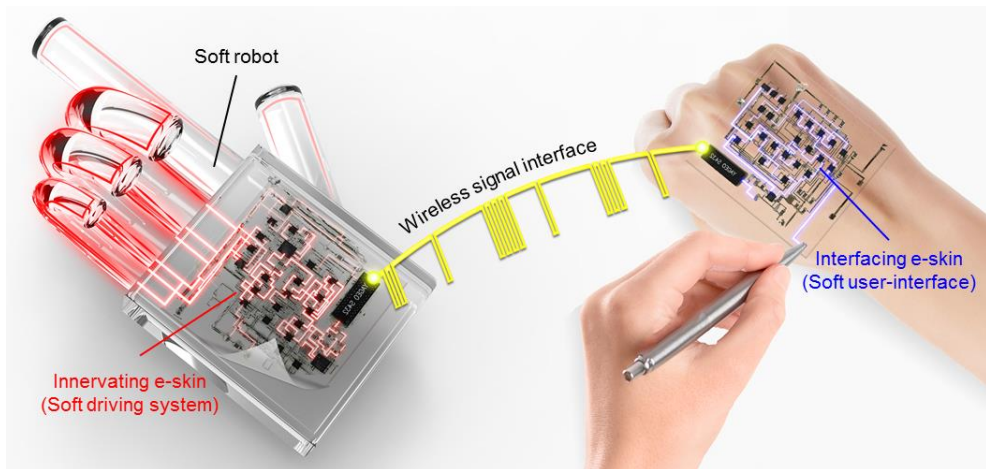


Figure 5.1 | Conceptual illustration of wirelessly interfaced e-skins for innervating a soft robot [197].

5.2 Fabrication, Layouts, and Physical Designs

The concept of fully integrated e-skins and their use in wirelessly innervating soft robots are illustrated in Figure 5.1. Obviating the need for additional rigid PCBs and bulky wires, a pair of fully-integrated e-skins were designed and fabricated for a skin-attachable HMI and a soft driving system for soft robots (Circuit diagrams and integrated components are described in Figure 5.2, 5.3, and Table 5.1). Layouts and an exploded view schematic illustration of the fully integrated e-skins are presented in Figure 5.4 and Figure 5.5, respectively. Both e-skins were comprised of 5 layers: SMDs (ICs, passive components, antenna, etc.), printed strain-isolating structures (Ag epoxy and epoxy), printed double-layer stretchable interconnects (Ag), and a soft foundation (20:1 PDMS). As described in Figure. 5.6, sequential steps of various printing techniques were employed to assemble multiple sets of SMDs directly onto the soft substrate. Total fabrication process was carried out at a prestrained condition ($\epsilon_x = \epsilon_y = 30\%$) (Figure 5.6 and 5.7). Thus the final step of releasing the prestrain generated 2D wrinkles both onto the printed Ag interconnects (Ag/PDMS bilayer) [162] and entire PDMS surface (SiO_x/PDMS bilayer), following the underlying mechanics in stressed bilayer structures (section 3.1.1). This out-of-plane geometry gave the whole e-skins the ability to stretch without electrical degradation (Figure 5.6–5.8).

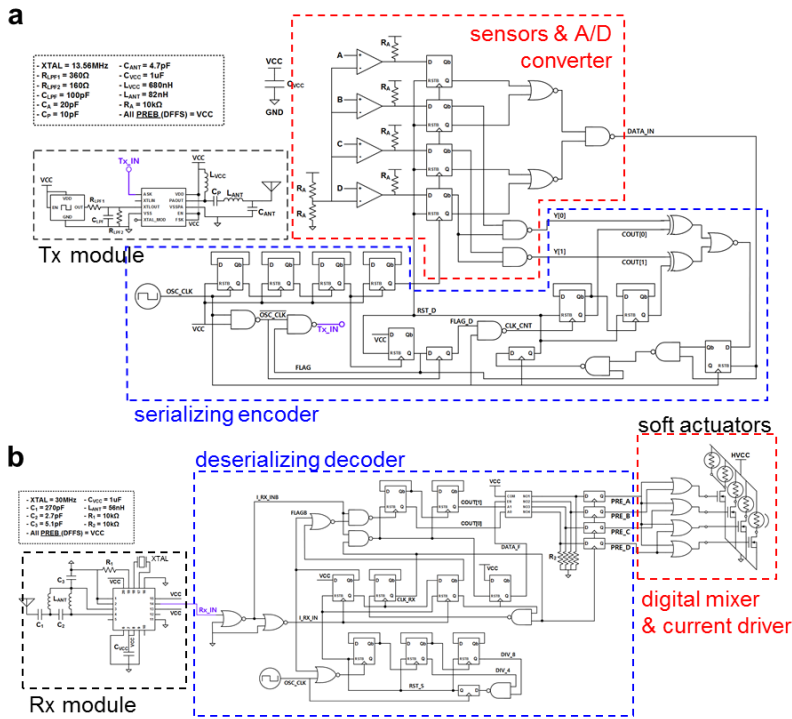


Figure 5.2 | Schematic logic diagrams of the interfacing e-skin (a) and the innervating e-skin (b) [197].

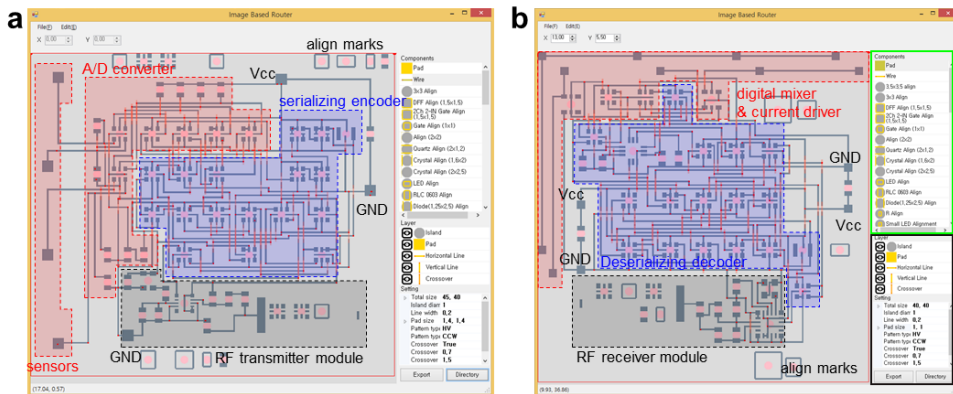


Figure 5.3 | Screenshot images of specific circuit routing for the interfacing e-skin (a) and the innervating e-skin (b) in the home-made circuit routing program [197].

Table 5.1 Specification of SMDs used in e-skins [197].

Device name	Company	Description	Dimension [mm ³]
ANT1204F002R0433A	Yageo	433MHZ CHIP ANTENNA	12.00 × 4.00 × 1.6
MICRF112YMU	Microchip Technology	ASK/FSK 433MHZ Tx IC	2.00 × 2.00 × 0.4
Si4356	Silicon Labs	ASK(OOK)/FSK 315 MHz ~ 917 MHz Rx IC	3.00 × 3.00 × 0.8
NC7WZ86L8X	Fairchild / ON Semiconductor	2CH 2-IN XOR GATE IC	1.60 × 1.60 × 0.55
SN74AUP2G00RSER	Texas Instruments	2CH 2-IN NAND GATE IC	1.50 × 1.50 × 0.6
SN74AUP2G02RSER	Texas Instruments	2CH 2-IN NOR GATE IC	1.50 × 1.50 × 0.6
SN74LVC1G74RSER	Texas Instruments	SINGLE D-FILP-FLOP	1.50 × 1.50 × 0.6
SN74AUP2G79RSER	Texas Instruments	DUAL D-FILP-FLOP	1.50 × 1.50 × 0.6
TLV1702AIRUGR	Texas Instruments	DUAL COMPARATOR IC	1.50 × 1.50 × 0.4
MAX4734ETC+	Maxim Integrated	4:1 MULTIPLEXER IC	3.00 × 3.00 × 0.75
FW3000010	Diodes Incorporated	30MHZ CRYSTAL	2.00 × 1.60 × 0.45
KC2016K13.5600C1GE00	AVX Corp/Kyocera Corp	13.56 MHZ CMOS OSC	2.00 × 1.60 × 0.8
ASTMK-2.048KHZ	Abracon LLC	2.048 KHZ MEMS OSCILLATOR	2.00 × 1.20 × 0.6
SSM6N58NU,LF	Toshiba Semiconductor and Storage	2CH 30V 4A MOSFET	2.00 × 2.00 × 0.75
CL10C2R7BB8NNNC	Samsung Electro-Mechanics America, Inc.	2.7PF 50V CAPACITOR	1.60 × 0.80 × 0.9
CL10C4R7BB8NNNC	Samsung Electro-Mechanics America, Inc.	4.7PF 50V CAPACITOR	1.60 × 0.80 × 0.9
CL10C5R1CB8NNNC	Samsung Electro-Mechanics America, Inc.	5.1PF 50V CAPACITOR	1.60 × 0.80 × 0.9
CL10C100JB8NCNC	Samsung Electro-Mechanics America, Inc.	10PF 50V CAPACITOR	1.60 × 0.80 × 0.9
CL10C200JB8NNNC	Samsung Electro-Mechanics America, Inc.	20PF 50V CAPACITOR	1.60 × 0.80 × 0.9
CL10C101JB8NNNC	Samsung Electro-Mechanics America, Inc.	100PF 50V CAPACITOR	1.60 × 0.80 × 0.9
CL10B271KB8NNNC	Samsung Electro-Mechanics America, Inc.	270PF 50V CAPACITOR	1.60 × 0.80 × 0.9
CC0603ZRY5V7BB105	Yageo	1uF 16V CAPACITOR	1.60 × 0.80 × 0.9
MLG1608B56NJTD25	TDK Corporation	56NH 400MA INDUCTOR	1.60 × 0.80 × 0.95
MLF1608DR68KTA00	TDK Corporation	680NH 70MA INDUCTOR	1.60 × 0.80 × 0.95
ERJ-3GEYJ161V	Panasonic Electronic Components	160Ω 0.1W RESISTOR	1.60 × 0.80 × 0.55
ERJ-3GEYJ361V	Panasonic Electronic Components	360Ω 0.1W RESISTOR	1.60 × 0.80 × 0.55
ERJ-3GEYJ103V	Panasonic Electronic Components	10KΩ 0.1W RESISTOR	1.60 × 0.80 × 0.55

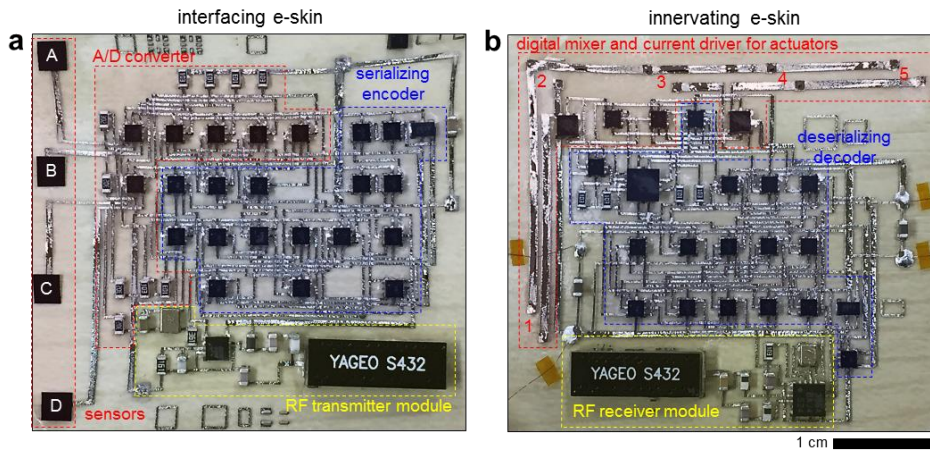


Figure 5.4 | Layouts and functions of e-skins (interfacing e-skin and innervating e-skin). (a) Photograph of the interfacing e-skin (or Tx e-skin) composed of sensors, analog-to-digital (A/D) converter, custom-built serializing encoder, and Tx module. (b) Photograph of the innervating e-skin (or Rx e-skin) composed of Rx module, custom-built deserializing decoder, digital mixer, and current driver for actuators [197].

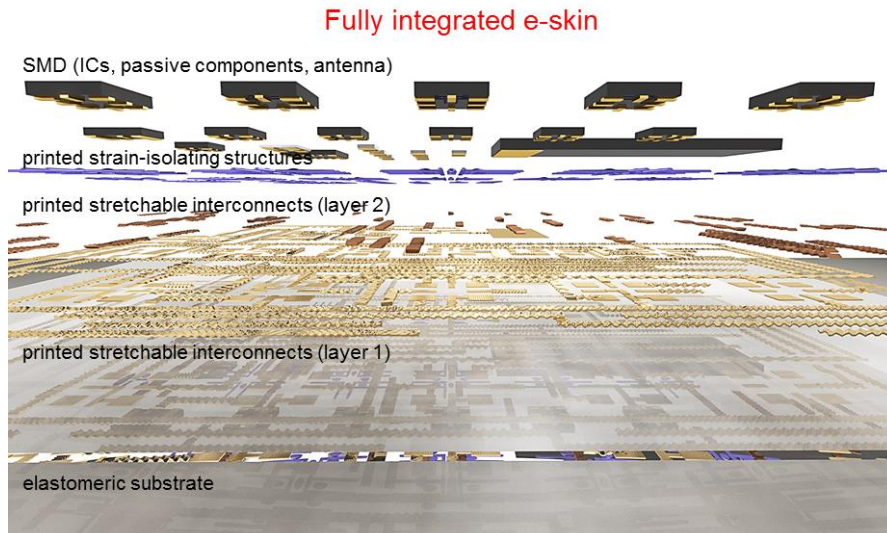


Figure 5.5 | Exploded-view schematic illustration of the fully-integrated e-skins [197].

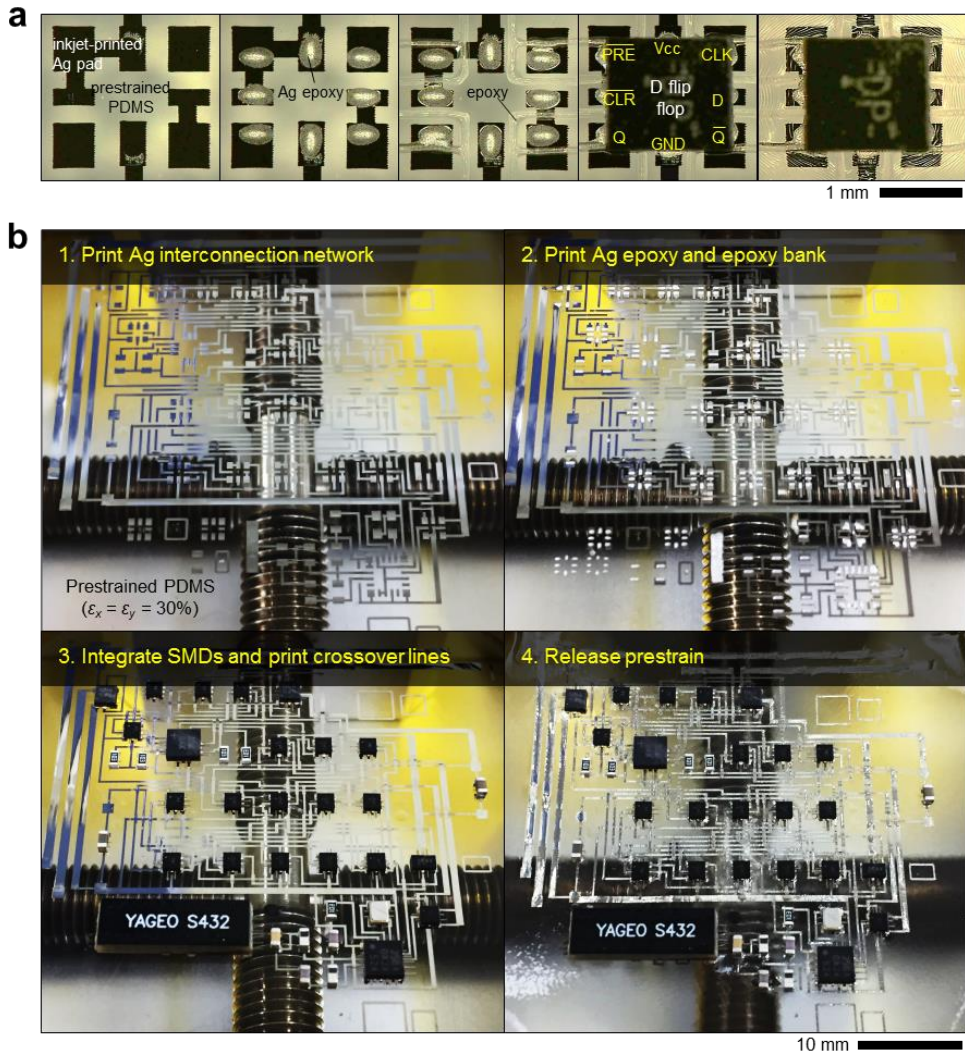


Figure 5.6 | Fabrication process for e-skins. (a) Sequential steps of printing-based SMD assembly. (b) Total fabrication process for e-skins [197].

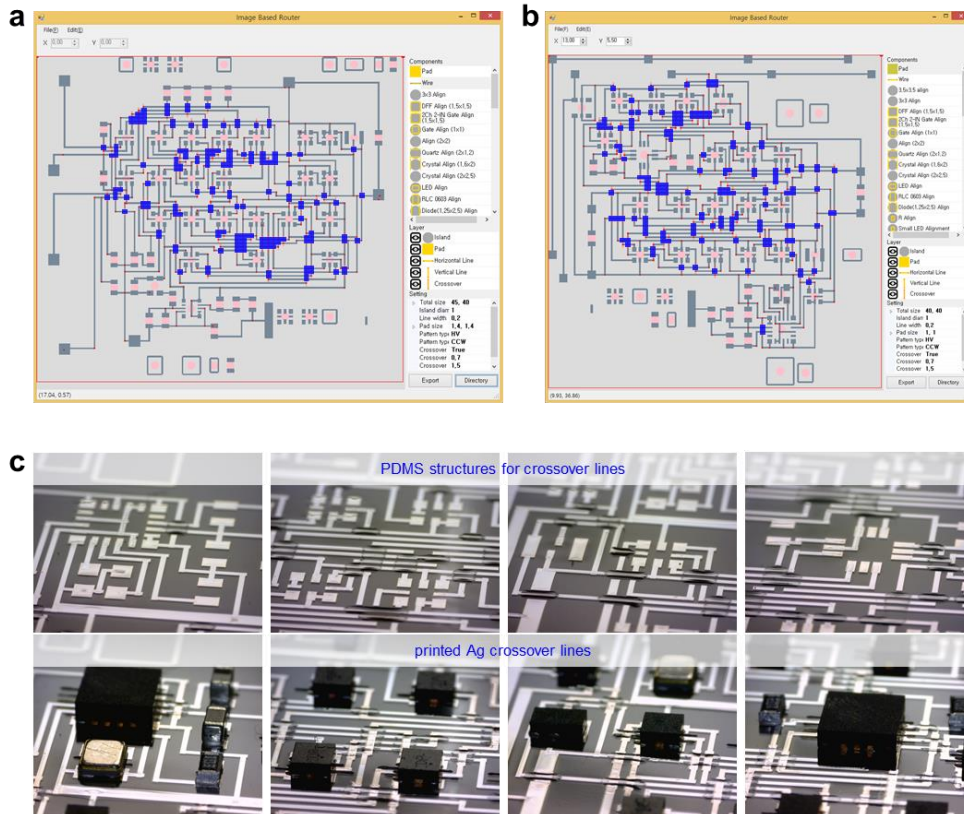


Figure 5.7 | Multilayer interconnection design in e-skins. (a and b) Spatial locations of line-crossing points in the interfacing e-skin (157 crossing points) (a) and innervating e-skin (153 crossing points) (b). (c) Optical images of typical regions that showed the formation of crossover lines [197].

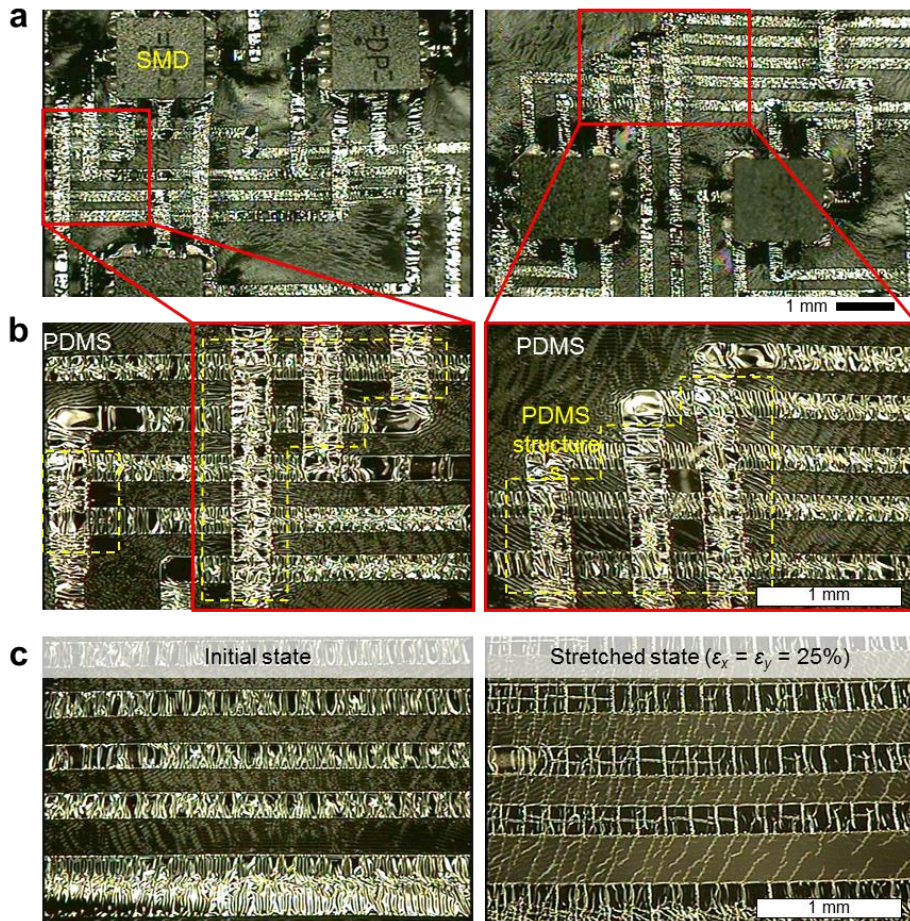


Figure 5.8 | 2D wrinkled morphologies on the entire surfaces of e-skins. (a and b) Large-area optical images (a) and corresponding magnified images (b) of 2D surface wrinkles both on the printed multilayer Ag interconnects and PDMS surface. These out-of-plane geometries are originated from the compressed bilayer structures of Ag/PDMS and SiO_x/PDMS (the SiO_x layer is generally formed by a UVO₃ treatment process during fabrication steps). (c) Optical images of wrinkled and corresponding flattened surfaces (Ag interconnects and PDMS) in response to the biaxial stretching ($\epsilon_x = \epsilon_y = 25\%$) [197].

In addition to the wrinkled interconnects, the geometric design of additive printing-based strain-isolating was exploited for reliable SMD integration. Extended from the basic epoxy patterns described in Figure 3.20 [153, 154], the architectural design of printed epoxy banks was modified to enable gradual strain-relief toward the contact areas of SMDs (Figure 5.9a). Because of large Young's moduli of epoxies (Ag epoxy: ~ 8.24 GPa, epoxy: ~ 8.17 GPa) and robust bonding with SMDs, the combined structure of fully annealed Ag epoxy, epoxy, and assembled SMD was able to serve as a localized rigid island for themselves. Although this island effect generally causes localized stress near the contact boundary, the devised design of parallelized epoxy structures was able to shield these contact areas of assembled SMDs. 3D finite element analysis verified that the effective strain near the contact areas (the distribution profile of which was perfectly matched with the contact pad configuration of standardized 1.5×1.5 mm² 8-UQFN SMDs) could gradually be reduced to a third or a fourth level of the applied biaxial strain (30% in this case) (Figure 5.9). This engineered strain field near the contact areas was indirectly validated by experimental evidence of fading wrinkles in the SiO_x/PDMS bilayer (Figure 5.10). The results suggest that the inclusion of parallelized epoxy structures contributed to the mitigation of the compressive stress, driven by releasing the prestrain, and thus to the formation of well-defined fading wrinkles (Figure 5.10a, b). In contrast, when epoxy structures were not defined, the mechanical stress was entirely applied and localized to the contact areas such that deep wrinkles were formed (Figure

5.10c, d).

Given that SMDs were robustly integrated with the strain-isolating epoxy structures and functionally bridged by multilayer wrinkled interconnects, the fabricated e-skins could stably keep their operating characteristics under repetitive stretching cycles (the operation of whole e-skins is presented in the next section). Furthermore, the entire e-skin layouts showed good stretchability (25–30%) and skin-conformability with the improved adhesion force via incorporating a soft, sticky adhesive layer (PS-2053, Polymer Science, Inc.) (Figure 5.11).

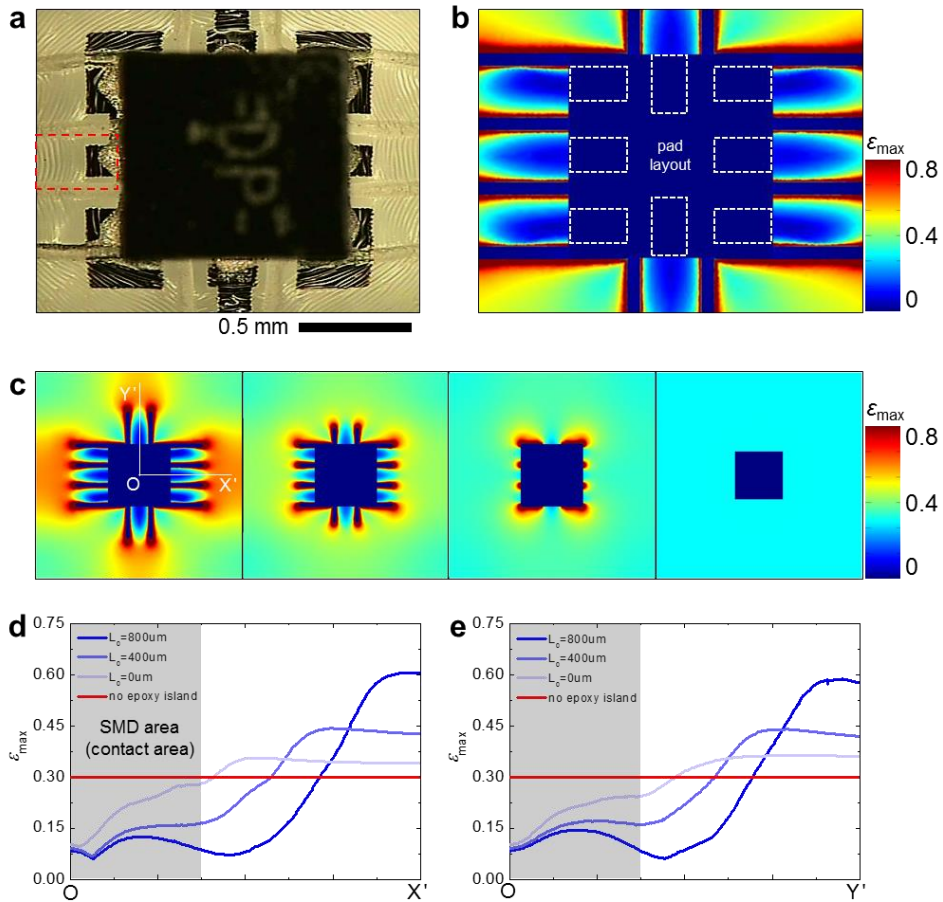


Figure 5.9 | 3D Finite element analysis (FEA) on printed strain-isolating architectures. (a) Optical image of the assembled SMD with printed epoxy architectures. The engineered wrinkle profile indirectly verified the engineered strain field. (b) Strain field distribution (maximum principal strain) in a SMD region obtained from FEA results. (c) Consecutive strain field distribution as a function of a specific length (L_0) of the extended epoxy bank structure (cases: $L_0 = 800, 400, 0 \mu m$, and no epoxy bank). (d and e) Surface strain profile along with the OX' line (d) and OY' line (e), both of which are defined in (c) [197].

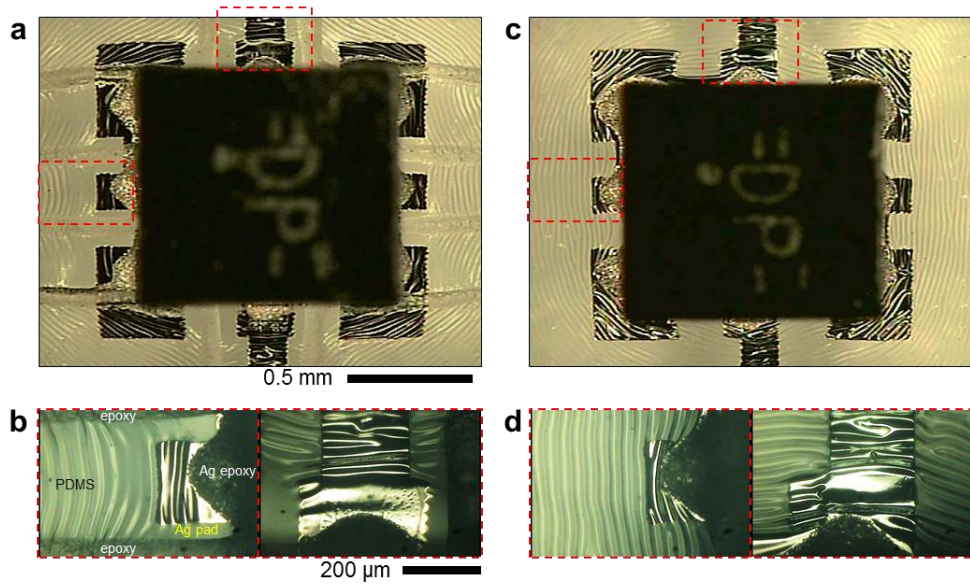


Figure 5.10 | Fading SiO_x/PDMS wrinkles near the contact areas of a SMD. (a) Optical image of the assembled SMD with printed epoxy architectures ($L_0 \sim 800 \mu\text{m}$), exhibiting the engineered wrinkle profile. (b) Magnified optical images of fading wrinkles near the contact areas, driven by gradual strain mitigation as evaluated in Figure 5.13. (c) Optical image of the assembled SMD without extended epoxy architectures ($L_0 = 0 \mu\text{m}$). (d) Magnified optical images of deep wrinkles near the contact areas [197].

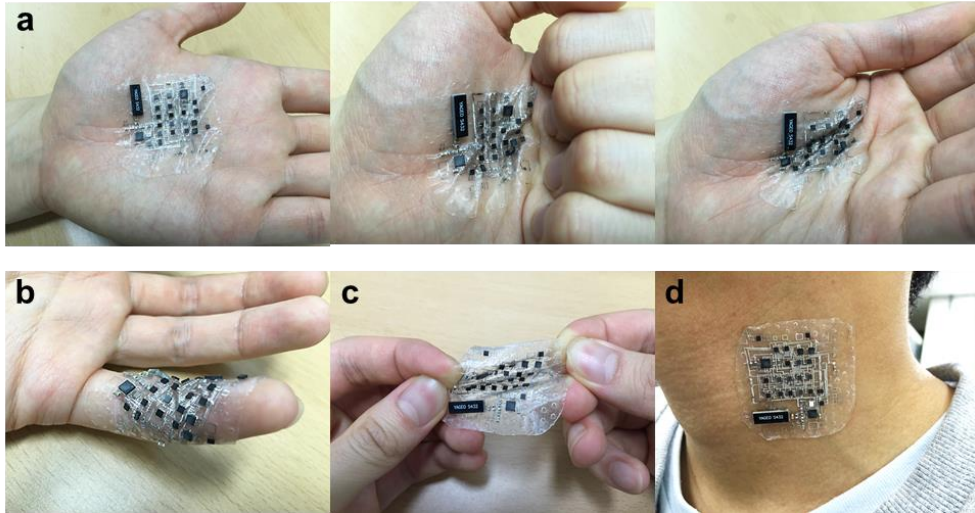


Figure 5.11 | Physical resilience and skin-conformability of e-skins. Soft features of e-skins allowed physical adaptations under multidimensional deformations such as crumpling with sequential hand movements (a), wrapping around a finger (b), stretching (c), and adhering to a neck [197].

5.3 Stretch-tolerant Wireless Signal Interfaces

In addition to the physical designs, the devised signal interfacing mechanism contributed to the stretch-tolerant operation of the e-skins, systemically. To be specific, the following aspects were addressed: (i) digitization of all signal sequences for circuitry tolerance to impedance variations and corresponding voltage drops, (ii) exploitation of the miniaturized scheme for wireless digital modulation (amplitude shift keying (ASK) modulation), and (iii) development of customized encoder/decoder whose modulation mechanism made data sequence tolerant to stretch-induced signal degradation and noise-induced signal distortion.

The e-skins were separated into two distinct parts according to their functions: interfacing e-skin (or transmitting (Tx) e-skin) and innervating e-skin (or receiving (Rx) e-skin). For the interfacing e-skin, the miniaturized functions of pressure sensors, analog-to-digital (A/D) converter, customized serializing encoder, and RF transmitter module were fully integrated into a common soft substrate through the aforementioned printing-based SMD assemblies (Figure 5.4a). On the other hand, the innervating e-skin was comprised of RF receiver module, customized deserializing decoder, digital mixer, and current drivers for in-skin activation of soft robots (Figure 5.4b). The entire wireless signal interfacing flow in the pair of e-skins is schematically described in Figure 5.12. The interfaced signal flow began with quantizing the parallelized analog output signals of four pressure sensors

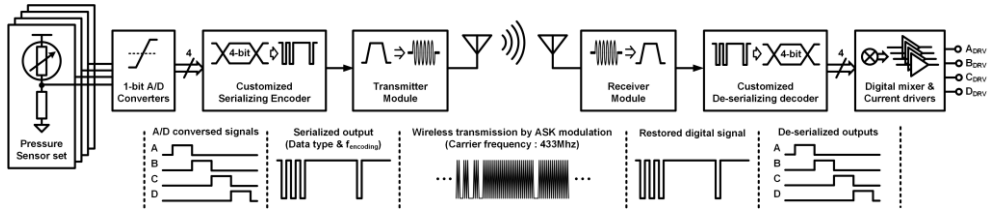


Figure 5.12 | Schematic diagram of an entire wireless signal interfacing flow in the pair of e-skins (interfacing and innervating e-skins) [197].

(A–D) in the interfacing e-skin. For signal quantization, each piezoresistive pressure sensor ($\sim 2 \times 2 \text{ mm}^2$, Velostat, Adafruit) was integrated with a voltage-dividing resistor (3 k Ω) and a set of IC devices, including a comparator, to generate a digital output signal (Figure 5.13a). Particularly, we used a metal rod to easily apply the pressure to the sensors; the tip of which was connected to the power (V_{cc}) for effective voltage dividing. Given the resistance profile and corresponding V_{sensor} (defined in Figure 5.13a) curve of the pressure sensor, reference voltages (V_{ref}) could be properly adopted for quantizing levels with consideration of a range of V_{sensor} (Figure 5.13b). Although the number of quantized levels could be diversified from 1-bit (2^1) to n-bits (2^n) for target applications, in this work, we handled only a 1-bit signal quantization for each pressure sensor based on the specific V_{ref} ($\sim V_{cc}/2$, red dot line in Figure 5.13b). Consequently 4 DOF signal modulation was achieved.

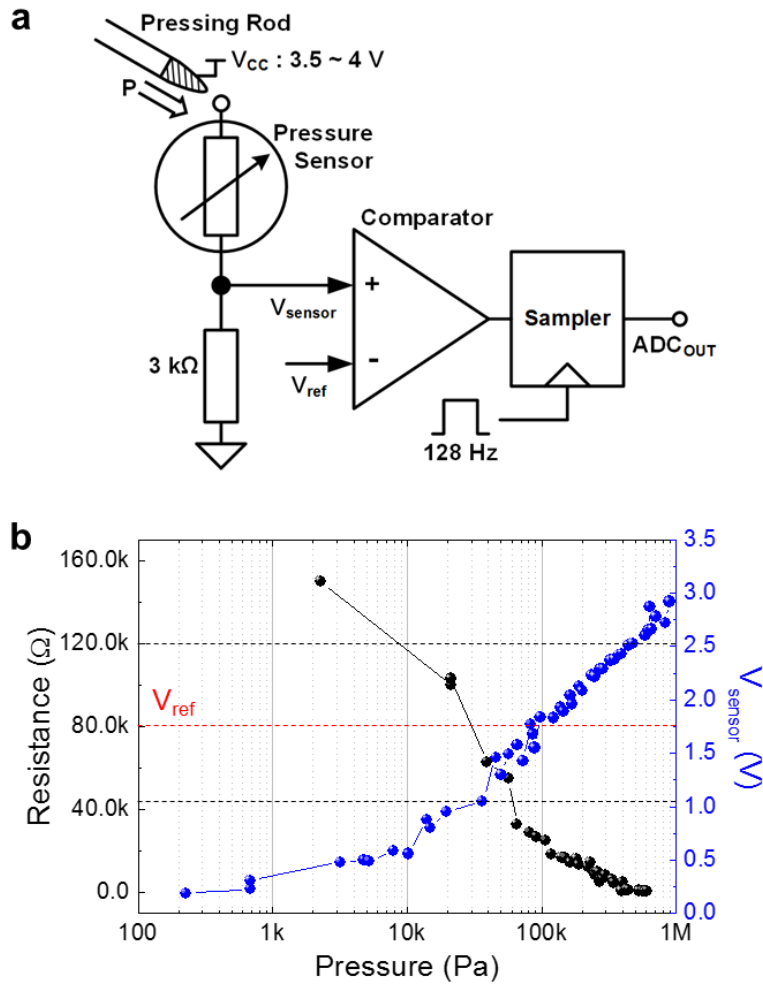


Figure 5.13 | Signal quantizing module in the interfacing e-skin. (a) Unit circuit diagram for signal quantization (A/D converter module). The circuit is composed of a sensor, a voltage-dividing resistor (3 k Ω), a comparator, and a sampler (D flip flops). V_{sensor} is defined as the divided voltage and thus could be controlled just by varying the voltage-dividing resistor (3 k Ω in this case). (b) Resistance and V_{sensor} profiles of a piezoresistive pressure sensor (Velostat, Adafruit) as a function of the applied pressure [197].

The 4-bit quantized signals were then encoded through the customized serializing encoder. Summarized in Figure 5.14 is the specific encoding /decoding principle for stretch-tolerant wireless signal interfacing. The key idea is to generate periodic information of input data (A–D) and encoding frequency (related to the system clock) in a serialized form (top part in Figure 5.14). The input data information was encoded into the number of negative edges (totally 5 states, 1: default, 2: A, 3: B, 4: C, 5: D), and the encoding frequency information was represented by the periodic negative pulses ($128 \text{ Hz} = 1/16 \times \text{system clock (2,048 Hz)}$). The specific encoding frequency of 128 Hz was selected to guarantee the ability to differentiate between the sequence of sensor touches (maximum frequency $< 10 \text{ Hz}$). Finally, the encoded signal was converted to the RF signal (carrier frequency = 433 MHz) in the RF transmitter module, and spread out through an antenna.

Based on the transmitted RF signal, the RF receiver module in the innervating e-skin then restored the digital signal which was the same profile as the encoded signal. Subsequently, the restored encoded signals were decoded through the customized deserializing decoder whose modulation mechanism was also presented in Figure 5.14. To be specific, the decoder generated parallelized 4-bit output signals based on the stretch-tolerant sampling with the involved clock information. Interestingly, the digital mixing of such output signals driven by co-integrated fundamental logics offered an opportunity for diversifying the output signal combinations for programmable, multi-stage movements of soft robots (4 DOF in this case)

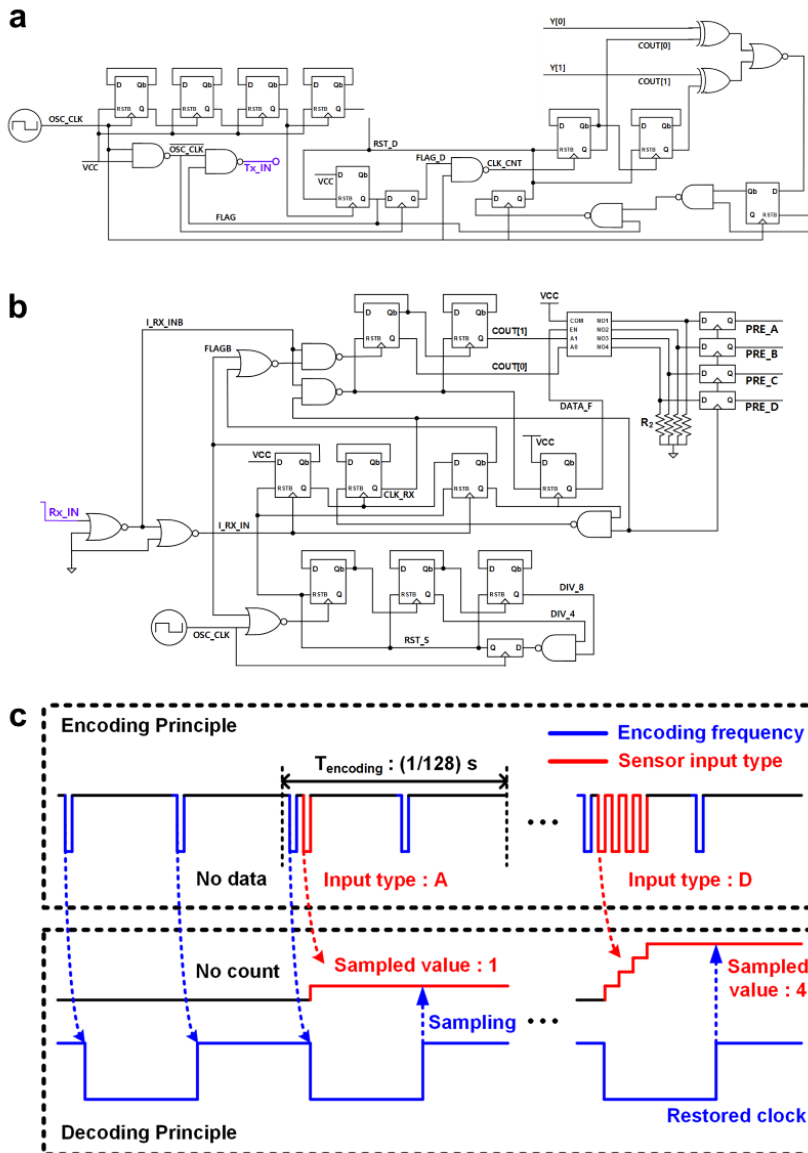


Figure 5.14 | Customized serializing encoder/serializing decoder. (a and b) Schematic diagram of the encoder (a) and decoder (b). (c) Encoding (decoding) mechanism of customized serializing encoder (serializing decoder) [197].

(Figure 5.15). Furthermore, the inclusion of current drivers (NMOSs) provided the capability for gate-controlled current modulation using an independent power source (~13–20 V) for reliable operation of the soft actuators.

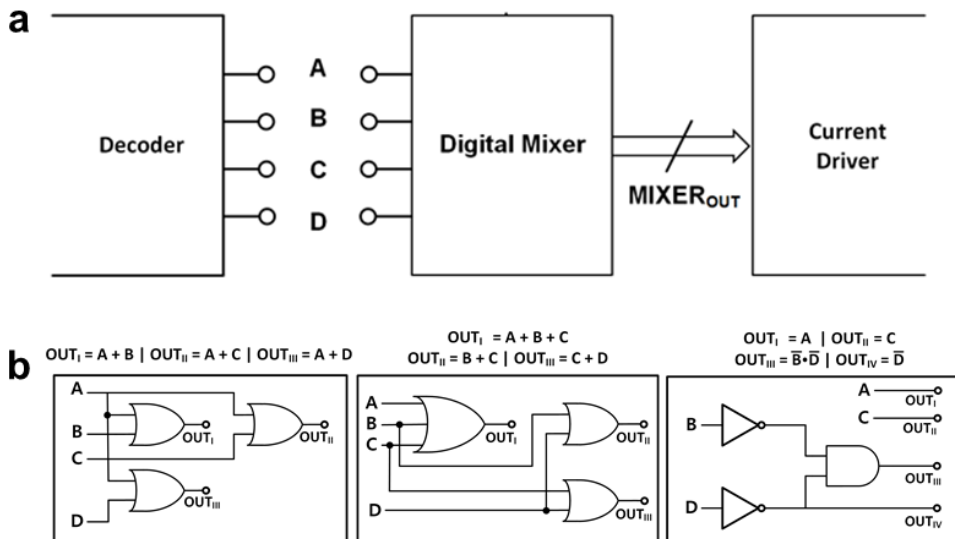


Figure 5.15 | Digital mixing of output signals in the innervating e-skin. (A) Miniaturized schematic of the innervating e-skin. (B) Examples of digital mixing of output signals. Inclusion of a few logic gates (OR, AND, inverter gates), connected to the output terminals of the decoder, can lead to the versatile combinations of output signals. Examples include the output sets of (A+B, A+C, A+D), (A+B+C, B+C, C+D), and (A, C, B'D', D'), and further combinations can be easily addressed. The output combination of (A, A+B, A+C, A+D) is used in this work [197].

In addition to the stretch-tolerant feature of the devised encoding mechanism, the validity for reliable wireless signal interfacing was also investigated in terms of the fidelity of data transmission. Given the inherent features of ASK modulation that is prone to be degraded by noise when the amplitude threshold is not settled on a proper level, we constructed artificially noise-defined environment for a reliability test. The experimental setup was composed of e-skins (Tx and Rx e-skins), a field-programmable gate array (FPGA) board, and a noise source. In particular, the e-skins and a noise source were arranged in a line, in the following order: Tx-Rx-noise) (Figure 5.16). A RF transmitter module and a function generator (AFG3102C, Tektronix) comprised the noise source (PCB type), generating 433 MHz noise RF signal whose amplitude was randomly changed. This artificial noise signal was spread out toward the e-skin pairs and affected the data transmission yield (Y_{data}).

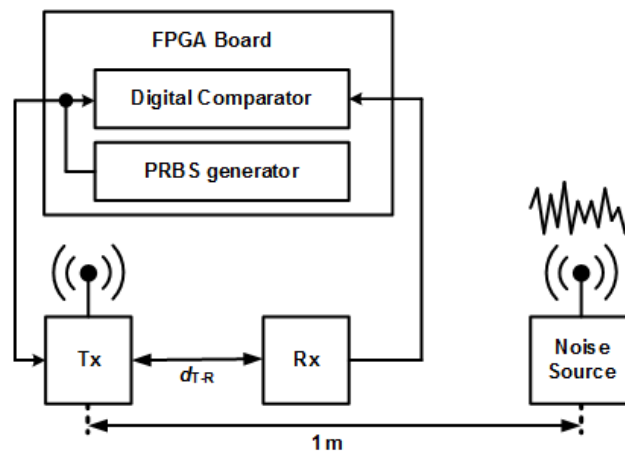


Figure 5.16 | Schematic of an experimental setup for a reliability test of wireless communication between e-skins [197].

To compare Y_{data} between non-encoded (only RF transmitter and RF receiver modules without encoder/decoder) and encoded cases (fully integrated modules), two distinct random signals (pseudo-random bit sequence, PRBS) were generated from the FPGA board and entered into both non-encoded and encoded Tx e-skins. As illustrated in Figure 5.17, in case of the non-encoded e-skin pair, 1-bit PRBS pattern with the updating cycle of 1/2048 s was generated and directly entered into the RF transmitter module. By contrast, for the encoded e-skin pair, randomized 4-bit signals (A–D) with the updating cycle of 1/128 s were converted into 1-bit serialized, periodic five-state signals (default, A–D) through the integrated A/D converter and encoder. Supported by the Fourier analysis on both signals (Figure 5.18), the periodicity of the encoded random signal was distinctly verified in comparison with the non-encoded random signal. For Fourier analysis, 2^{20} sampled data were used in both cases, and the sampling frequency was 4096 Hz (two times the system clock).

Given these typical waveforms of the non-encoded and encoded signals, Y_{data} was explored as a function of distance between the Tx and Rx e-skins ($d_{\text{T-R}} = 0.1\text{--}0.95$ m) to figure out the noise-tolerant characteristic and associated communication reliability (Figure 5.19). For encoded signals, it was noted that the well-regulated periodicity helped the amplitude threshold settle at an optimal level, thus making the wireless interface noise-tolerant and ultimately achieving high-quality Y_{data} (the minimum Y_{data} was $\sim 98.63\%$ measured at $d_{\text{T-R}} = 0.95$ m, the nearest region to a noise source). On the other

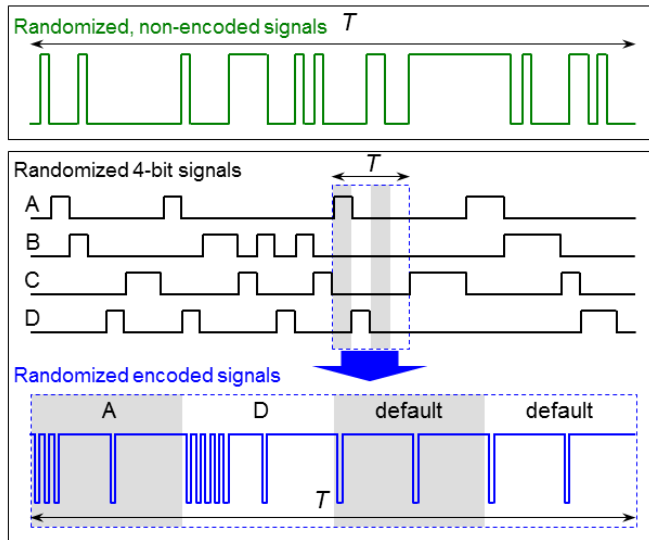


Figure 5.17 | Typical waveforms of randomized, non-encoded/encoded signals [197].

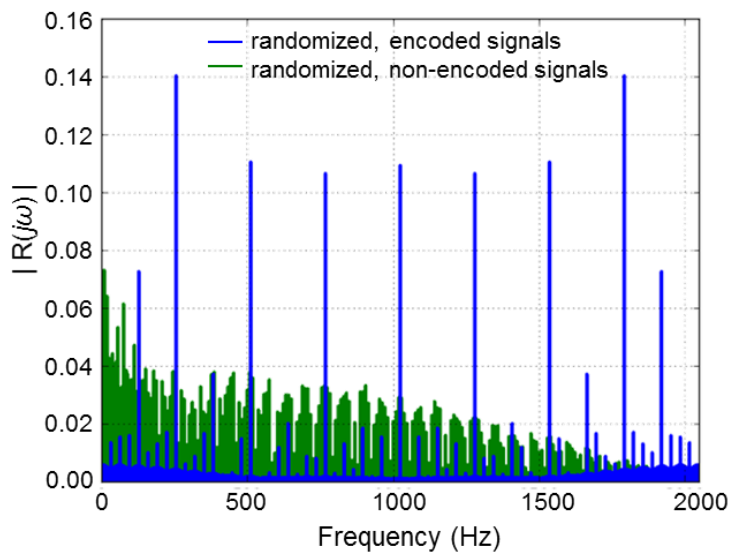


Figure 5.18 | Fourier analysis data on randomized, non-encoded and encoded signals [197].

hand, the Y_{data} profile of the non-encoded data suggested that non-periodic, randomized signals impeded the settling of the threshold, thus leading to an initial reduction in Y_{data} (~95%) at $d_{\text{T-R}} = 0.01$ m. Furthermore, instability coming from the unsettled threshold exacerbated the impact on Y_{data} along with the augmented noise level (increasing $d_{\text{T-R}}$) such that Y_{data} decreased to ~70% at $d_{\text{T-R}} = 0.95$ m (0.05 m apart from a noise source).

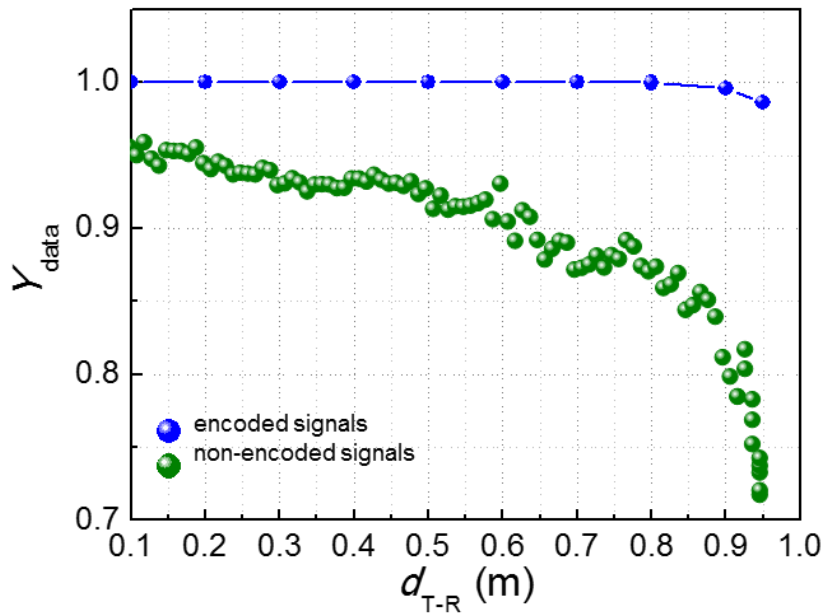


Figure 5.19 | Data transmission yield of non-encoded and encoded signals as a function of $d_{\text{T-R}}$ [197].

Real-time in-skin signal modulation and specific encoded signal profiles in each state of pressure sensing are explored in Figure 5.20. Short-term continuous monitoring (20 s) of the encoded signals in the interfacing (just after encoding, blue line) and innervating (just after restoring from the RF receiver module, red line) e-skins verified that the periodic signal profile, normally a stable 128 Hz pulse at a default state, became locally dense in response to a series of sensor touches (A–D) due to the variation in the number of negative edges (Figure 5.20a). The enlarged views of encoded waveforms—measured from both e-skins— in each state advocate that a complete set of variable negative pulses (1 to 5) was clearly defined according to the input type (default, A–D) without both stretch (25% biaxial strain)-induced degradation and meaningful signal delay ($\sim 12.6 \mu\text{s}$) between both e-skins (Figure 5.20b and 5.21). Moreover, the synchronized sampling and corresponding decoding capability with the restored clock information, as described in Figure 5.14c, was investigated by analyzing the real-time responses of the 4-bit decoded signals to dynamic sequences of the serialized, randomly encoded signal (Figure 5.22). The results suggested that well-defined pulse sequences were generated for 4 different states (A–D), exhibiting accurate synchronized timing with the input sequences.

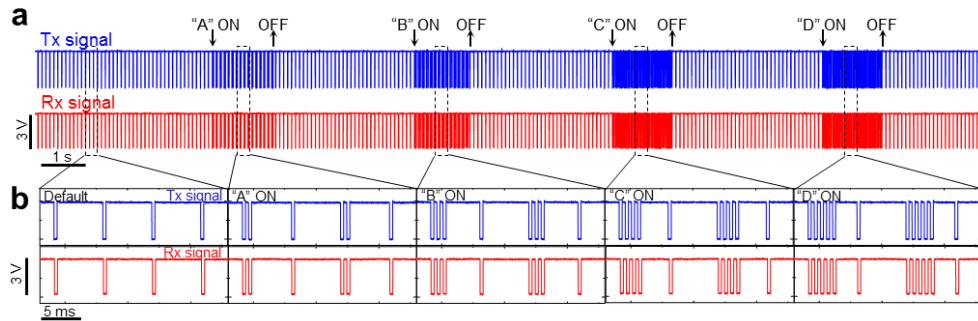


Figure 5.20 | Real-time in-skin signal modulation and specific encoded signal profiles in each state of finger touches. (a) Short-term continuous monitoring (20 s) of encoded signals in the interfacing and innervating e-skins in each state. (b) Enlarged view of encoded waveforms in each state (default, A to D) [197].

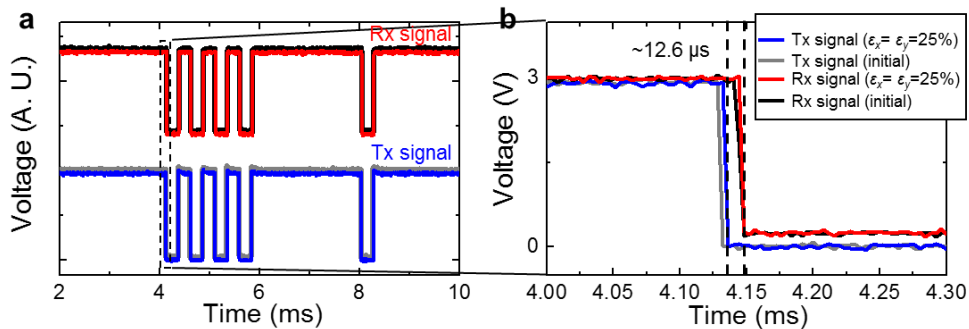


Figure 5.21 | Stretch-tolerant feature of the wireless signal interfaces between e-skins. (a) Typical transmitting (blue and gray lines, measured just after the signal encoding process in the interfacing e-skin) and receiving (red and black lines, measured just after the signal restoring process in the innervating e-skin) waveforms in the “C” state. The encoded signals show the stretch-tolerant feature in both e-skins (25% biaxial strain). (b) Magnified view of the waveform in a. Wireless communication delay of $\sim 12.6 \mu\text{s}$ is observed without meaningful degradation under 25% biaxial strain [197].

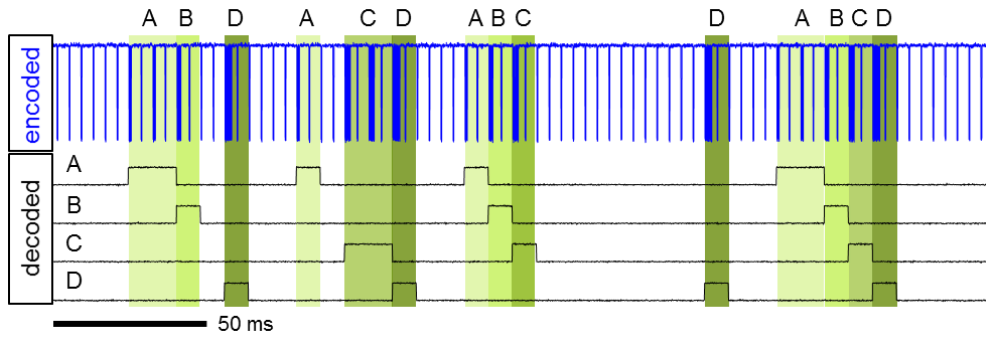


Figure 5.22 | Real-time decoding process of serialized, encoded signal sequences in response to dynamic sequences of 4-bit random signals [197].

5.4 E-skin-mediated Wireless Innervation of Soft Robots

The novel concept of wireless, user-interactive “in-skin” signal interfacing in fully-integrated e-skins was finally used to achieve wireless innervation of soft robots. Given the fully-printed designs of e-skins, the inclusion of a facile writing process of thin film actuators and a lamination process proposed the potential scheme for realizing fully-printed, e-skin-driven, soft robots—accomplishing softness both for the driving circuit and the body. Sequential frames of schematic (Figure 5.23a), photographic (Figure 5.23b), and thermographic images (Figure 5.23c) present the simple steps of innervating process. First, we prepared the initially dormant soft body (~200 μm thick transparent PDMS hand in this case). Subsequently, we drew PEDOT:PSS thin films (resistance in each sample ~1.3–1.8 $\text{k}\Omega$) at appropriate positions by an inkjet-printing process (Figure 5.24 for a specific design and characterization). Given that the PEDOT:PSS/PDMS bilayer tends to be actuated in response to Joule-heating-induced water desorption [198], these predefined patterns were designed to have a role in “artificial muscles” that could be innervated and thus actuated by an electronic nervous system. In the last step, just by attaching the innervating e-skin (Rx e-skin) onto the soft hand and applying proper power to both e-skin (3.5–4 V) and actuators (13–20 V), we accomplished dynamic actuations in this integrated soft robotic hand in conjunction with sequential finger touches in the interfacing e-skin.

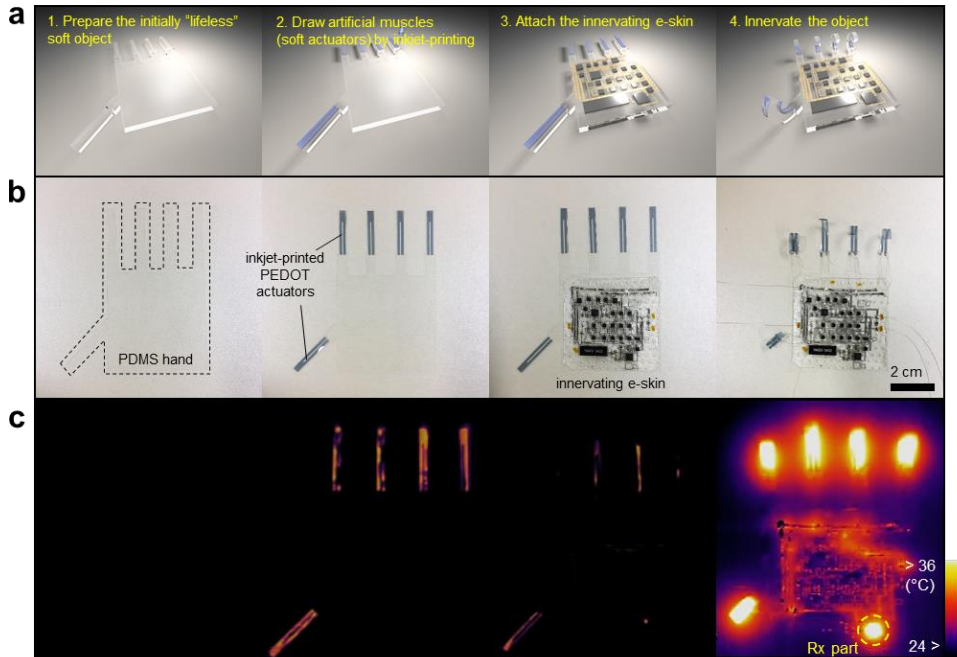


Figure 5.23 | E-skin-mediated wireless formation of an electronic nervous system onto a soft robot. (a) Schematic, (b) photographic, and (c) thermo-graphic images of process steps for e-skin-mediated wireless innervation [197].

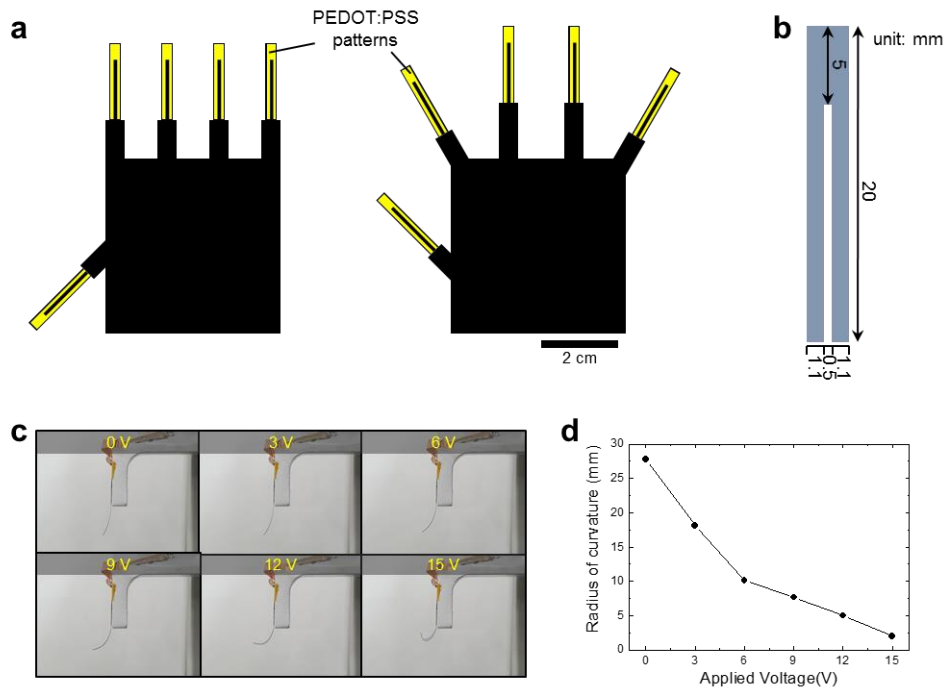


Figure 5.24 | Inkjet-printed PEDOT:PSS thin-film soft actuators. (a) Schematic design of the fabricated soft robotic hands with specific positions of soft actuators (or artificial muscles). (b) Schematic design of the printed PEDOT:PSS pattern. (c) Sequential optical images of the actuation mode of an individual bilayer (PEDOT:PSS/PDMS) soft actuator. (d) Curvature data of the individual soft actuator as a function of the applied voltage [197].

The total operation of the e-skin pair and corresponding versatile manipulation of the soft robotic hand were visualized by thermographic imaging (Figure 5.25). Considering that the bypassed electric current generated Joule heat throughout the entirety of the e-skins (even fine interconnects) and actuators, the mapping images showed what appeared to be the operating interfacing e-skin (HMI) (Figure 5.25, top) and the “innervated” nervous system in the soft robotic hand (Figure 5.25, bottom). The point of interest here is that the state of touch sensing was clearly discriminated by the movement of hotspots (resistor regions, highlighted as yellow circular lines) (Figure 5.25, top). In addition, it is noteworthy that specific regions near the RF transmitter/receiver module were strikingly heated as the “heart” of the e-skins, validating the wireless communication between the e-skins. When receiving the modulated signals via wireless communication and decoding them, the embedded innervating e-skin started to activate the soft robotic hand, creating 4 DOF motion states matched to the input types in the interfacing e-skin (Figure 5.25, bottom). Besides, a set of motion states and bending curvature of the robotic fingers were easily controllable by the strategy of mixing digital output signals (Figure 5.15) and changing the bias voltage of the soft actuators (Figure 5.24 c, d), respectively. Also, it is worth noting that the current flow distribution in the operating electronic nervous system of the soft robotic hand varied according to which finger was operated, as if actual movements of human fingers are controlled by the operation of involved motor neurons (Figure 5.25, bottom). A series of

reliable operations of the integrated soft robotic hand under sequential multi-dimensional deformations like bending, stretching, and folding supported the proposed distinct advantages of complete softness in both the body and driving circuit (Figure 5.26).

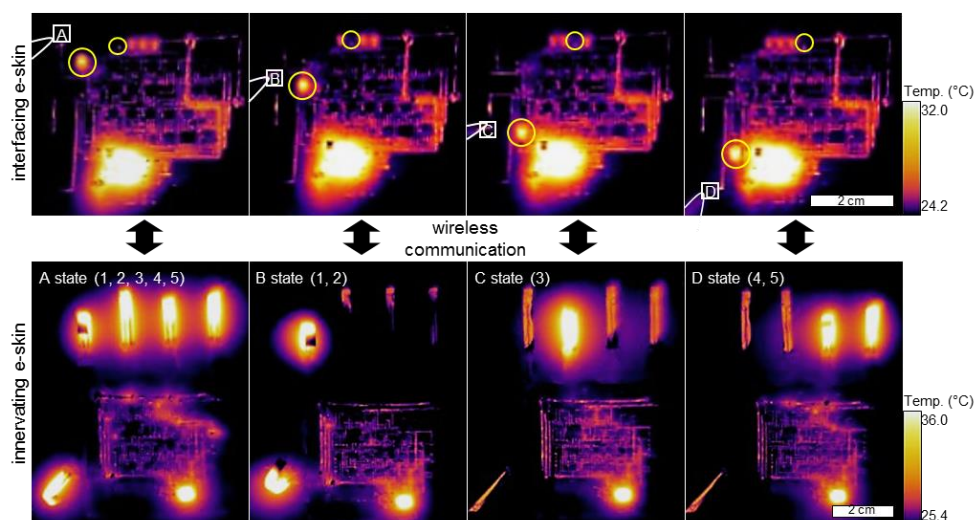


Figure 5.25 | Thermographic images of the operating interfacing e-skin (top) and innervating e-skin (bottom) in each input state. Based on the specific digital mixing, each input state was programmed to activate different robotic fingers (A: “1, 2, 3, 4, 5”, B: “1, 2”, C: “3”, D: “4, 5”). Because of the larger resistance of the PEDOT:PSS thin films ($\sim 1.3\text{--}1.8\text{ k}\Omega$) than Ag interconnects ($\sim 20\ \Omega$ for the same length), the prevailing Joule heat was clearly observed near the actuator region [197].

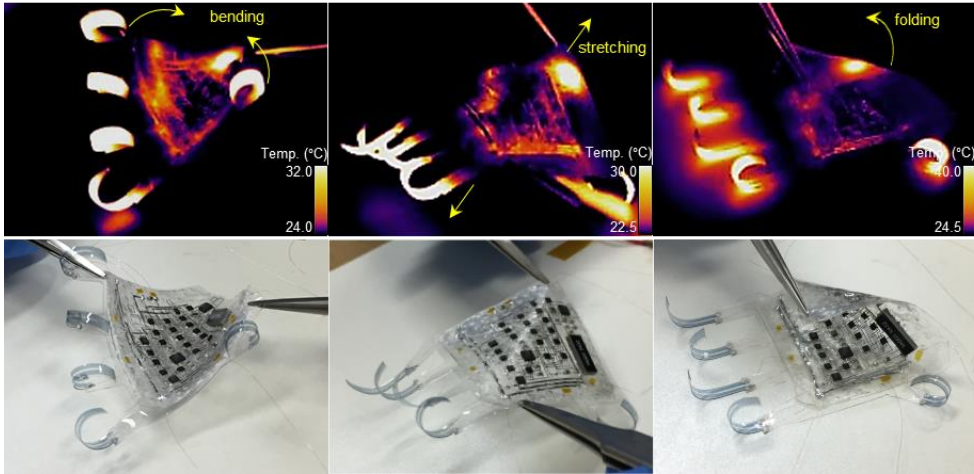


Figure 5.26 | Sequential thermographic and corresponding photographic images of the innervated soft robotic hand under physical deformations such as bending (left), stretching (middle), and folding (right) [197].

Salient features of the e-skin-mediated wireless innervation through the lamination process proposed the simplest and most attractive way to vitalize various soft robots with a single e-skin. Figure 5.27a shows a conceptual experimental design for consecutive innervation of distinct soft robotic hands through sequential lamination processes. First, three different soft robots were prepared with a distinct “muscle” design (spread finger design for robot 2, 3) and a physical state (curvilinear surface for robot 3) (Figure 5.27b). In the following step, the sequential lamination of the innervating e-skin allowed for the consecutive formation of an embedded electronic nervous system in each dormant soft robot, ultimately leading to the vitalized soft robots. Different actuation states (C, D, and B states as described in Figure 5.25) were adopted for each robot specifically for comparison between operations (Figure 5.27c). This simple experimental demonstration suggests that the proposed strategy of the e-skin-mediated wireless innervation process has numerous potential for driving soft robots in terms of a miniaturized design, complete softness (thus, good physical adaptations), and the capability of multi-robot innervation with a single e-skin. It is expected that the presented concept would provide a deep insight into the design and operation of the future soft robots, and further propose the way to interact with biological organisms in a fully integrated design.

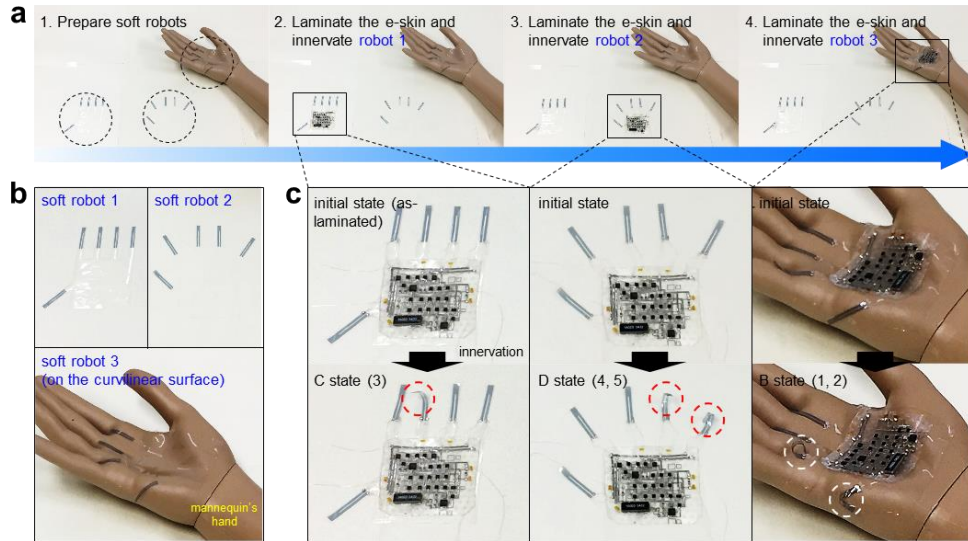


Figure 5.27 | E-skin-mediated consecutive multi-robot innervation. (a) A process flow of consecutive innervation of distinct soft robots by sequential lamination processes. Specifically, three different soft robotic hands with distinct “muscle” designs and physical states were utilized. (b) Enlarged view of each soft robotic hand before a lamination process. (c) Enlarged view of wireless manipulation of soft robotic hands with distinct operation states. For comparison, different actuation states in response to the input types (C, D, and B states) were demonstrated for each robot [197].

Chapter 6

Conclusion

In this dissertation, a printing-based methodology for fully-integrated e-skins in terms of “Stretchable Hybrid Electronics” and its use in significant applications of skin computer and fully soft robots were presented. First, the embedded form of PRIs was exploited to build reliable sites on a soft substrate. Studies on geometry/morphology engineering of such PRIs and corresponding quantitative surface strain analysis provided guidelines for reliable device integration from a structural point of view. Based on this soft substrate engineering technology, combinational technologies of inkjet-printed multilayer interconnection wiring, image-based customizable circuit routing, and robust SMD bonding established an optimized scheme for printing-based implementation of system-level, hybrid-type soft electronics. Numerous sets of soft electronic systems with diverse functions and circuit

configurations advocated the usefulness of this methodology.

The ability to construct much complex network layouts and functions between numerous IC devices in a soft, miniaturized form allowed us to implant soft electronics into unexplored subjects. The first application was highly integrated, high-speed, self-computable e-skins that provided “in-skin” computing capability. Single droplet printing-based methodology for PRI and core-shell via formation allowed rapid and scalable assembly of both constituents, and a series of analyses on island morphology, surface strain mapping, and electrical characteristics provided optimized schemes for geometric design of a double-side USE platform. Based on this novel platform, we for the first time demonstrated double-side integrated, stretchable 1 MHz computational logic networks via fully printable SMD assemblies.

The final part of this dissertation focused on the first use of fully-integrated e-skins to soft robots as a driving core. We developed a pair of e-skins with a distinct function of a soft HMI or an embedded electronic nervous system innervating a soft robot. Perfect wireless interfacing and soft form factors of e-skins would render a complete softness to any types of fully soft robotic system. Importantly, the reliable operation of the e-skins under severe physical deformations is guaranteed by both strain-isolating physical and stretch-tolerant electrical architectures (signal interfaces). Furthermore, unprecedented features of the e-skin-mediated soft robot innervation concept

even allowed for the most attractive way to activate multi-robot system through consecutive innervation with a single e-skin.

The studies and corresponding demonstrations handled in this dissertation would pave a way toward integrated soft electronics and also provide potential for changing the paradigm of soft robotics in terms of design, operating mechanism, and multi-robot interaction. Especially, it is expected that associated upcoming studies about advanced HMIs (with fully integrated functionalities), fully soft robots, soft IoTs (featuring wireless communication between several e-skins or e-skin-attached objects), and communication with biological organs and plants (with capabilities of wireless monitoring and active feedbacks) would be supported by this work.

Bibliography

- [1] J.A. Rogers, T. Someya, Y. Huang, *Science* **327**, 1603 (2010).
- [2] S. Wagner, S. Bauer, *MRS Bulletin* **37**, 207 (2012).
- [3] D.-H. Kim, R. Ghaffari, N. Lu, J.A. Rogers, *Annu. Rev. Biomed. Eng.* **14**, 113 (2012).
- [4] A.Z. Kattamis, N. Giebink, I. Cheng, S. Wagner, S. R. Forrest, Y. Hong, V. Cannella, *J. Soc. Inf. Display* **15**, 433 (2007).
- [5] Y. Hong, J. Kanicki, *IEEE Trans. Electron Dev.* **51**, 1562 (2004).
- [6] H.-C. Yuan, Z. Ma, *Appl. Phys. Lett.* **89**, 212105 (2006).
- [7] T. Sekitani, T. Yokota, U. Zschieschang, H. Klauk, S. Bauer, K. Takeuchi, M. Takamiya, T. Sakurai, T. Someya, *Science* **326**, 1516 (2009).
- [8] T. Sekitani, U. Zschieschang, H. Klauk, T. Someya, *Nature Mater.* **9**, 1015 (2010).
- [9] C. Wang, J.-C. Chien, K. Takei, T. Takahashi, J. Nah, A.M. Niknejad, A. Javey, *Nano Lett.* **12**, 1527 (2012).
- [10] F. Garnier, R. Hajlaoui, A. Yassar, P. Srivastava, *Science* **265**, 1684 (1994).

- [11] H. Sirringhaus, T. Kawase, R.H. Friend, T. Shimoda, M. Inbasekaran, W. Wu, E. P. Woo, *Science* **290**, 2123 (2000).
- [12] R. Parashkov, E. Becker, T. Riedl, H.-H. Johannes, W. Kowalsky, *Proc. IEEE* **93**, 1321 (2005).
- [13] R.A. Street, W.S. Wong, S.E. Ready, M.L. Chabinyc, A.C. Arias, S. Limb, A. Salleo, R. Lujan, *Materials Today* **9**, 32 (2006).
- [14] B.Y. Ahn, E.B. Duoss, M.J. Motala, X. Guo, S.-I. Park, Y. Xiong, J. Yoong, R.G. Nuzzo, J.A. Rogers, J. A. Lewis, *Science* **323**, 1590 (2009).
- [15] Y. Xia, G.M. Whitesides, *Annu. Rev. Mater. Sci.* **28**, 153 (1984).
- [16] G.M. Whitesides, E. Ostuni, S. Takayama, X. Jiang, D.E. Ingber, *Annu. Rev. Biomed. Eng.* **3**, 335 (2001).
- [17] E. Menard, M.A. Meitl, Y. Sun, J.-U. Park, D.J.-L. Shir, Y.-S. Nam, S. Jeon, J.A. Rogers, *Chem. Rev.* **108**, 1117 (2007).
- [18] J.A. Rogers, Z. Bao, K. Baldwin, A. Dodabalapur, B. Crone, V.R. Raju, V. Kuck, H. Katz, K. Amundson, J. Ewing, P. Drzaic, *Proc. Natl. Acad. Sci. USA* **98**, 4835 (2001).
- [19] A. Russo, B.Y. Ahn, J.J. Adams, E.B. Duoss, J.T. Bernhard, J.A. Lewis, *Adv. Mater.* **23**, 3426 (2011).
- [20] S.H. Ko, H. Pan, C.P. Grigoropoulos, C.K. Luscombe, J.M.J. Frechet, D. Poulidakos, *Nanotechnology* **18**, 345202 (2007).
- [21] Z. Suo, E.Y. Ma, H. Gleskova, S. Wagner, *Appl. Phys. Lett.* **74**, 1177 (1999).
- [22] J. Lewis, *Materials Today* **9**, 38 (2006).
- [23] P.I. Hsu, H. Gleskova, M. Huang, Z. Suo, S. Wagner, J.C. Sturm, *J. Non-Cryst. Solids* **299**, 1355 (2002).

- [24] H.C. Ko, M.P. Stoykovich, J. Song, V. Malyarchuk, W. M. Choi, C.-J. Yu, J.B. Geddes, J. Xiao, S. Wang, Y. Huang, J.A. Rogers, *Nature* **454**, 748 (2008).
- [25] Y. M. Song, Y. Xie, V. Malyarchuk, J. Xiao, I. Jung, K.-J. Choi, Z. Liu, H. Park, C. Lu, R.-H. Kim, R. Li, K. B. Crozier, Y. Huang, J.A. Rogers, *Nature* **497**, 95 (2013).
- [26] J. A. Rogers, Y. Huang, *Proc. Natl. Acad. Sci. U.S.A.* **106**, 10875 (2009).
- [27] J. A. Rogers, *JAMA* **313**, 561 (2015).
- [28] Y. Cheng, R. Wang, J. Sun, L. Gao, *ACS Nano* **9**, 3887 (2015).
- [29] S. Xu, Y. Zhang, J. Cho, J. Lee, X. Huang, L. Jia, J.A. Fan, Y. Su, J. Su, H. Zhang, H. Cheng, B. Lu, C. Yu, C. Chuang, T.-I. Kim, T. Song, K. Shigeta, S. Kang, C. Dagdeviren, I. Petrov, P.V. Braun, Y. Huang, U. Paik, J.A. Rogers, *Nat. Commun.* **4**, 1543 (2013).
- [30] C. Larson, B. Peele, S. Li, S. Robinson, M. Totaro, L. Beccai, B. Mazzolai, R. Shepherd, *Science* **351**, 1071 (2016).
- [31] S. Takamatsu, T. Lonjaret, E. Ismailova, A. Masuda, T. Itoh, G. G. Malliaras, *Adv. Mater.* **28**, 4485 (2016).
- [32] T. Someya, T. Sekitani, S. Iba, Y. Kato, H. Kawaguchi, T. Sakurai, *Proc. Natl. Acad. Sci. USA* **101**, 9966 (2004).
- [33] D. J. Lipomi, M. Vosgueritchian, B. C. -K. Tee, S. L. Hellstrom, J. A. Lee, C. H. Fox, Z. Bao, *Nature Nanotech.* **6**, 788 (2011).
- [34] D. Rus, M. T. Tolley, *Nature* **521**, 467 (2015).
- [35] M. Wehner, R. L. Truby, D. J. Fitzgerald, B. Mosadegh, G. M. Whitesides, J. A. Lewis, R. J. Wood, *Nature* **536**, 451 (2016).
- [36] D. -H. Kim, N. Lu, R. Ma, Y. -S. Kim, R. -H. Kim, S. Wang, J. Wu, S.

- M. Won, H. Tao, A. Islam, K. J. Yu, T. -I. Kim, R. Chowdhury, M. Ying, L. Xu, M. Li, H. -J. Chung, H. Keum, M. McCormick, P. Liu, Y.-W. Zhang, F. G. Omenetto, Y. Huang, T. Coleman, J. A. Rogers, *Science* **333**, 838 (2011).
- [37] D. Son, J. Lee, S. Qiao, R. Ghaffari, J. Kim, J. E. Lee, C. Song, S. J. Kim, D.J. Lee, S. W. Jun, S. Yang, M. Park, J. Shin, K. Do, M. Lee, K. Kang, C. S. Hwang, N. Lu, T. Hyeon, D. -H. Kim, *Nature Nanotech.* **9**, 397 (2014).
- [38] S. -K. Kang, R. K. J. Murphy, S. -W. Hwang, S. M. Lee, D. V. Harburg, N. A. Krueger, J. Shin, P. Gamble, H. Cheng, S. Yu, Z. Liu, J. G. McCall, M. Stephen, H. Ying, J. Kim, G. Park, R. C. Webb, C. H. Lee, S. Chung, D. S. Wie, A. D. Gujar, B. Vemulapalli, A. H. Kim, K. -M. Lee, J. Cheng, Y. Huang, S. H. Lee, P. V. Braun, W. Z. Ray, J. A. Rogers, *Nature* **530**, 71 (2016).
- [39] T. -M. Fu, G. Hong, T. Zhou, T. G. Schuhmann, R. D. Viveros and C. M. Lieber, *Nat. Methods* **13**, 875 (2016).
- [40] J. W. Hutchinson, Z. Suo, *Adv. Appl. Mech.* **29**, 63 (1992).
- [41] M. F. Doerner, W. D. Nix, *Crit. Rev. Solid State Mater. Sci.* **14**, 225 (1988).
- [42] Z. Suo, J. W. Hutchinson, *Int. J. Fracture* **43**, 1 (1990).
- [43] N. Lu, J. Yoon, Z. Suo, *Int. J. Mater. Res.* **98**, 717 (2007).
- [44] T. Li, Z. Suo, *Int. J. Solids Struct.* **43**, 2351 (2006).
- [45] J. Song, H. Jiang, Z. J. Liu, D. Y. Khang, Y. Huang, J. A. Rogers, C. Lu, C. G. Koh, *Int. J. Solids Struct.* **45**, 3107 (2008).
- [46] Z. Xue, J. W. Hutchinson, *Int. J. Solids Struct.* **45**, 3769 (2008).
- [47] S. P. Lacour, S. Wagner, Z. Huang, Z. Suo, *Appl. Phys. Lett.* **82**, 2404

- (2003).
- [48] T. Li, Z. Huang, Z. Suo, S. P. Lacour, S. Wagner, *Appl. Phys. Lett.* **85**, 3435 (2004).
- [49] S. P. Lacour, D. Chan, S. Wagner, T. Li, Z. Suo, *Appl. Phys. Lett.* **88**, 204103 (2006).
- [50] D. -H. Kim, J. Xiao, J. Song, Y. Huang, J. A. Rogers, *Adv. Mater.* **22**, 2108 (2010).
- [51] T. Sekitani, T. Someya, *Adv. Mater.* **22**, 2228 (2010).
- [52] D. S. Gray, J. Tien, C. S. Chen, *Adv. Mater.* **16**, 393 (2004).
- [53] D. Brosteaux, F. Axisa, M. Gonzalez, J. Vanfleteren, *IEEE Electron Dev. Lett.* **28**, 552 (2007).
- [54] M. Gonzalez, F. Axisa, M. V. Bulcke, D. Brosteaux, B. Vandeveld, J. Vanfleteren, *Microelectron. Reliab.* **48**, 825 (2008).
- [55] B. Huyghe, H. Rogier, J. Vanfleteren, *IEEE Trans. Adv. Pack.* **31**, 802 (2008).
- [56] H. -J. Kim, C. Son, B. Ziaie, *Appl. Phys. Lett.* **92**, 011904 (2008).
- [57] H. -J. Kim, T. Maleki, P. Wei, B. Ziaie, *J. Microelectromech. Syst.* **18**, 138 (2009).
- [58] S. Cheng, Z. Wu, P. Hallbjorner, K. Hjort, A. Rydberg, *IEEE Trans. Antenn. Propag.* **57**, 3765 (2009).
- [59] J. A. Fan, Y. -H. Yeo, Y. Su, Y. Hattori, W. Lee, S. -Y. Jung, Y. Zhang, Z. Liu, H. Cheng, L. Falgout, M. Bajema, T. Coleman, D. Gregoire, R. J. Larsen, Y. Huang, J. A. Rogers, *Nat. Commun.* **5**, 3266 (2014).
- [60] Y. Cho, J. -H. Shin, A. Costa, T. A. Kim, V. Kunin, J. Li, S. Y. Lee, S. Yang, H. N. Han, I. -S. Choi, D. J. Srolovitz, *Proc. Natl. Acad. Sci. USA*

- 111**, 17390 (2014).
- [61] Y. Tang, G. Lin, L. Han, S. Qiu, S. Yang, J. Yin, *Adv. Mater.* **27**, 7181 (2015).
- [62] T. C. Shyu, P. F. Damasceno, P. M. Dodd, A. Lamoureux, L. Xu, M. Shlian, M. Shtein, S. C. Glotzer, N. A. Kotov, *Nature Mater.* **14**, 785 (2015).
- [63] T. Sekitani, Y. Noguchi, K. Hata, T. Fukushima, T. Aida, T. Someya, *Science* **321**, 1468 (2008).
- [64] T. Takahashi, K. Takei, A. G. Gillies, R. S. Fearing, A. Javey, *Nano Lett.* **11**, 5408 (2011).
- [65] T. Someya, Y. Kato, T. Sekitani, S. Iba, Y. Noguchi, Y. Murase, H. Kawaguchi, T. Sakurai, *Proc. Natl. Acad. Sci. USA* **102**, 12321 (2005).
- [66] C. Wu, X. Wang, L. Lin, H. Guo, Z. L. Wang, *ACS Nano* **10**, 4652 (2016).
- [67] M. K. Bles, A. W. Barnard, P. A. Rose, S. P. Roberts, K. L. McGrill, P. Y. Huang, A. R. Ruyack, J. W. Kevek, B. Kobrin, D. A. Muller, P. L. McEuen, *Nature* **524**, 204 (2015).
- [68] P. Z. Hanakata, Z. Qi, D. K. Campbell, H. S. Park, *Nanoscale* **8**, 458 (2016).
- [69] Z. Qi, D. K. Campbell, H. S. Park, *Phys. Rev. B* **90**, 245437 (2014).
- [70] Z. Y. Huang, W. Hong, Z. Suo, *J. Mech. Phys. Solids* **53**, 2101 (2005).
- [71] H. Jiang, D. -Y. Khang, J. Song, Y. Sun, Y. Huang, J. A. Rogers, *Proc. Natl. Acad. Sci. USA* **104**, 15607 (2007).
- [72] D. -Y. Khang, H. Jiang, Y. Huang, J. A. Rogers, *Science* **311**, 208 (2006).
- [73] D. -H. Kim, J. -H. Ahn, W. M. Choi, H. -S. Kim, T. -H. Kim, J. Song, Y. Y. Huang, Z. Liu, C. Lu, J. A. Rogers, *Science* **320**, 507 (2008).

- [74] S. H. Chae, W. J. Yu, J. J. Bae, D. L. Duong, D. Perello, H. Y. Jeong, Q. H. Ta, T. H. Ly, Q. A. Vu, M. Yun, X. Duan, Y. H. Lee, *Nature Mater.* **12**, 403 (2013).
- [75] K. Park, D. –K. Lee, B. –S. Kim, H. Jeon, N. –E. Lee, D. Whang, H. –J. Lee, Y. J. Kim, J. –H. Ahn, *Adv. Funct. Mater.* **20**, 3577 (2010).
- [76] D. J. Lipomi, B. C. –K. Tee, M. Vosgueritchian, Z. Bao, *Adv. Mater.* **23**, 1771 (2011).
- [77] J. Zang, S. Ryu, N. Pugno, Q. Wang, Q. Tu, M. J. Buehler, X. Zhao, *Nature Mater.* **12**, 321 (2013).
- [78] J. Zang, C. Cao, Y. Feng, J. Liu, X. Zhao, *Sci. Rep.* **4**, 6492 (2014).
- [79] F. Xu, Y. Zhu, *Adv. Mater.* **24**, 5117 (2012).
- [80] Y. Joo, J. Byun, N. Seong, J. Ha, H. Kim, S. Kim, T. Kim, H. Im, D. Kim, Y. Hong, *Nanoscale*, **7**, 6208 (2015).
- [81] Y. Sun, W. M. Choi, H. Jiang, Y. Y. Huang, J. A. Rogers, *Nature Nanotech.* **1**, 201 (2006).
- [82] H. Jiang, Y. Sun, J. A. Rogers, Y. Huang, *Appl. Phys. Lett.* **90**, 133119 (2007).
- [83] H. Jiang, Y. Sun, J. A. Rogers, Y. Huang, *Int. J. Solids Struct.* **45**, 2014 (2008).
- [84] D. –H. Kim, Z. Liu, Y. –S. Kim, J. Wu, J. Song, H. –S. Kim, Y. Huang, K. –C. Hwang, Y. Zhang, J. A. Rogers, *Small* **5**, 2841 (2009).
- [85] D. –H. Kim, J. Song, W. M. Choi, H. –S. Kim, R. –H. Kim, Z. Liu, Y. Y. Huang, K. –C. Hwang, Y. –W. Zhang, J. A. Rogers, *Proc. Natl. Acad. Sci. USA* **105**, 18675 (2008).
- [86] S. Xu, Z. Yan, K. –I. Jang, W. Huang, H. Fu, J. Kim, Z. Wei, M. Flavin,

- J. McCracken, R. Wang, A. Badea, Y. Liu, D. Xiao, G. Zhou, J. Lee, H. U. Chung, H. Chen, W. Ren, A. Banks, X. Li, U. Paik, R. G. Nuzzo, Y. Huang, Y. Zhang, J. A. Rogers, *Science* **347**, 154 (2015).
- [87] S. Yao, Y. Zhu, *Adv. Mater.* **27**, 1480 (2015).
- [88] M. M. J. Treacy, T. W. Ebbesen, J. M. Gibson, *Nature* **381**, 678 (1996).
- [89] R. H. Baughman, A. A. Zakhidov, W. A. de Heer, *Science* **297**, 787 (2002).
- [90] H. Dai, *Acc. Chem. Res.* **35**, 1035 (2002).
- [91] T. Sekitani, H. Nakajima, H. Maeda, T. Fukushima, T. Aida, K. Hata, T. Someya, *Nature Mater.* **8**, 494 (2009).
- [92] K. -Y. Chun, Y. Oh, J. Rho, J. -H. Ahn, Y. -J. Kim, H. R. Choi, S. Baik, *Nature Nanotech.* **5**, 853 (2010).
- [93] M. K. Shin, J. Oh, M. Lima, M. E. Kozlov, S. J. Kim, R. H. Baughman, *Adv. Mater.* **22**, 2663 (2010).
- [94] K. H. Kim, M. Vural, M. F. Islam, *Adv. Mater.* **23**, 2865 (2011).
- [95] Z. Yu, X. Niu, Z. Liu, Q. Pei, *Adv. Mater.* **23**, 3989 (2011).
- [96] L. Hu, M. Pasta, F. L. Manita, L. Cui, S. Jeong, H. D. Deshazer, J. W. Choi, S. M. Han, Y. Cui, *Nano Lett.* **10**, 708 (2010).
- [97] H. Lee, J. -K. Yoo, J. -H. Park, J. H. Kim, K. Kang, Y. S. Jung, *Adv. Energy Mater.* **2**, 976 (2012).
- [98] K. Liu, Y. Sun, P. Liu, X. Lin, S. Fan, K. Jiang, *Adv. Funct. Mater.* **21**, 2721 (2011).
- [99] C. Feng, K. Liu, J. -S. Wu, L. Liu, J. -S. Cheng, Y. Zhang, Y. Sun, Q. Li, S. Fan, K. Jiang, *Adv. Funct. Mater.* **20**, 885 (2010).

- [100] Y. Zhang, C. J. Sheehan, J. Zhai, G. Zou, H. Luo, J. Xiong, Y. T. Zhu, Q. X. Jia, *Adv. Mater.* **22**, 3027 (2010).
- [101] K. Jiang, J. Wang, Q. Li, L. Liu, C. Liu, S. Fan, *Adv. Mater.* **23**, 1154 (2011).
- [102] Y. Shang, X. He, Y. Li, L. Zhang, Z. Li, C. Ji, E. Shi, P. Li, K. Zhu, Q. Peng, C. Wang, X. Zhang, R. Wang, J. Wei, K. Wang, H. Zhu, D. Wu, A. Cao, *Adv. Mater.* **24**, 2896 (2012).
- [103] D. S. Hecht, L. Hu, G. Irvin, *Adv. Mater.* **23**, 1482 (2011).
- [104] T. Akter, W. S. Kim, *ACS Appl. Mater. Interfaces* **4**, 1855 (2012).
- [105] D. -S. Leem, A. Edwards, M. Faist, J. Nelson, D. D. C. Bradley, J. C. de Mello, *Adv. Mater.* **23**, 4371 (2011).
- [106] S. Han, S. Hong, J. Ham, J. Yeo, J. Lee, B. Kang, P. Lee, J. Kwon, S. S. Lee, M. -Y. Yang, S. H. Ko, *Adv. Mater.* **26**, 5808 (2014).
- [107] H. Wu, D. Kong, Z. Ruan, P. -C. Hsu, S. Wang, Z. Yu, T. J. Carney, L. Hu, S. Fan, Y. Cui, *Nature Nanotech.* **8**, 421 (2013).
- [108] H. Wu, L. Hu, M. W. Rowell, D. Kong, J. J. Cha, J. R. McDonough, J. Zhu, Y. Yang, M. D. McGehee, Y. Cui, *Nano Lett.* **10**, 4242 (2010).
- [109] M. Park, J. Im, M. Shin, Y. Min, J. Park, H. Cho, S. Park, M. -B. Shim, S. Jeon, D. -Y. Chung, J. Bae, J. Park, U. Jeong, K. Kim, *Nature Nanotech.* **7**, 803 (2012).
- [110] B. W. An, B. G. Hyun, S. -Y. Kim, M. Kim, M. -S. Lee, K. Lee, J. B. Koo, H. Y. Chu, B. -S. Bae, J. -U. Park, *Nano Lett.* **14**, 6322 (2014).
- [111] K. K. Kim, S. Hong, H. M. Cho, J. Lee, Y. D. Suh, J. Ham, S. H. Ko, *Nano Lett.* **15**, 5240 (2015).
- [112] S. Hong, H. Lee, J. Lee, J. Kwon, S. Han, Y. D. Suh, H. Cho, J. Shin,

- J. Yeo, S. H. Ko, *Adv. Mater.* **27**, 4744 (2015).
- [113] S. J. Mazlouman, X. J. Jiang, A. Mahanfar, C. Menon, R. G. Vaughan, *IEEE Trans. Antenn. Propag.* **59**, 4406 (2011).
- [114] E. Palleau, S. Reece, S. C. Desai, M. E. Smith, M. D. Dickey, *Adv. Mater.* **25**, 1589 (2013).
- [115] C. Ladd, J. –H. So, J. Muth, M. D. Dickey, *Adv. Mater.* **25**, 5081 (2013).
- [116] J. W. Boley, E. L. White, G. T. –C. Chiu, R. K. Kramer, *Adv. Funct. Mater.* **24**, 3501 (2014).
- [117] M. Kubo, X. Li, C. Kim, M. Hashimoto, B. J. Wiley, D. Ham, G. M. Whitesides, *Adv. Mater.* **22**, 2749 (2010).
- [118] S. Zhu, J. –H. So, R. Mays, S. Desai, W. R. Barnes, B. Pourdeyhimi, M. D. Dickey, *Adv. Funct. Mater.* **23**, 2308 (2013).
- [119] J. Yoon, S. Y. Hong, Y. Lim, S. –J. Lee, G. Zi, J. S. Ha, *Adv. Mater.* **26**, 6580 (2014).
- [120] K. S. Kim, Y. Zhao, H. Jang, S. Y. Lee, J. M. Kim, K. S. Kim, J. –H. Ahn, P. Kim, J. –Y. Choi, B. H. Hong, *Nature* **457**, 706 (2009).
- [121] Y. Zhao, J. Liu, Y. Hu, H. Cheng C. Hu, C. Jiang, L. Jiang, A. Cao, L. Qu, *Adv. Mater.* **25**, 591 (2013).
- [122] G. D. Moon, G. –H. Lim, J. H. Song, M. Shin, T. Yu, B. Lim, U. Jeong, *Adv. Mater.* **25**, 2707 (2013).
- [123] J. –Y. Sun, X. Zhao, W. R. K. Illeperuma, K. H. Oh, D. J. Mooney, J. J. Vlassak, Z. Suo, *Nature* **489**, 133 (2012).
- [124] C. Keplinger, J.-Y. Sun, C. C. Foo, P. Rothmund, G. M. Whitesides, Z. Suo, *Science* **341**, 984 (2013).

- [125] C. -C. Kim, H. -H. Lee, K. H. Oh, J. -Y. Sun, *Science* **353**, 682 (2016).
- [126] J. -Y. Sun, C. Keplinger, G. M. Whitesides, Z. Suo, *Adv. Mater.* **26**, 7608 (2014).
- [127] S. Wagner, S. P. Lacour, J. Jones, P. I. Hsu, J. C. Sturm, T. Li, Z. Suo, *Physica E* **25**, 326 (2004).
- [128] N. Matsuhisa, M. Kaltenbrunner, T. Yokota, H. Jinno, K. Kuribara, T. Sekitani, T. Someya, *Nat. Commun.* **6**, 7461 (2015).
- [129] M. Drack, I. Graz, T. Sekitani, T. Someya, M. Kaltenbrunner, S. Bauer, *Adv. Mater.* **27**, 34 (2015).
- [130] D. Kim, D. Kim. H. Lee, Y. R. Jeong, S.-J. Lee, G. Yang, H. Kim, G. Lee, S. Jeon, G. Zi, J. Kim, J. S. Ha, *Adv. Mater.* **28**, 748 (2016).
- [131] R. Libanori, R. M. Erb, A. Reiser, H. L. Ferrand, M. J. Suess, R. Spolenak, A. R. Studart, *Nat. Commun.* **3**, 1265 (2012).
- [132] J. Lee, J. Wu, M. Shi, J. Yoon, S.-I. Park, M. Li, Z. Liu, Y. Huang, J. A. Rogers, *Adv. Mater.* **23**, 986 (2011).
- [133] J. Yoon, S. Y. Hong, Y. Lim, S.-J. Lee, G. Zi, J. S. Ha, *Adv. Mater.* **26**, 6580 (2014).
- [134] I. M. Graz, D. P. J. Cotton, A. Robinson, S. P. Lacour, *Appl. Phys. Lett.* **98**, 124101 (2011).
- [135] A. Romeo, Q. Liu, Q. Suo, S. P. Lacour, *Appl. Phys. Lett.* **102**, 131904 (2013).
- [136] H. C. Ko, G. Shin, S. Wang, M. P. Stoykovich, J. W. Lee, D.-H. Kim, J. S. Ha, Y. Huang K.-C. Hwang, J. A. Rogers, *Small* **5**, 2703 (2009).
- [137] J. Song, Y. Huang, J. Xiao, S. Wang, K. C. Hwang, H. C. Ko, D.-H.

- Kim, M. P. Stoykovich, J. A. Rogers, *J. Appl. Phys.* **105**, 123516 (2009).
- [138] D.-H. Kim, Y.-S. Kim, J. Wu, Z. Liu, J. Song, H.-S. Kim, Y. Y. Huang, K.-C. Hwang, J. A. Rogers, *Adv. Mater.* **21**, 3703 (2009).
- [139] H. Cheng, J. Wu, M. Li, D.-H. Kim, Y.-S. Kim, Y. Huang, Z. Kang K. C. Hwang, J. A. Rogers, *Appl. Phys. Lett.* **98**, 061902 (2011).
- [140] H. C. Ko, M. P. Stoykovich, J. Song, V. Malyarchuk, W. M. Choi, C.-J. Yu, J. B. Geddes, J. Xiao, S. Wang, Y. Huang, J. A. Rogers, *Nature* **454**, 748 (2008).
- [141] D.-H. Kim, N. Lu, R. Ghaffari, Y.-S. Kim, S. P. Lee, L. Xu, J. Wu, R.-H. Kim, J. Song, Z. Liu, J. Viventi, B. de Graff, B. Elolampi, M. Mansour, M. J. Slepian, S. Hwang, J. D. Moss, S.-M. Won, Y. Huang, B. Litt, J. A. Rogers, *Nature Mater.* **10**, 316 (2011).
- [142] R.-H. Kim, D.-H. Kim, J. Xiao, B. H. Kim, S.-I. Park, B. Panilaitis, R. Ghaffari, J. Yao, M. Li, Z. Liu, V. Malyarchuk, D. G. Kim, A.-P. Le, R. G. Nuzzo, D. L. Kaplan, F. G. Omenetto, Y. Huang, Z. Kang, J. A. Rogers, *Nature Mater.* **9**, 929 (2010).
- [143] J.-W. Jeong, W.-H. Yeo, A. Akhtar, J. J. S. Norton, Y.-J. Kwack, S. Li, S.-Y. Jung, Y. Su, W. Lee, J. Xia, H. Cheng, Y. Huang, W.-S. Choi, T. Bretl, J. A. Rogers, *Adv. Mater.* **25**, 6839 (2013).
- [144] B. Xu, A. Akhtar, Y. Liu, H. Chen, W.-H. Yeo, S. I. Park, B. Boyce, H. Kim, J. Yu, H.-Y. Lai, S. Jung, Y. Zhou, J. Kim, S. Cho, Y. Huang, T. Bretl, J. A. Rogers, *Adv. Mater.* **28**, 4462 (2016).
- [145] R. C. Webb, Y. Ma, S. Krishnan, Y. Li, S. Yoon, X. Guo, X. Feng, Y. Shi, M. Seidel, N. H. Cho, J. Kurniawan, J. Ahahd, N. Sheth, J. Kim, J. G. Taylor, T. Darlington, K. Cheng, W. Huang, J. Ayers, A. Gruebele, R. M. Pielak, M. J. Slepian, Y. Huang, A. M. Gorbach, J. A. Rogers, *Sci. Adv.* **1**, 21500701 (2015).

- [146] J. J. S. Norton, D. S. Lee, J. W. Lee, W. Lee, O. Kwon, P. Won, S.-Y. Jung, H. Cheng, J.-W. Jeong, A. Akce, S. Umunna, I. Na, Y. H. Kwon, X.-Q. Wang, Z. Liu, U. Paik, Y. Huang, T. Bretl, W.-H. Yeo, J. A. Rogers, *Proc. Natl. Acad. Sci. U.S.A.* **112**, 3920 (2015).
- [147] L. Xu, S. R. Gutbrod, A. P. Bonifas, Y. Su, M. S. Sulkin, N. Lu, H.-J. Chung, K.-I. Jang, Z. Liu, M. Ying, C. Lu, R. C. Webb, J.-S. Kim, J. I. Laughner, H. Cheng, Y. Liu, A. Ameen, J.-W. Jeong, G.-T. Kim, Y. Huang, I. R. Efimov, J. A. Rogers, *Nat. Commun.* **5**, 3329 (2014).
- [148] R. Canovas, M. Parrilla, P. Mercier, F. J. Andrade, J. Wang, *Adv. Mater. Tech.* **1**, 1600061 (2016).
- [149] W. Gao, S. Emaminejad, H. Y. Y. Nyein, S. Challa, K. Chen, A. Peck, H. M. Fahad, H. Ota, H. Shiraki, D. Kiriya, D.-H. Lien, G. A. Brooks, R. W. Davis, A. Javey, *Nature* **529**, 509 (2016).
- [150] S. Xu, Y. Zhang, L. Jia, K. E. Mathewson, K.-I. Jang, J. Km, H. Fu, X. Huang, P. Chava, R. Wang, S. Bhole, L. Wang, Y. J. Na, Y. Guan, M. Flavin, Z. Han, Y. Huang, J. A. Rogers, *Science* **344**, 70 (2014).
- [151] Y. Liu, J. J. S. Norton, R. Qazi, Z. Zou, K. R. Ammann, H. Liu, L. Yan, P. L. Tran, K.-I. Jang, J. W. Lee, D. Zhang, K. A. Kilian, S. H. Jung, T. Bretl, J. Xiao, M. J. Slepian, Y. Huang, J.-W. Jeong, J. A. Rogers, *Sci. Adv.* **2**, e1601185 (2016).
- [152] Y. Khan, M. Garg, Q. Gui, M. Schadt, A. Gaikwad, D. Han, N. A. D. Yamamoto, P. Hart, R. Welte, W. Wilson, S. Czarnecki, M. Poliks, Z. Jin, K. Ghose, F. Egitto, J. Turner, A. C. Arias, *Adv. Funct. Mater.* **26**, 8764 (2016).
- [153] J. Byun, B. Lee, E. Oh, H. Kim, S. Kim, S. Lee, Y. Hong, *Sci. Rep.* **7**, 45328 (2017).
- [154] J. Byun, E. Oh, B. Lee, S. Kim, S. Lee, Y. Hong, *Adv. Funct. Mater.*

in press.

- [155] T. Okuzono, M. Kobayashi, M. Doi, *Phys. Rev. E* **80**, 021603 (2009).
- [156] K. Ozawa, E. Nishitani, M. Doi, *Jpn. J. Appl. Phys.* **44**, 4229 (2005).
- [157] A. Romeo, Q. Liu, Q. Suo, S. P. Lacour, *Appl. Phys. Lett.* **102**, 131904 (2013).
- [158] F. Bossuyt, T. Vervust, J. Vanfleteren, *IEEE Trans. Compon. Pack. A* **3**, 229 (2013).
- [159] J. Sandby-Moller, T. Poulsen, H. C. Wulf, *Acta. Derm. Venereol.* **83**, 410 (2003).
- [160] D. J. Chen, F. P. Chiang, Y. S. Tan, H. S. Don, *Appl. Optics* **32**, 1839 (1993).
- [161] S. Chung, J. Lee, H. Song, S. Kim, J. Jeong, Y. Hong, *Appl. Phys. Lett.* **98**, 153110 (2011).
- [162] J. Lee, S. Chung, H. Song, S. Kim, Y. Hong, *J. Phys. D: Appl. Phys.* **46**, 105305 (2013).
- [163] G. S. Jeong, D.-H. Baek, H. C. Jung, J. H. Song, J. H. Moon, S. W. Hong, I. Y. Kim, S.-H. Lee, *Nat. Commun.* **3**, 977 (2012).
- [164] Y. Yu, Y. Zhang, K. Li, C. Yan, Z. Zeng, *Small* **11**, 3444 (2015).
- [165] X. Chen, J. Yin, *Soft Matter* **6**, 5667 (2010).
- [166] J. Genzer, J. Groenwold, *Soft Matter* **2**, 310 (2006).
- [167] S. Yang, K. Khare, P.-C. Lin, *Adv. Funct. Mater.* **20**, 2550 (2010).
- [168] C. Yu, H. Jiang, *Thin Solid Films* **519**, 818 (2010).
- [169] J.-Y. Sun, S. Xia, M.-W. Moon, K. H. Oh, K.-S. Kim, *Proc. R. Soc. A* **468**, 932 (2012).

- [170] V. Arumugam, V. Naresh, R. Sanjeevi, *J. Biosci.* **18**, 307 (1994).
- [171] D. Rus, M. T. Tolley, *Nature* **521**, 467 (2015).
- [172] E. Stavrinidou, R. Gabrielsson, E. Gomez, X. Crispin, O. Nilsson, D. T. Simon, M. Berggren, *Sci. Adv.* **1**, e1501136 (2015).
- [173] E. Oh, J. Byun, B. Lee, S. Kim, D. Kim, J. Yoon, Y. Hong, *Adv. Electron. Mater.* **3**, 1600517 (2017).
- [174] D. Rus, M. T. Tolley, *Nature* **521**, 467 (2015).
- [175] C. Laschi, B. Mazzolai, M. Cianchetti, *Sci. Robot.* **1**, eaa3690 (2016).
- [176] M. Calisti, M. Giorelli, G. Levy, B. Mazzolai, B. Hochner, C. Laschi, P. Dario, *Bioinspir. Biomim.* **6**, 036002 (2011).
- [177] C. Laschi, M. Cianchetti, B. Mazzolai, L. Margheri, M. Follador, P. Dario, *Adv. Robot.* **26**, 709 (2012).
- [178] H.T. Lin, G. G. Leisk, B. Trimmer, *Bioinspir. Biomim.* **6**, 026007 (2011).
- [179] R. F. Shepherd, F. Ilievski, W. Choi, S. A. Morin, A. A. Stokes, A. D. Mazzeo, X. Chen, M. Wang, G. M. Whitesides, *Proc. Natl. Acad. Sci. U.S.A.* **108**, 20400 (2011).
- [180] Y.-L. Park, B. Chen, N. O. Perez-Arancibia, D. Young, L. Stirling, R. J. Wood, E. C. Goldfield, R. Nagpal, *Bioinspir. Biomim.* **9**, 016007 (2014).
- [181] A. D. Marchese, D. D. Onal, D. Rus, *Soft Robot.* **1**, 75 (2014).
- [182] S. Kim, C. Laschi, B. Trimmer, *Trends Biotech.* **31**, 287 (2013).
- [183] M. Rogoz, H. Zeng, C. Xuan, D. S. Wiersma, P. Wasylczyk, *Adv. Optical Mater.* **4**, 1689 (2016).

- [184] K. Jung, J. C. Koo, J. Nam, Y. K. Lee, H. R. Choi, *Bioinspir. Biomim.* **2**, S42 (2007).
- [185] N. W. Bartlett, M. T. Tolley J. T. B. Overvelde, J. C. Weaver, B. Mosadegh, K. Bertoldi, G. M. Whitesides, R. J. Wood, *Science* **349**, 161 (2015).
- [186] B. Mosadegh, P. Polygerinos, C. Keplinger, S. Wennstedt, R. F. Shepherd, U. Gupta, J. Shim, K. Bertoldi, C. J. Walsh, G. M. Whitesides, *Adv. Funct. Mater.* **24**, 2163 (2014).
- [187] M. T. Tolley, R. F. Shepherd, B. Mosadegh, K. C. Galloway, M. Wehner, M. Karpelson, R. J. Wood, G. M. Whitesides, *Soft Robot.* **1**, 213 (2014).
- [188] M. Wehner, M. T. Tolley, Y. Menguc, Y.-L. Park, A. Mozeika, Y. Ding, C. Onal, R. F. Shepherd, G. M. Whitesides, R. J. Wood, *Soft Robot.* **2**, 1 (2014).
- [189] T. Li, G. Li, Y. Liang, T. Cheng, J. Dai, X. Yang, B. Liu, Z. Zeng, Z. Huang, Y. Luo, T. Xie, W. Yang, *Sci. Adv.* **3**, e1602045 (2017).
- [190] M. Wehner, R. L. Truby, D. J. Fitzgerald, B. Mosadegh, G. M. Whitesides, J. A. Lewis, R. J. Wood, *Nature* **536**, 451 (2016).
- [191] A. Chortos, J. Liu, Z. Bao, *Nature Mater.* **15**, 937 (2016).
- [192] N. Lu, D.-H. Kim, *Soft Robot.* **1**, 53 (2014).
- [193] Y. Liu, J. J. S. Norton, R. Qazi, Z. Zou, K. R. Ammann, H. Liu, L. Yan, P. L. Tran, K.-I. Jang, J. W. Lee, D. Zhang, K. A. Kilian, S. H. Jung, T. Bretl, J. Xiao, M. J. Slepian, Y. Huang, J.-W. Jeong, J. A. Rogers, *Sci. Adv.* **2**, e1601185 (2016).
- [194] S. Lim, D. Son, J. Kim, Y. B. Lee, J.-K. Song, S. Choi, D. J. Lee, J. H. Kim, M. Lee, T. Hyeon, D.-H. Kim, *Adv. Funct. Mater.* **25**, 375 (2015).

- [195] B. Xu, A. Akhtar, Y. Liu, H. Chen, W.-H. Yeo, S. I. Park, B. Boyce, H. Kim, J. Y. H.-Y. Lai, S. Jung, Y. Zhou, J. Kim, S. Cho, Y. Huang, T. Bretl, J. A. Rogers, *Adv. Mater.* **28**, 4462 (2016).
- [196] J.-K. Song, D. Son, J. Kim, Y. J. Yoo, G. J. Lee, L. Wang, M. K. Choi, J. Yang, M. Lee, K. Do, J. H. Koo, N. Lu, J. H. Kim, T. Hyeon, Y. M. Song, D.-H. Kim, *Adv. Funct. Mater.* **27**, 1605286 (2017).
- [197] J. Byun, Y. Lee, J. Yoon, B. Lee, E. Oh, S. Chung, J. Kim, Y. Hong, “Wireless interface electronic skins for innervating soft robots”, manuscript in preparation.
- [198] S. Taccola, F. Greco, E. Sinibaldi, A. Mondini, B. Mazzolai, V. Mattoli, *Adv. Mater.* **27**, 1668 (2015).

Publication List

Journal Papers

7. **J. Byun**, Y. Lee, J. Yoon, E. Oh, B. Lee, S. Chung, J. Kim, Y. Hong, “Wireless interface electronic skins for innervating soft robots”, in preparation.
6. **J. Byun**, E. Oh, B. Lee, S. Kim, S. Lee, Y. Hong, “A single droplet-printed double-side universal soft electronic platform for highly-integrated stretchable hybrid electronics”, *Adv. Funct. Mater.*, in press.
5. **J. Byun**, B. Lee, E. Oh, H. Kim, S. Kim, S. Lee, Y. Hong, “Fully printable, strain-engineered electronic wrap for customizable soft electronics”, *Sci. Rep.* **7**, 45328 (2017).
4. E. Oh, **J. Byun**, B. Lee, S. Kim, D. Kim, J. Yoon, Y. Hong, “Modulus-gradient conductive core-shell structures formed by magnetic self-assembling and printing processes for highly stretchable via applications”, *Adv. Electron. Mater.* **3**, 1600517 (2017).
3. S. Kim, S. Choi, E. Oh, **J. Byun**, H. Kim, B. Lee, S. Lee, Y. Hong, “Revisit to three-dimensional percolation theory: accurate analysis for highly stretchable conductive composite materials”, *Sci. Rep.* **6**, 34632 (2016).
2. Y. Joo, **J. Byun**, N. Seong, J. Ha, H. Kim, S. Kim, T. Kim, H. Im, D. Kim, Y. Hong, “Silver nanowire-embedded PDMS with multiscale structure for highly sensitive and robust flexible pressure sensor”, *Nanoscale* **7**, 6208 (2015).
1. S. Kim, **J. Byun**, S. Choi, D. Kim, T. Kim, S. Chung, Y. Hong, “Negatively strain-dependent electrical resistance of magnetically arranged nickel composites: application to highly stretchable electrodes and stretchable

lighting devices” *Adv. Mater.* **26**, 3094 (2014).

Conference Presentations

6. **J. Byun**, E. Oh, B. Lee, S. Kim, Y. Hong, “Fully-printed, double-side integrated high-speed stretchable digital logic circuits for self-computable electronic skin”, The Materials Research Society (MRS 2017), Phoenix, Arizona, April (2017).

5. **J. Byun**, B. Lee, E. Oh, Y. Hong, “Fully printed, custom-designed high-performance stretchable digital electronics”, The 8th International Workshop on Flexible & Printable Electronics (IWFPE 2016), Jeonju, Korea, November (2016) (***Best Poster Award***).

4. **J. Byun**, B. Lee, E. Oh, S. Kim, H. Kim, S. Choi, Y. Hong, “Stretchable and deformable LED configurations based on inkjet-printed chip-bonding technology”, The 15th international Meetings on Information Display (IMID 2015), Daegu, Korea, August (2015) (***Best Poster Award***).

3. **J. Byun**, B. Lee, S. Kim, Y. Hong, “Guided crack formation and stress localization of metallic thin film by using inkjet-printed embedded polymeric micro-islands for stretchable electronic applications”, International Conference on Electronic Materials and Nanotechnology for Green Environment 2014 (ENGE 2014), Jeju, Korea, November (2014).

2. **J. Byun**, S. Kim, S. Chung, Y. Hong, “High-performance stretchable silver electrode with scalable inkjet-patterned photo-curable strain modulators”, Materials Research Society (MRS) Fall Meeting, Boston, USA, December (2013).

1. **J. Byun**, S. Kim, S. Chung, H. Im, Y. Hong, “Controlled wrinkling via artificially modulated surface stress using inkjet-printed transparent rigid island structures”, Materials Research Society (MRS) Fall Meeting, Boston, USA, November (2012).

Patents

2. “Forming method of stretchable substrate, stretchable substrate and electronic device having stretchable substrate”, Yongtaek Hong, **Junghwan Byun**, Sangwoo Kim, US patent; US 9565753 B2.
1. “신축성 기판 형성 방법, 신축성 기판 및 신축성 기판을 가지는 전자장치”, 홍용택, **변정환**, 김상우, 10-1541618.

Other Publications

3. Yongtaek Hong, Byeongmoon Lee, Eunho Oh, **Junghwan Byun**, “Stretchable Displays: From Concept Toward Reality”, *Information Display (SID)* **33**, 4, pp. 6-11 (2017).
2. 홍용택, **변정환**, 오은호, 이병문, “전자피부 기술 동향”, 인포메이션 디스플레이 (KIDS) 제17권 제5호, pp. 3-13 (2016).
3. 김상우, **변정환**, 홍용택, “인쇄공정을 이용한 flexible sensor 및 인공피부”, 전자공학회지 제38권 제4호, pp. 299-304 (2011).

국문 초록

전자 소자 및 회로는 일반적으로 단단하고, 깨지기 쉬운 물리적 형태를 지니기 때문에 인간 또는 자연의 부드러운 표면 또는 형태에 융화되기 어렵다. 이러한 점에 입각하여 최근에는 전자 소자 및 회로에 소프트한 성질을 부여하는 연구들이 상당수 진행되어왔으며, 이는 전자공학과 자연 사이의 인터페이스 및 기능적인 측면에서의 간극을 줄일 수 있는 가능성을 제시해왔다. 다방면의 기술들이 집적되어 유연성을 넘어선 신축성 전자공학 구현을 위한 신소재 개발, 구조적 모델링, 및 기반 역학 분석 등을 확립해왔으며, 이에 대한 결과로써 생체 조직 및 기관과 전자 소자 간의 소프트한 인터페이스를 형성하여 생체 신호를 측정하는 가능성들을 제시해왔다. 더 나아가 현재에는 소자 수준의 연구가 아닌 시스템 레벨의 소프트 전자 소자 및 회로 집적에 관한 연구에 상당수 초점이 맞춰져 있다. 그럼에도 불구하고, 기존 연구들의 접근 방식은 상당 부분이 소프트 전자 시스템의 배선 및 센서 부위에 대해서만 연구가 국한되어있으며, 통합된 시스템의 필수 요소들인 데이터 연산부의 소프트화에 대한 인식 및 방법론이 극히 미미한 실정이다. 따라서 기존 연구들은 소프트 센서 등으로부터 받아들인 데이터들의 처리를 물리적으로 분리되어있는 단단한 연산 처리 회로 및 PC 등에서 수행했으며, 이를 위한 다수의 와이어들의 이용이 불가피하였다. 이러한 한계점들은 데이터 연산 회로 및 컴퓨팅 시스템을

소프트한 형태로 집적하는 기술의 부재로부터 야기되었으며, 이는 시스템 수준의 신축성 전자공학의 진보를 가로막았다.

본 학위 논문에서는 “통합된 전자 피부” 라는 개념을 도입하여 센싱, 고속 데이터 연산, 맞춤형 신호 처리 및 무선 RF 통신과 같은 통합된 기능성을 소프트화하는 연구를 진행하여 앞서 언급한 기술적 간극들을 탈피하였다. 이 개념을 통하여서는, 데이터 전송을 위한 다수의 와이어들과 데이터 연산을 위한 물리적으로 분리되어있는 단단한 연산 처리 회로 및 PC의 사용 대신, 그 모든 기능들을 소프트한 플랫폼 상에 집적시켜 하나의 통합된 전자 피부 내에서 진행할 수 있다. 특별히, 방법론적으로는 전 인쇄 공정을 이용하여 표면 실장형 전자소자들의 안정적인 집적을 위한 소프트 기판의 표면 변형률 제어 기법과 소프트 기판 상에 신축성 전자 회로 시스템을 제작하는 기법을 확립시켰다. 소프트 기판의 표면 변형률 제어 기법에 관련해서는, 인쇄 공정 기법을 이용하여 만든 PMMA 물질 기반의 “Printed Rigid Islands” 라는 개념을 도입하여 소프트 기판 상의 선택적 변형률 제어를 가능하게 하였으며, printed rigid island의 형태 제어 및 그에 따른 표면 변형률 분석을 통해 구조 최적화를 진행하였다. 이렇게 변형률이 제어된 소프트 기판 상에 인쇄 공정을 기반으로 신축성 전자 회로를 설계하고 제작하는 기술로는, 잉크젯 프린팅 기법으로 인쇄된 다층 구조의 배선망 형성 기술, 이미지를 바탕으로 진행하는 맞춤형 회로 라우팅 기술, 그리고 에폭시 기반의 단단한 표면 실장용 소자 집적 기술이 개발되었다. 이 모든 기술들이 통합되어 전 인쇄 공정으로 하이브리드 타입의 신축성 전자 시스템 제작을 위한 최적화된 방법론을 제시하였다. 이 방법의

효용성을 입증하기 위하여 다양한 레이아웃을 갖는 시스템 레벨의 소프트 전자 회로를 제작하였다.

본 논문에서 개발한 인쇄 공정 기반의 신속한 소프트 회로 제작 기술은 기존에 보고된 어떠한 기법보다도 훨씬 손쉬운 표본 제작 및 소프트 기판 상의 고속 연산과 다양한 기능성 구현에 강점을 보이며, 따라서 상당히 복잡한 수준의 집적 회로 네트워킹도 소프트한 레이아웃으로 형성할 수 있는 가능성을 지녔다. 이러한 관점에서, 본 연구는 소프트 전자 시스템의 기능성을 고집적화 및 고속 연산이 피부 내에서 가능한 자가 연산 전자 피부로 확장시켰다. 특별히, 양면 집적 기술을 고안하여 전 인쇄 공정 기반, 양면 집적된 신축성 1 MHz 구동 컴퓨팅 회로를 최초로 제작하였다. 뿐만 아니라, 이러한 통합된 전자 피부 기술은 기존의 소프트 로봇 분야의 드라이빙 회로로 사용되던 크고 단단한 전자 회로들을 소프트한 전자 피부 한 장으로 대체할 수 있는 가능성을 제시하였다. 실제 생명체 모델들의 신경 전달 및 그에 따른 근육의 움직임에 착안하여, 소프트한 몸체에 온전히 집적되어 전자 신경망을 형성하는 개념의 신경망 형성 전자 피부라는 개념을 도입하였으며, 소프트한 사용자 인터페이스(UI)와 결합시켜 전자 피부들만으로 소프트 로봇을 무선으로 제어할 수 있는 기술을 최초로 보고하였다.

본 학위 논문은 완전한 신축성 전자 시스템 구현에 가장 큰 걸림돌이었던 신축성 컴퓨팅 회로 구현에 대한 방법론적 해결책을 제시했다는 데에 의의가 있다. 뿐만 아니라, 최초로 제시된 신경망 형성 전자 피부 개념은 소프트 로봇 분야 이외에도 향후 연구될 소프트한

사물 인터넷 (IoT) 및 생체, 자연과의 교감에도 큰 영감을 줄 것으로 기대한다.

주요어 : 신축성 전자공학, 전자 피부, 인쇄 전자공학, 피부 컴퓨터,
소프트 로봇

학번 : 2011-20858